



MONASH UNIVERSITY

School of Chemistry

**Surfactant mediated control of aqueous graphene oxide
dispersions**

Thomas Malcolm McCoy

A thesis submitted for the degree of *Doctor of Philosophy* at Monash University

August 2018

To my parents,

Copyright notice

© Thomas Malcolm McCoy (2018).

I certify that I have made all reasonable efforts to secure copyright permissions for third-party content included in this thesis and have not knowingly added copyright content to my work without the owner's permission.

Abstract

The work presented in this thesis focuses primarily on aqueous dispersions of 2-dimensional carbon nanomaterials, surfactants, and synergistic effects between the two. The carbon nanomaterials investigated in this work are two oxidised analogues of graphene, known as graphene oxide and reduced graphene oxide. These materials feature the atomically thin carbon lattice of graphene, however, it is functionalised with oxygen groups that render the materials hydrophilic, and thus dispersible in water. Surfactants are incorporated into aqueous dispersions of these carbon nanomaterials as a facile means to induce specific colloidal effects, such as particle flocculation and adsorption at interfaces.

The experiments to unpick the complex relationships between surface chemistry, intermolecular interactions, self-assembly and interfacial thermodynamics for these systems involved a broad combination of experimental techniques, including small-angle scattering measurements for the analysis of bulk properties, and a combination of reflectivity and tensiometry measurements to interrogate interfacial properties. Imaging techniques such as atomic force microscopy and optical microscopy were also exploited for characterisation purposes. These techniques and their foundational theory are discussed in Chapter 3.

The first results chapter (Chapter 4), presents a novel method for controlling the dispersion of graphene oxide and reduced graphene oxide sheets in aqueous solution using light. The method utilises an oppositely charged, photo-switchable surfactant molecule that readily adheres to the surfaces of the sheets, causing them to aggregate. The system can then be irradiated with ultraviolet light, inducing a structural change in the adsorbed surfactant molecules that renders them more water soluble. A significant proportion of the surfactants subsequently desorb from the sheets, allowing them to redisperse. The method is completely reversible, as blue light can then be used to recapture the sheets.

Chapter 5 explores the physical basis for achieving spontaneous adsorption of graphene oxide sheets at the air–water interface. This effect occurs synergistically by using a cationic surfactant at ideal ratios with graphene oxide. Adsorption of the surfactant to the sheets results in a surface active composite that readily locates at the air–water interface over time. The surfactant used is photo-responsive, providing a mechanistic probe for conflating surfactant chemistry with interfacial activity. The system is also capable of stabilising oil–in–water emulsions, with much higher efficiency than either component independently.

A comprehensive study combining a broad array of structurally diverse surfactant and polymer compounds with aqueous dispersions of graphene oxide and reduced graphene oxide is presented in Chapter 6. The approach provides a systematic overview of how various compounds that differ in key chemical aspects will interact with these materials in a bulk aqueous phase. In systems where surfactant adsorption occurs, evidence of sheet flattening in solution is apparent from the scattering data, an effect dubbed ‘nano-ironing’. Polymer adsorption to these materials appeared to be more

entropic in origin compared to the surfactants, favouring interaction with reduced graphene oxide over graphene oxide to minimise solvent interactions.

The final results chapter (Chapter 7) presents the optimisation of a method for capturing graphene oxide sheets from aqueous solution by froth flotation. A common cationic surfactant is first deployed to cause aggregation of the sheets by neutralising their surface charge, and increasing their surface activity. Ultrasonication is then performed to generate bubbles in the solution that the surfactant-coated sheets can adhere to, causing them to separate in the form of a concentrated foam or froth above the bulk solution.

The Appendices present an additional theme that is tangential to the main theme of the thesis. The theme concerns the self-assembly of two zwitterionic betaine surfactants that spontaneously form viscoelastic wormlike micelles in solution, and how this structure as well as the properties of the fluid change when exposed to a variety of scientifically (and industrially) relevant additives. In Appendix A, the betaine surfactant is mixed with a series of oils, salts and (co-)surfactants, yielding a rich array of nanostructures including disks, spheres and rods, and even vesicles and branched wormlike networks. The final structure is hypothesised to be dictated by the specific partitioning of the additive within the micellar structure. In Appendix B, a more systematic study investigating changes in the self-assembly and rheology of a slightly shorter chain betaine surfactant in response to a series of organic additives is shown. Again, the specific partitioning of the additives within the micelles is key with regards to the internal structure. However, significant differences in fluid viscosity are also observed when polar additives with resonance stabilising effects were incorporated, believed to stem from intermolecular interactions between the surfactant and additive that inhibit the ability of the micelles to break apart and reform.

Publications during enrolment

1. **Thomas M. McCoy**, Amelia C. Y. Liu and Rico F. Tabor, Light-controllable dispersion and recovery of graphenes and carbon nanotubes using a photo-switchable surfactant. *Nanoscale*, 2016, **8**, 6969-6974.
2. **Thomas M. McCoy**, Alsu Valiakhmetova, Matthew J. Pottage, Christopher J. Garvey, Liliana de Campo, Christine Rehm, Dmitry A. Kuryashov and Rico F. Tabor, Structural Evolution of Wormlike Micellar Fluids Formed by Erucyl Amidopropyl Betaine with Oil, Salts, and Surfactants. *Langmuir*, 2016, **32**, 12423-12433.
3. **Thomas M. McCoy**, Stephen A. Holt, Ashley M. Rozario, Toby D. M. Bell and Rico F. Tabor, Surfactant-Enhanced Adsorption of Graphene Oxide for Improved Emulsification of Oil in Water. *Adv. Mater. Interfaces*, 2017, **4**, 1700803.
4. **Thomas M. McCoy**, Huw C. W. Parks and Rico F. Tabor, Highly efficient recovery of graphene oxide by froth flotation using a common surfactant. *Carbon*, 2018, **135**, 164-170.
5. **Thomas M. McCoy**, Liliana de Campo, Anna V. Sokolova, Isabelle Grillo, Ekaterina I. Izgorodina and Rico F. Tabor, Bulk properties of aqueous graphene oxide and reduced graphene oxide with surfactants and polymers: adsorption and stability. *Phys. Chem. Chem. Phys.*, 2018, **20**, 16801-16816.
6. **Thomas M. McCoy**, Joshua P. King, Jackson E. Moore, Veena T. Kelleppan, Anna V. Sokolova, Liliana de Campo, Madhura Manohar, Tamim A. Darwish and Rico F. Tabor, The effects of small molecule organic additives on the self-assembly and rheology of betaine wormlike micellar fluids. *J. Colloid Interface Sci.*, 2019, **534**, 518-532.

Declaration: Thesis including published works

I hereby declare that this thesis contains no material which has been accepted for the award of any other degree or diploma at any university or equivalent institution and that, to the best of my knowledge and belief, this thesis contains no material previously published or written by another person, except where due reference is made in the text of the thesis.

This thesis includes 6 original papers published in peer reviewed journals. The core theme of the thesis is functional materials based on graphene oxide and surfactants in synergy. However, there is an additional theme in the Appendices focussed on complex fluids and self-assembly.

The ideas, development and writing up of all the papers in the thesis were the principal responsibility of myself, the student, working towards the degree of Doctor of Philosophy under the supervision of Dr Rico Tabor.

The inclusion of co-authors reflects the fact that the work came from active collaboration between researchers and acknowledges input into team-based research.

In the case of Chapters 4, 5, 6, 7, **Appendix A** and **Appendix B** contributions to the work involved the following:

Thesis Chapter	Publication Title	Status	Nature and % of student contribution	Co-author name(s) Nature and % of Co-author's contribution*	Co-author(s), Monash student Y/N*
4	Light-controllable dispersion and recovery of graphenes and carbon nanotubes using a photo-switchable surfactant	Published	95%, Concept development, data collection and analysis, writing first draft	1) Amelia C. Y. Liu, 5%, TEM	N

5	Surfactant-Enhanced Adsorption of Graphene Oxide for Improved Emulsification of Oil in Water	Published	95%, Concept development, data collection and analysis, writing first draft	1) Stephen Holt, 3%, reflectivity guidance, BAM 2) Ashley Rozario, 1%, widefield microscopy 3) Toby Bell, 1%, widefield microscopy	N Y N
6	Bulk properties of aqueous graphene oxide and reduced graphene oxide with surfactants and polymers: adsorption and stability	Published	95%, Concept development, data collection and analysis, writing first draft	1) Liliana de Campo, 2%, beamline support 2) Anna Sokolova, 1%, beamline support 3) Isabelle Grillo, 1%, beamline support 4) Ekaterina Izgorodina, 1%, concept explanation	N N N N
7	Highly efficient recovery of graphene oxide by froth flotation using a common surfactant	Published	65%, Concept development, data analysis, experimental design, some experiments, writing first draft	1) Huw Parks, 35%, lab experiments	N
Appendix A	Structural Evolution of Wormlike Micellar Fluids Formed by Erucyl Amidopropyl Betaine with Oil, Salts, and Surfactants	Published	80%, Data collection and analysis, writing first draft	1) Alsu Valiakhmetova, 15%, concept development, viscometry, materials synthesis 2) Matthew Pottage, 1%, beamline support 3) Chris Garvey, 1%, beamline support 4) Liliana de Campo, 1%, beamline support 5) Christine Rehm, 1%, beamline support 6) Dmitry Kuryashov, 1%, concept development	N Y N N N N
Appendix B	The effects of small molecule organic additives on the self-assembly and rheology of betaine wormlike micellar fluids	Published	85%, Concept development, data collection and analysis, writing first draft	1) Joshua King, 10%, rheology measurements 2) Jackson Moore, 1%, beamline support, surfactant synthesis 3) Veena Kelleppan, 1%, surfactant synthesis 4) Anna Sokolova, 1%, beamline support 5) Liliana de Campo, 2%, beamline support 6) Madhura Manohar, 1%, surfactant synthesis 7) Tamim Darwish, 1%, surfactant synthesis	N Y N N N N

I have renumbered sections of submitted or published papers in order to generate a consistent presentation within the thesis.

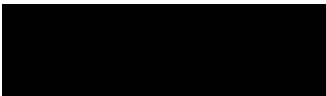
Student signature:



Date: 7/6/2018

The undersigned hereby certify that the above declaration correctly reflects the nature and extent of the student's and co-authors' contributions to this work. In instances where I am not the responsible author I have consulted with the responsible author to agree on the respective contributions of the authors.

Main Supervisor signature:



Date: 13/6/2018

Acknowledgements

My PhD has been nurtured and supported by a great number of incredible people that have helped me achieve more than I knew I was capable of, and this thesis marks the fruition of their tireless and devoted collaboration. At the apex of that human pyramid is my supervisor Rico. He has not only been the perfect role model and mentor to me, but also an exceptional friend, and the amount I've gained from his teachings and support is more than I could possibly repay. From the bottom of my heart Rico, thank you.

In addition, I have also been incredibly fortunate to be apart of a fantastic research group. The people I was surrounded by were all warm and easy-going, and it made for the ideal working environment. A huge part of the success I've had is because of them. In particular, I would like to thank Huw Parks and Josh King for their significant contributions to my work that essentially enabled me to write two extra papers in my final year. Also deserving of special mentions are Jackson Moore and Josh Marlow, for their assistance during rigorous neutron experiments.

A huge thank you to my beamline scientists Lela de Campo, Anna Sokolova and Stephen Holt. For not only constantly giving me bonus instrument time, but going well and truly over and above in helping me make my scattering experiments successful. Also, many thanks to Katya Pas and Toby Bell for their support and guidance throughout my development as a scientist.

This research was supported by an Australian Government Research Training Program (RTP) Scholarship. I would also like to acknowledge the Australian Institute of Nuclear Science and Engineering, the Monash Centre for Atomically Thin Materials, and Monash University for funding and endorsing my PhD.

Lastly, to my amazingly supportive, considerate and loving family, the demands that my university endeavours have required of me have been infinitely more manageable because of all of you. Uncle Pete, Paola and Aunty Julie, your continued interest and encouragement has meant the world to me. My big brother Ben, and my big sister Kathryn, thank you both for being such good friends to me and supporting me unconditionally. And finally, to mum and dad, thank you so much for everything. Much love to you all.

Contents

Contents	11
1 Introduction	13
1.1 2D carbon nanomaterials	13
1.2 Surfactants	14
1.2.1 Photoswitchable surfactants	15
1.3 Surface activity of 2D carbon nanomaterials	16
2 Literature review – Interfacial properties of graphene oxide: surfactant or particle?	18
2.1 Graphene oxide chemistry: variability and aqueous dispersibility	18
2.2 Graphene oxide interfacial activity	21
2.2.1 Air–liquid interfaces	22
2.2.2 Liquid–liquid interfaces	23
2.3 Concluding remarks	25
3 Instrumental methodology	26
3.1 Bulk scattering techniques	26
3.1.1 Small and ultra-small-angle neutron scattering	26
3.1.2 Dynamic and phase analysis light scattering	30
3.2 Surface techniques	34
3.2.1 Pendant drop tensiometry	34
3.2.2 X–ray reflectivity	35
3.3 Imaging techniques	37
3.3.1 Atomic force microscopy	37
3.4 Spectroscopic techniques	40
3.4.1 Ultraviolet–visible spectrophotometry	40
Bibliography	42
4 Light-controllable dispersion and recovery of graphenes and carbon nanotubes using a photo-switchable surfactant	51
5 Surfactant-Enhanced Adsorption of Graphene Oxide for Improved Emulsification of Oil in Water	86

6	Bulk properties of aqueous graphene oxide and reduced graphene oxide with surfactants and polymers: adsorption and stability	125
7	Highly efficient recovery of graphene oxide by froth flotation using a common surfactant	163
8	Conclusions and future directions	181
	Appendices	186
A	Structural Evolution of Wormlike Micellar Fluids Formed by Erucyl Amidopropyl Betaine with Oil, Salts, and Surfactants	187
B	The effects of small molecule organic additives on the self-assembly and rheology of betaine wormlike micellar fluids	207

Chapter 1

Introduction

1.1 2D carbon nanomaterials

Atomically thin layers of carbon, or ‘graphene’ as they are now better known, have become a subject of intense interest since their discovery and isolation more than a decade ago.^{1,2} This sheet-like substrate comes from the very cheap and naturally occurring material graphite, which is a 3-dimensional assembly of stacked carbon monolayers;³ each of these single layers can be considered a single sheet of graphene, and can be obtained by various methods,⁴ most commonly the mechanical exfoliation of graphite⁵ and chemical vapour deposition,⁶ both of which are low yielding. Graphene is almost entirely composed of sp^2 hybridised carbon atoms arranged in a planar, honeycomb lattice (Fig. 1.1). As a result of this bonding geometry and surface-wide delocalisation of electrons, graphene sheets possess extraordinarily high mechanical strength and conductivity.² These properties make graphene an extremely appealing material for many applications including electronics, energy storage and composite materials.^{3,7,8}

However, graphene is extremely hydrophobic, and hence it aggregates in water without the aid of surfactant or polymer stabilisers.^{9–13} This makes its handling, processing and use in aqueous systems considerably less practical, as the stabilisers not only increase the expense, but can also inhibit the action of the sheets themselves. Thus, alternatives to pure graphene are required if 2-dimensional materials are to be practical candidates for solution-based applications.^{14,15} Such alternative materials include colloidal suspensions of graphene oxide (GO) and reduced graphene oxide (rGO), both of which are derivatives of graphene (Fig. 1.1), and dispersible in water.^{16,17}

Graphene oxide is usually produced by the aggressive oxidation of graphite flakes in concentrated sulfuric acid using potassium permanganate, a process known commonly as the Hummers method.¹⁸ The resultant product is similar to graphene in that it has an underlying sheet-like carbon structure, however the carbon sheet is functionalised with polar, oxygen-containing groups. These take the form of carboxylic acid groups located around the periphery of the sheets, and epoxy and hydroxy groups that appear on the basal plain.^{19,20} These groups make GO sheets much more hydrophilic than graphene, and give the sheets a large negative surface charge through deprotonation of the periphery carboxylic acid groups.^{21,22} Therefore GO readily disperses in water and has an enhanced stability

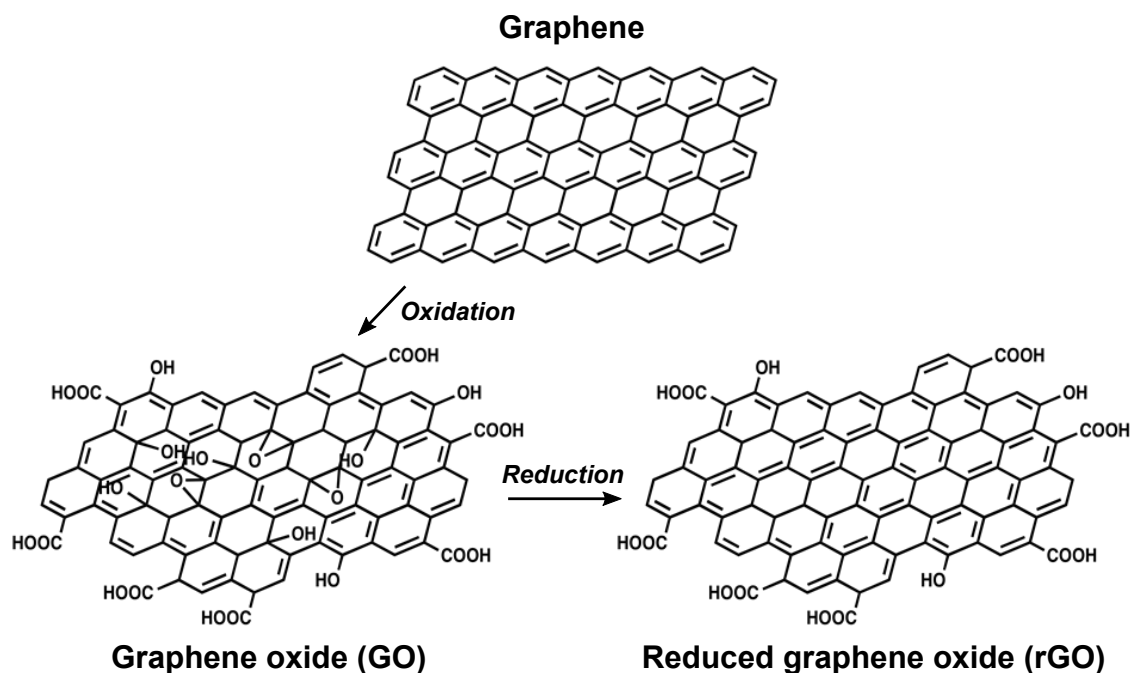


Figure 1.1: Exemplar structures of graphene, graphene oxide (GO) and reduced graphene oxide (rGO).

against flocculation through electrostatic repulsion between sheets. The conductive properties of graphene are mostly removed by these changes, although electrical conductivity is often not required in aqueous processing. Thus, GO has its own unique set of potential applications in water treatment,^{23,24} stabilisation of interfaces^{25–27} and biosensing,¹⁵ for which conductivity is non-essential. Reduced graphene oxide is also a useful and promising material that can exist as a stable aqueous dispersion, and is obtained by the reduction of GO.^{21,28} During reduction, a significant proportion of the oxygen functionality is removed, and the resultant product occupies an intermediate state between graphene and GO. Therefore, without added stabilisers, pure rGO is not as stable in water as pure GO. However, due to the restoration of aromaticity on the basal plane, it is much more electrically conductive than GO, and thus is considered to be a viable route to the large scale production of graphene-like materials through chemical exfoliation.²⁹ GO and rGO are the central carbon nanomaterials used in this project, and are synthesised using the modified Hummers’ method that was published by Marcano and co-workers for GO,³⁰ and the hydrazine reduction method by Li and co-workers to reduce GO into rGO.²¹

1.2 Surfactants

Surface active agents or surfactants present another class of material that are of great interest to the field of physical chemistry due to the unique set of properties they exhibit in solution. Their high capacity for adsorbing at interfaces, as well as their ability to self-assemble into a diverse variety of molecular aggregates or micelles, make surfactants extremely useful in applications associated with stabilisation, encapsulation and nanoscale templating.³¹ Hence, there is constant

drive to develop and understand new and improved systems exploiting their properties. The key characteristic underpinning the behaviour of these molecules is their amphiphilic structure. Surfactants possess a hydrophilic head-group, and a hydrophobic tail-group (Fig. 1.2). Therefore, when dissolved in aqueous solution, their adsorption at the interface, be it solid-liquid (*i.e.* particle-water), liquid-liquid (*i.e.* oil-water) or gas-liquid (*i.e.* air-water), is often energetically favoured (spontaneous) because the interface allows the surfactant to minimise solvent interactions with their hydrophobic regions, lowering the interfacial free energy of the system.^{32,33} Surfactants therefore have a thermodynamic drive to interact with materials in solution to yield interesting and potentially useful noncovalent composite materials that spontaneously self-assemble.

Surfactants are typically classed as being cationic, anionic, nonionic or zwitterionic depending on the nature of the their head-groups (Fig. 1.2), and the introduction of branching or additional carbons to their tail-groups offers a means to alter their hydrophobicity.³⁴ Therefore, by systematically altering their key physical characteristics, surfactants provide an almost unlimited library of molecules for exploring and understanding molecular interactions and self-assembly with a specific material. This not only provides key chemical insight into the nature and behaviour of the material itself, but also the ability to tailor and optimise composite systems towards a particular application, mediated by the choice of surfactant.

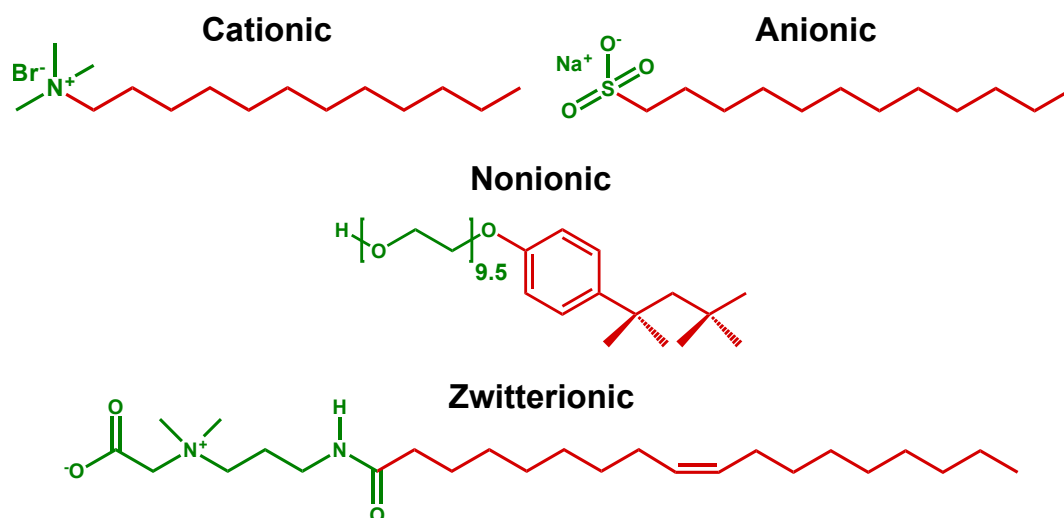


Figure 1.2: Exemplar structures of a cationic surfactant (dodecyltrimethylammonium bromide), anionic surfactant (sodium dodecyl sulphate), nonionic surfactant (Triton X-100) and zwitterionic surfactant (oleyl amidopropyl betaine) used in this project. The hydrophilic head-groups are shown in green and hydrophobic tail-groups in red.

1.2.1 Photoswitchable surfactants

An interesting subset of surfactants are so-called photoswitchable surfactant molecules. Due to the incorporation of a photo-responsive chromophore such as azobenzene, these molecules can undergo reversible structural reconfigurations, often between a *trans* and *cis* geometric isomer,

depending on the specific illumination conditions.³⁵ For surfactants with these functional groups incorporated into their tail-groups, this isomerisation is accompanied by marked changes in surfactant properties, such as altered surface activity and aggregate morphologies, due to the significant difference in dipole moment between the two isomers.^{36–38} This light-induced isomerisation is shown for a well known cationic photosurfactant, azoTAB (Fig. 1.3), which is used in this project to enable *in situ*, photo-responsive control of aqueous GO and rGO dispersions in bulk solution and at interfaces. Photosurfactants have the added advantage of serving as mechanistic probes for adsorption phenomena in colloidal systems, as the substantial differences in the physical properties for the two isomers provides a well-defined reference point for understanding the predominant chemical interactions that dictate the overall behaviour of a given system.

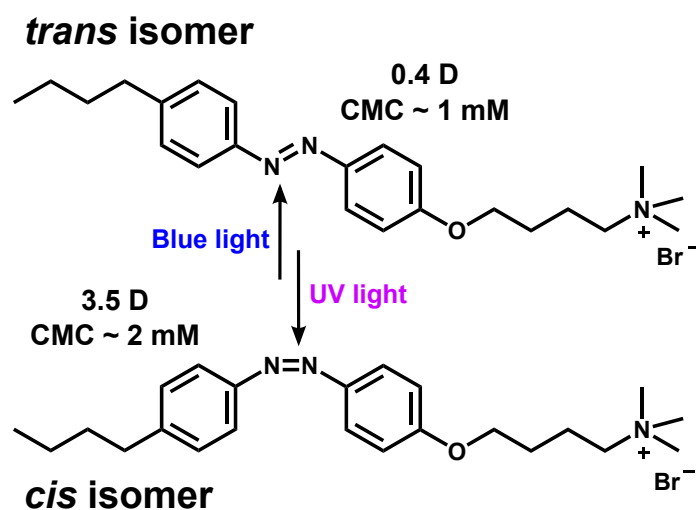


Figure 1.3: Chemical structure of butyl-phenyl-4-diazeno-4-butoxyphenyltrimethylammonium bromide (azoTAB) and its reversible photo-induced isomerisation between the *trans* and *cis* isomers.

1.3 Surface activity of 2D carbon nanomaterials

GO and rGO, like surfactant molecules, are thought of as having amphiphilic structures in which the periphery of the sheets are hydrophilic, and the basal plain is hydrophobic.^{39,40} This structural characteristic to some extent explains why GO is able to locate at interfaces and stabilise oil-in-water emulsions.²⁶ However, the stability of such emulsions has been found to be strongly pH dependent, with adsorption of the sheets only occurring when driven by intense sonication or sparging,^{27,40} and not significantly impacting interfacial tension.⁴¹ In this regard, GO can be thought to be behaving as a particle, as surfactant adsorption at the interface generally occurs spontaneously without the need for the external input of energy.

Therefore, the major theme of this thesis involves the incorporation of surfactants with GO and rGO materials, with the goal of not only gaining a deeper understanding of the bulk and interfacial behaviour of aqueous GO and rGO dispersions, but also to develop new and effective, interfacially

active composite materials that synergistically enhance the unique advantages of both GO and surfactants, overcoming the limitations of each material on their own. The surface activity of these carbon nanomaterials and how this can be modulated is discussed in detail in the proceeding chapter.

Chapter 2

Literature review – Interfacial properties of graphene oxide: surfactant or particle?

Graphene oxide (GO) is a two-dimensional material that can be obtained by the oxidation of graphite.^{18,30} Research surrounding this material surged after the discovery of graphene,² as GO was posited to offer a chemical route to scalable graphene production.⁴² However, GO itself has also received considerable research interest due to its own unique properties. The main property for focused discussion in this review is the amphiphilic nature of GO, and how this relates to its ability to act as a stabiliser. Several in depth reviews that report on this topic have already been published.^{43–45} However, although GO is clearly capable of stabilising interfaces of various types, there is little consensus on the underlying thermodynamics, with many literature sources claiming that GO is surfactant-like in nature, and others stating that it is a Pickering or particle-type stabiliser. Therefore, this short review aims to highlight and discuss the key literature surrounding the colloidal and interfacial properties of aqueous GO dispersions, and address whether the material is more akin to a surfactant or a particle from a fundamental perspective, isolating the possible reasons for the apparently conflicting results seen in the extant literature.

2.1 Graphene oxide chemistry: variability and aqueous dispersibility

The most commonly accepted structure of GO sheets is a continuous and atomically thin, two-dimensional array of carbon atoms that is functionalised with epoxy and hydroxy groups on the carbon basal plane, and carboxy groups around the edges.^{20,46} As a significant proportion of the basal plane is believed to still comprise sp^2 carbon domains,⁴⁷ these regions of the sheets are thought to be relatively hydrophobic, whereas the highly acidic edge regions are proposed to be hydrophilic.⁴⁰ Therefore, GO is considered to have an amphiphilic structure.^{26,40,44}

There are several well known synthetic procedures for oxidising bulk graphite to produce GO.²⁰ The Hummers method is the most commonly used today, and involves reacting natural graphite

flakes in a mixture of concentrated sulfuric acid and potassium permanganate.¹⁸ Marcano and co-workers developed a modified version of Hummers' method that includes a tenth proportion of concentrated phosphoric acid by volume in addition, and this is seen to improve the oxidation process.³⁰ The interlayer spacing between sheets increases as a result of the oxidation process, resulting in a material commonly called graphite oxide, and water can then be used to exfoliate individual sheets of GO from this into an aqueous dispersion.⁴⁸ Due to the variety of chemical procedures for synthesising GO and the numerous sources of graphite starting materials available, it can be difficult to make comparisons between many studies with GO, as there is often a high degree of chemical variability between GO products.⁴⁹ The key factors that affect the properties of GO, especially as an aqueous dispersion, are the lateral sizes of the sheets, their level of oxidation and purity of the dispersion, particularly from small (<200 Da), highly oxidised organic fragments.

The dispersibility of GO and rGO in water has mostly been attributed to its strongly charged nature, which arises from deprotonation of the peripheral carboxylic acid groups.^{21,22} The surprisingly low pK_a of these acidic functionalities means that GO retains a negative charge to low pH values. However, its stability in water is still pH dependent, with highly acidic conditions ($pH \leq 1$ for GO) causing the material to aggregate due to protonation, and thus charge neutralisation of the carboxylate groups.^{27,50} Both GO and rGO exhibit negative zeta potentials in water (Fig. 2.1), however the difference in magnitude between the zeta potential of GO and rGO is not hugely significant. Therefore, the differences in their surface charging characteristics does not fully explain the vast differences in dispersibility observed for GO and rGO in water. For instance, GO can form stable hydrogels of concentrations as high as 60 mg/mL.⁵¹ Following GO reduction with hydrazine and elevated temperature, the reduced graphene oxide (rGO) suspension is only stable at concentrations below 0.5 mg/mL.²¹ Therefore, given the substantial difference in dispersion capacity for the two materials, the level of oxidation and thus hydrophilicity of the materials is clearly also a significant contributor to the dispersion of these materials. GO has a substantially higher oxygen content than rGO, and is therefore much more readily processable in aqueous media.

Another important consideration surrounding GO aqueous stability is the ionic strength of the solution. Some studies have shown the tendency of GO and rGO to aggregate in the presence of salt in accordance with classical DLVO theory and the Schulze-Hardy rule.^{52–54} DLVO theory describes the colloidal stability of particles as a balance between attractive Van der Waals forces and repulsive electrical double-layer forces that the particles experience when dispersed.^{55–58} Therefore, when electrolytes are introduced to the dispersion, the surface charge of the particles becomes shielded and the electrical double-layer compresses, allowing shorter range attractive Van der Waals interactions to dominate, causing the particles to aggregate. In addition, the Schulze-Hardy rule states that the destabilisation of the system by salt is modulated by the counter-ion and its valency;^{58,59} for GO and rGO the counterions are the cations present in the system. Chowdhury and co-workers measured the critical coagulation concentrations of 0.01 mg/mL GO at pH 5.5 to be 44 mM with NaCl and 0.9 mM with $CaCl_2$.⁵³ For rGO, the critical coagulation concentration with NaCl was estimated at 30 mM.⁵⁴ These are all characteristic of colloidal 'particles', and the two-dimensional

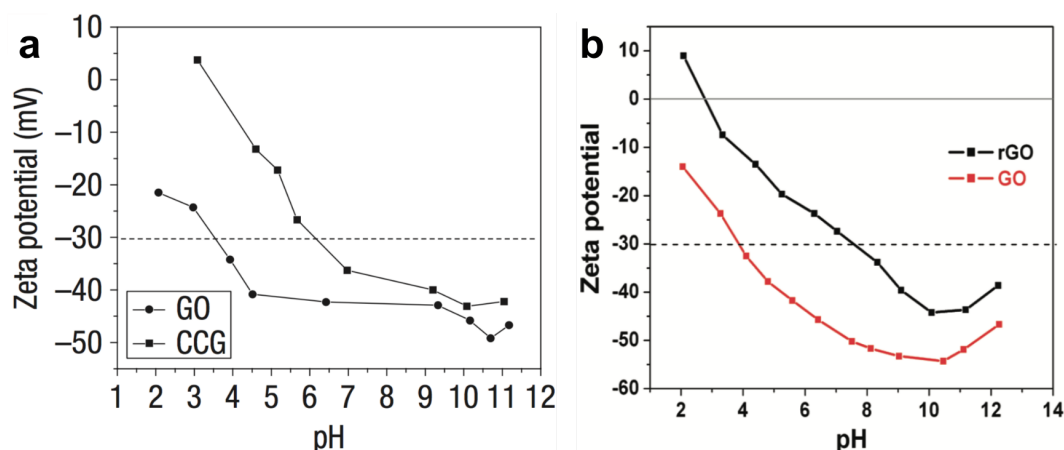


Figure 2.1: (a) Zeta potentials of aqueous GO and chemically converted graphene (rGO) dispersions from Li *et al.*²¹ Reproduced with permission from the Nature Publishing Group. (b) Zeta potentials of aqueous GO and rGO dispersions from Konkena *et al.*²² Reproduced with permission from ACS Publications.

morphology of GO and rGO is believed to add further aid to their aqueous dispersion.⁵²

Again, it is important to note that an individual batch of GO or rGO can exhibit highly different chemical variability from the next.^{45,47} The degree of oxidation for both materials is highly dependent on reaction conditions such as temperature, reaction time, and amount of oxidant/reductant added. Therefore, the pH and salt dependent stability of both GO and rGO materials used in one study can change drastically from those used in another study, and therefore may not be valid for comparison. A consistent method for characterising and comparing separate batches of graphene oxides will thus be essential for the clear understanding and development of these materials.

An alternate perspective on the dispersion of GO in water is the influence of so-called ‘oxidative debris’. This term is used to describe small structures or ‘fragments’ of highly oxidised carbon materials (similar to GO), that noncovalently adsorb to the GO surfaces and facilitate their dispersion by rendering the sheets hydrophilic (Fig. 2.2).⁶⁰ Washing the GO with base ($\text{pH} \geq 12$) can then remove the oxidative debris by dissolution, leaving a much darker dispersion of only slightly oxidised and unstable GO.⁶¹ Strangely however, this effect could not be reversed by readjusting the solution back to neutral conditions. Other studies have attributed the deoxygenation of GO in strongly basic conditions to chemical reactions that result in the formation of CO_2 (*i.e.* reduction).^{62,63}

As the syntheses for GO materials include significant quantities of concentrated acids and oxidising agents, these results emphasise the importance of adequate workup procedures to ensure as much of the spectator ions or additional products such as oxidative debris are removed as possible. Residual contaminants clearly can have significant impacts on the dispersion behaviour of GO, and only add to the difficulty of deciphering the relationship between the highly variable chemical functionality of GO samples that arise from the various preparation routes and starting materials, along with the complex physical chemistry of aqueous GO dispersions.

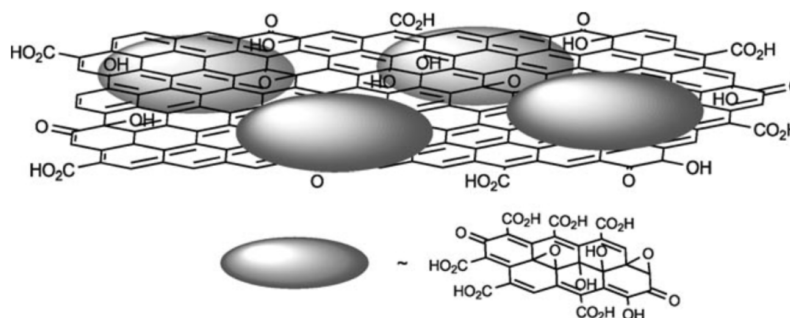


Figure 2.2: (a) Schematic of a GO sheet with adsorbed chunks of stabilising oxidative debris. Reproduced with permission from Wiley Online Library.⁶⁰

2.2 Graphene oxide interfacial activity

The interfacial and stabilising capabilities of GO are now well known, with much of the pioneering work coming from the group of Jiaying Huang at Northwestern University.^{26,40} The main justification put forward for this behaviour is that GO sheets are amphiphilic, in a similar fashion to surfactant molecules, and as such their adsorption at interfaces is spontaneous.^{44,64} This amphiphilicity is considered to be tunable according to three key factors: sheet size, pH and oxidation. Smaller sheets are considered more hydrophilic because they have a larger edge to plain ratio.⁶⁵ Conversely, protonated sheets at low pH and reduced GO sheets are considered more hydrophobic because of their lower charge densities.⁶⁴

Furthermore, at high concentrations (≥ 10 mg/mL), GO has been found to form liquid crystals, a unique form of self-assembly caused by preferential alignment of the sheets in solution due to volume exclusion or reduced configurational entropy effects.^{66–68} Due to the large lateral polydispersity of GO sheets and their unusual structure, consistently sized aggregates or ‘micelles’ are not really feasible, and therefore nematic liquid crystals are the only type of self-assembly that has reliably been observed for GO. This behaviour indicates a more particle-like system again, as many anisotropic particles are known to form liquid crystalline phases without aggregating into typical molecular (surfactant-like) self-assembly structures such as micelles.

Thus far, despite GO’s amphiphilic nature and ability to locate at interfaces, evidence indicates behaviour dominated by particle-like characteristics. Due to its large size, the adsorption of GO at interfaces is less reversible than is typical for molecular surfactants. This is because the energy input required to detach or desorb large particles from interfaces is significantly higher than for small molecules, which constantly redissolve in the bulk solution in a dynamic equilibrium. The additional adsorption energy for particles would be amplified even more for high aspect ratio materials such as GO, a concept familiar from the literature on stabilisation of emulsions by clay platelets. In addition, solid particles do not have to be amphiphilic in order to adsorb at interfaces.⁶⁹ GO is not

like Janus particles, which have very clearly defined regions with opposing chemical characteristics. Even though the basal plane of GO is considered hydrophobic due to small pockets of aromatic carbon groups, the chemical composition is mostly homogeneous in terms of oxygen functionality. Therefore, the surface activity of GO more feasibly originates from the much greater minimum energy required to detach particles from interfaces, which increases dramatically with particle size. This is more akin to a two-dimensional analogue of a patchy particle.

Furthermore, the liquid crystalline character of GO can be justified by the considerable concentrations necessary for the aggregation to take effect, rather than the self-assembly of amphiphilic materials. At sufficiently high concentrations, the sheets are forced to align due to the dense packing in solution: a particle-like behaviour. Also, much larger sheets have been found to form liquid crystals more readily by promoting interactions between sheet faces.^{70,71}

2.2.1 Air–liquid interfaces

Kim and co-workers have shown a method for facilitating the enrichment of GO sheets at the air–water interface by sparging the dispersion with gas bubbles (Fig. 2.3).⁴⁰ N₂ and CO₂ were used to similar outcomes, whereby the microscopic bubbles produced by blowing the gas through fritted glass collected the GO sheets as a flotation process, depositing them at the macroscopic air–water interface above. The authors claim that the GO sheets would locate at the interface slowly over time, however due to their large size regimes, diffusion to the interface would be very slow and the sparging process was simply employed to accelerate their deposition.

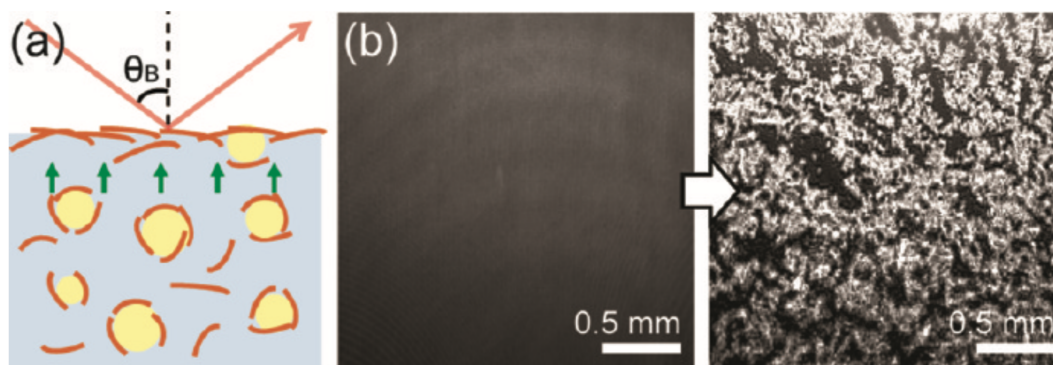


Figure 2.3: (a) Schematic of GO sheets enriching at the air–water interface when sparging with gas bubbles. (b) Brewster-angle microscopy images of the surface of a GO dispersion before and after sparging with gas bubbles. The bright spots are believed to be GO sheets. Reproduced with permission from ACS Publications.⁴⁴

We show later in this thesis however, that GO sheets are too hydrophilic and too strongly charged to spontaneously adsorb at the air–water interface, and thus posit that in the work described above, air–water film deposition of GO would not have occurred without the sparging step. Furthermore, Kim *et al.* performed surface pressure measurements by compressing the air–water interface between two barriers and recorded significant increases in surface pressure after the sparging step.⁴⁰ This indicates

irreversible particle adsorption at the interface, as molecular surfactants tend to re-equilibrate back into the bulk solution during compression because of their small desorption energy, resulting in a zero surface pressure effect. In spite of this fact, the authors state that GO adsorption at interfaces mimics that of molecular amphiphiles.

More recent work has provided additional insight into the adsorption of GO at the gas–liquid interfaces.⁷² Bonatout and co-workers observed assembly of GO at the air–water interface by X-ray reflectivity with increasing surface pressure conditions, claiming adsorption to be spontaneous.⁷³ Measurements were conducted over 5 hours using commercial GO (Sigma), making it difficult to know the exact properties and purity of the material due to unknown workup procedures. Therefore, adsorption of the sheets at the interface may have been affected by solvent evaporation over the long measurement time and potentially impurities in the suspension.

Deposition of rGO thin films has also been reported at the air–water interface by incorporating background salt to screen charge repulsions, indicating that affinity of these materials at the interface is tied with their dispersion stability.⁷⁴ Interestingly, unlike GO, rGO has been found not to exhibit surface pressure effects, believed to be due to the reduced oxygen functionality allowing sheets to slide over one another because of weaker interactions between sheets.⁷⁵ These recent findings further support the particle-like behaviour for GO and rGO.

2.2.2 Liquid–liquid interfaces

GO can also effectively accumulate at liquid–liquid interfaces to stabilise oil-in-water emulsions. This phenomenon was also first noted by Huang’s group using GO to stabilise toluene droplets in water (Fig. 2.4a–g).²⁶ The attributed surfactant properties of GO are again credited with causing adsorption of the sheets at the oil–water interface.^{26,43} However, the emulsions were claimed to be stable for a number of months, corresponding to especially high kinetic stability, not typically observed for surfactant stabilised emulsions (aside from thermodynamically stable microemulsions). The emulsions are thus considered to be particle stabilised or Pickering emulsions,^{76,77} which tend to be much more stable against coalescence due to the higher energies associated with particle desorption from interfaces, and reduced potential for ripening due to interfacial jamming of particles.⁶⁹ The authors claim that in these instances, GO is behaving as a ‘colloidal surfactant’.

A large number of additional studies have been conducted on GO stabilised Pickering emulsions, exploring factors such as pH,²⁷ sonication⁷⁸ and oil phase polarity.⁷⁹ The dispersed phase can also be reversed using rGO to form water-in-oil emulsions.⁸⁰ In the case of pH, emulsification of the oil has been consistently found to occur more readily in extremely acidic conditions (Fig. 2.4h).²⁷ At pH values around 1, the strong negative surface charge of GO is diminished due to protonation of the carboxyl groups, and as a result, the material can pack at the interface much more densely because the interparticle repulsions between sheets are minimised. This has been stated as rendering the GO sheets more amphiphilic, increasing their affinity for the oil–water interface.^{26,44,64} However, an alternative explanation for the pH dependent stability of GO stabilised emulsions is that the

low pH conditions simply lower the hydrophilicity of the sheets, and hence they partition to the interface more readily than when the sheets are strongly charged.

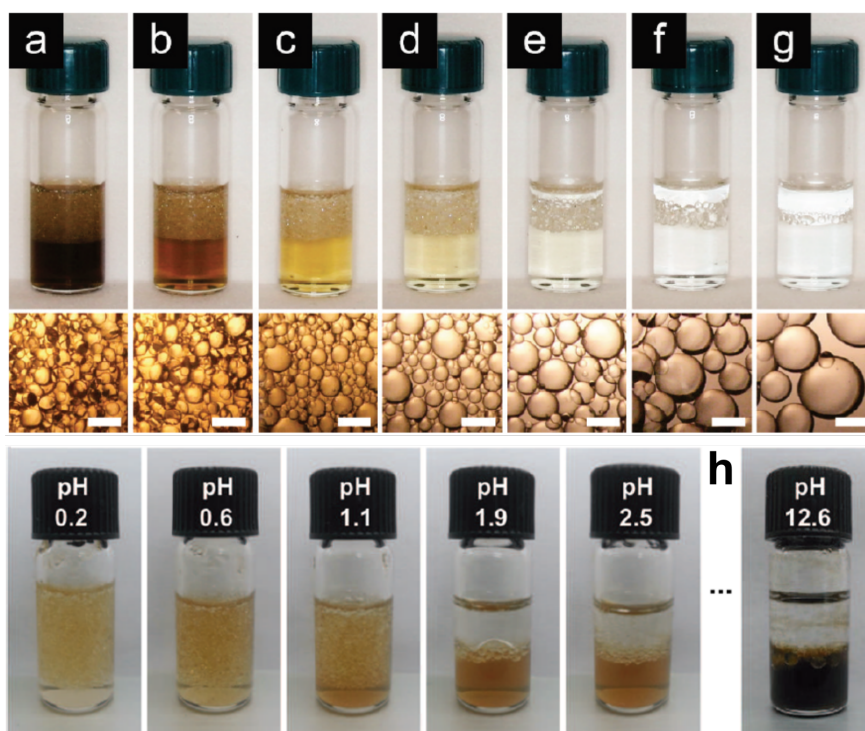


Figure 2.4: (a-g) Oil-in-water emulsions made using different concentrations of aqueous GO dispersion.²⁶ (h) Oil-in-water emulsions generated by vigorous manual shaking of 0.5 mL of toluene and 0.5 mL of aqueous GO dispersion at different pH values.²⁷ Adapted with permission from ACS Publications. The oil is toluene in all samples.

The behaviour of GO at liquid interfaces is clearly particulate in nature (Pickering type), and not surfactant-like, given that emulsions with GO have unprecedented long-term stability and cannot be phase separated by conventional methods. These features clearly stem from the much stronger affinity of particles at interfaces. Furthermore, optical microscopy images of GO stabilised emulsion droplets show large proportions of non-spherical droplets.^{27,78} Molecular surfactants do not form non-spherical emulsion droplets due to interfacial forces,⁸¹ however, large, anisotropic particles at the interface are more rigid, and can deform the drop boundaries.^{69,77} These results again point towards particle, not surfactant properties for GO behaviour at interfaces.

A method for spontaneously enriching GO sheets at oil-water interfaces has been achieved by using surface active polymers to render the sheets more interfacially active.⁸²⁻⁸⁴ In these experiments, a series of diblock copolymers are solubilised in the oil phase, and rapidly adsorb to the interface with aqueous GO dispersion and lower the interfacial tension. The GO sheets then interact favourably with the adsorbed polymer chains and coassemble at the interface to form a film composite. Extraction of the aqueous phase causes the interface to buckle (Fig. 2.5),^{82,83} confirming particle-type adsorption at the interface. Conceptually similar methods for enriching GO at interfaces are explored in this

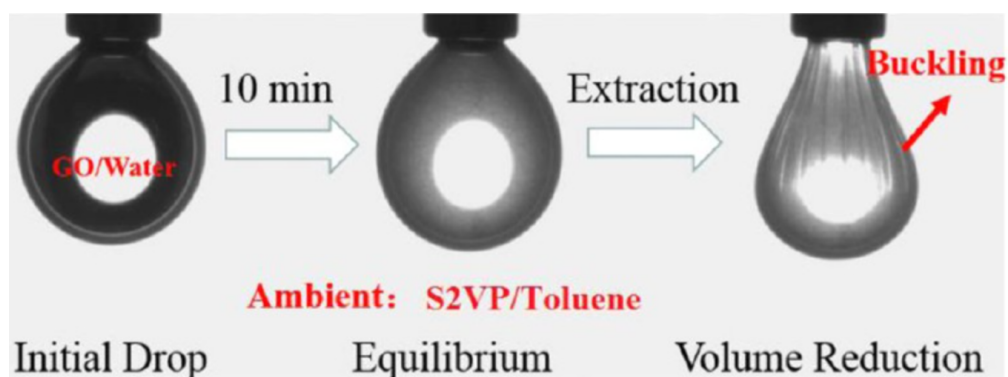


Figure 2.5: Buckling of an aqueous GO pendant drop in a toluene continuous phase upon reducing the drop volume after synergistic adsorption of polymer and GO has occurred at the interface. Reproduced with permission from ACS Publications.⁸²

thesis using molecular surfactants. Here however, the two materials are both dissolved/dispersed in the aqueous phase and examined at the air–water interface as well as the oil–water interface.

2.3 Concluding remarks

The path towards understanding the colloidal and interfacial behaviour of aqueous GO dispersions has seen tremendous progress over the past decade, with numerous breakthrough systems and methods for exploiting GO in the stabilisation of interfaces. A fundamental description of GO that properly categorises and explains the true behaviour of the material is still, we believe, elusive. The current body of literature ascribes molecular surfactant-like characteristics to GO sheets, in order to justify their interfacial properties. Through the work in this thesis, we will show that GO behaves as a colloidal particle, and the key question concerning this material should be not ‘is GO a surfactant or particle?’ but rather ‘in what size regimes does GO behave as a particle, and when does it behave as a molecule?’

Chapter 3

Instrumental methodology

In this chapter, descriptions of the major instrumental techniques and their foundational theory are detailed. Only techniques used extensively in the project are discussed.

3.1 Bulk scattering techniques

3.1.1 Small and ultra-small-angle neutron scattering

Small-angle neutron scattering (SANS) is an experimental technique for analysing the internal structure of materials based on their interaction with, and subsequent scattering of a neutron beam (Fig. 3.1). In a SANS measurement, the incident beam trajectory is perpendicular to the sample (transmission mode), and neutrons scattered by the sample are captured by a position-sensitive detector, and represented as bright spots on the resulting transduced image of the detector. The angle at which the neutrons are scattered in relation to the incident beam is characteristic of the spacing between and orientation of atoms in the sample. Therefore, SANS can be used to determine the size and shape of particles in dispersion, typically between 1 and 100 nm.⁸⁵

For a SANS measurement to be meaningful, the wavelength of the incident neutrons must be smaller than the structures of interest. The nuclei of these structures then essentially can be seen as point scatterers, and an interference (scattering) pattern is captured by the detector that sums the constructive (in phase) and destructive (out of phase) interference from all nuclei in the structures. To account for the wavelength of the incident radiation, the intensity of the scattered neutrons is typically presented as a function of the momentum transfer or scattering vector, q , where:

$$q = \frac{4\pi}{\lambda} \sin \frac{\theta}{2} .$$

Therefore, the scattering angle, θ , and thus the distances within the sample structure are measured relative to the wavelength of the incident neutrons, λ . The scattering vector is an inverse length scale (\AA^{-1}), therefore scattering intensity at lower q values represents larger objects or features.

The extent to which materials scatter radiation is relative to their respective scattering length densities (SLD). In order to distinguish (contrast) the substrate of interest within a sample, its SLD

must be sufficiently different from that of its surroundings (*i.e.* the solvent). Neutrons interact with the nuclei of atoms, opposed to X-rays which interact with their electron clouds. Therefore, small-angle scattering experiments performed with neutrons can provide very different insight on the internal structure of materials compared to an equivalent experiment with X-rays. The neutron SLD of a molecule or material is dependent on the sum of the neutron scattering lengths (b_i) for the atoms present:

$$SLD = \frac{\sum_{i=1}^n b_i}{V_m}$$

where n is the number of atoms and V_m is the molecular or material volume. The scattering length density for X-rays is calculated similarly, however rather than using the neutron scattering length (b_i) of a given element, one must instead multiply its atomic number by the radius of an electron. Neutrons are especially useful for characterising soft matter systems because of the large difference in neutron scattering length between hydrogen and deuterium (-3.74 and 6.67 fm respectively). The incoherent scattering cross section of hydrogen is significantly larger than its coherent scattering cross section, meaning its scattering often counteracts that of the adjacent carbon, oxygen or nitrogen atom (all of which have positive neutron scattering lengths). Hence, by selectively substituting hydrogenous components of a sample with their deuterated analogues, it is possible to control the neutron contrast; this method is known as contrast variation. In this work, solvent H_2O was replaced with D_2O for SANS samples to provide contrast.

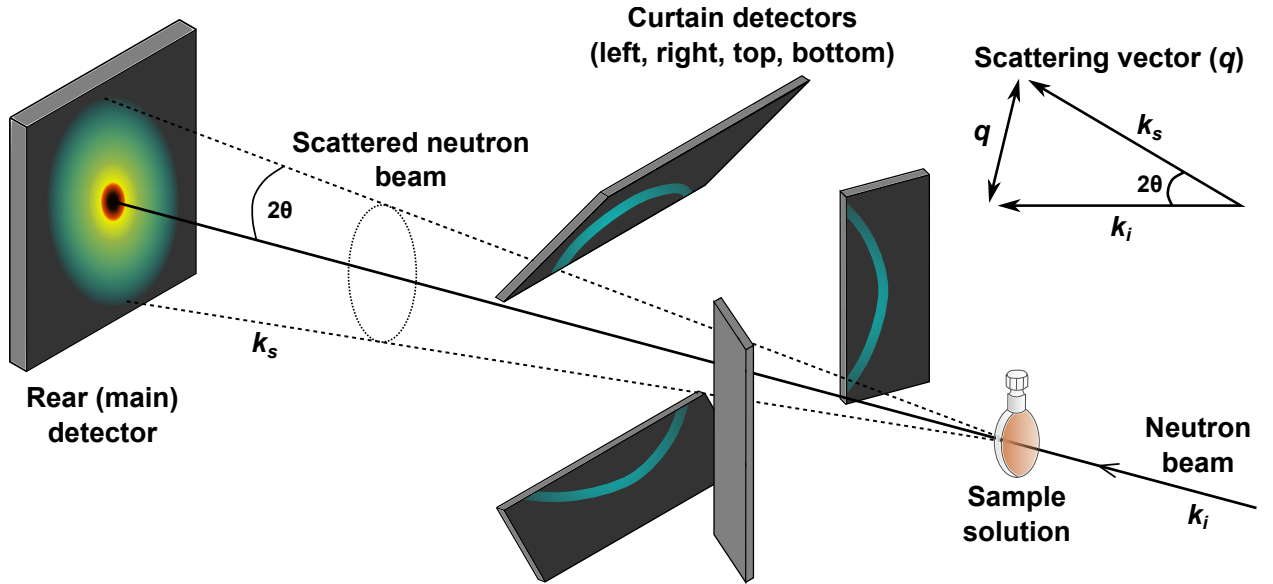


Figure 3.1: Schematic of a small angle neutron scattering measurement. The detector setup is representative of Bilby, the time-of-flight SANS instrument at ANSTO which features 4 curtain detectors in addition to the main rear detector to achieve a large simultaneous q -range. In relation to the schematic, the derivation of the scattering vector, q , is shown in the upper right.

In order to obtain a one-dimensional scattering profile (Fig. 3.2b) from a detector image (Fig. 3.2a), the data contained within a detector image must be reduced. During this process, the measured

counts per pixel on the detector as scattered by the sample are radially averaged to produce absolute intensity profiles. After this, they are then corrected against the neutron wavelength, an empty beam transmission measurement, and a blocked beam scattering measurement. The sample scattering is normalised against the sample transmission so that intensities are consistent, irrespective of measurement time or sample thickness.

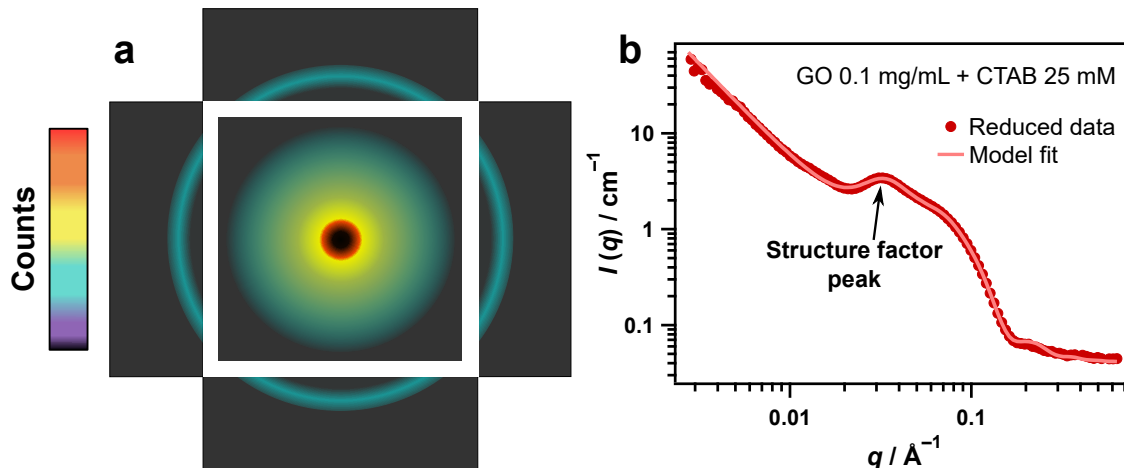


Figure 3.2: (a) A hypothetical two-dimensional detector image produced from a SANS measurement. Scattering is radially isotropic, and a beam stop is positioned in the center of the main detector to absorb transmitted neutrons. (b) A one-dimensional scattering profile obtained from a detector image by reduction of the raw scattering counts.

The SANS instruments used in this project were Bilby⁸⁶ and Quokka,⁸⁷ located at the Australian Centre for Neutron Scattering, Australian Nuclear Science and Technology Organisation (ANSTO). Bilby is a time-of-flight SANS instrument that utilises a range of wavelengths (2–20 Å in this project) to yield a large simultaneous q -range, and higher data resolution compared to conventional, monochromated SANS. Scattering profiles obtained from Bilby are thus an average across some or all of the wavelengths used. Bilby also includes 4 curtain detectors in addition to the main detector (Fig. 3.1), which allows the full q -range to be obtained simultaneously. This is achieved by positioning the main detector far from the sample (18 m) to increase the spacing between small scattering angles (large length scales), while the curtain detectors are positioned nearer to the sample (3 and 4 m) to capture neutrons scattered at large angles (small length scales). Quokka is a monochromatic SANS instrument that utilises a velocity selector to filter neutrons of a specific wavelength (5 Å in this project). Quokka has a single, main detector, and therefore sample scattering must be measured at multiple detector positions (typically 2 and 14 m in this work) in order to obtain a broad q -range. For both Bilby and Quokka, the detectors are kept under vacuum in large tanks to minimise scattering from air molecules.

In principle, ultra-small-angle neutron scattering (USANS) is treated the same as SANS in terms of scattering theory, however it extends the length scale offered by SANS well into the micrometer regime (up to 10 μm). In order to access these extremely low q values, a significantly different

instrument geometry is required (Fig. 3.3a). USANS measurements presented in this work were performed using the Kookaburra beamline at ANSTO.^{88,89}

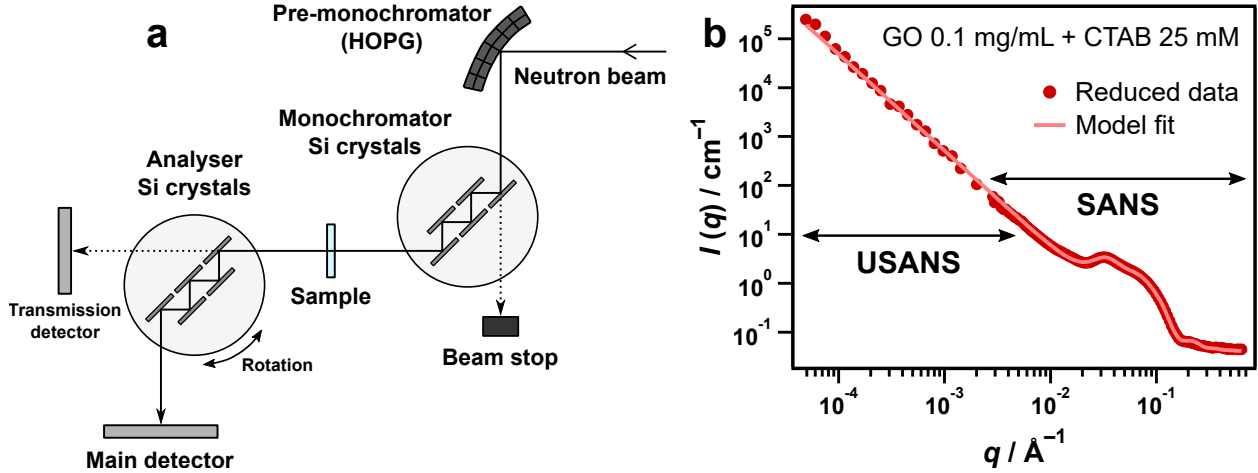


Figure 3.3: (a) Schematic of the key instrumentation and neutron path for Kookaburra, the USANS instrument at ANSTO. (b) Combined SANS and USANS scattering data for the same sample of GO and CTAB surfactant shown in Figure 3.2b.

Kookaburra is a Bonse–Hart diffractometer.⁹⁰ The instrument is designed to channel neutrons with ultra-precise wavelength, and includes a premonochromator made from highly oriented pyrolytic graphite (HOPG), which selectively reflects neutrons approximately 4.74 and 2.37 Å in wavelength, according to its first and second order Bragg reflections respectively. The neutron wavelength used in this work was 4.74 Å, which provides a higher beam intensity than 2.37 Å and thus is more suitable for weakly scattering samples. The beam then passes through another monochromator comprising a quintuple array of defect-free, channel-cut Si crystals (Si(111) for 4.74 Å neutrons), before interacting with the sample (Fig. 3.3a). A second array of identical crystals serves to analyse the small-angle scattering from the sample, by rotating with ultra-high precision to produce a so-called ‘rocking curve’. Scattering onto the detector is therefore obtained at fixed angles, and can be translated into the scattering vector (q).

The size and shape of a particle is predicted from the form factor of the scattering profile,⁹¹ denoted as $P(q)$, which in turn is determined from the scattering pattern on the detector (Fig. 3.2a). The slope of the form factor in the Guinier region (low q) is usually determined by the overall size of the particles.⁹² The Porod region (high q) typically contains the information about the surface.^{93,94} Concentrated systems may also exhibit a structure factor, $S(q)$, in which the interactions between particles become significant.⁹⁵ In these instances, the scattering pattern may show an additional peak, characteristic of a particular (favoured) separation. Using the q value at the maximum of this peak, q_{peak} , the associated distance, d , can be calculated using Bragg’s Law:

$$d = \frac{2\pi}{q_{peak}}$$

The scattering intensity after the structure factor peak may decrease at lower q values if the particles are experiencing repulsive interactions. However, if the interactions are attractive, the particles may aggregate into larger structures, and the intensity at low q will continue to increase. Modelling a structure factor also allows determination of the volume fraction of the particles in dispersion, which relates to the magnitude of the scattering intensity. Therefore, when modelling SANS data without a significant structure factor, an arbitrary scale factor is instead applied to the form factor to allow the model to match the intensities obtained from the measurement. Therefore, the general equation for a scattering profile, $I(q)$, is given by:

$$I(q) = \text{Scale factor} \times P(q)S(q) + \text{background}$$

in which the scale factor equals 1 if $S(q)$ is non-negligible (*i.e.* deviates significantly from 1). Coupling particle interactions and orientations (the structure factor) for non-spherical particles becomes significantly more complex, and as such, the above equation is applicable for spherical particles. The background is a small scattering contribution from the empty cell and solvent, and can be subtracted prior to modelling. Form factors in this work were deduced by microscopy for GO and rGO, and literature results for surfactant systems. Structure factor contributions observed for charged systems were modelled using the Hayter–Penfold mean spherical approximation.^{96–100} An example scattering profile measured using SANS is shown in Figure 3.2b. The structure factor peak originates from a large background concentration of cationic CTAB micelles.

Samples for SANS and USANS in this work were a combination of surfactant solutions and aqueous GO or rGO dispersions in D₂O. Samples were analysed in 2 and 1 mm pathlength quartz cells for SANS and USANS respectively. Modelling of scattering data was performed using the software ‘SasView’ (<http://www.sasview.org>). For all scattering profiles presented throughout this work, solid symbols represent the raw experimental scattering data, and solid lines are model fits generated as described in the text. Specific model details and fitting parameters used are described in the supplementary sections of each results chapter. In all instances, the scattering from either an empty cell or D₂O was subtracted from each data set prior to modelling. Before USANS data can be combined with SANS data, they must be desmeared, which is a data manipulation process that accounts for instrument geometry. This was achieved using a specially developed Igor Pro package.¹⁰¹

3.1.2 Dynamic and phase analysis light scattering

Light scattering techniques can be used for determining the size of particles in a colloidal suspension as well as their zeta potential based on their interactions with light. Dynamic light scattering (DLS) or quasi-elastic light scattering is used for measuring the average size of particles in a dispersion by detecting fluctuations in the intensity of light scattered by the sample as a function of time.¹⁰² A laser is directed at the sample and the detector is positioned at a fixed angle in relation to the incident beam. An angle of 90° is the most conventional because it avoids bias towards certain particles sizes (Fig. 3.4a).

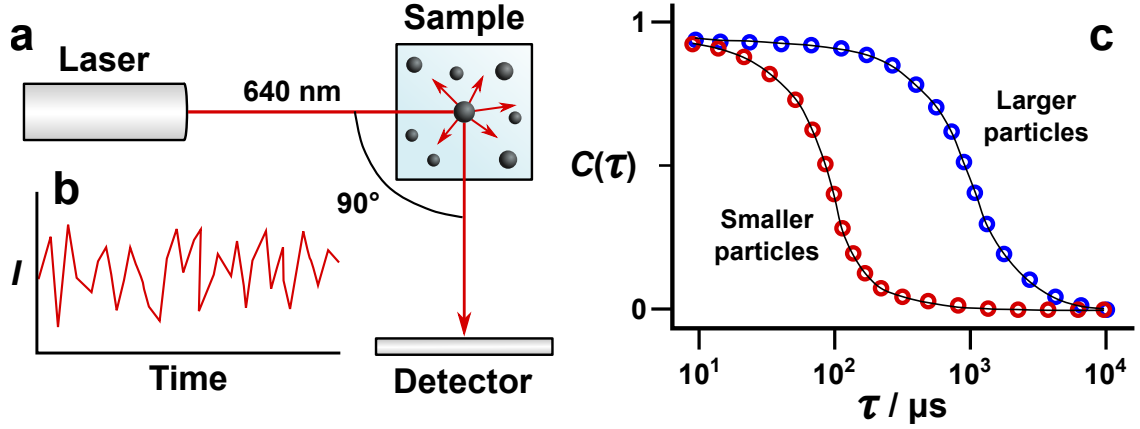


Figure 3.4: (a) Schematic of dynamic light scattering from particles in aqueous dispersion measured at 90° . (b) Temporal fluctuations in scattering intensity for a particle dispersion in liquid. (c) Exemplar autocorrelation functions exhibited by small (red) and large (blue) particles. The black lines are models fit to the data.

The fluctuations in scattering intensity (I) occur due to the random diffusion (Brownian motion) of the particles in dispersion, which causes the number of photons reaching the detector to vary with time as particles diffuse into and out of the illuminated area, changing their intensities (Fig. 3.4b). The variability in these fluctuations over time is much greater for smaller particles due to their faster movement by diffusion, and therefore, the decay times for these fluctuations relate to the diffusion rates and by extension, size. As a result, a correlation ($C(\tau)$) between the average scattered intensity of the particles over increasing time intervals (τ) can be made.¹⁰³ This is known as an autocorrelation function (Fig. 3.4c), and can be modelled to calculate the particle diffusion coefficient, D :

$$C(\tau) = \exp^{-2Dq^2\tau}$$

where q is the scattering vector or momentum transfer as with SANS, however when using light as the radiation source the refractive index of the suspending liquid, n , must also be accounted for:

$$q = \frac{4\pi n}{\lambda} \sin \frac{\theta}{2}$$

The diffusion coefficient can then be translated into the effective particle diameter using the Stokes–Einstein equation:

$$D = \frac{k_B T}{6\pi\eta R_H}$$

where k_B is Boltzmann’s constant, T is absolute temperature (K), η is the solvent viscosity and R_H is the hydrodynamic radius of the particles. This approximation is for spherical particles, although is believed to work well for colloidal GO and rGO sheets according to a corroborative TEM study;¹⁰⁴ however, the relationship between the diameter of a sphere and diameter of the platelets in this study is not quite 1:1 so should be interpreted with caution.

Scattering intensity increases substantially with particle size according to the power law, d^6 . Therefore, solvents must be filtered to remove dust and other large particles that will essentially dominate the scattering. In addition, samples must be sufficiently dilute so that detected photons are from single scattering events, as multiply scattered photons yield inaccurate results.¹⁰⁵ Furthermore, sample dilution minimises interparticle attractive interactions which can misleadingly increase measured particle sizes. A series of sample concentrations should be analysed to account for these effects by observing where the effective particle diameter for the suspension does not vary significantly while still maintaining an adequate signal to noise ratio. Hence, further experiments can then be conducted at optimal particle loadings.

Phase analysis light scattering (PALS) can be used to measure zeta potential of particles in dispersion, giving an approximation of their surface charge. The technique is similar in principle to DLS, however the particles are subjected to an electric field that influences their mobility rather than purely Brownian motion (Fig. 3.5a), and the scattered light is detected in the forward direction as a phase shift (Fig. 3.5c).¹⁰⁶ The origin of particle surface charging in solution resides in the formation of the electrical double layer (Fig. 3.5b). A particle acquires surface charge typically as a result of ionisation of surface groups by protonation/deprotonation reactions, or due to adsorption of charged species such as ions or ionic molecules.⁵⁸ Both phenomena are relevant for aqueous dispersions of GO and rGO with surfactants. Counter-ions then adsorb to the surface to form a tightly-bound layer known as the Stern layer. A diffuse layer of ions (predominately counter-ions) then locate near the Stern layer within a so-called slipping plane (Fig. 3.5b). The Stern layer and diffuse layer before the slipping plane are collectively known as the electrical double layer. Zeta potential is measured at the slipping plane (Fig. 3.5b), hence why it is considered an approximation.

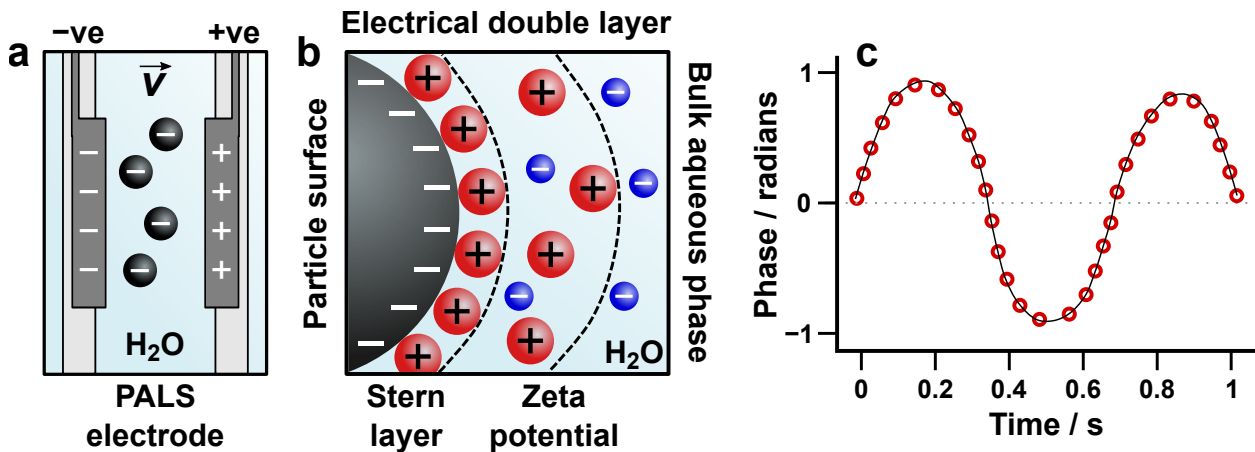


Figure 3.5: (a) Schematic of a PALS electrode immersed in aqueous solution and migration of the particles towards the oppositely charged electrode. (b) Schematic of the electrical double layer for a negatively charged particle in water. (c) Hypothetical phase analysis data showing the phase shift over time for a particle suspension as a results of an applied alternating electric field. The black line represents the model fit to the data.

The phase change over time of the scattered light (Fig. 3.5c), $Q(t)$, relates to the mobility of

the particles in response to an alternating electric field, $E(t)$, allowing determination of their electrophoretic mobility, μ_E :

$$Q(t) - Q(0) = Aq\mu_E \int_0^t E(t') dt'$$

where A is the amplitude of the scattered light and q is the scattering vector. A sinusoidal field was applied for all PALS measurements in this project. The electrophoretic mobility can then be used to calculate zeta potential, ζ , using the Smoluchowski equation:

$$\mu_E = \frac{\nu_E}{E} = \frac{\zeta\epsilon}{\eta}$$

where ν_E is the electrophoretic velocity, E is the electric field strength, ϵ is the dielectric constant of the suspending liquid (water) and η is its viscosity. The Smoluchowski equation is applicable to large particles where the size of the electrical double layer is small by comparison to the particle radius (*i.e.* GO and rGO sheets).

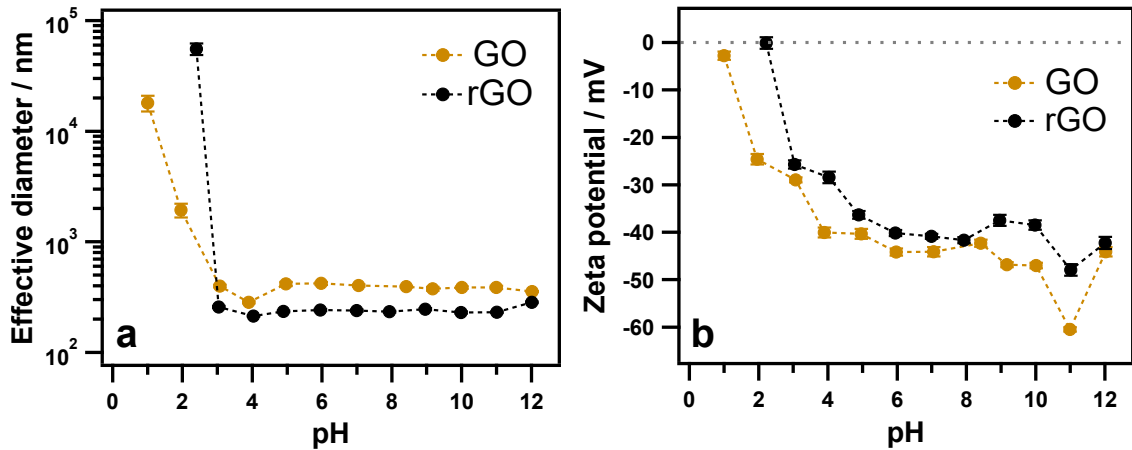


Figure 3.6: Dynamic light scattering data (a) and phase analysis light scattering data (b) for GO and rGO at different values of pH.

DLS and PALS measurements in this project were performed using a Brookhaven Nanobrook Omni with a laser wavelength of 640 nm. All samples comprised GO or rGO with surfactants, and were measured as aqueous suspensions in 1 cm pathlength polystyrene cuvettes. Ultrapure water was syringe filtered ($0.2 \mu\text{m}$) for all DLS samples, and individual measurements consisted of five, 2 minute runs from which the average was determined. For PALS, a palladium electrode was carefully immersed in the solution so as not to introduce bubbles. Then, each measurement involved five consecutive runs comprising at least 20 phase cycles. Again, the average of each run was taken as the final data point. All DLS and PALS measurements were conducted at 25°C . Figure 3.6 shows DLS and PALS data for GO and rGO, obtained using a spherical particle model to determine effective diameter, and the Smoluchowski model for calculating zeta potentials.

3.2 Surface techniques

3.2.1 Pendant drop tensiometry

Pendant drop tensiometry is a technique for determining the surface or interfacial tension of liquids by analysis of their drop profiles. A measurement is performed by suspending a drop from the end of a blunt needle of accurately known diameter (Fig. 3.7a). A light source and diffuser enhance the contrast by creating a silhouette of the drop, after which a high resolution image of the drop is captured by a digital camera. The image can then be iteratively modelled with the Young-Laplace equation to calculate the surface tension:

$$\Delta P = \gamma \left(\frac{1}{r_1} + \frac{1}{r_2} \right)$$

where ΔP is the pressure difference across the curved surface, r_1 and r_2 are the two radii of the deformed drop and γ is the surface or interfacial tension.

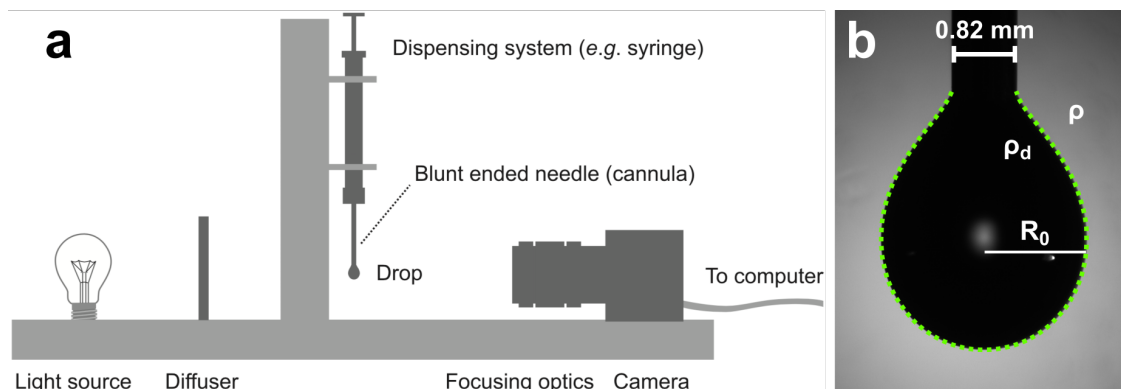


Figure 3.7: (a) Schematic of the experimental setup for pendant drop tensiometry. (b) Drop profile image with key input parameters and iterative fit for the boundaries. Adapted with permission from Elsevier.¹⁰⁷

The surface tension of a liquid arises from the reduced opportunity for stabilising interactions of the molecules at the surface, compared to those in the bulk. Therefore, liquids surrounded by air (or another immiscible fluid) tend to form a spherical (droplet) shape to minimise these interactions by reducing their surface area. In order to achieve accurate results, the pendant drop method relies on adequate deformation of a suspended droplet under gravity to counter-balance the effects of surface tension.¹⁰⁷ Therefore, gravity serves as the test (applied) force for determining surface tension by this method, and the drop must be of sufficient volume for the effect of gravity to be significant (Fig. 3.7b). The Laplace pressure across the interface (ΔP) is determined with reference to the hydrostatic pressure, which is the density difference ($\Delta\rho$) between the drop phase, ρ_d , and the continuous phase, ρ , multiplied by a gravitational constant. In this work, these media were water and air respectively, and the densities are specified in the fitting algorithm prior to measurement. In addition, an accurate value for the diameter of the needle is required in order to spatially calibrate the imaging system (Fig. 3.7b). Then, by specifying the needle region in the image (Fig. 3.7b), the

software is able to calibrate pixels with length, allowing simultaneous determination of the drop radii (r_1 and r_2), volume and surface area. This process is repeated for a number of images over the course of a measurement to obtain dynamic interfacial tension data. (Fig. 3.8).

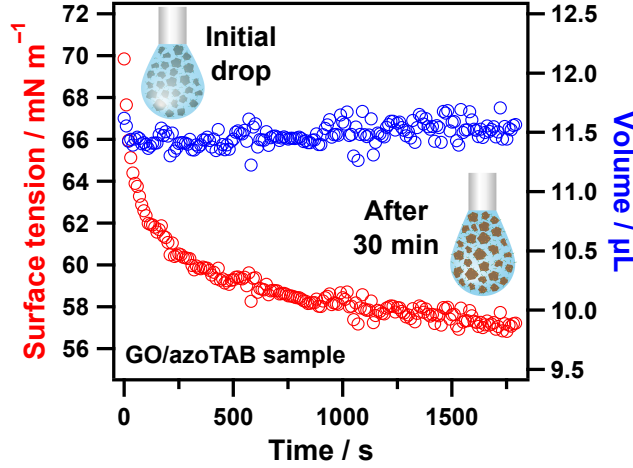


Figure 3.8: Exemplar dynamic surface tension data for a sample of GO and azoTAB. The insets show the change in shape of the drop over time as the surfactant coated sheets adsorb at the surface.

In this work, tensiometry measurements were performed at room temperature (*ca.* 25°C) using a custom-made pendant drop setup with a CMOS camera (Flea3, Point Grey, Richmond, BC, Canada). All measurements were conducted in air, with the drop contained inside a cuvette to minimize evaporation. Drop analysis was completed using OpenDrop software.¹⁰⁷ All pendant drop measurements were performed for a sufficient time to achieve equilibration at the interface (*i.e.* where further surface tension changes were insignificant).

3.2.2 X-ray reflectivity

X-ray reflectivity (XRR) is a surface scattering technique for examining the physical and structural characteristics of thin films and interfaces. Scattering in reflection mode differs from bulk scattering in that detection occurs only at the angle of incidence (Fig. 3.9), representative of specular reflectivity (R). This minimises errors caused by surface roughness (deviations in height or thickness of the reflective layer). To penetrate the sample layer at different depths, the angle of the incident beam is altered during a measurement. Thus, to ensure reflectivity is measured at specular angles only, the scattering vector (Q) must be treated differently than for bulk scattering to account for the x and y vectors, in addition to the z vector. Reflectivity is therefore represented as the ratio between the intensity of the reflected beam at specular angles, $I(Q)$, and the intensity of the incident beam, I_0 :

$$R = \frac{I(Q)}{I_0} = \left| \frac{q_z - \sqrt{q_z^2 - q_c^2 - iB}}{q_z + \sqrt{q_z^2 - q_c^2 - iB}} \right|^2 e^{-(\frac{\sigma^2 q_z^2}{2})}$$

where q_c is the critical scattering vector below which the X-ray beam is fully reflected, B is the absorption coefficient which relates to the density of the surface layer, and σ is the root-mean-square

roughness of the film.

X-rays interact with the electron clouds of atoms, and therefore the scattering power of materials tends to increase with atomic number (electron density), providing very different contrast to neutrons.¹⁰⁸ The reflectivity measurements performed in this work were of surfactant and GO/surfactant composites at the air–water interface (Fig. 3.9). Therefore, X-rays were used instead of neutrons because they provide better contrast for surfactant tails in air, which have a similar neutron scattering length density (*ca.* 0 \AA^{-2}).

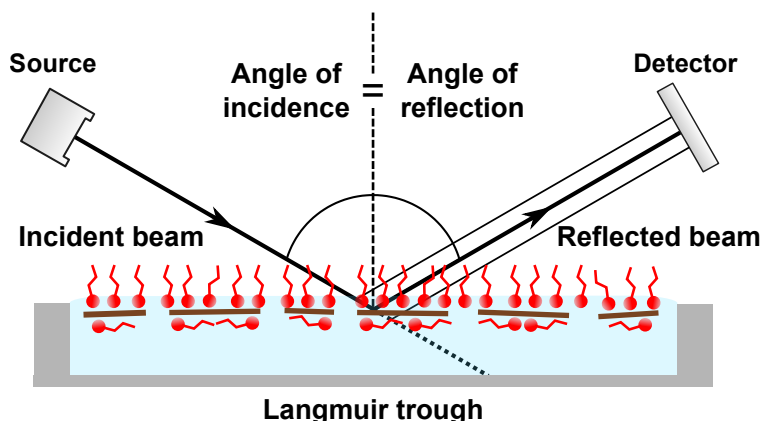


Figure 3.9: Schematic of a reflectivity measurement on the air–water interface for a GO/surfactant system.

The specular reflectivity of a surface or interface depends on three key parameters: thickness, roughness and scattering length density. Hence, all can be determined by modelling the reflectivity data (Fig. 3.10a). The modelling can also distinguish layers within a film if their scattering length densities are sufficiently different. The data in Figure 3.10a have been fit with a three layer model; the collective thickness of these layers is approximately 4.5 nm, presumed to comprise a layer of surfactant tails in air, graphene oxide, and then adsorbed surfactants lying down on the sheets in solution (Fig. 3.9). For especially thin films ($<5 \text{ nm}$) as observed in this work, displaying the data on a RQ^4 axis, rather than a $\log R$ axis helps to accentuate features in the scattering such as fringes (Fig. 3.10a). Modelling the data can also be performed to produce a scattering length density profile (Fig. 3.10b), providing a map of the interface based on the scattering length densities of each layer within the film. For Figure 3.10b, the plateaus at 0 and $9.35 \times 10^{-6} \text{ \AA}^{-2}$ represent the scattering length densities of air and water respectively, either side of the surface film. For XRR measurements, the scattering length density axis can be converted to electron density by dividing by the radius of an electron.

Surface roughness is a key factor influencing the quality of reflectivity data. Rough surfaces cause diffuse reflectivity (reflection at non-specular angles) which significantly reduces the strength of the specular signal and decreases fringe resolution.^{109,110} Therefore, overly rough surfaces are not suited to reflectivity measurements and must be optimised. Diffuse scattering measured by the

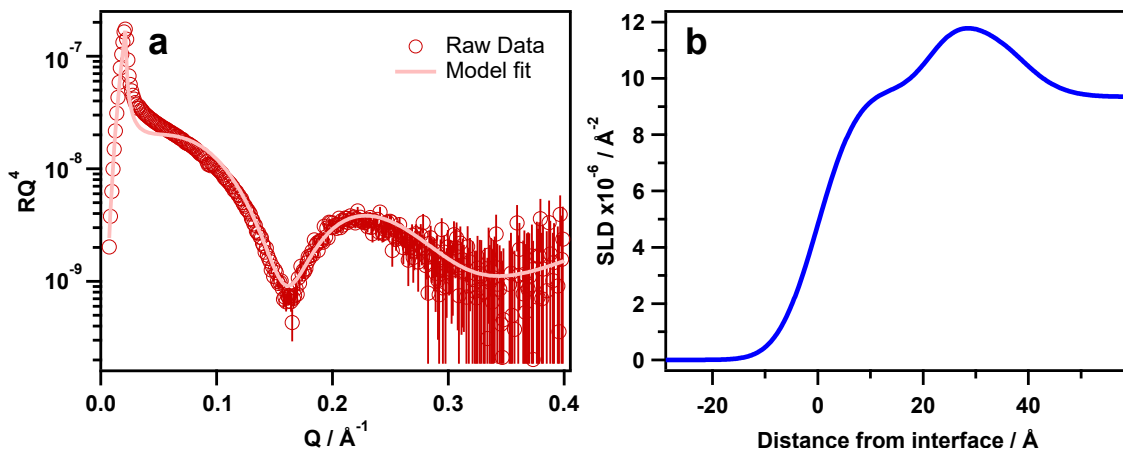


Figure 3.10: (a) XRR data and model fit for a sample of 0.1 mg/mL GO and 0.2 mM OAPB surfactant. (b) The corresponding scattering length density profile determined from the model.

detector was partially accounted for by subtracting a background reflectivity curve measured with the detector at a slightly higher angle than the incident X-ray beam.

All XRR measurements were obtained from GO and surfactant systems at the air–water interface, and performed using a PANanalytical X-Pert PRO reflectometer (high tension = 45 kV, current = 40 mA) with a radiation wavelength (Cu- K_{α}) of 0.15418 nm. Measurements times were typically 60 minutes at 30°C, during which the incident angle was increased from approximately 0.01 to 0.7\AA^{-1} (q range). Samples were contained in Langmuir troughs within a closed environment to minimize evaporation. All reflectivity data was modelled using MOTOFIT,¹¹¹ a reflectivity analysis software package run within the IGOR Pro environment.

3.3 Imaging techniques

3.3.1 Atomic force microscopy

Atomic force microscopy (AFM) is a surface reconstruction technique used to generate topographical ‘images’ of materials, and measure associated forces and mechanical properties.¹¹² The AFM exploits the interactions or contact of an atomically sharp tip with a sample surface in order to generate high-resolution reconstructions (‘images’), and therefore can be used on both conducting and insulating surfaces, unlike its predecessor the scanning tunnelling microscope.¹¹³ The tip is attached to the end of a flexible cantilever that bends in response to the forces it experiences, generally reflecting changes in surface height (Fig. 3.11a). A piezoelectric actuator rasters the cantilever and tip across a specified area of the sample surface with sub-nanometer precision.

The reflection of a laser from the back of the cantilever near the tip into a position-sensitive detector serves as an optical sensor for detecting displacement of the cantilever (Fig. 3.11a), and triggers complementary responses from the piezoelectric actuator in the z direction. This feedback loop relieves strain from the back of the cantilever and maintains a constant force between the tip and

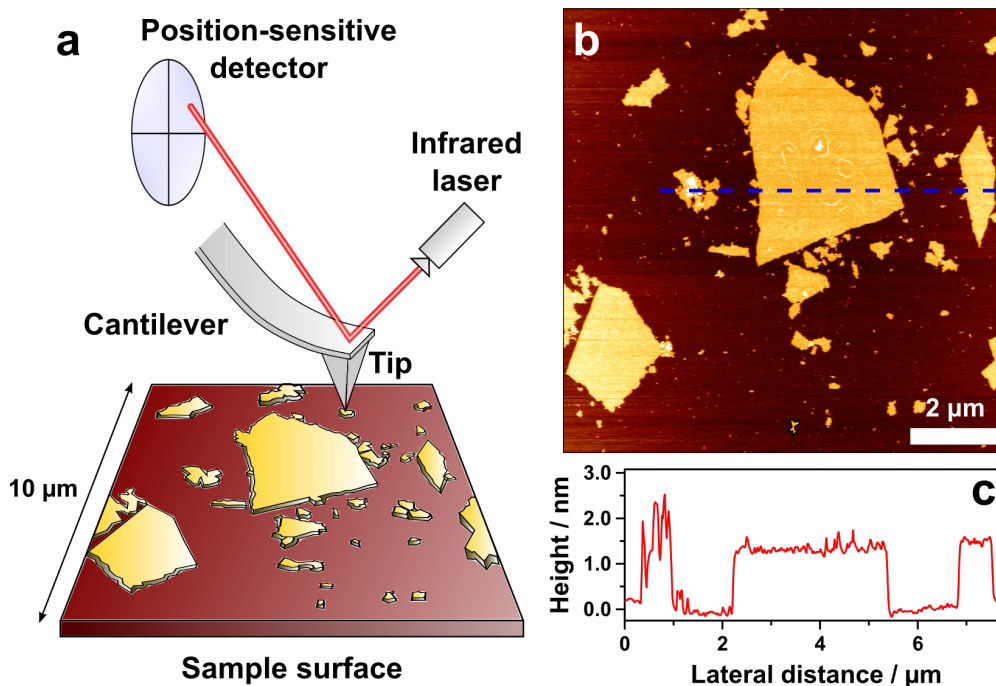


Figure 3.11: (a) Schematic of atomic force microscopy imaging setup. (b) AFM height image of GO sheets dried onto mica. (c) The corresponding height profile for the blue cross section shown in the image.

sample surface.¹¹⁴ Changes in the position of the z -piezo are controlled by applied voltages, hence this electrical input translates to the topographic information for creating a 3-dimensional or height image. Data is usually represented using a colour gradient to describe differences in sample height for a given image (Fig. 3.11b,c). AFM can also be used for determining surface forces for a variety of systems (force spectroscopy) through controlled tip interactions with the substrate,^{81,115} however, these types of measurements were not performed in this work.

AFM is most commonly performed in one of three imaging modes: contact mode, tapping mode or non-contact mode. Alternating contact or ‘tapping’ mode relies on supplying the cantilever with a sinusoidal oscillation near its measured resonant frequency to cause vibration of the cantilever. The tip is then allowed to tap the surface of the sample, offering a gentler approach to imaging materials compared to contact mode, which involves the tip remaining in constant contact with the surface.^{114,116} In non-contact mode, the tip remains a few nanometers above the surface to experience attractive van der Waals forces that are detected for constructing an image. These forces are substantially weaker than those experienced by the tip during the contact imaging modes.¹¹⁷ Hence, non-contact mode is the least commonly used mode of imaging due to its associated technical challenges.

Since the AFM tip directly probes the surface of a sample to generate images, the tip interactions with the surface can also give insight on the physical nature of the sample, such as its softness/hardness (phase imaging). In this process, the AFM measures the phase difference between the supplied

oscillation at the back of the cantilever and the measured oscillation at the tip, giving information on how the supplied energy is dissipated by the surface material (elastically or inelastically). The set-point value, which relates to the strength of the force by which the tip pushes against the sample surface, must be optimised in order to obtain significant phase contrast between materials.¹¹⁸ In tapping mode, lower set-point values correspond to stronger forces or firmer pressing of the tip against the sample surface. An example height image of rGO and its corresponding phase image are shown in Figure 3.12. Two distinct sheet-like structures are observed in the height image, however in the phase image the non-porous sheet is almost unnoticeable, implying it is much harder and likely composed of a different material to the porous sheet.

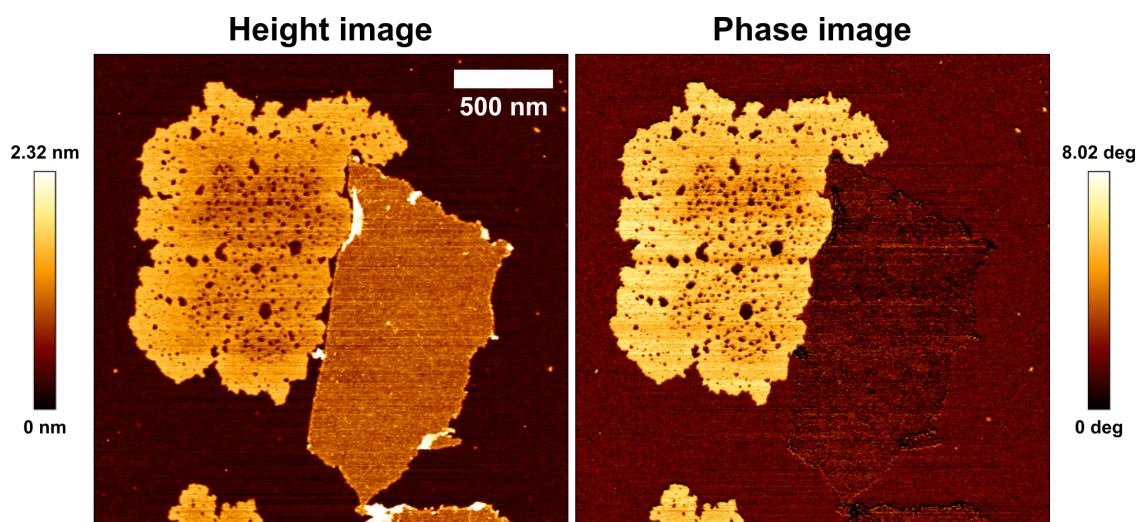


Figure 3.12: AFM height image and corresponding phase image of rGO dried onto mica.

The AFM instrument utilised in this work was a JPK NanoWizard 3, and was used primarily for imaging and characterising the morphology and lateral size distribution of the synthesized GO and rGO materials, as well as providing evidence of surfactant or polymer adsorption on these materials. All imaging was performed in tapping mode using Bruker NCHV model cantilevers, with resonant frequencies around 340 kHz, and spring constants between 20 and 80 N/m. The spring constant describes the stiffness or rigidity of the cantilever, and is an essential quantity when performing force measurements. Image areas varied from sub-micron to tens of microns depending on sample nature, and imaging parameters such as set-point value, line rate, and gain (piezo response) were optimised to obtain the highest resolution possible at 512×512 pixels. Samples for AFM were prepared by spin-coating a small aliquot of dilute aqueous dispersions of the materials on mica (ProSciTech).

Processing of images to optimise their clarity and obtain height profiles was performed using the JPK Data Processing software, and involved the subtraction of a polynomial background (no greater than second order) from each scan line independently to achieve a consistently flat background for each image. Lateral dimensions for GO and rGO sheets were measured using the software package Gwyddion (<http://gwyddion.net>).¹¹⁹

3.4 Spectroscopic techniques

3.4.1 Ultraviolet–visible spectrophotometry

Ultraviolet–visible spectrophotometry is a molecular spectroscopy technique that measures the absorption of light by an analyte solution in the ultraviolet (UV) and visible regions of the electromagnetic spectrum. Conventional instrumentation includes a light source, a monochromator for controlling wavelength, a sample port and a photo-detector (Fig. 3.13a). The photons that reach the detector (transmitted intensity, I) are compared to the photons emitted from the light source (incident intensity, I_0). The photons absorbed can then be related to the concentration of the sample with Beer’s law:¹²⁰

$$A = \log \frac{I_0}{I} = \epsilon cl$$

where A is the absorbance, ϵ is the molar extinction coefficient, l is the cell pathlength and c is the analyte concentration.

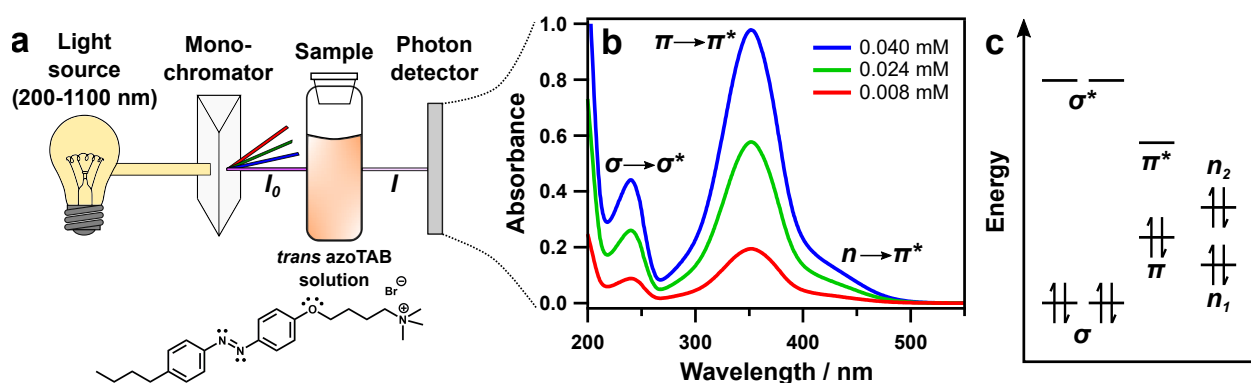


Figure 3.13: (a) Simple schematic of a spectrophotometry measurement for a solution of azoTAB in the *trans* configuration. (b) UV spectra of *trans* azoTAB at different concentrations, with annotations of the electronic excitations associated with each absorption band. (c) An approximate molecular orbital energy diagram for the excitations of azobenzene. The two non-bonding orbitals (n_1 and n_2) correspond to the lone pairs on the azo nitrogens.³⁵ For simplicity, the non-bonding orbitals for the oxygen atom have been omitted.

The absorption of light typically results in excitations of bonding and non-bonding electrons into higher energy orbitals. Therefore spectrophotometry provides insight into bond types and functional groups within a sample.¹²¹ An example of these absorption bands and their corresponding electronic excitations are shown for *trans* azoTAB solutions (Fig. 3.13a,b). Absorption bands occur at shorter (higher energy) wavelengths for larger energy gaps between orbitals, hence the $\sigma \rightarrow \sigma^*$ transition is assigned to the shortest wavelength absorption band (Fig. 3.13b,c).

UV–visible spectrophotometry measurements in this work were performed using a Cary 60 instrument from Agilent Technologies. The technique was used to characterise the optical properties of GO and rGO, monitor transitions between *trans* and *cis* azoTAB, create calibration curves and determine adsorption isotherms for surfactants on GO and rGO sheets. Measurements were typically performed

across the wavelength range of 200-800 nm in 1 cm pathlength quartz cuvettes. To account for loss of beam intensity due to reflection and attenuation effects from the analyte and cuvette, the beam transmittance was first determined in a similar cell containing solvent only, which for these measurements was always water.

Bibliography

- [1] Lu, X., Yu, M., Huang, H., Ruoff, R. S. Tailoring graphite with the goal of achieving single sheets. *Nanotechnology* **1999** *10*, 269.
- [2] Novoselov, K. S., Geim, A. K., Morozov, S. V., Jiang, D., Zhang, Y., Dubonos, S. V., Grigorieva, I. V., Firsov, A. A. Electric Field Effect in Atomically Thin Carbon Films. *Science* **2004** *306*, 666–669.
- [3] Geim, A. K., Novoselov, K. S. The rise of graphene. *Nat. Mater.* **2007** *6*, 183–191.
- [4] Novoselov, K. S., Fal’ko, V. I., Colombo, L., Gellert, P. R., Schwab, M. G., Kim, K. A roadmap for graphene. *Nature* **2012** *490*, 192–200.
- [5] Yi, M., Shen, Z. A review on mechanical exfoliation for the scalable production of graphene. *J. Mater. Chem. A* **2015** *3*, 11700–11715.
- [6] Mattevi, C., Kim, H., Chhowalla, M. A review of chemical vapour deposition of graphene on copper. *J. Mater. Chem.* **2011** *21*, 3324–3334.
- [7] Stankovich, S., Dikin, D. A., Dommett, G. H., Kohlhaas, K. M., Zimney, E. J., Stach, E. A., Piner, R. D., Nguyen, S. T., Ruoff, R. S. Graphene-based composite materials. *Nature* **2006** *442*, 282.
- [8] Geim, A. K. Graphene: status and prospects. *Science* **2009** *324*, 1530–1534.
- [9] Si, Y., Samulski, E. T. Synthesis of Water Soluble Graphene. *Nano Lett.* **2008** .
- [10] Lotya, M., King, P. J., Khan, U., De, S., Coleman, J. N. High-Concentration, Surfactant-Stabilized Graphene Dispersions. *ACS Nano* **2010** *4*, 3155–3162.
- [11] Elbourne, A., McLean, B., Voitchovsky, K., Warr, G. G., Atkin, R. Molecular resolution in situ imaging of spontaneous graphene exfoliation. *J. Phys. Chem. Lett.* **2016** *7*, 3118–3122.
- [12] Texter, J., Ager, D., Vasantha, V. A., Crombez, R., England, D., Ma, X., Maniglia, R., Tambe, N. Advanced Nanocarbon Materials Facilitated by Novel Stimuli-responsive Stabilizers. *Chem. Lett.* **2012** *41*, 1377–1379.
- [13] Ager, D., Arjunan Vasantha, V., Crombez, R., Texter, J. Aqueous graphene dispersions—optical properties and stimuli-responsive phase transfer. *ACS Nano* **2014** *8*, 11191–11205.

- [14] Ruoff, R. Graphene: Calling all chemists. *Nat. Nanotechnol.* **2008** *3*, 10–11.
- [15] Loh, K. P., Bao, Q., Eda, G., Chhowalla, M. Graphene oxide as a chemically tunable platform for optical applications. *Nature Chem.* **2010** *2*, 1015–1024.
- [16] Park, S., Ruoff, R. S. Chemical methods for the production of graphenes. *Nat. Nanotechnol.* **2009** *4*, 217–224.
- [17] Zhu, Y., Murali, S., Cai, W., Li, X., Suh, J. W., Potts, J. R., Ruoff, R. S. Graphene and Graphene Oxide: Synthesis, Properties, and Applications. *Adv. Mater.* **2010** *22*, 3906–3924.
- [18] Hummers Jr, W. S., Offeman, R. E. Preparation of Graphitic Oxide. *J. Am. Chem. Soc.* **1958** *80*, 1339.
- [19] Dikin, D. A., Stankovich, S., Zimney, E. J., Piner, R. D., Dommett, G. H. B., Evmenenko, G., Nguyen, S. T., Ruoff, R. S. Preparation and characterization of graphene oxide paper. *Nature Letters* **2007** *448*, 457–460.
- [20] Dreyer, D. R., Park, S., Bielawski, C., Ruoff, R. S. The Chemistry of Graphene Oxide. *Chem. Soc. Rev.* **2010** *39*, 228–240.
- [21] Li, D., Muller, M. B., Gilje, S., Kaner, R. B., Wallace, G. G. Processable Aqueous Dispersions of Graphene Nanosheets. *Nat. Nanotechnol.* **2008** *3*, 101–105.
- [22] Konkena, B., Vasudevan, S. Understanding Aqueous Dispersibility of Graphene Oxide and Reduced Graphene Oxide through pK_a Measurements. *J. Phys. Chem. Lett.* **2012** *3*, 867–872.
- [23] Kyzas, G. Z., Deliyanni, E. A., Matis, K. A. Graphene oxide and its application as an adsorbent for wastewater treatment. *J. Chem. Technol. Biotechnol.* **2014** *89*, 196–205.
- [24] McCoy, T. M., Brown, P., Eastoe, J., Tabor, R. F. Noncovalent Magnetic Control and Reversible Recovery of Graphene Oxide Using Iron Oxide and Magnetic Surfactants. *ACS Appl. Mater. Interfaces* **2015** *7*, 2124–2133.
- [25] Shao, J.-J., Lv, W., Yang, Q.-H. Self-Assembly of Graphene Oxide at Interfaces. *Adv. Mater.* **2014** *26*, 5586–5612.
- [26] Kim, J., Cote, L. J., Kim, W., F. Yuan, Shull, K. R., Huang, J. Graphene Oxide Sheets at Interfaces. *J. Am. Chem. Soc.* **2010** *132*, 8180–8186.
- [27] McCoy, T. M., Pottage, M. J., Tabor, R. F. Graphene Oxide-Stabilized Oil-in-Water Emulsions: pH-Controlled Dispersion and Flocculation. *J. Phys. Chem. C* **2014** *118*, 4529–4535.
- [28] Stankovich, S., Dikin, D. A., Piner, R. D., Kohlhaas, K. A., Kleinhammes, A., Jia, Y., Wu, Y., Nguyen, S. T., Ruoff, R. S. Synthesis of Graphene Based Nanosheets via Chemical Reduction of Exfoliated Graphite Oxide. *Carbon* **2007** *45*, 1558–1565.
- [29] Segal, M. Selling graphene by the ton. *Nat. Nanotechnol.* **2009** *4*, 612–614.

- [30] Marcano, D. C., Kosynkin, D. V., Berlin, J. M., Sinitskii, A., Sun, Z., Slesarev, A., Alemany, L. B., Lu, W., Tour, J. M. Improved Synthesis of Graphene Oxide. *ACS Nano* **2010** *4*, 4806–4814.
- [31] Eastoe, J., Tabor, R. F. Surfactants and nanoscience. In *Colloidal Foundations of Nanoscience*. Elsevier, **2014**, pages 135–157.
- [32] Rosen, M. J., Kunjappu, J. T. *Surfactants and interfacial phenomena*. John Wiley & Sons, **2012**.
- [33] de Gennes, P. G., Brochard-Wyatt, F., Quere, D. *Capillarity and Wetting Phenomena - Drops, Bubbles, Pearls, Waves*. Springer, New York, **2004**.
- [34] Czajka, A., Hazell, G., Eastoe, J. Surfactants at the Design Limit. *Langmuir* **2015** *31*, 8205–8217.
- [35] Griffiths, J. II. Photochemistry of Azobenzene and its Derivatives. *Chem. Soc. Rev.* **1972** *1*, 481–493.
- [36] Kunitake, T., Nakashima, N., Shimomura, M., Okahata, Y., Kano, K., Ogawa, T. Unique properties of chromophore-containing bilayer aggregates: enhanced chirality and photochemically induced morphological change. *J. Am. Chem. Soc.* **1980** *102*, 6642–6644.
- [37] Eastoe, J., Vesperinas, A. Self-assembly of light-sensitive surfactants. *Soft Matter* **2005** *1*, 338–347.
- [38] Tabor, R. F., McCoy, T. M., Hu, Y., Wilkinson, B. L. Physicochemical and Biological Characterisation of Azobenzene-containing Photoswitchable Surfactants. *Bull. Chem. Soc. Jpn* **2018** *91*, 932–939.
- [39] Hontoria-Lucas, C., Lopez-Peinado, A. J., Lopez-Gonzalez, J. d. D., Rojas-Cervantes, M. L., Martin-Aranda, R. M. Study of Oxygen-Containing Groups in a Series of Graphite Oxides: Physical and Chemical Characterization. *Carbon* **1995** *33*, 1585–1592.
- [40] Kim, F., Cote, L. J., Huang, J. Graphene Oxide: Surface Activity and Two-Dimensional Assembly. *Adv. Mater.* **2010** *22*, 1954–1958.
- [41] Ali, M., McCoy, T. M., McKinnon, I. R., Majumder, M., Tabor, R. F. Synthesis and Characterization of Graphene Oxide–Polystyrene Composite Capsules with Aqueous Cargo via a Water–Oil–Water Multiple Emulsion Templating Route. *ACS Appl. Mater. Interfaces* **2017** *9*, 18187–18198.
- [42] Tao, H., Zhang, Y., Gao, Y., Sun, Z., Yan, C., Texter, J. Scalable exfoliation and dispersion of two-dimensional materials—an update. *Phys. Chem. Chem. Phys.* **2017** *19*, 921–960.
- [43] Shao, Y., van de Ven, T. G. M. Spinning of partially engulfed drops. *Langmuir* **1989** *5*, 1234–1241.

- [44] Kim, J., Cote, L. J., Huang, J. Two dimensional soft material: new faces of graphene oxide. *Acc. Chem. Res* **2012** *45*, 1356–1364.
- [45] Texter, J. Graphene oxide and graphene flakes as stabilizers and dispersing aids. *Curr. Opin. Colloid Interface Sci* **2015** *20*, 454–464.
- [46] Lerf, A., He, H., Forster, M., Klinowski, J. Structure of Graphite Oxide Revisited. *J. Phys. Chem. B* **1998** *102*, 4477–4482.
- [47] Erickson, K., Erni, R., Lee, Z., Alem, N., Gannett, W., Zettl, A. Determination of the local chemical structure of graphene oxide and reduced graphene oxide. *Adv. Mater.* **2010** *22*, 4467–4472.
- [48] Dimiev, A. M., Tour, J. M. Mechanism of Graphene Oxide Formation. *ACS Nano* **2014** *8*, 3060–3068.
- [49] Feicht, P., Siegel, R., Thurn, H., Neubauer, J. W., Seuss, M., Szabó, T., Talyzin, A. V., Halbig, C. E., Eigler, S., Kunz, D. A., Fery, A., Papastavrou, G., Senker, J., Breu, J. Systematic evaluation of different types of graphene oxide in respect to variations in their in-plane modulus. *Carbon* **2017** *114*, 700–705.
- [50] Shih, C.-J., Lin, S., Sharma, R., Strano, M. S., Blankschtein, D. Understanding the pH-Dependent Behavior of Graphene Oxide Aqueous Solutions: A Comparative Experimental and Molecular Dynamics Simulation Study. *Langmuir* **2012** *28*, 235–241.
- [51] Akbari, A., Sheath, P., Martin, S. T., Shinde, D. B., Shaibani, M., Banerjee, P. C., Tkacz, R., Bhattacharyya, D., Majumder, M. Large-area graphene-based nanofiltration membranes by shear alignment of discotic nematic liquid crystals of graphene oxide. *Nature communications* **2016** *7*, 10891.
- [52] Gudarzi, M. M. Colloidal stability of graphene oxide: aggregation in two dimensions. *Langmuir* **2016** *32*, 5058–5068.
- [53] Chowdhury, I., Duch, M. C., Mandsukhani, N. D., Hersam, M. C., Bouchard, D. Colloidal Properties and Stability of Graphene Oxide Nanomaterials in the Aquatic Environment. *Environ. Sci. Technol.* **2013** *47*, 6288–6296.
- [54] Chowdhury, I., Mansukhani, N. D., Guiney, L. M., Hersam, M. C., Bouchard, D. Aggregation and stability of reduced graphene oxide: complex roles of divalent cations, pH, and natural organic matter. *Environ. Sci. Technol.* **2015** *49*, 10886–10893.
- [55] Derjaguin, B., Landau, L. Theory of the stability of strongly charged lyophobic sols and of the adhesion of strongly charged particles in solution of electrolytes. *Acta Physicochim: USSR* **1941** *14*, 633–662.
- [56] Overbeek, J. T. G. Recent developments in understanding of colloidal stability. *J. Colloid Interface Sci.* **1977** *58*, 408–422.

- [57] Israelachvili, J. N. *Intermolecular and Surface Forces*. Academic Press, San Diego, **1991**.
- [58] Hunter, R. J. *Foundations of Colloid Science*. Oxford University Press, Oxford, **2001**, 2 edition.
- [59] Overbeek, J. T. G. The rule of Schulze and Hardy. *Pure Appl. Chem.* **1980** *52*, 1151–1161.
- [60] Rourke, J. P., Pandey, P. A., Moore, J. J., Bates, M., Kinloch, I. A., Young, R. J., Wilson, N. R. The Real Graphene Oxide Revealed: Stripping the Oxidative Debris from the Graphene-like Sheets. *Angew. Chem. Int. Ed.* **2011** *50*, 3173–3177.
- [61] Thomas, H. R., Day, S. P., Woodruff, W. E., Valles, C., Young, R. J., Kinloch, I. A., Morley, G. W., Hanna, J. V., Wilson, N. R., Rourke, J. Deoxygenation of Graphene Oxide: Reduction or Cleaning? *Chem. Mater.* **2013** *25*, 3580–3588.
- [62] Fan, X., Peng, W., Li, Y., Li, X., Wang, S., Zhang, G., Zhang, F. Deoxygenation of exfoliated graphite oxide under alkaline conditions: a green route to graphene preparation. *Adv. Mater.* **2008** *20*, 4490–4493.
- [63] Dimiev, A. M., Alemany, L. B., Tour, J. M. Graphene oxide. Origin of acidity, its instability in water, and a new dynamic structural model. *ACS Nano* **2012** *7*, 576–588.
- [64] Cote, L. J., Kim, J., Tung, V. C., Luo, J., Kim, F., Huang, J. Graphene oxide as surfactant sheets. *Pure Appl. Chem.* **2010** *83*, 95–110.
- [65] Luo, J., Cote, L. J., Tung, V. C., Tan, A. T. L., Goins, P. E., Wu, J., Huang, J. Graphene Oxide Nanocolloids. *J. Am. Chem. Soc.* **2010** *132*, 17667–17669.
- [66] Kim, J. E., Han, T. H., Lee, S. H., Kim, J. Y., Ahn, C. W., Yun, J. M., Kim, S. O. Graphene oxide liquid crystals. *Angew. Chem.* **2011** *123*, 3099–3103.
- [67] Xu, Z., Gao, C. Aqueous liquid crystals of graphene oxide. *ACS Nano* **2011** *5*, 2908–2915.
- [68] Narayan, R., Kim, J. E., Kim, J. Y., Lee, K. E., Kim, S. O. Graphene oxide liquid crystals: discovery, evolution and applications. *Adv. Mater.* **2016** *28*, 3045–3068.
- [69] Binks, B. P., Horozov, T. S. *Colloidal Particles at Liquid Interfaces*. Cambridge University Press, Cambridge, UK, **2006**.
- [70] Aboutalebi, S. H., Gudarzi, M. M., Zheng, Q. B., Kim, J.-K. Spontaneous formation of liquid crystals in ultralarge graphene oxide dispersions. *Adv. Funct. Mater.* **2011** *21*, 2978–2988.
- [71] Dan, B., Behabtu, N., Martinez, A., Evans, J. S., Kosynkin, D. V., Tour, J. M., Pasquali, M., Smalyukh, I. I. Liquid crystals of aqueous, giant graphene oxide flakes. *Soft Matter* **2011** *7*, 11154–11159.
- [72] Valtierrez-Gaytan, C., Ismail, I., Macosko, C., Stottrup, B. L. Interfacial activity of graphene oxide: Anisotropy, loading efficiency and pH-tunability. *Colloids Surf. A* **2017** *529*, 434–442.

- [73] Bonatout, N., Muller, F., Fontaine, P., Gascon, I., Konovalov, O., Goldmann, M. How exfoliated graphene oxide nanosheets organize at the water interface: evidence for a spontaneous bilayer self-assembly. *Nanoscale* **2017** *9*, 12543–12548.
- [74] Silverberg, G. J., Pearce, P., Vecitis, C. D. Controlling Self-Assembly of Reduced Graphene Oxide at the Air–Water Interface: Quantitative Evidence for Long-Range Attractive and Many-Body Interactions. *ACS Appl. Mater. Interfaces* **2015** *7*, 3807–3815.
- [75] Harrison, K. L., Biedermann, L. B., Zavadil, K. R. Mechanical properties of water-assembled graphene oxide Langmuir monolayers: guiding controlled transfer. *Langmuir* **2015** *31*, 9825–9832.
- [76] Pickering, S. U. Emulsions. *J. Chem. Soc., Trans.* **1907** *91*, 2001–2021.
- [77] Binks, B. P., Lumsdon, S. O. Pickering Emulsions Stabilized by Monodisperse Latex Particles: Effects of Particle Size. *Langmuir* **2001** *17*, 4540–4547.
- [78] He, Y., Wu, F., Sun, X., Li, R., Guo, Y., Li, C., Zhang, L., Xing, F., Wang, W., Gao, J. Factors that Affect Pickering Emulsions Stabilized by Graphene Oxide. *ACS Appl. Mater. Interfaces* **2013** *5*, 4843–4855.
- [79] Thickett, S. C., Zetterlund, P. B. Graphene oxide (GO) nanosheets as oil-in-water emulsion stabilizers: Influence of oil phase polarity. *J. Colloid Interface Sci.* **2015** *442*, 67–74.
- [80] Gamot, T. D., Bhattacharyya, A. R., Sridhar, T., Beach, F., Tabor, R. F., Majumder, M. Synthesis and stability of water-in-oil emulsion using partially reduced graphene oxide as a tailored surfactant. *Langmuir* **2017** *33*, 10311–10321.
- [81] Tabor, R. F., Lockie, H., Chan, D. Y., Grieser, F., Grillo, I., Mutch, K. J., Dagastine, R. R. Structural forces in soft matter systems: unique flocculation pathways between deformable droplets. *Soft Matter* **2011** *7*, 11334–11344.
- [82] Sun, Z., Feng, T., Russell, T. P. Assembly of graphene oxide at water/oil interfaces: tessellated nanotiles. *Langmuir* **2013** *29*, 13407–13413.
- [83] Chen, D., Sun, Z., Russell, T. P., Jin, L. Coassembly Kinetics of Graphene Oxide and Block Copolymers at the Water/Oil Interface. *Langmuir* **2017** *33*, 8961–8969.
- [84] Gudarzi, M. M., Sharif, F. Self assembly of graphene oxide at the liquid–liquid interface: A new route to the fabrication of graphene based composites. *Soft Matter* **2011** *7*, 3432–3440.
- [85] Zemb, T., Lindner, P. *Neutrons, X-rays and light: scattering methods applied to soft condensed matter*. North-Holland, **2002**.
- [86] Sokolova, A., Christoforidis, J., Eltobaji, A., Barnes, J., Darmann, F., Whitten, A. E., de Campo, L. BILBY: Time-of-flight small angle scattering instrument. *Neutron News* **2016** *27*, 9–13.

- [87] Gilbert, E. P., Schulz, J. C., Noakes, T. J. Quokka - the small-angle neutron scattering instrument at OPAL. *Physica B* **2006** 385-386, 1180–1182.
- [88] Rehm, C., Brûlé, A., Freund, A. K., Kennedy, S. J. Kookaburra: the ultra-small-angle neutron scattering instrument at OPAL. *J. Appl. Crystallogr.* **2013** 46, 1699–1704.
- [89] Rehm, C., de Campo, L. KOOKABURRA: The Ultra-Small-Angle Neutron Scattering Instrument at ANSTO. *Neutron News* **2016** 27, 30–32.
- [90] Rehm, C., Campo, L. d., Brûlé, A., Darmann, F., Bartsch, F., Berry, A. Design and performance of the variable-wavelength Bonse–Hart ultra-small-angle neutron scattering diffractometer KOOKABURRA at ANSTO. *J. Appl. Crystallogr.* **2018** 51, 1–8.
- [91] Guinier, A., Fournet, G., Walker, C. *Small angle scattering of X-rays*. J. Wiley & Sons, New York, **1955**.
- [92] Glatter, O. The interpretation of real-space information from small-angle scattering experiments. *J. Appl. Crystallogr.* **1979** 12, 166–175.
- [93] Mittelbach, R., Glatter, O. Direct structure analysis of small-angle scattering data from polydisperse colloidal particles. *J. Appl. Crystallogr.* **1998** 31, 600–608.
- [94] Fritz, G., Bergmann, A. Interpretation of small-angle scattering data of inhomogeneous ellipsoids. *J. Appl. Crystallogr.* **2004** 37, 815–822.
- [95] Kotlarchyk, M., Chen, S.-H. Analysis of small angle neutron scattering spectra from polydisperse interacting colloids. *J. Chem. Phys.* **1983** 79, 2461–2469.
- [96] Hayter, J. B., Penfold, J. An analytic structure factor for macroion solutions. *Mol. Phys.* **1981** 42, 109–118.
- [97] Hayter, J. B., Penfold, J. Self-consistent Structural and Dynamic Study of Concentrated Micelle Solutions. *J. Chem. Soc., Faraday Trans. I* **1981** 77, 1851–1863.
- [98] Hansen, J.-P., Hayter, J. B. A rescaled MSA structure factor for dilute charged colloidal dispersions. *Molecular Physics* **1982** 46, 651–656.
- [99] Hayter, J. B., Penfold, J. Determination of Micelle Structure and Charge by Small-Angle Neutron Scattering. *Colloid Polym. Sci.* **1983** 261, 1022–1030.
- [100] Wu, C., Chan, D. Y., Tabor, R. F. A simple and accurate method for calculation of the structure factor of interacting charged spheres. *J. Colloid Interface Sci.* **2014** 426, 80–82.
- [101] Kline, S. R. Reduction and analysis of SANS and USANS data using IGOR Pro. *J. Appl. Crystallogr.* **2006** 39, 895–900.
- [102] Chu, B. *Laser light scattering: basic principles and practice*. Courier Corporation, **2007**.
- [103] Pecora, R. *Dynamic light scattering: applications of photon correlation spectroscopy*. Springer Science & Business Media, **2013**.

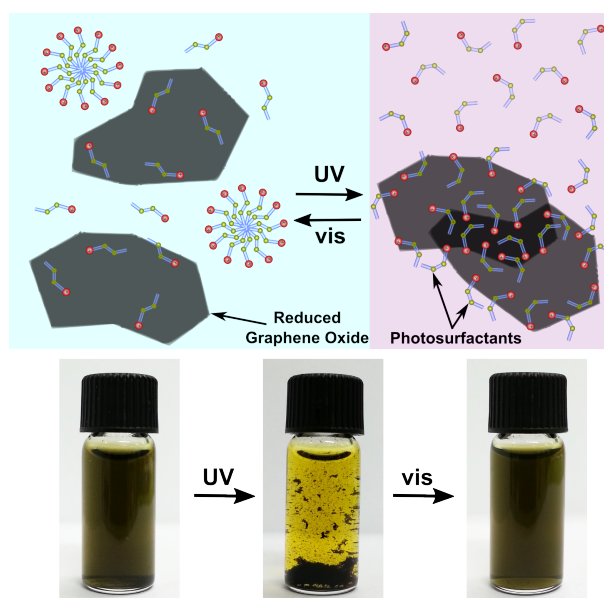
- [104] Lotya, M., Rakovich, A., Donegan, J. F., Coleman, J. N. Measuring the lateral size of liquid-exfoliated nanosheets with dynamic light scattering. *Nanotechnology* **2013** *24*, 265703.
- [105] Schätzel, K. Suppression of multiple scattering by photon cross-correlation techniques. *J. Mod. Opt.* **1991** *38*, 1849–1865.
- [106] Sze, A., Erickson, D., Ren, L., Li, D. Zeta-potential measurement using the Smoluchowski equation and the slope of the current–time relationship in electroosmotic flow. *J. Colloid. Interface Sci.* **2003** *261*, 402–410.
- [107] Berry, J. D., Neeson, M. J., Dagastine, R. R., Chan, D. Y., Tabor, R. F. Measurement of Surface and Interfacial Tension using Pendant Drop Tensiometry. *J. Colloid Interface Sci.* **2015** *454*, 226 – 237.
- [108] Daillant, J., Gibaud, A. *X-ray and neutron reflectivity: principles and applications*, volume 770. Springer, **2008**.
- [109] Sinha, S., Sirota, E., Garoff, S., Stanley, H. X-ray and neutron scattering from rough surfaces. *Phys. Rev. B* **1988** *38*, 2297.
- [110] Gibaud, A., Hazra, S. X-ray reflectivity and diffuse scattering. *Curr. Sci.* **2000** , 1467–1477.
- [111] Nelson, A. Co-refinement of Multiple-Contrast Neutron/X-ray Reflectivity Data using *MOTOFIT*. *J. Appl. Crystallogr.* **2006** *39*, 273–276.
- [112] Binnig, G., Quate, C. F., Gerber, C. Atomic force microscope. *Phys. Rev. Lett.* **1986** *56*, 930–933.
- [113] Binnig, G., Rohrer, H., Gerber, C., Weibel, E. Surface studies by scanning tunneling microscopy. *Phys. Rev. Lett.* **1982** *49*, 57.
- [114] Giessibl, F. J. Advances in atomic force microscopy. *Rev. Mod. Phys.* **2003** *75*, 949–983.
- [115] Tabor, R. F., Wu, C., Lockie, H., Manica, R., Chan, D. Y. C., Grieser, F., Dagastine, R. R. Homo- and Hetero-Interactions between Air Bubbles and Oil Droplets Measured by Atomic Force Microscopy. *Soft Matter* **2011** *7*, 8977–8983.
- [116] Takano, H., Kenseth, J. R., Wong, S.-S., O’Brie, J. C., Porter, M. D. Chemical and biochemical analysis using scanning force microscopy. *Chem. Rev.* **1999** *99*, 2845–2890.
- [117] Giessibl, F. J. Forces and frequency shifts in atomic-resolution dynamic-force microscopy. *Phys. Rev. B* **1997** *56*, 16010–16015.
- [118] Paredes, J., Villar-Rodil, S., Solís-Fernández, P., Martínez-Alonso, A., Tascon, J. Atomic force and scanning tunneling microscopy imaging of graphene nanosheets derived from graphite oxide. *Langmuir* **2009** *25*, 5957–5968.
- [119] Nečas, D., Klapetek, P. Gwyddion: an open-source software for SPM data analysis. *Open Physics* **2012** *10*, 181–188.

- [120] Strong, F. C. Theoretical basis of Bouguer-Beer law of radiation absorption. *Anal. Chem.* **1952** *24*, 338–342.
- [121] Jaffé, H. H., Orchin, M. *Theory and applications of ultraviolet spectroscopy*. Wiley, **1962**.

Chapter 4

Light-controllable dispersion and recovery of graphenes and carbon nanotubes using a photo-switchable surfactant

Published: Thomas M. McCoy, Amelia C. Y. Liu and Rico F. Tabor, Light-controllable dispersion and recovery of graphenes and carbon nanotubes using a photo-switchable surfactant. *Nanoscale*, 2016, **8**, 6969-6974.





Cite this: *Nanoscale*, 2016, **8**, 6969

Received 5th January 2016,

Accepted 6th March 2016

DOI: 10.1039/c6nr00075d

www.rsc.org/nanoscale

Light-controllable dispersion and recovery of graphenes and carbon nanotubes using a photo-switchable surfactant†

Thomas M. McCoy,^a Amelia C. Y. Liu^b and Rico F. Tabor^{*a}

The aqueous dispersibility of carbon-based nanomaterials, namely graphene oxide (GO), reduced graphene oxide (rGO) and carbon nanotubes (CNTs), can be controlled by light *via* the photoisomerisation of a photoswitchable surfactant molecule adsorbed to the surface of these materials. By incorporating a cationic azobenzene photosurfactant into these systems, GO, rGO and CNT dispersions can be separated and redispersed on command utilising UV radiation at 365 nm, whereby the surfactant molecules change from the *trans* to the *cis* isomer. This increases their aqueous solubility and in turn, alters their adsorption affinity for the GO and rGO sheets such that the ratio of free to adsorbed surfactant molecules changes significantly, allowing for reversible phase separation of the colloids. These effects present a unique method for controlling the dispersion behaviour of two-dimensional nanomaterials using light as a clean and low energy external stimulus.

Introduction

Graphene and related carbon nanomaterials (CNMs) show exceptional potential in a vast number of technological applications, stemming from their leading conductive and mechanical properties.¹ However, the largely hydrophobic nature of graphene causes it to be colloiddally unstable in water without the aid of surfactant stabilisers,² and hence processing and deploying it in aqueous systems remains challenging. Conversely, graphene oxide (GO) and reduced graphene oxide (rGO) sheets present hydrophilic functional groups and bear large negative surface potentials in water,^{3,4} causing them to disperse readily, and making their use in aqueous systems viable. This important feature, along with the enormous surface area of GO/rGO sheets have paved the way for the use of these

materials as excellent stabilisers of oil–water interfaces,^{5,6} as well as promising adsorbents for the treatment of wastewater.⁷

To enable the scale-up in both synthesis and use of CNMs, effective methods for their dispersion and recovery from aqueous systems must be developed. Many GO and rGO composites have been developed with stimulus-responsive properties that facilitate this process, with a particular focus on magnetic recovery.⁸ Magnetic GO/rGO composites have been formulated for the purpose of environmental decontamination,⁹ although the vast majority focus on covalent tethering of magnetic particles, limiting the uses of the recovered CNM. Despite this, the use of external stimuli to control CNM dispersion is particularly appealing, and of the possible stimuli, light is perhaps the ‘cleanest’.

In other soft systems and dispersions, photoswitchable stabilisers have been used to great effect to control stability and cause phase separations that enable recovery of materials from DNA to metal nanoparticles.^{10,11} Molecular switches that change their structural configuration – and hence properties – when exposed to light of a specific wavelength are of great interest for the development of light-tunable devices and photo-modulation of dispersion stability.^{12,13} The cationic surfactant butylphenyl-4-diazeno-4-butoxyphenyl-trimethylammonium bromide (azoTAB) contains the widely-used azobenzene chromophore, known for its *trans*–*cis* photoisomerisation when exposed to UV light at *ca.* 350 nm (Fig. 1g).^{14–16} In this process, the C–N=N–C dihedral angle changes from 180° to around 11°,¹⁷ and the $\pi \rightarrow \pi^*$ absorption band becomes dramatically lower in intensity (Fig. 1h). With this altered structure comes a significant increase in dipole moment (typically from *ca.* 0.4 to 3.5 D) that serves to increase the aqueous solubility of the surfactant.¹⁸

Here, we utilise a simple photoswitchable surfactant (azoTAB – chemical and photochemical characterization provided in ESI†) to reversibly control the stability of carbon nanomaterials, specifically demonstrating the effect for GO, rGO and CNTs (Fig. 1a–f). By exploring the molecular basis for adsorption and stabilisation/flocculation effects, we are able to unravel the complex interplay of charge, π -stacking and hydrophobic

^aSchool of Chemistry, Monash University, Clayton, VIC 3800, Australia.

E-mail: rico.tabor@monash.edu

^bMonash Centre for Electron Microscopy and School of Physics and Astronomy, Monash University, Clayton, VIC 3800, Australia

†Electronic supplementary information (ESI) available: Includes further details on materials characterization, photo response, adsorption and SANS analysis. See DOI: 10.1039/c6nr00075d

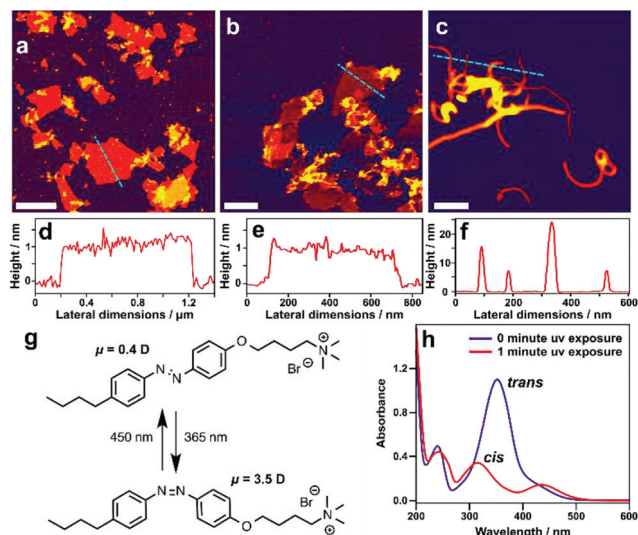


Fig. 1 (a, b & c) AFM height images of GO (a), rGO (b) and CNTs (c) dried onto mica. The dashed lines correspond to the height profiles in d, e and f and the scale bars represent 1 μm , 500 nm and 200 nm respectively. (g) Structural schematic showing the reversible, photo-induced *trans*→*cis* isomerisation of azoTAB. (h) UV-visible spectra of *trans*- and *cis*-azoTAB.

interactions that determine stability in these systems. These systems provide new horizons for the deployment and capture of carbon nanomaterials in aqueous environments, providing reversible separations at low materials and energy cost.

Results and discussion

Reduced graphene oxide

The dispersibility of CNMs is intimately related to their dimensions, charge and hydrophobicity,^{4,19} and here we start by investigating the photo-induced phase separation of rGO, the most 'graphene like' of the materials explored. When GO is chemically or physically reduced to rGO, its innate hydrophobicity increases due to the loss of hydrophilic functional groups, and rGO is therefore generally only metastable in aqueous conditions.^{3,20,21} When adding a cationic surfactant that would be expected to adsorb readily to the negative charge sites on rGO²² thereby reducing its effective surface potential and increasing its hydrophobicity, it is thus unsurprising that the dispersion fully flocculates, even at very low concentrations of azoTAB in both *trans*- and *cis*-dominated isomerisation states (Fig. 2a and b). By only modest changes in concentration, essentially full dispersion or flocculation can be achieved (Fig. 2c).

It is important to note here that azobenzene molecules do not exclusively exist in one isomeric state, but instead equilibrate to a statistical photostationary state comprising a proportion of both isomers, which varies depending on the illumination conditions.^{23–26} Upon irradiation with UV light, the proportion of *cis* configured molecules increases; for the

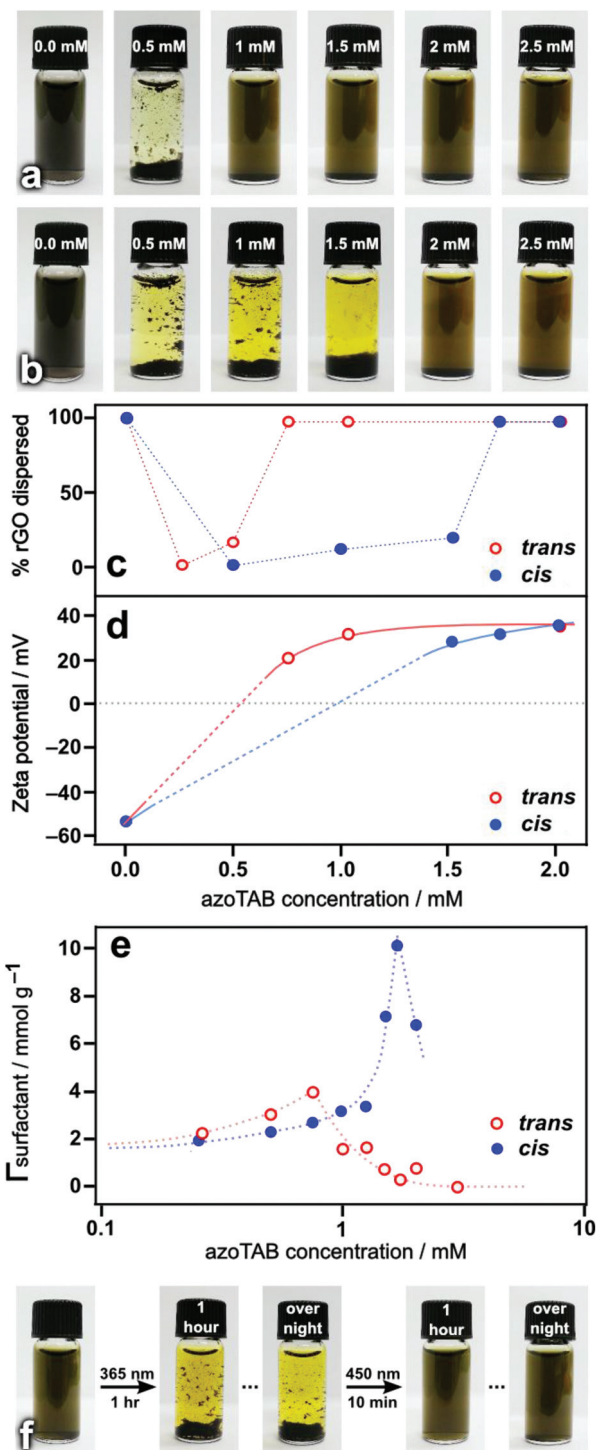


Fig. 2 (a) Samples containing 0.1 mg per mL rGO and the specified concentrations of azoTAB, 30 minutes after preparation. (b) Identical samples in which the azoTAB solution was irradiated at 365 nm for 10 minutes before the rGO was added. (c) Quantification of the % of rGO dispersed for various concentrations of azoTAB, obtained spectrophotometrically. (d) Phase analysis light scattering data of rGO for increasing azoTAB concentrations. Measurements could not be conducted in the dashed regions as the rGO dispersion was unstable here. (e) Adsorption isotherm of azoTAB in *trans* and *cis* dominated states onto rGO. All samples are at pH 11. (f) An image series of the same 0.1 mg per mL rGO dispersion, demonstrating the effects of photo-isomerisation of the surfactant (1.2 mM).

surfactant chemistry used in these experiments, the *cis* isomer proportion has been shown previously^{27,28} to be 25% in the *trans*-dominated photostationary state that exists in ambient lighting conditions, and 95% in the *cis*-dominated photostationary state that exists after equilibration under UV light at 365 nm (assessed by UV-visible spectrophotometric measurements here, see ESI†). For the sake of brevity henceforth we use the terms *trans* and *cis* to refer to the *trans*-dominated and *cis*-dominated states respectively.

As surfactant concentration is increased to the CMC of azoTAB (1 mM in the *trans* state and 2 mM in the *cis* state, see ESI†) and beyond, the rGO remains fully dispersed. It can also be observed quantitatively in the azoTAB/rGO adsorption isotherm (Fig. 2e) that azoTAB adsorption drops off significantly at and past these concentrations. This unexpected result indicates that steric stabilisation by further surfactant adsorption is unlikely to be the effect causing stability of the rGO dispersions at high surfactant loadings. Instead, the highly positive zeta potentials (>30 mV) obtained (Fig. 2d) indicate re-stabilisation by charging of the colloids, presumably *via* surfactant adsorption through π -stacking interactions. It has been noted in previous molecular modelling studies that for small aromatics adsorbing to carbon nanotubes, π -stacking interactions are “the most important ingredient” in adsorption,²⁹ and substituents play only a minor role.³⁰ This would indicate that the aromatic core of the azoTAB surfactant used here would experience favourable interactions with the aromatic regions of the CNMs. The reduction in adsorbed amount is curious, and may reflect a reconfiguration of the partitioning within the system when moving to a 3-state equilibrium (adsorbed, monomeric and micellised surfactant).

The difference in surfactant concentration of the two isomers required to induce flocculation of the rGO provides an accessible window in which the dispersibility of the material can be reversibly controlled by exploiting the photo-induced switch of the azobenzene group. By choosing a concentration between 1 and 2 mM (*e.g.* 1.2 mM), it can be seen that it is possible to reversibly flocculate and redisperse the rGO by using light (Fig. 2f). It is noteworthy that significantly longer illumination times were required to destabilise the colloid when the rGO was present compared to Fig. 2b, where the surfactant solutions were irradiated before the rGO was added, due to added optical density of the rGO dispersion. Irradiation with blue light (*ca.* 450 nm) then served to restabilise the rGO, and although not required, this process could be accelerated by short bursts of ultrasonication. The retained stability of the dispersion after being left overnight shows that the restabilisation is a direct result of the isomerisation state of the surfactant.

To further characterise the morphology and aggregation of the carbon nanomaterials, we performed high-resolution transmission electron microscopy (HR-TEM) of two samples: rGO (Fig. 3a) and rGO with azoTAB (Fig. 3b). Upon drying the samples for TEM, the materials are observed in both cases as large aggregates or clumps at low magnification (see ESI†), which is unsurprising given the hydrophobic nature of rGO. However, by observing these aggregates at high resolution

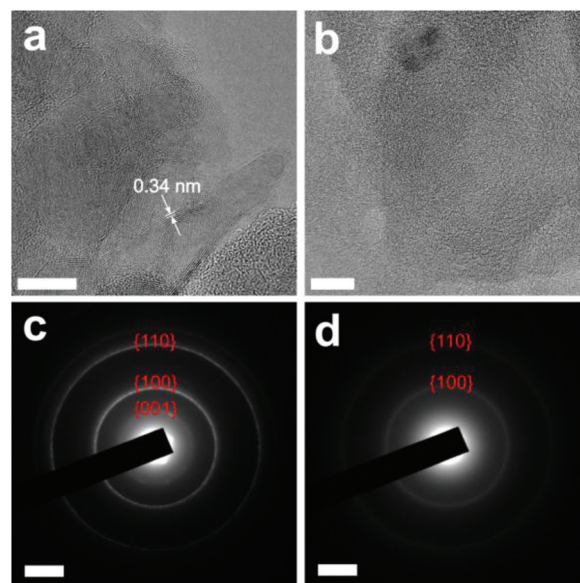


Fig. 3 (a & b) High-resolution TEM images of rGO aggregates prepared from aqueous samples without (a) and with azoTAB present (b). The scale bars represent 10 nm. For the rGO only sample, the arrows indicate the apparent spacing between sheets, which is on average 0.34 nm. The corresponding selected area electron diffraction (SAED) patterns (c & d) are shown below the images to which they correspond. The scale bars represent 3 nm^{-1} , and the numbers are the Miller indices for the interplanar and in-plane spacings.

(Fig. 3a and b), there are noticeable differences in the structure of the aggregates that are formed. When azoTAB is not present, the rGO sheets aggregate and form curved stacks, indicating the presence and alignment of graphitic regions, but also highlighting the presence of defects in the layers. The average interlayer spacing of these stacks is 0.34 nm, which is consistent with previous findings.^{31,32} When azoTAB is present however, the sheets do not stack uniformly. This suggests that adsorbed surfactant molecules disrupt the strong π -stacking interactions that occur between the naked rGO sheets, pointing to a disordered fractal-type aggregation (as confirmed by small-angle neutron scattering measurements below). These differences indicate the significance of surfactant adsorption, and are reinforced by the corresponding selected area electron diffraction (SAED) patterns (Fig. 3c and d). There is a much higher degree of paracrystalline order in the rGO sample with no surfactant, as indicated by the sharp rings in the diffraction pattern (Fig. 3c). These rings correspond to the interplanar spacing of $0.34 \pm 0.02 \text{ nm}$ and the in-plane spacings of $0.21 \pm 0.02 \text{ nm}$ and $0.12 \pm 0.02 \text{ nm}$. The SAED pattern from the rGO/azoTAB sample (Fig. 3d) shows significantly more diffuse rings, with only the in-plane spacings present, reaffirming the absence of stacked sheets. Further information on sample preparation and image analysis can be found in the ESI.†

Carbon nanotubes

It is seen that another hydrophobic CNM in the form of carbon nanotubes (CNTs) could be dispersed and recovered

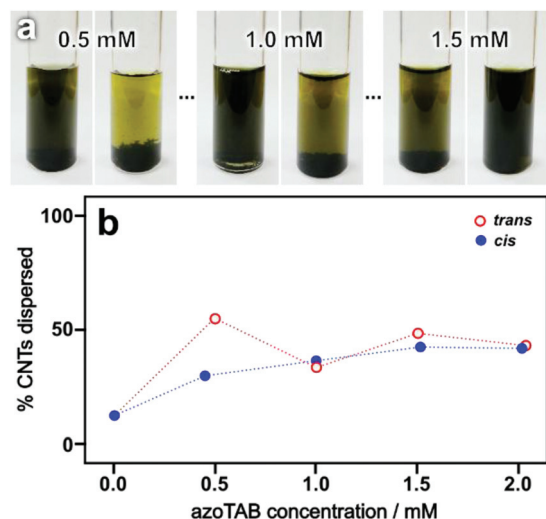


Fig. 4 (a) Samples containing 0.05 mg mL^{-1} of CNTs and azoTAB in *trans*-dominated (left) and *cis*-dominated (right) states. These samples were sonicated for approximately 2 minutes and images were taken after 1 hour. (b) Quantification of the % of CNTs dispersed for various concentrations of azoTAB, obtained spectrophotometrically.

using the same method as for rGO above. CNTs do not typically disperse in water, but have been found to do so with the aid of surfactant molecules and sonication.³³ In the case of azoTAB, the CNTs are found to disperse well when the surfactant is in the more surface active *trans* configuration, with dispersions achieved at sub-CMC concentrations (0.5 mM), whereas it can be seen that the *cis* isomer does not effectively disperse the CNTs at concentrations below 1.5 mM and they settle out after only 1 hour (Fig. 4a). When using azoTAB as a dispersant for CNTs, dispersion was incomplete, with few systems achieving greater than 50% dispersion (Fig. 4b), however these results could be significantly improved with longer sonication times and the experiments performed here were intended to distinguish the effects of the *trans* versus *cis* configuration. In addition, the highly polydisperse nature of the multiwalled CNTs used here meant that the separation was not as 'clean' (*i.e.* complete) as for rGO, and therefore further studies were not performed.

Graphene oxide

It is unsurprising that on moving to graphene oxide, a hydrophilic and water-dispersible CNM, that very different behaviour is seen. Here, the dispersion stability is innately much higher and it is therefore more challenging to effect destabilisation through surfactant adsorption. Although significant adsorption was seen in the isotherm when mixing GO with azoTAB at pH 3 (Fig. 5c), at the surfactant concentrations where rGO flocculated, GO is instead stable. Notably, a significant difference can be observed in the level of adsorption between not only the *trans* and *cis* forms of azoTAB, but also when the photosurfactant solution is irradiated pre-adsorption to the GO when compared to UV irradiation of the already-adsorbed *trans*

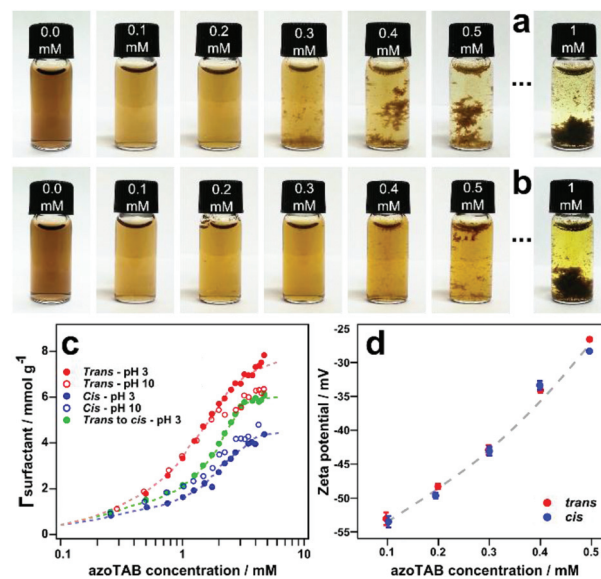


Fig. 5 (a) Samples comprising 0.2 mg mL^{-1} GO and the specified concentrations of azoTAB 30 min (0–0.5 mM) or 12 h (1 mM) after preparation. (b) Identical samples in which the azoTAB was irradiated at 365 nm for 10 minutes before the GO was added. All samples are at approximately pH 10. (c) Adsorption isotherm of azoTAB photosurfactant onto GO at high (open symbols) and low (solid symbols) pH. The green data series corresponds to samples that were irradiated with UV light for 10 minutes after GO was incorporated into the system. (d) Phase analysis light scattering data showing the change in zeta potential of GO for increasing concentrations of azoTAB in the *trans* and *cis* state. The dashed line is a guide to the eye.

dominated azoTAB. This result is in line with expectation from the larger dipole moment and increased solubility of the *cis* isomer, which would cause a shift in the dynamic equilibrium of the system such that the surfactant partitions more into the bulk solution. The difference in adsorption from isomerisation pre- versus post-adsorption could indicate that adsorption of the surfactant to the GO in the *trans* form means that molecules are somewhat stabilised towards desorption.

When examining the same systems in basic conditions (pH 10), it was found that higher concentrations of azoTAB ($>0.3 \text{ mM}$) were required to flocculate the GO (Fig. 5a and b). It can also be seen that flocculation occurred less readily when the surfactant was in the *cis* state (Fig. 5b), reinforcing the notion that light can be used to control the aggregation state of these systems. Surprisingly, when the same isotherm was determined at pH 10 (Fig. 5c, hollow symbols) there was no significant change in the adsorbed amount of surfactant, suggesting that adsorption is not driven solely by electrostatics. As discussed previously, this is likely due to favourable π -stacking interactions between the azobenzene core and aromatic regions of the GO sheets, indicated by previous density functional theory (DFT) studies on carbon nanotubes.^{29,30} Investigation of the surface charge on the GO sheets showed that increasing the concentration of azoTAB resulted in a gradual increase in the zeta potential of the system (Fig. 5d). This accounts for the destabilisation of the dispersion due to

insufficient electrical double-layer interactions between sheets. However, given that the zeta potential of the GO increases only marginally with added azoTAB, it is clear that charge-based interactions are not the predominant mode of adsorption in these systems, and that the interactions due to π -stacking^{29,30} and potentially hydrophobicity are more significant. The important role of hydrophobic interactions between the tail-group and carbon nanomaterial in adsorption of surfactants onto CNMs has been indicated previously;³⁴ combined with the capacity for strong π -stacking interactions, it therefore becomes clear that in this case, it is likely that tail-group chemistry is more significant than the surfactant head-group in determining the level and mode of surfactant adsorption.

SANS analysis

To further explore the aggregation mechanism and morphology induced by interaction of azoTAB with GO and rGO, small-angle neutron scattering (SANS) was employed, whereby the effects of surfactant concentration and irradiation on assembly were analysed. The scattering seen (Fig. 6a–c) is characteristic of fractal aggregation, where intensity increases rapidly at low scattering vector q (an inverse length scale), indicating the formation of large structures with poorly defined

morphology; thus a mass fractal model was used to fit these data. It can be seen that scattering intensity is greater for GO than rGO systems, and also greater for *trans* than *cis* (Fig. 6a–c). Given the previous results of the isotherms this is not surprising, as the surfactant molecules were found to have a higher affinity for GO than rGO, and are responsible for the majority of the scattered intensity due to their greater contrast than the CNMs (see ESI†).

By exploring systems where the photosurfactant concentration is changed as well as its isomerisation state (Fig. 6a–c), it becomes clear that the level of surfactant adsorption is the key process driving flocculation in these systems (Fig. 6d). Differences in the fitting parameters from the mass fractal model used to quantify these data³⁵ indicate that the spatially inhomogeneous flocs become more compacted with increased surfactant loading. Fractal aggregates are known to be metastable, as at first they possess a large surface area to volume ratio and then undergo a relaxation towards a more stable configuration.³⁶ By observing these GO/rGO surfactant systems over time, it can be seen that this is indeed the case (see insets to (Fig. 6a–c)), as the flocs eventually settle into a more condensed network at the bottom of their vessels (see also ESI†); similar compaction over time of fractal aggregates has been observed recently in yttrium aluminium garnet systems also analysed by SANS.³⁷

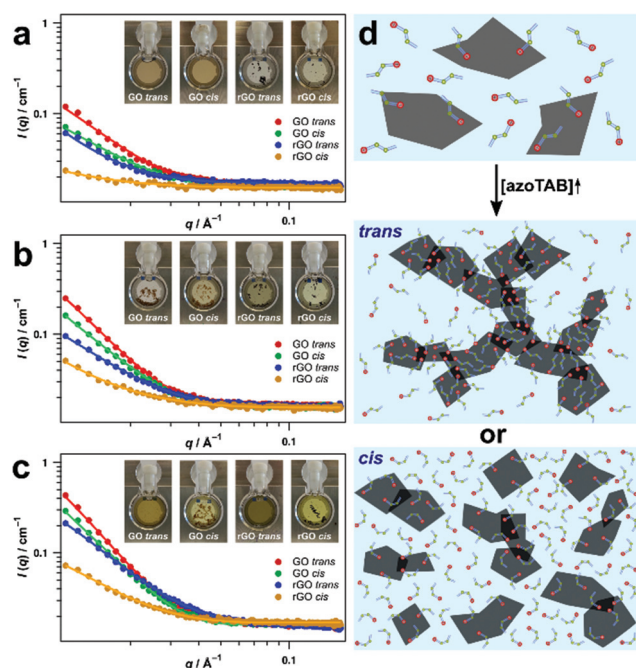


Fig. 6 Small-angle neutron scattering data of GO (0.15 mg mL^{−1}) or rGO (0.1 mg mL^{−1}) in 0.25 mM (a), 0.5 mM (b) and 1 mM (c) solutions of azoTAB. Symbols represent the experimental SANS data and solid lines are the corresponding theoretical fits. The insets are images of each measured sample in 2 mm path-length quartz cells. (d) A schematic showing the proposed formation of fractal aggregates as surfactant loadings are increased in the *trans* and *cis* state. For simplicity, surfactant molecules are displayed in only one isomeric state rather than the respective photostationary states.

Conclusions

In summary, we have shown that by incorporating a photosensitive surfactant molecule with a cationic head-group into aqueous carbon nanomaterial systems, it is possible to control the dispersion state of these materials using only light as a clean and low energy external stimulus. Using photoisomerisation to subtly shift the equilibrium between free and adsorbed surfactant, the carbon-based materials can be reversibly dispersed and flocculated. Crucially, by exploring a wide range of conditions including concentration and pH effects, it becomes clear that charge is not the only factor at play, and that surfactant adsorption occurs also *via* π -stacking and van der Waals type interactions. The photo-modulated flocculation of CNMs provides a facile means of recovering these materials from solution, enhancing opportunities for their application, processing and deployment in aqueous systems.

Acknowledgements

We thank the Monash Centre for Atomically Thin Materials for providing funding that supported this project, and we acknowledge the support of the Bragg Institute, Australian Nuclear Science and Technology Organisation, in providing the neutron research facilities used in this work. We would also like to acknowledge the Monash Centre for Electron Microscopy for the use of their facilities.

References

- 1 K. S. Novoselov, A. K. Geim, S. V. Morozov, D. Jiang, Y. Zhang, S. V. Dubonos, I. V. Grigorieva and A. A. Firsov, *Science*, 2004, **306**, 666–669.
- 2 M. Lotya, P. J. King, U. Khan, S. De and J. N. Coleman, *ACS Nano*, 2010, **4**, 3155–3162.
- 3 D. Li, M. B. Muller, S. Gilje, R. B. Kaner and G. G. Wallace, *Nat. Nanotechnol.*, 2008, **3**, 101–105.
- 4 B. Konkena and S. Vasudevan, *J. Phys. Chem. Lett.*, 2012, **3**, 867–872.
- 5 F. Kim, L. J. Cote and J. Huang, *Adv. Mater.*, 2010, **22**, 1954–1958.
- 6 T. M. McCoy, M. J. Pottage and R. F. Tabor, *J. Phys. Chem. C*, 2014, **118**, 4529–4535.
- 7 G. Z. Kyzas, E. A. Deliyanni and K. A. Matis, *J. Chem. Technol. Biotechnol.*, 2014, **89**, 196–205.
- 8 T. M. McCoy, P. Brown, J. Eastoe and R. F. Tabor, *ACS Appl. Mater. Interfaces*, 2015, **7**, 2124–2133.
- 9 K. C. Kemp, H. Seema, M. Saleh, N. H. Le, K. Mahesh, V. Chandra and K. S. Kim, *Nanoscale*, 2013, **5**, 3149–3171.
- 10 A. Estévez-Torres, C. Crozatier, A. Diguët, T. Hara, H. Saito, K. Yoshikawa and D. Baigl, *Proc. Natl. Acad. Sci. U. S. A.*, 2009, **106**, 12219–12223.
- 11 A. Vesperinas, J. Eastoe, S. Jackson and P. Wyatt, *Chem. Commun.*, 2007, 3912–3914.
- 12 S. L. Gilat, S. H. Kawai and J.-M. Lehn, *Chem. – Eur. J.*, 1995, **1**, 275–284.
- 13 A. S. Kumar, T. Ye, T. Takami, B.-C. Yu, A. K. Flatt, J. M. Tour and P. S. Weiss, *Nano Lett.*, 2008, **8**, 1644–1648.
- 14 S. Shinkai, K. Matsuo, A. Harada and O. J. Manabe, *Chem. Soc., Perkin Trans. 2*, 1982, 1261–1265.
- 15 X. Liu and N. L. Abbott, *J. Colloid Interface Sci.*, 2009, **339**, 1–18.
- 16 P. Brown, C. P. Butts and J. Eastoe, *Soft Matter*, 2013, **9**, 2365–2374.
- 17 M. Dubecky, R. Derian, L. Mitas and I. Stich, *J. Chem. Phys.*, 2010, **133**, 244301.
- 18 J. Eastoe and A. Vesperinas, *Soft Matter*, 2005, **1**, 338–347.
- 19 L. Vaisman, H. D. Wagner and G. Marom, *Adv. Colloid Interface Sci.*, 2006, **128**, 37–46.
- 20 S. Stankovich, D. A. Dikin, R. D. Piner, K. A. Kohlhaas, A. Kleinhammes, Y. Jia, Y. Wu, S. T. Nguyen and R. S. Ruoff, *Carbon*, 2007, **45**, 1558–1565.
- 21 S. Park, J. An, I. Jung, R. D. Piner, S. J. An, X. Li, A. Velamakanni and R. S. Ruoff, *Nano Lett.*, 2009, **9**, 1593–1597.
- 22 G. K. Ramesha, A. V. Kumara, H. B. Muralidhara and S. Sampath, *J. Colloid Interface Sci.*, 2011, **361**, 270–277.
- 23 E. Fischer, M. Frankel and R. Wolovsky, *J. Chem. Phys.*, 1995, **23**, 1367.
- 24 J. Griffiths, *Chem. Soc. Rev.*, 1972, **1**, 481–492.
- 25 E. Chevallier, A. Mamane, H. A. Stone, C. Tribet, F. Lequeux and C. Monteux, *Soft Matter*, 2011, **7**, 7866–7874.
- 26 H. M. D. Bandara and S. C. Burdette, *Chem. Soc. Rev.*, 2012, **41**, 1809–1825.
- 27 C. T. Lee Jr., K. A. Smith and T. A. Hatton, *Langmuir*, 2009, **25**, 13784–13794.
- 28 A.-L. Le Ny and C. T. Lee Jr., *J. Am. Chem. Soc.*, 2006, **128**, 6400–6408.
- 29 L. M. Woods, Ş. C. Bădescu and T. L. Reinecke, *Phys. Rev. B: Condens. Matter*, 2007, **75**, 155415.
- 30 Y. Liu, J. Zhang, X. Chen, J. Zheng, G. Wang and G. Liang, *RSC Adv.*, 2014, **4**, 58036.
- 31 Y. Zhu, W. Cai, R. D. Piner, A. Velamakanni and R. S. Ruoff, *Appl. Phys. Lett.*, 2009, **95**, 103104.
- 32 I. K. Moon, J. Lee, R. S. Ruoff and H. Lee, *Nat. Commun.*, 2010, **1**, 73.
- 33 J. Yu, N. Groissord, C. E. Koning and J. Loos, *Carbon*, 2007, **45**, 618–623.
- 34 O. Matarredona, H. Rhoads, Z. Li, J. H. Harwell, L. Balzano and D. E. Resasco, *J. Phys. Chem. B*, 2003, **107**, 13357–13367.
- 35 W. W. Mullins and R. F. Sekerka, *J. Appl. Phys.*, 1963, **34**, 323–329.
- 36 R. Q. Hwang, J. Schröder, C. Günther and R. J. Behm, *Phys. Rev. Lett.*, 1991, **67**, 3279–3282.
- 37 J. Bahadur, S. Mazumder, D. Sen and S. J. Ramanathan, *Phys.: Condens. Matter*, 2010, **22**, 195107.

Light-controllable dispersion and recovery of graphenes and carbon nanotubes using a photo-switchable surfactant

Electronic Supplementary Information

Thomas M. McCoy ^a, Amelia C. Y. Liu^b and Rico F. Tabor^{a*}

^a School of Chemistry, Monash University, Clayton, VIC 3800, Australia

^b Monash Centre for Electron Microscopy and School of Physics and Astronomy,

Monash University, Clayton, VIC 3800, Australia

* 

Materials

Synthesis of graphene oxide

GO was synthesised from graphite flakes (Sigma, +100 mesh) using the improved Hummers method described in Marcano *et al.*¹ The graphite flakes (1 g) were dispersed in 113 mL of concentrated sulphuric and phosphoric acids in a 9:1 ratio, both from ChemSupply (>99%). This mixture was then stirred while potassium permanganate (6 g, Sigma) was added slowly in small increments. After addition was complete, the temperature was elevated to 50 °C and the reaction was left to stir overnight. The resultant orange/brown mixture was then cooled to room temperature and poured over ice (*ca.* 300 mL) with approximately 1 mL 30% w/w hydrogen peroxide. Large particles were removed from the crude reaction mixture by filtration. The mixture was then centrifuged repeatedly at 4000 rpm with increasing durations of centrifugation. The supernatant liquid was discarded and replaced with ultrapure water between each wash cycle. This process was repeated several times. A final gentle centrifugation step (2000 rpm, 10 minutes) of the product served to remove any particularly large particles or unreacted graphite and the clean GO in the supernatant was then removed. This solution was then sonicated for 30 minutes in a bath to maximise exfoliation of the sheets.

Synthesis of reduced graphene oxide

Reduced GO was synthesised according to the procedure detailed in Li *et al.*². A dilute solution of GO (30 mL, 0.4 mg/mL) made as previously described was put under stirring, following which 21 μ L of hydrazine monohydrate (Sigma, 50% w/w) and 105 μ L of aqueous ammonia (ChemSupply, 28% w/w) was added. The mixture was then left to stir at *ca.* 80 °C for 90 minutes which yielded a black dispersion. The rGO was then dialysed for 2 days to minimise salt content using cellulose dialysis tubing (Sigma) which was prepared by immersing the tubing in ice water for 2.5 hours, followed by 30 minutes in sulfuric acid solution (0.2% v/v) and then 10 minutes in hot water.

Carbon nanotubes were purchased from PlasmaChem, with a reported purity of >95% and the number of walls ranging from 3-15.

Synthesis of azoTAB

AzoTAB was synthesised as described previously.³ The final surfactant was purified by twice recrystallising from dried absolute ethanol, and was characterised using ¹H NMR spectroscopy and electrospray ionisation (ESI) mass spectrometry:

Characterisation: Yield: 9.6 g (42%) ¹H NMR: (300 MHz, DMSO-d₆, 25 °C, TMS): δ = 0.91 (t, J=7.5 Hz, 3H, CH₃), 1.27-1.39 (m, 2H, CH₂), 1.55-1.65 (m, 2H, CH₂), 1.76-1.94 (m, 4H, 2CH₂), 2.67 (t, J=7.5 Hz, 2H, CH₂), 3.08 (s, 9H, 3CH₃), 3.37-3.42 (m, 2H, CH₂), 4.15 (t, J=6.0 Hz, 2H, CH₂), 7.14 (d, J=9.0 Hz, 2H, 2CH), 7.39 (d, J=9.0 Hz, 2H, 2CH), 7.77 (d, J=6.0 Hz, 2H, 2CH), 7.88 (d, J=9.0 Hz, 2H, 2CH).

MS (+ESI): m/z: 368.3 ([M-Br]⁺) – see Fig. S1 below.

AzoTAB has a known molar extinction coefficient of 21.6×10^3 L mol⁻¹ cm⁻¹.³ Its critical micelle concentration (CMC) was found to be 1.2 mM and 2.7 mM in *trans*- and *cis*-dominated photostationary states respectively³ and these values compare favourably with the surface tension data presented below.

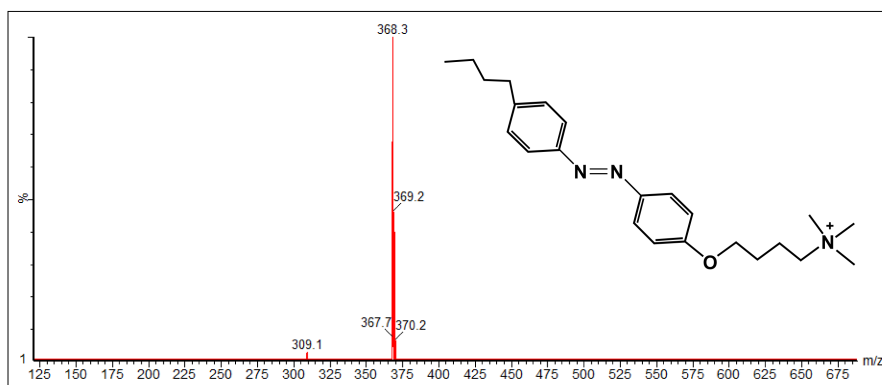


Figure S1: Positive ion electrospray-ionisation mass spectrum of the azoTAB photosurfactant using cone +35 V.

Characterisation of materials

GO and rGO were characterised by several techniques to ensure the materials were well defined and not too chemically similar. To examine the shape and appearance of the GO and rGO as well as the CNTs, atomic force microscopy (AFM) imaging was performed using a JPK Nanowizard 3 AFM in AC (intermittent contact or ‘tapping’) mode. Dilute samples (< 0.1 mg/mL) of GO and rGO were deposited on a mica surface and dried by spin coating. Cantilevers were Bruker NCHV model and had nominal resonant frequencies of 310 kHz, and spring constants of 20 - 80 N/m. Images were obtained with a set-point force of <0.8 nN and refined using JPK data processing software. Mica disks used as substrates for AFM imaging were from ProSciTech (Thuringowa, QLD, Australia) and were freshly cleaved before use. Refer to the main article for details and images.

Optical properties of GO and rGO were analysed by UV-visible spectrophotometry (Fig. S2c,d). The spectra for GO exhibited the typical features known for the material⁴: a strong absorption maximum at 230 nm due to $\pi \rightarrow \pi^*$ transitions and a noticeable shoulder at approximately 300 nm due to $n \rightarrow \pi^*$ transitions. Similar analysis of rGO saw the absorption maximum red shift to 260 nm and become significantly broader, as well as baseline absorbance being much greater across all wavelengths. These differences can be accounted for by substantial restoring of the aromaticity across the face of the sheets, which will cause

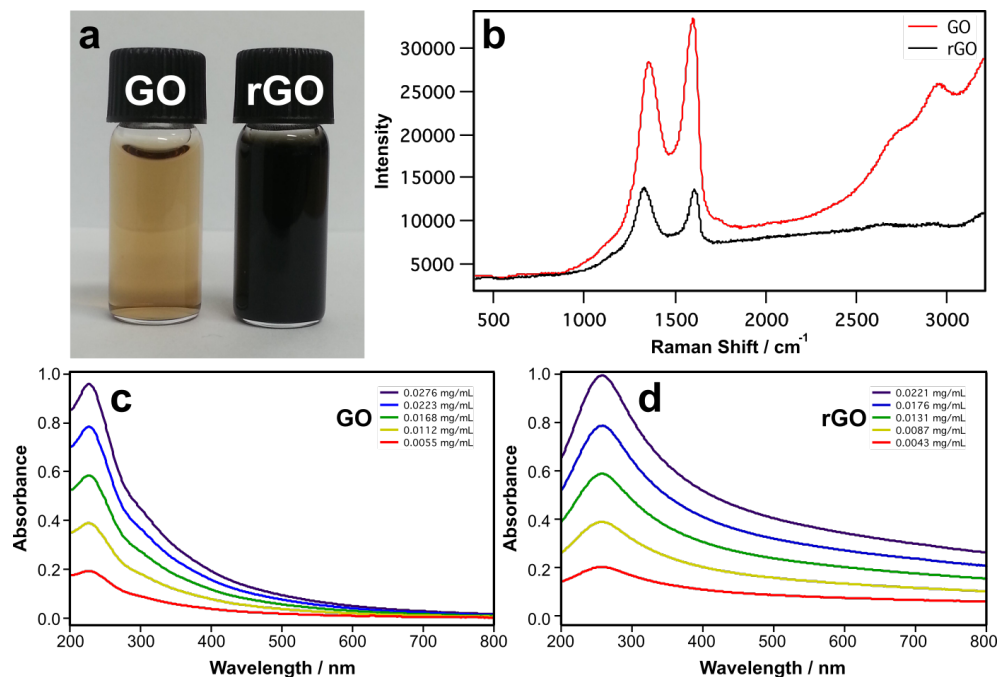


Figure S2: (a) Image of aqueous GO and rGO suspensions, both 0.2 mg/mL. (b) Raman spectra for GO and rGO. UV-visible spectra of GO (c) and rGO (d) at various concentrations.

the material to absorb significantly more light, hence the black appearance.

Functional group chemistry of GO and rGO was analysed by Raman spectroscopy using a Renishaw Invia instrument equipped with a 613 nm argon ion laser for rGO and a 514 nm laser for GO. GO was dried down to be analysed, meanwhile the rGO was analysed as a 0.2 mg/mL solution. The spectra resemble those typically found for graphene-like materials⁵, with strong G bands at approximately 1580 cm⁻¹ as a result of first-order scattering of the E_{2g} mode and also strong D bands for each material at around 1350 cm⁻¹ which indicates a size reduction of the in-plane sp^2 domains, originating from the heavy oxidation process. For rGO, the D band is level height with the G band which is thought to be a result of the sp^2 domains being even further reduced in average size. Pristine graphene does not possess a D band because the sheets are devoid of any defects⁶. The significantly greater intensity of GO is most likely due to its fluorescent properties as well as the measurement being performed on a dry sample.

Methods

Interconversion between the *trans* and *cis* isomers of the azoTAB photosurfactant was examined by UV-visible spectrophotometry using a Cary 60 instrument from Agilent Technologies across the wavelength range of 200 - 800 nm using clean quartz cuvettes with 1 cm pathlengths. Initial *trans* to *cis* conversion was analysed by taking a spectrum before and after irradiating a 0.04 mM solution of the surfactant for 1 minute with a UV lamp. The UV light source used had a radiant power of 19.9 mW cm⁻² incident at the sample, centred at a wavelength of 365 nm and with a characteristic FWHM of 22 nm. The blue light source used had a radiant power of 26.4 mW cm⁻² incident at the sample, centred at a wavelength of 450 nm and with a characteristic FWHM of 12 nm. The ambient laboratory lighting was from fluorescent tubes with a typical incident power at the sample of 1 mW cm⁻². Reversion back to the more favoured *trans* conformation was then monitored over the course of an hour in the ambient laboratory light conditions by performing measurements every 2 minutes. Reversion in complete darkness was assessed in a similar manner, but over 20 hours with measurements performed hourly. In addition, it is important to note that non-quartz glass does not effectively transmit all wavelengths of light. However transmittance at 365 nm is not hindered by the borosilicate glass vials used when experiments were not performed in quartz vessels (see *e.g.* <http://www.schott.com> for the transmission spectrum of the borosilicate glass containers used here).

To obtain surface tension data, standard solutions of azoTAB photosurfactant in the concentration range of 0.1–5.0 mM were prepared. Pendant drop tensiometry was then used to measure the air-water interfacial tension of each solution. This was achieved by suspending a droplet of the sample solution from a syringe with a known needle diameter of 0.72 mm. To ensure that there was deformation of the droplets due to gravitational forces, each droplet was made as large as possible without detaching. A high resolution camera then takes an image of the droplet, and the interfacial tension is calculated based on the dimensions of the drop, by balancing the gravitational forces causing deformation with surface tension. This phenomenon is represented by the Young-Laplace equation for non-spheres:

$$\Delta p = \gamma \left(\frac{1}{r_1} + \frac{1}{r_2} \right)$$

where Δp is the pressure difference across the curved surface, r_1 and r_2 are the two radii of the deformed drop and γ is the surface or interfacial tension. A full description of this method is provided in Berry *et al.*⁷

Adsorption of the photosurfactant was quantified by UV-visible spectrophotometry. Two similar series of samples were prepared: one series was exposed to a 365 nm UV lamp for 10 minutes to effect *trans*→*cis* photoisomerisation before the GO or rGO was added, and the other had no UV exposure. A second set of measurements was also carried out on the previously unexposed samples which were irradiated with UV light for 10 minutes, in order to see how much surfactant would be released back into the system (desorbed). All samples were allowed to equilibrate overnight before measurements were made. Corresponding the measured absorbance values to prepared calibration curves for both isomers of the photosurfactant were performed to obtain the post-adsorption concentrations of each material (Fig. ??). In all cases, it was the supernatant solution of each sample that was analysed and the measurements were performed over a 200 - 800 nm wavelength range in clean, quartz cuvettes with pathlengths of 1 cm. Any GO or rGO was centrifuged down to ensure that the spectra obtained were representative of free surfactant only.

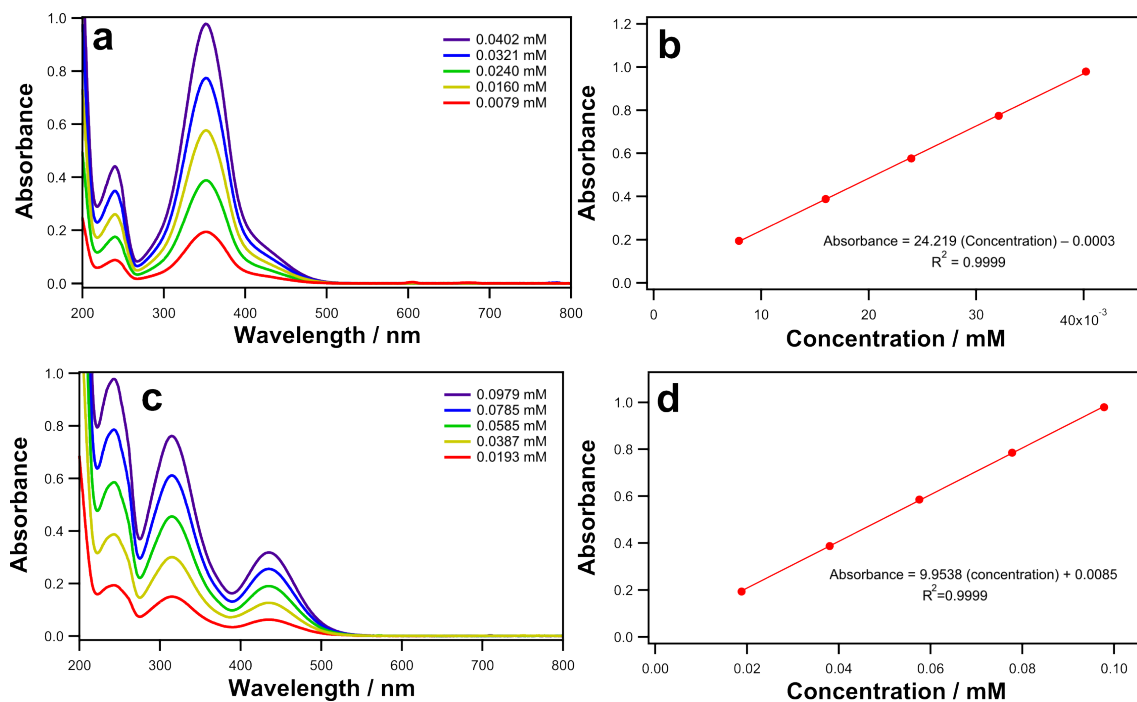


Figure S3: UV-visible spectrophotometry data of azoTAB in the *trans* (a) and *cis* (c) configuration at several concentrations. The corresponding calibration curve for each data set is presented to the right of the spectra (b) and (d), by taking the absorbance values at 351 nm and 240 nm respectively.

Zeta potentials of GO/photosurfactant systems were determined by phase analysis light scattering (PALS) using a Brookhaven Nanobrook Omni. Two series of samples were prepared at pH 10, one of which was irradiated for 5 minutes with 365 nm UV light before being mixed with GO. Samples, were prepared in 1 cm pathlength polystyrene cuvettes, and comprised 0.2 mg/mL aqueous GO dispersion and differing concentrations of azoTAB within the range of 0.1 - 0.5 mM. A palladium PALS electrode was immersed in each sample solution and an alternating current was applied. Measurements each consisted of 30 cycles and 5 runs, hence the displayed data points were mean values with error bars representing the standard error of the mean. The electrophoretic mobilities, u_E , were calculated according to light scattered by each sample which were then translated into zeta potentials, ζ , using the Smoluchowski equation:

$$u_E = \frac{\nu_E}{E} = \frac{\zeta \epsilon}{\eta}$$

where ν_E is the electrophoretic viscosity, E is the electric field strength, ϵ is the permittivity and η is the viscosity of the medium.

Small-angle neutron scattering (SANS) measurements were made at the Bragg Institute, Lucas Heights, Australia using the Quokka beamline. Samples were prepared on site using the equivalent quantity of deuterium oxide, and were analysed in quartz ‘banjo’ cells with 2 mm pathlength and volume of $\approx 0.6 \text{ cm}^3$ at a constant temperature of 25°C. A single detector position at 4 m was used with no detector offset, giving an effective q -range of 0.01 - 0.19 \AA^{-1} and a neutron wavelength of 5 \AA was used. The scattering from an empty cell was subtracted from the 2D scattering pattern obtained, and this was then radially averaged under the assumption of radially isotropic scattering. All scattering patterns were modelled using a mass fractal dimension analysis.⁸

Additional data

Research involving the use of photo-sensitive compounds must be planned with careful consideration to ensure that results are not biased by external factors such as light or heat exposure. To assist with experimental design, a study of the isomerisation kinetics was conducted in which the changes in the absorption spectrum of the photosurfactant were monitored over time in response to certain illumination conditions (Fig. S3).

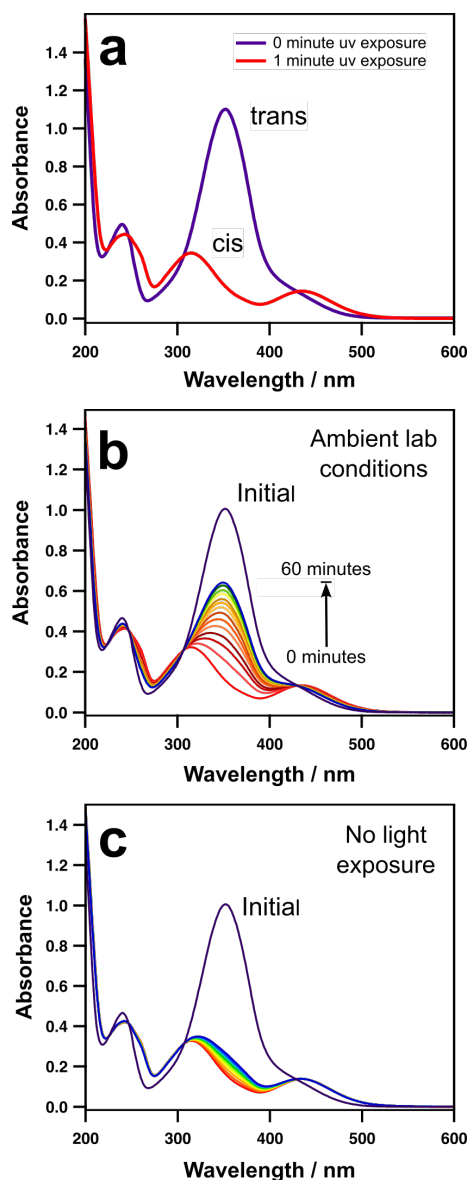


Figure S4: (a) The change in UV-visible spectrum of the azoTAB photosurfactant following 1 minute of irradiation with UV light at 365 nm. (b) Reversion of azoTAB under ambient light conditions with changes recorded over a 60 minute time period. (c) Reversion of azoTAB when subjected to total darkness with changes measured over 20 hours. In both cases (b & c), the surfactant has been irradiated with UV light for 3 minutes following an initial reading being taken prior to irradiation.

The UV spectra of the *cis* and *trans* isomer differ markedly. Irradiation of a dilute solution of

azoTAB (*ca.* 0.04 mM) with 365 nm light for 1 minute appeared to be sufficient for maximal conversion to the *cis* isomer at this concentration (Fig. S3a), with increased durations of exposure not causing any further changes in the spectral signature of the surfactant. The strong 360 nm absorption maximum of the *trans* isomer, which appears due to $\pi \rightarrow \pi^*$ transitions, is seen to undergo a substantial decrease in absorbance intensity, meanwhile the absorption band at 430 nm originating from $n \rightarrow \pi^*$ transitions slightly increased in intensity. This is a result of the *cis* isomer predominating, which is less energetically favourable due to a significant increase in steric hindrance⁹.

Light at around 450 nm facilitates conversion back to the *trans* isomer¹⁰, hence the effects of exposure to the ambient light conditions of the laboratory were analysed. Fast reversion to the *trans* isomer was observed over the course of 1 hour (Fig. S3b). However, when kept in complete darkness, very minimal reversion was apparent over many hours (Fig. S3c). Hence, all subsequent experiments involving azoTAB were conducted with as little light exposure as possible to ensure that the stability of both the *cis* and *trans* isomers was maintained.

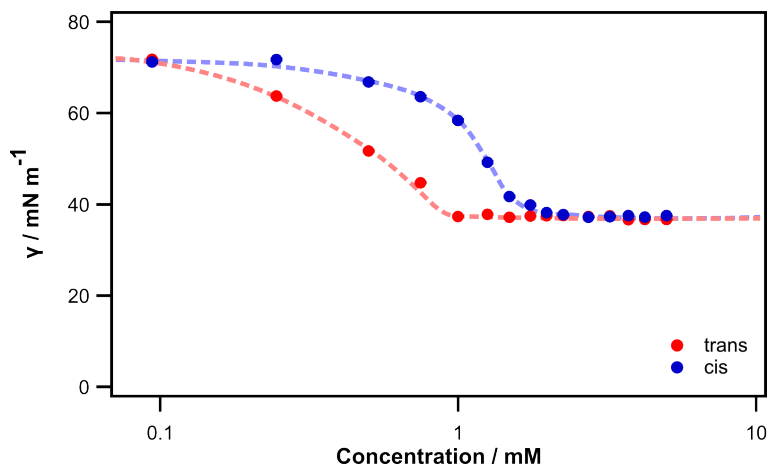


Figure S5: Pendant drop tensiometry data of azoTAB photosurfactant before (*trans*) and after (*cis*) irradiation with 365 nm light.

To properly assess the surface activity of azoTAB, surface tension measurements using a pendant drop apparatus were performed for different concentrations of the surfactant. A

significant difference in surface tension was noted before and after UV irradiation of the surfactant solution, with the non-irradiated form (*trans*) causing a much more rapid decline in surface tension (Fig. S4). Water has a well known surface tension of 72.8 mN/m at 20 °C¹¹. It can be seen in Figure S4 that in the absence of UV, a concentration of at least 1 mM azoTAB can reduce the surface tension of water to 37 mN/m before levelling out. With UV exposure, it does not reach this value until at least 2 mM of surfactant are present. These values correspond to the critical micelle concentrations for each photoisomer and the difference can be accounted for by the change in dipole moment associated with isomerisation to the *cis* conformation. The *cis* isomer has a larger dipole moment than the *trans*, making its tail-group more soluble. Therefore in this conformation, the surfactant will not adsorb as readily to the interface and partitions more into the bulk aqueous phase than the *trans* isomer⁹. Interestingly, the *cis* form does eventually level out at the same surface tension value (*ca.* 37 mN/m) as the non-irradiated solution. Previous studies state that at higher concentrations, the solution may need to be irradiated for longer to achieve maximum conversion^{12,10}, due to the strong absorbance of the azobenzene chromophore¹³. In addition, it is noteworthy that complete conversion to a particular isomer cannot be achieved due to the system reaching a so-called ‘photostationary state’, comprising a mixture of both geometric isomers where the rate of formation of one is now equal to the rate of reversion to the other¹⁴. Therefore, as the concentration of surfactant is increased, so is the amount of *trans* isomer, despite the solution being illuminated with UV. Hence the additional, more surface active *trans* molecules will invariably increase in number at higher concentrations and by more readily accumulating at the surface, eventually lower the surface tension of water to the same value as for the *trans*-dominated photostationary state.

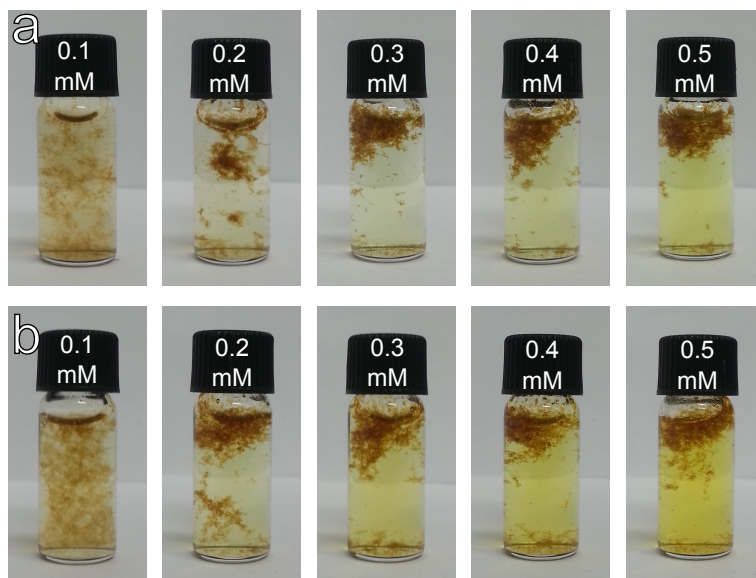


Figure S6: (a) Images of 1.5 mL sample vials containing 0.2 mg/mL GO and the specified concentrations of azoTAB 30 minutes after preparation. (b) Identical samples in which the azoTAB was irradiated for 5 minutes before the GO was added. All samples are at pH 3.

The physical effects of the photosurfactant on GO are somewhat similar to those previously observed when GO has been recovered using magnetic surfactants¹⁵, whereby mixing causes immediate flocculation of the GO (Fig. S5). However, an interesting effect is observed whereby flocculation using azoTAB causes flotation of the aggregates. This suggests that the network formed is initially very loosely linked and in terms of GO capture, flotation would allow for easier recovery of the GO. Also, given the extremely low concentrations of azoTAB required to cause flocculation, it is obvious that the photosurfactant has a very strong affinity for GO and hence can be considered a good adsorbate in these systems. However at this pH ($\text{pH} \approx 3$), there is no discernible difference between *cis* and *trans* and destabilisation of the GO is too immediate and final for photocontrol of the dispersion to be possible.

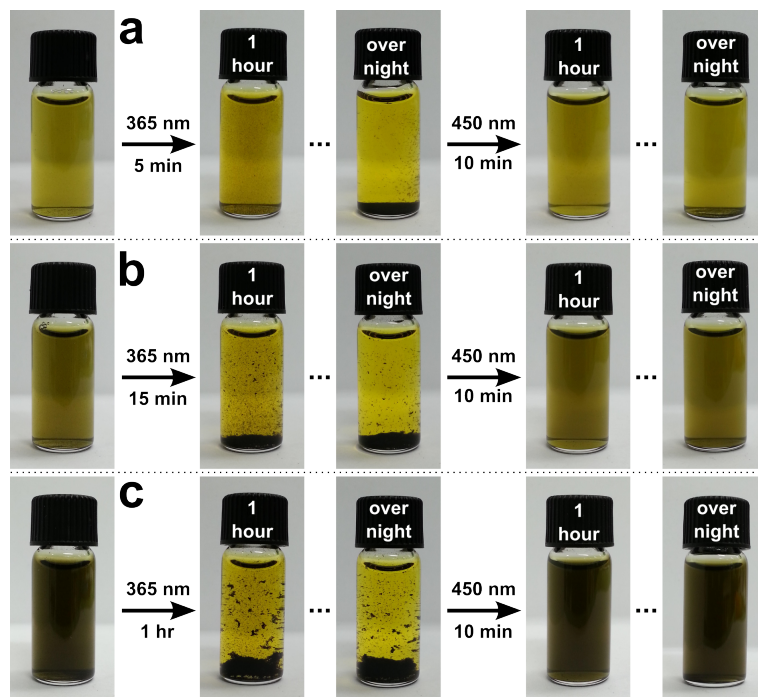


Figure S7: (a, b and c) Digital images of a 1.5 mL sample vials, each containing 1.2 mM of azoTAB and a different concentration of rGO: (a) 0.025 mg/mL, (b) 0.05 mg/mL and (c) 0.1 mg/mL. Initial photos on the far left were taken 2 hours after mixing (*trans*). Each sample was then irradiated with 365 nm light until a noticeable degree of flocculation could be seen (5 minutes for a, 15 minutes for b and 1 hour for c). Photos were then taken after a further 1 hour of settling and again overnight. The samples were then irradiated for 10 minutes with 450 nm light with photos again taken after 1 hour of equilibration time and overnight. Each sample was shaken gently by hand between each irradiation step. To assist with redispersion, short sonication times of 1, 2 and 3 minutes (according to increasing rGO concentrations) were performed to assist with breaking up the flocs.

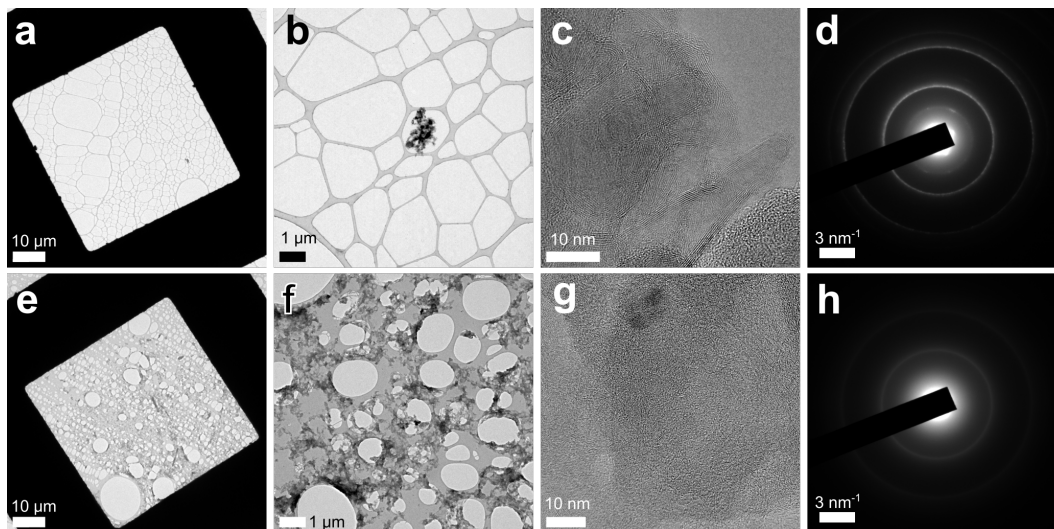


Figure S8: (a & b) Low-magnification TEM images of rGO prepared from an aqueous suspension. (c) A high-resolution TEM image of rGO with the corresponding selected area electron diffraction pattern are shown in (d). (e-h) A similar series for a sample including azoTAB surfactant. Refer to scale bars for precise size dimensions.

TEM imaging and diffraction was performed at the Monash Centre for Electron Microscopy using a JEOL JEM-2100F microscope operating at 200 keV. Images were acquired using a Gatan Ultrascan 1000 (2048x2048). Samples were prepared by depositing dilute aqueous suspensions (0.05 mg/mL) of rGO and rGO/azoTAB onto lacey carbon grids. For the rGO/azoTAB sample, the material was twice washed by centrifugation to remove extraneous surfactant from the bulk solution, thus ensuring higher image quality and minimising contamination. The high resolution images and diffraction patterns are presented and discussed in the main paper.

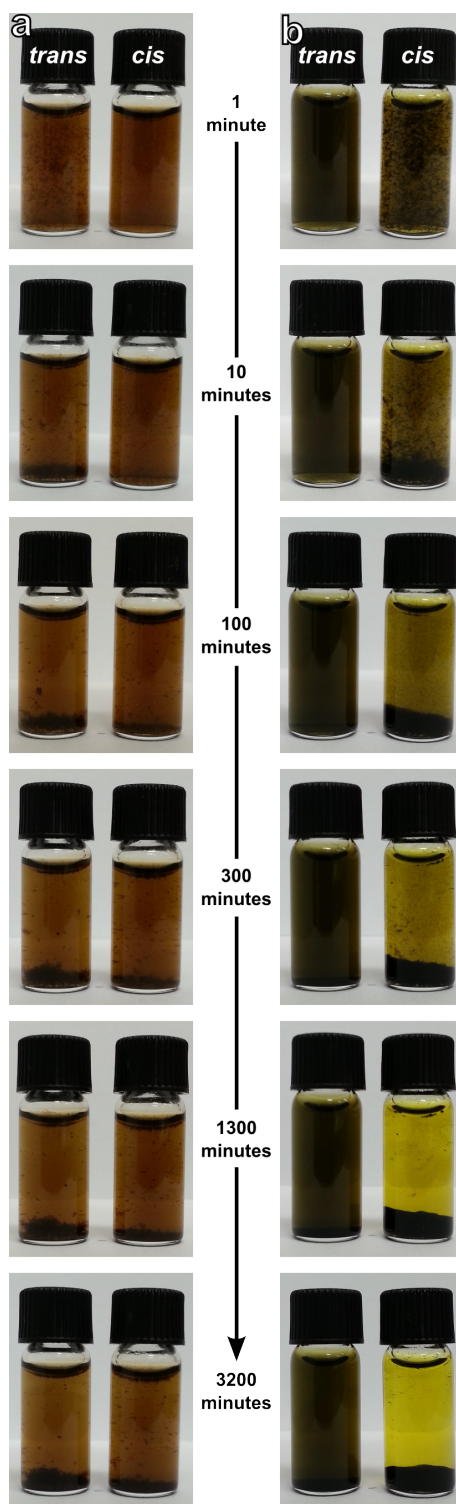


Figure S9: Digital photographs of 1.5 mL sample vials at specific time intervals. (a) Two identical samples that contain 0.25 mg/mL of GO and 0.5 mM of azoTAB. The right hand vial of the series (*cis*) was irradiated with 365 nm for 10 minutes light prior to the GO being added. (b) An experimentally similar pair of vials containing 0.1 mg/mL of rGO and 1.5 mM of azoTAB.

Tables S1 and S2 show the raw data values for the *cis* vs *trans* adsorption isotherm on rGO in Figure 2c of the main paper.

Table S1: Adsorption details for non-irradiated azoTAB on rGO at pH 11. C_I is the initial surfactant concentration, C_{ads} is the surfactant concentration following adsorption, Γ is the amount of surfactant adsorbed and % ads. is the percentage of surfactant adsorbed.

C_I / mM	C_{ads} / mM	Γ / mmol g ⁻¹	% ads.
0.26	0.04	2.24	85.9
0.50	0.20	3.08	60.4
0.75	0.35	3.99	53.4
1.00	0.84	1.55	15.7
1.25	1.09	1.66	13.1
1.49	1.41	0.75	5.2
1.73	1.69	0.32	1.9
2.00	1.92	0.76	3.9
2.98	2.98	0.00	0.0

Table S2: Adsorption details for azoTAB on rGO at pH 11 when the surfactant solutions were irradiated for 10 minutes. C_I is the initial surfactant concentration, C_{ads} is the surfactant concentration following adsorption, Γ is the amount of surfactant adsorbed and % ads. is the percentage of surfactant adsorbed.

C_I / mM	C_{ads} / mM	Γ / mmol g ⁻¹	% ads.
0.25	0.06	1.96	75.9
0.50	0.27	2.34	46.8
0.75	0.45	2.72	39.0
0.98	0.65	3.19	33.0
1.23	0.89	3.40	27.8
1.49	0.77	7.15	48.5
1.67	0.64	10.15	61.6
2.04	0.60	14.26	70.4
2.78	2.26	5.14	18.4

Tables 4-8 show the raw data values for the adsorption isotherm on GO in Figure 3c of the main paper.

Table S3: Adsorption details for non-irradiated azoTAB on GO at pH 3. C_I is the initial surfactant concentration, C_{ads} is the surfactant concentration following adsorption, Γ is the amount of surfactant adsorbed and % ads. is the percentage of surfactant adsorbed.

C_I / mM	C_{ads} / mM	Γ / mmol g ⁻¹	% ads.
0.26	0.01	0.99	96.5
0.50	0.05	1.79	89.2
0.76	0.12	2.56	84.5
1.00	0.18	3.33	82.1
1.26	0.24	4.08	81.2
1.48	0.30	4.72	79.5
1.75	0.42	5.27	76.0
2.00	0.56	5.71	71.8
2.22	0.76	5.95	65.8
2.51	0.92	6.33	63.2
2.71	1.07	6.60	60.4
3.00	1.34	6.59	55.3
3.23	1.48	7.00	54.1
3.48	1.75	6.95	49.8
3.76	2.02	6.96	46.2
4.00	2.17	7.32	45.8
4.25	2.39	7.37	43.8
4.44	2.55	7.52	42.5
4.69	2.79	7.84	40.5

Table S4: Adsorption details for non-irradiated azoTAB on GO at pH 10. C_I is the initial surfactant concentration, C_{ads} is the surfactant concentration following adsorption, Γ is the amount of surfactant adsorbed and % ads. is the percentage of surfactant adsorbed.

C_I / mM	C_{ads} / mM	Γ / mmol g ⁻¹	% ads.
0.29	0.01	1.13	97.1
0.48	0.01	1.88	97.4
0.77	0.08	2.80	89.8
0.99	0.14	3.42	85.8
1.31	0.24	4.10	81.8
1.49	0.32	4.71	78.6
1.73	0.45	5.03	73.8
1.99	0.66	5.44	66.9
2.23	0.93	5.23	58.3
2.75	1.34	5.44	51.3
3.04	1.64	5.55	46.2
3.22	1.74	6.07	45.9
3.50	1.97	6.00	43.6
4.02	2.50	6.28	37.9
4.27	2.71	6.31	36.5
4.46	2.87	6.17	35.5
4.66	3.00	6.36	35.5
4.67	3.07	6.34	34.2

Table S5: Adsorption details for azoTAB on GO at pH 3 when the surfactant solutions were irradiated for 10 minutes. C_I is the initial surfactant concentration, C_{ads} is the surfactant concentration following adsorption, Γ is the amount of surfactant adsorbed and % ads. is the percentage of surfactant adsorbed.

C_I / mM	C_{ads} / mM	Γ / mmol g ⁻¹	% ads.
0.26	0.05	0.83	81.6
0.51	0.21	1.19	58.0
0.75	0.41	1.37	45.4
1.01	0.59	1.64	41.3
1.24	0.74	1.93	40.2
1.52	0.94	2.23	37.9
1.75	1.23	2.07	30.1
1.99	1.28	2.71	35.4
2.22	1.41	3.10	36.8
2.49	1.63	3.30	34.7
2.73	1.78	3.58	34.8
3.47	2.41	3.96	30.6
3.71	2.60	4.03	30.0
3.97	2.86	3.95	28.1
4.71	3.75	4.38	20.5

Table S6: Adsorption details for azoTAB on GO at pH 10 when the surfactant solutions were irradiated for 10 minutes. C_I is the initial surfactant concentration, C_{ads} is the surfactant concentration following adsorption, Γ is the amount of surfactant adsorbed and % ads. is the percentage of surfactant adsorbed.

C_I / mM	C_{ads} / mM	Γ / mmol g ⁻¹	% ads.
0.26	0.03	0.91	89.4
0.49	0.13	1.43	73.9
0.74	0.28	1.84	62.3
1.02	0.49	2.10	52.5
1.23	0.64	2.32	48.2
1.49	0.88	2.54	41.0
1.77	1.04	2.90	41.0
2.01	1.15	3.49	42.6
2.22	1.21	3.59	45.7
2.75	1.70	4.17	38.3
3.02	1.92	4.19	36.6
3.26	2.16	4.16	33.8
3.47	2.29	4.27	33.9
4.22	3.00	4.80	28.8

Table S7: Adsorption details for azoTAB on GO at pH 10 when the surfactant solutions were irradiated for 10 minutes *after* being mixed with the GO. C_I is the initial surfactant concentration, C_{ads} is the surfactant concentration following adsorption, Γ is the amount of surfactant adsorbed and % ads. is the percentage of surfactant adsorbed.

C_I / mM	C_{ads} / mM	Γ / mmol g ⁻¹	% ads.
0.26	0.01	0.99	96.3
0.50	0.12	1.52	75.9
0.76	0.30	1.84	60.6
1.00	0.47	2.15	53.0
1.26	0.61	2.57	51.2
1.48	0.73	3.01	50.6
1.75	0.87	3.47	50.1
2.00	1.00	3.96	49.9
2.22	1.14	4.41	48.9
2.51	1.28	4.89	48.9
2.71	1.41	5.25	48.1
3.00	1.59	5.60	46.9
3.23	1.78	5.79	44.8
3.48	2.11	5.51	39.5
3.76	2.30	5.84	38.8
4.00	2.51	5.97	37.3
4.25	2.78	5.80	34.5
4.44	2.97	5.87	33.2
4.69	3.20	6.14	31.7
4.68	3.20	6.06	31.7

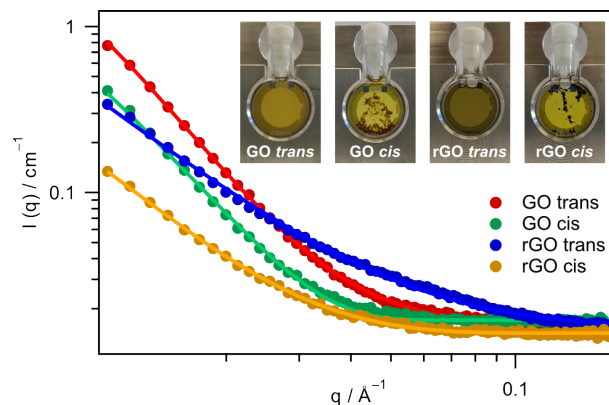


Figure S10: Small-angle neutron scattering data of GO and rGO 2 mM of azoTAB. All samples contained either 0.15 mg/mL of GO or 0.1 mg/mL of rGO. The solid points represent the actual experimental data, meanwhile the trendlines are the corresponding fits to each data set. The insets are digital images of each sample measured in quartz banjo cells with 2 mm pathlengths. All *cis* samples were irradiated with UV light for 10 minutes prior to the GO/rGO being added.

Table S8: Table quantifying concentrations and adsorption for samples used for SANS. These samples can be seen in the insets of Figure S9. The values for adsorption and % adsorption were estimated using the isotherms presented in the main paper.

Sample	C_I / mM	Γ / mmol g ⁻¹	% ads.
	0.25	1.1	98
GO	0.49	1.8	97
<i>trans</i>	1.01	3.3	86
	1.99	5.6	67
	0.25	0.8	88
GO	0.50	1.1	74
<i>cis</i>	0.99	1.6	50
	1.96	2.5	40
	0.25	1.1	86
rGO	0.51	3.0	60
<i>trans</i>	0.99	2.0	15
	2.02	0.2	4
	0.25	0.9	76
rGO	0.51	1.1	47
<i>cis</i>	1.01	3.1	33
	1.98	7.6	74

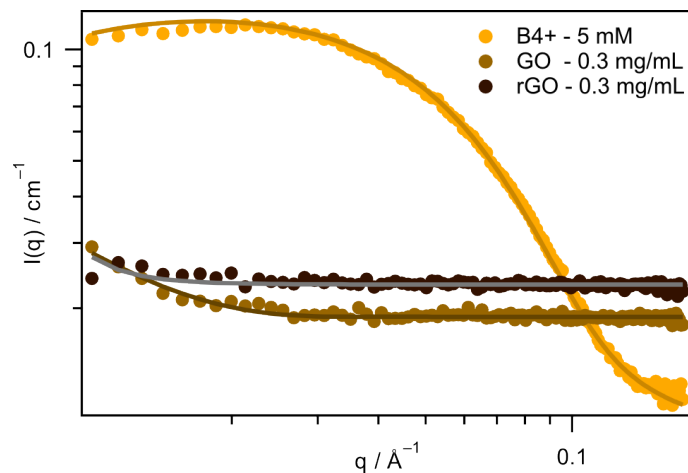


Figure S11: Small-angle neutron scattering data of azoTAB photosurfactant (labelled using its shorthand structural name ‘B4+’ in this figure), and aqueous graphene oxide and reduced graphene oxide solutions. Solid symbols represent the data points and the solid lines are the fits of the data. Experiments were performed at 25 °C and a sample–detector distance of 4 m.

SANS analysis of non-mixed systems (*i.e.* the pure components) was performed in order to see the scattering patterns of the ‘blank’ materials (Fig. S10). The fitting parameters for these samples, as well as the ones presented in the main article are shown in Tables S9 and S10.

Table S9: Fitting parameters used to describe the scattering patterns of the SANS data with a mass fractal model. C_{length} is the correlation length, $M_{dim.}$ is the mass dimension and R is the radius of the particles.

	Sample	Background	C_{length}	$M_{dim.}$	Scale	$R / \text{\AA}$
GO	0.3 mg/mL	0.019	300	1.6	7.8×10^{-6}	130
rGO	0.3 mg/mL	0.020	6.2	1.6	0.03	570
GO/azoTAB <i>trans</i>	0.25 mM	0.016	167	2.7	3.8×10^{-6}	20
	0.5 mM	0.016	170	2.7	2.7×10^{-6}	55
	1 mM	0.017	200	2.4	4.4×10^{-6}	65
	2 mM	0.016	200	2.1	3.8×10^{-6}	65
GO/azoTAB <i>cis</i>	0.25 mM	0.017	220	2.4	9.6×10^{-6}	70
	0.5 mM	0.016	858	2.3	1.1×10^{-5}	70
	1 mM	0.016	1000	1.9	2.6×10^{-5}	75
	2 mM	0.016	400	1.6	2.6×10^{-5}	70
rGO/azoTAB <i>trans</i>	0.25 mM	0.016	1500	1.9	5.1×10^{-5}	15
	0.5 mM	0.016	150	2.4	5.7×10^{-6}	30
	1 mM	0.016	200	2.0	8.9×10^{-6}	50
	2 mM	0.016	300	2.2	1.6×10^{-6}	30
rGO/azoTAB <i>cis</i>	0.25 mM	0.014	220	2.2	6.8×10^{-6}	40
	0.5 mM	0.017	150	2.1	5.5×10^{-6}	50
	1 mM	0.015	300	2.0	3.7×10^{-6}	30
	2 mM	0.015	250	1.8	2.6×10^{-6}	45

Table S10: Fitting parameters used to describe the scattering pattern of azoTAB SANS data with an ellipsoid model.

	C / mM	Background	Scale factor	Temperature / K	Charge	Radii a,b / Å
azoTAB	5	0.01	1	298.15	+2.39	18.2, 39.9

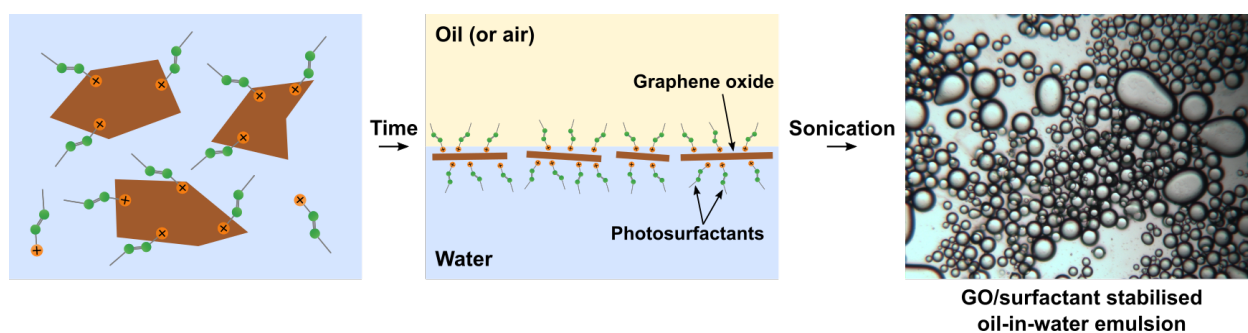
References

- [1] D. C. Marcano, D. V. Kosynkin, J. M. Berlin, A. Sinitskii, Z. Sun, A. Slesarev, L. B. Alemany, W. Lu and J. M. Tour, *ACS Nano*, 2010, **4**, 4806–4814.
- [2] D. Li, M. B. Muller, S. Gilje, R. B. Kaner and G. G. Wallace, *Nat. Nanotechnol.*, 2008, **3**, 101–105.
- [3] T. Hayashita, T. Kurosawa, T. Miyata, K. Tanaka and M. Igawa, *Colloid Polym. Sci.*, 1994, **272**, 1611–1619.
- [4] Q. Lai, S. Zhu, X. Luo, M. Zuo and S. Huang, *AIP Advances*, 2012, **2**, 1–5.
- [5] S. Stankovich, D. A. Dikin, R. D. Piner, K. A. Kohlhaas, A. Kleinhammes, Y. Jia, Y. Wu, S. T. Nguyen and R. S. Ruoff, *Carbon*, 2007, **45**, 1558–1565.
- [6] Y. Zhu, S. Murali, W. Cai, X. Li, J. W. Suh, J. R. Potts and R. S. Ruoff, *Adv. Mater.*, 2010, **22**, 3906–3924.
- [7] J. Berry, M. Neeson, R. Dagastine, D. Chan and R. Tabor, *Journal of Colloid and Interface Science*, 2015, **454**, 226–237.
- [8] D. F. R. Mildner and P. L. Hall, *J. Phys. D: Appl. Phys.*, 1986, **19**, 1535–1545.
- [9] T. Shang, K. A. Smith and T. A. Hatton, *Langmuir*, 2003, **19**, 10764–10773.
- [10] E. Chevallier, A. Mamane, H. A. Stone, C. Tribet, F. Lequeux and C. Monteux, *Soft Matter*, 2011, **7**, 7866–7874.
- [11] N. B. Vargaftik, B. N. Volkov and L. D. Voljak, *J. Phys. Chem. Ref. Data*, 1983, **12**, 817–820.
- [12] L. Yang, N. Takisawa, T. Hayashita and K. Shirahama, *J. Phys. Chem.*, 1995, **99**, 8799–8803.
- [13] J. Griffiths, *Chem. Soc. Rev.*, 1972, **1**, 481–493.
- [14] E. Fischer, M. Frankel and R. Wolovsky, *J. Chem. Phys.*, 1955, **23**, 1367.
- [15] T. M. McCoy, P. Brown, J. Eastoe and R. F. Tabor, *ACS Appl. Mater. Interfaces*, 2015, **7**, 2124–2133.

Chapter 5

Surfactant-Enhanced Adsorption of Graphene Oxide for Improved Emulsification of Oil in Water

Published: Thomas M. McCoy, Stephen A. Holt, Ashley M. Rozario, Toby D. M. Bell and Rico F. Tabor, Surfactant-Enhanced Adsorption of Graphene Oxide for Improved Emulsification of Oil in Water. *Adv. Mater. Interfaces*, 2017, 4, 1700803.



Surfactant-Enhanced Adsorption of Graphene Oxide for Improved Emulsification of Oil in Water

Thomas M. McCoy, Stephen A. Holt, Ashley M. Rozario, Toby D. M. Bell, and Rico F. Tabor*

Graphene oxide (GO) can be enriched at the air–water interface by the adsorption of surfactant molecules to the surfaces of the GO sheets. The synergism between the surfactant and GO is shown to be responsible for the improved interfacial performance of the composite through a subtle balance of surface charge and surface activity. The use of a photoaddressable surfactant provides a unique probe for investigating the fundamental mechanisms that control adsorption, by inducing spatiotemporal modulation of the surfactant properties by irradiation with light of certain wavelengths. Tensiometry measurements uncover the interfacial activity of the materials, whereas X-ray reflectivity serves to independently determine the interfacial structure and composition. The ratio between the surfactant and GO appears to be the key factor controlling adsorption, with pH and salt offering additional finer control of interfacial properties. This synergism between GO sheets and a surface active small molecule surfactant is utilized to stabilize oil-in-water emulsions with unprecedented effectiveness.

1. Introduction

The ability of atomically thin materials to locate at interfaces and stabilize Pickering-type emulsions and foams with unprecedented long-term stability has sparked a promising area of research in the field of surface science.^[1] Graphene oxide (GO) is particularly appealing for this purpose as it can be readily processed as an aqueous dispersion due to the large proportion of oxygen-containing functional groups that decorate its carbon lattice.^[2] The oxygen heteroatoms serve to increase the aqueous compatibility of the sheets, and the extremely high surface area arising from the 2D structure of the precursor graphite is retained. The presence of both the polar oxygen groups and the nonpolar sp² carbon domains means that GO sheets are in fact amphiphilic, which greatly increases their affinity for interfaces such as that between oil and water or air and water.^[3] Furthermore, the enormous surface area of GO

means that emulsification or foaming can be efficiently achieved by utilizing only small amounts of material compared to the spherical particles conventionally used for Pickering emulsification.^[4–7] The 2D geometry also allows for favorable packing at interfaces, making their removal more difficult and thus giving these emulsions and foams enhanced stability.^[8–10]

Due to the deprotonation of peripheral carboxylic acid groups, GO sheets bear a high negative surface charge across the majority of the pH scale (>pH 1).^[11,12] As a result, GO tends to remain colloidally dispersed and only locates at interfaces through energetic manipulation. For instance sparging with gas bubbles has been shown to assist in driving GO sheets to the air–water interface,^[13] whereas oil-in-water emulsions stabilized with GO have been found to form more readily in

extremely acidic conditions (<1).^[14] Intense and long sonication times are also shown to facilitate these processes.^[15] Hence, the development of low energy methods for driving GO to these interfaces is necessary to increase its commercial viability as a stabilizer.

Unlike GO, surfactants are small molecules and their adsorption and desorption at interfaces is typically on microsecond to second timescales and is spontaneous.^[16,17] Hence, the enhanced long-term stability of GO-stabilized emulsions likely stems from the higher energy input required to effect its desorption from the interface, stemming from the substantially larger particle sizes and dimensions. Therefore a system containing both surfactants and GO may show enhanced stability. Surfactants have been previously incorporated into aqueous GO systems to yield appealing characteristics such as magnetic response,^[18] as well as thin film deposition at the liquid–gas interface.^[19] However little research has focused on improving and understanding interfacial adsorption of these materials for enhancing their combined stabilizing capacity. Butylphenyl-4-diazeno-4-butoxyphenyltrimethylammonium bromide, referred to as azoTAB, contains the widely-used azobenzene group, known for its *trans*–*cis* photoisomerization when exposed to UV light at ≈ 365 nm (Figure 1a), which overall causes a shift in the photostationary state (PSS).^[20,21] The surfactant interfacial properties change markedly with isomerization,^[22] hence use of a photosurfactant offers an easy method for altering the physical chemistry of a system without introducing extra materials, providing an external trigger for probing the mechanisms underlying overall system behavior.

T. M. McCoy, A. M. Rozario, Dr. T. D. M. Bell, Dr. R. F. Tabor
School of Chemistry
Monash University
Clayton 3800, Australia

Dr. S. A. Holt
Australian Centre for Neutron Scattering
ANSTO
Lucas Heights, New South Wales 2234, Australia

 The ORCID identification number(s) for the author(s) of this article can be found under <https://doi.org/10.1002/admi.201700803>.

DOI: 10.1002/admi.201700803

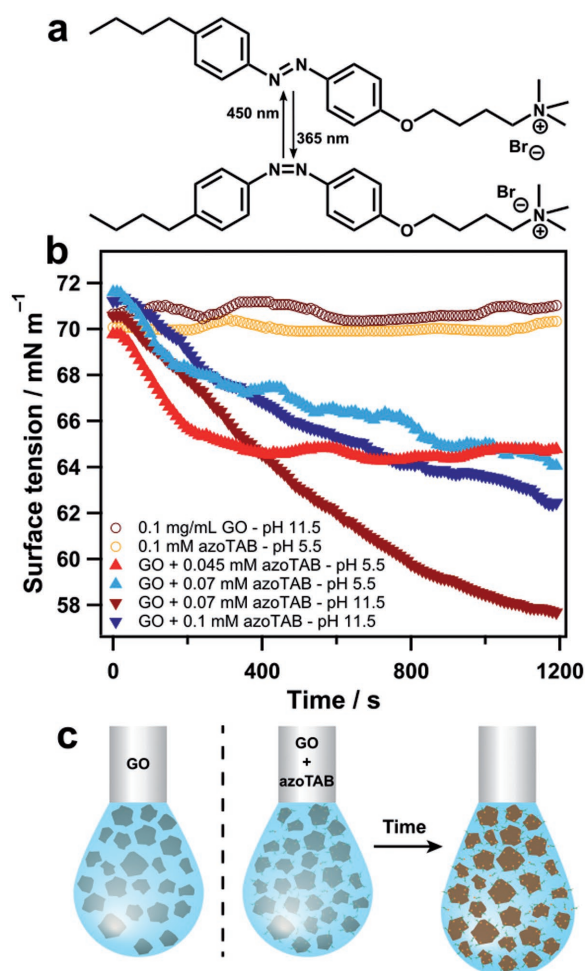


Figure 1. a) Structure of azoTAB and reversible photoisomerization between *trans* and *cis* isomers. b) Dynamic surface tension for GO, azoTAB, and mixtures at different pH values. AzoTAB is in the *trans*-dominated photostationary state and the GO concentration is 0.1 mg mL⁻¹. c) Schematic of the pendant drop measurement showing enrichment of surfactant-coated GO sheets at the interface over time and increased drop deformation compared to the pure GO solution.

Previously, we utilized azoTAB to effect photocontrol over the bulk colloidal stability of graphene oxides.^[23] In this work, we precisely monitor the concomitant adsorption of GO and azoTAB specifically at the air–water interface. In order to understand the complex relationships between the intermolecular interactions of both species and their combined adsorption at the air–water interface, we analyze the effects of surfactant and GO chemistry in terms of hydrophobicity and oxidation of the graphitic materials, and the two geometric isomers of the surfactant, as well as varying solution conditions such as pH and ionic strength.

2. Results

We begin by exploring the synergism between the photoresponsive surfactant molecule azoTAB and GO. AzoTAB has

a cationic head-group and thus readily adsorbs in solution to the negatively charged GO, initially through electrostatic attraction at low concentrations, but also via polar and hydrophobic interactions at higher surfactant loadings.^[23] As surfactants are inherently surface active due to their amphiphilicity, it is expected that as well as making the surface potential of GO more positive due to its cationic head-group, the adsorption of azoTAB will also cause the sheets to become more surface active and assist in driving them to the interface. It is also possible that the surfactant could preferentially adsorb to the interface alone, inhibiting the adsorption of GO. Therefore we seek to fundamentally understand when or if each situation is occurring in order to design more effective GO Pickering systems. To assess the adsorption of these materials at the air–water interface, we utilized pendant drop tensiometry.^[24]

At pH 5.5, a significant decrease in surface tension over time was seen when GO was present with azoTAB, when compared to pure azoTAB at a similar concentration (Figure 1b). This observation suggests that synergistic effects between the two materials occur, and the interface is becoming enriched with additional surfactant. As azoTAB adsorbs strongly to GO (shown previously with adsorption data^[23]), this enhancement could arise from GO sheets coated with surfactant molecules adsorbing to the interface, and we explain this in a later section. As the surfactant affinity for GO is high due to not only charge-based interactions, but van der Waals and hydrophobic forces as well, the concentration of surfactant accumulated at the interface is consequentially higher as a result of the sheets adsorbing. GO on its own has no significant effect on the surface tension of water due to its adsorption being apparently nonspontaneous (Figure 1b), a result that has been noted previously.^[1,25] Therefore changes in surface tension must be attributed to surfactant at the interface and not GO.

The proposed mechanism is shown schematically in Figure 1c, where for a pure GO dispersion the sheets remain in the bulk solution, however with GO and azoTAB they simultaneously diffuse to the interface over time, lowering the surface tension and resulting in further deformation of the droplet. At pH 5.5 for an aqueous GO dispersion of 0.1 mg mL⁻¹, samples were unstable with azoTAB loadings between 0.1×10^{-3} and 1.0×10^{-3} M (Figure 2a). This flocculation effect appears to occur where insufficient charge repulsion between the sheets exists as to allow them to remain dispersed (Figure 2c), at which point any surface effects from the composite material become negligible because the sample is no longer homogeneous and the partitioning has changed. Tensiometry measurements conducted for such samples thus showed smaller effects compared to the pure surfactant at the same concentrations (Figure 2b). Therefore, the pH of the system was subsequently elevated moderately to between 8.5 and 11.5, where the sheets become more stable due to increased deprotonation of the carboxylate groups (Figure 2c). The surfactant concentration could thus be increased further without the GO suspension flocculating (unstable from 0.45×10^{-3} to 0.70×10^{-3} M at these pHs, Figure 2a), allowing additional control over the system. Images of the samples are in the Supporting Information.

At pH 8.5 and 9.5 across the same azoTAB concentration range explored, the combined system does not show an improved capacity for reducing surface tension compared to

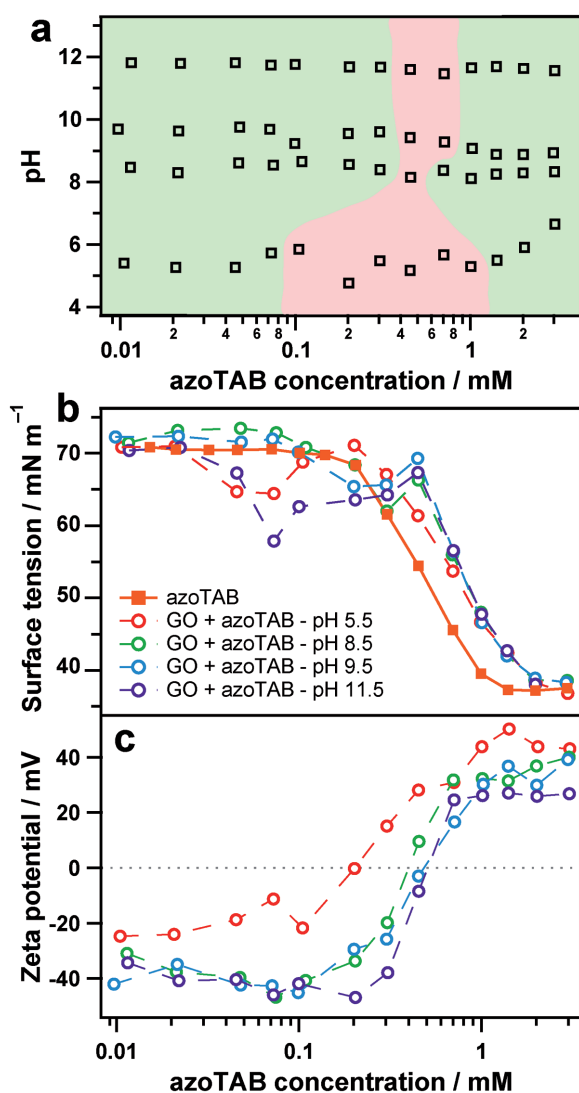


Figure 2. a) Phase diagram showing the colloidal stability of aqueous GO dispersion at varying concentrations of azoTAB for different pH values. The green regions represent colloidal stability while the red regions represent colloidal destabilization or flocculation (i.e., leading to macroscopic phase separation). b) Equilibrium surface tension of pure azoTAB, and azoTAB with GO at different values of pH. c) Zeta potential of GO with azoTAB at different values of pH. In all instances azoTAB is in the *trans*-dominated photostationary state and the GO concentration is 0.1 mg mL⁻¹.

the pure surfactant (Figure 2b). We suspect this is because the enhanced stability or greater surface charge of the GO at these pH values causes the materials to preferentially remain in the bulk solution in spite of surfactant adsorption. A charge inversion still occurs at high surfactant loadings, however the increase to positive zeta potentials is much more sudden compared to pH 5.5 (Figure 2c). For all pH series at high surfactant concentrations ($>1 \times 10^{-3}$ M), the reduced surface activity of the combined system versus the pure azoTAB system is similarly due to stabilization of the GO by azoTAB, this time by overcharging such that they now carry a net positive zeta potential (Figure 2c). However due to adsorption to the GO surface, the

amount of free surfactant in these samples is also lower hence the surface tension is not reduced as much in these instances. At pH 11.5 however, a substantial difference is seen for certain surfactant ratios, with the 0.07×10^{-3} M sample reducing the surface tension by up to 14 mN m⁻¹ (Figure 1b). All pH adjustments were made with NaOH, hence there is a proportion of Na⁺ ions in the mixture ($\approx 3 \times 10^{-3}$ M at pH 11.5) which could serve to screen some of the charge repulsions between the sheets, reducing their aqueous stability not so far as to cause flocculation, but allowing them to more effectively adsorb at the interface. This theory is addressed in more detail later. At high surfactant concentrations, the pH 11.5 samples conform to the same trend as the other series. Note that azoTAB is in the *trans*-dominated photostationary state for all measurements shown in Figures 1b and 2.

As stated above, any decreases in surface tension are ascribed to surfactant adsorption at the air–water interface and not GO. Therefore the results in Figure 1 do not directly prove that GO is at the interface. To address this issue, we exploit X-ray reflectivity (XRR), a surface specific technique that distinguishes materials at interfaces based on their electron densities. By modeling XRR data, it is possible to determine the number of distinct layers present and their respective thicknesses,^[26] providing quantitative structural insight into the materials at the interface. Comparing the reflectivity of GO/azoTAB to that of the pure surfactant appears to confirm the hypothesis that GO was indeed at the interface. A sample with 0.1 mg mL⁻¹ of GO and 0.1×10^{-3} M *trans* azoTAB at pH 10.5 exhibits significantly more features in the XRR pattern compared to the corresponding sample without the GO (i.e., 0.1×10^{-3} M azoTAB, Figure 3a). At 0.1×10^{-3} M of azoTAB, the system is significantly below the critical micelle concentration (CMC) for the *trans*-dominated photostationary state of $\approx 1 \times 10^{-3}$ M (see the Supporting Information), therefore the amount of surfactant adsorbed at the interface would be low and unevenly distributed. A lack of uniformity or roughness at the interface causes the XRR pattern to become more diffuse, accounting for the lack of features exhibited by this sample. Above the CMC at 1.4×10^{-3} M azoTAB, a smooth decline of a single fringe is observed, confirming the presence of additional surfactant and saturation of the interface (Figure 3a). At 1.4×10^{-3} M where GO is also in the sample, the reflectivity curve again becomes more diffuse, in line with the hypothesis that less surfactant is at the interface due to adsorption to the GO sheets (Figure 3a), and that the sheets are not adsorbing due to overcharging (shown schematically in Figure 3e). These conclusions are also supported by the corresponding electron density profiles for these measurements, where for the higher concentration samples, the electron density at the interface increases beyond that of the background water (≈ 0.33 Å⁻³), whereas for the 0.1×10^{-3} M sample the profile is essentially featureless indicating a lack of material at the interface (Figure 3b). The shift in the peak maximum to a shorter distance from the interface when GO was also present at 1.4×10^{-3} M azoTAB suggests that surfactant orientation may be different when the interface is not fully saturated. A two layer model was applied to these data to improve the accuracy of the fit, commonly used for surfactants at the air–water interface due to differences in electron density between the head and tail groups.^[27]

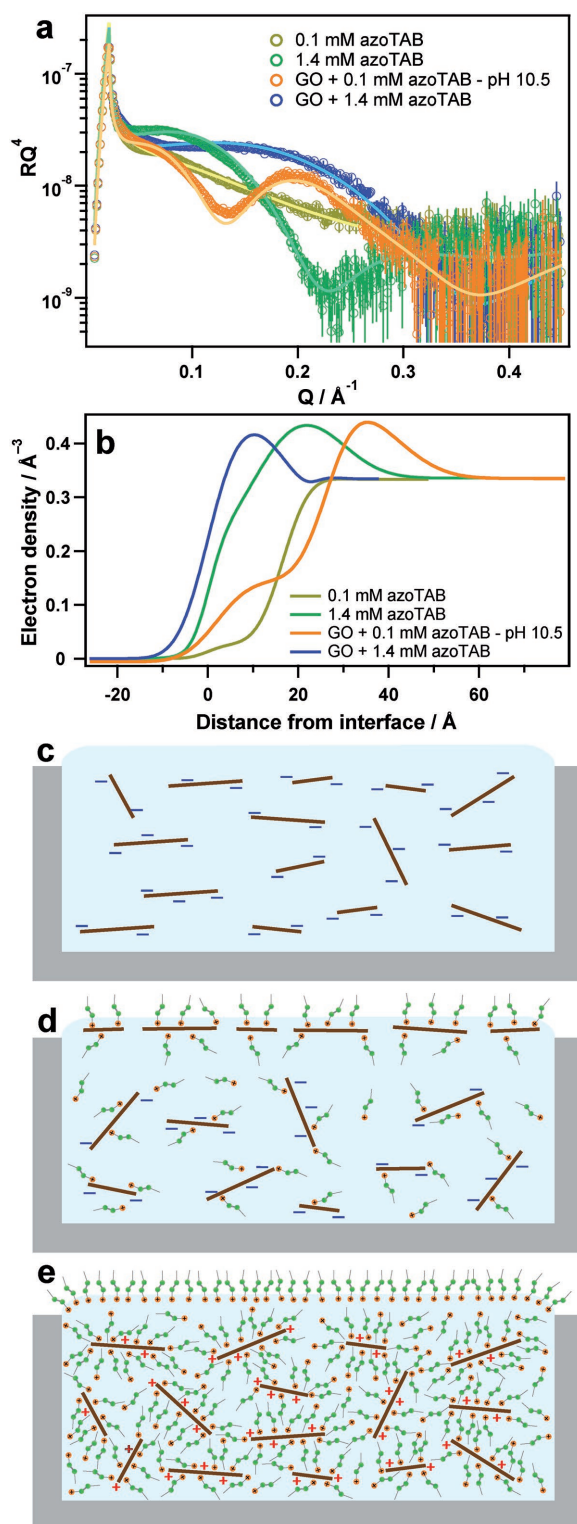


Figure 3. a) X-ray reflectivity data of samples containing 0.1 mg mL⁻¹ GO and/or *trans* azoTAB at the specified concentrations. The hollow symbols represent the experimental data points and the solid lines are model fits. b) The corresponding electron density profiles for the results in (a). Schematic representations of the reflectivity data: c) a pure solution of negatively charged GO sheets partitioned predominately in the bulk solution, d) an optimal ratio of azoTAB to GO facilitating adsorption of the

By far the most feature rich scattering pattern is exhibited by the sample with GO and azoTAB at $0.1 \times 10^{-3} \text{ M}$ (Figure 3a). These data were best fit using a three-layer model with layer thicknesses of 24.6, 8.1, and 8.9 Å (see the Supporting Information). This is hypothesized to be a thin film formation at the interface comprising surfactant-GO-surfactant (Figure 3d). As the surfactant and GO have similar electron densities, it is difficult to unambiguously differentiate between their respective scattering (Figure 3b). However the total thickness is again too great to represent a surfactant monolayer, indicating that the interface has become enriched with surfactant-coated GO sheets. The electron density profile obtained from the model fitting suggests that the first layer, corresponding to the shoulder at $\approx 10 \text{ Å}$ from the interface, is a mixture of air and surfactant tail-groups. Hence the electron density of this layer is a function of the volume fraction and density of the surfactant tail-groups, explaining why the value is significantly lower than that of the solvent water molecules (0.33 Å^3). The second layer will then comprise the volume fractions and densities of the GO sheets, surfactant head-groups and water, giving a value higher than that of pure water (maximum at 35 Å from the interface). The electron density of the final layer will thus be a combination of surfactant adsorbed on the underside of the GO (presumably lying flat) and water. Again where GO is in solution on its own, minimal reflectivity is observed, reinforcing that the sheets do not spontaneously adsorb (Figure 3c), and that the surfactants are indeed necessary to promote adsorption of these materials at the interface. The large error bars at high Q are a result of subtracting a water background from each data set. The XRR data for the plain aqueous carbon nanomaterials are available in the Supporting Information, as well as all fitting parameters.

To provide physical evidence of GO at the air-water interface, various imaging methods and deposition techniques specifically targeted toward the examination of interfaces were used (Figure 4). To analyze the GO/azoTAB system in situ at the air-water interface, we used Brewster-angle microscopy (BAM), a surface specific imaging technique that distinguishes materials at the interface based on their refractive indices. At the Brewster angle (53°) no reflection can occur, and as such, any bright spots in the image can be attributed to materials on the surface. Imaging a pH 10 dispersion of GO using BAM showed no discernible material at the air-water interface, confirming the previous results and expectation that the highly charged sheets remain in dispersion (Figure 4a). However, upon adding $0.05 \times 10^{-3} \text{ M}$ *trans* azoTAB, the interface starts to become decorated with bright spots, some of which have the appearance of jagged sheets (Figure 4b). As surfactant molecules are far too small to observe by the resolving power of this technique, these regions are interpreted as GO-based materials. Increasing the azoTAB concentration to $0.1 \times 10^{-3} \text{ M}$, appears to drive more GO to the surface (Figure 4b), demonstrating the importance of the surfactant in modulating this process. This experiment is shown schematically in Figure 4d.

sheets at the air-water interface, and e) a sample with high surfactant loading showing redispersion of the GO into the bulk and saturation of the interface with surfactant molecules.

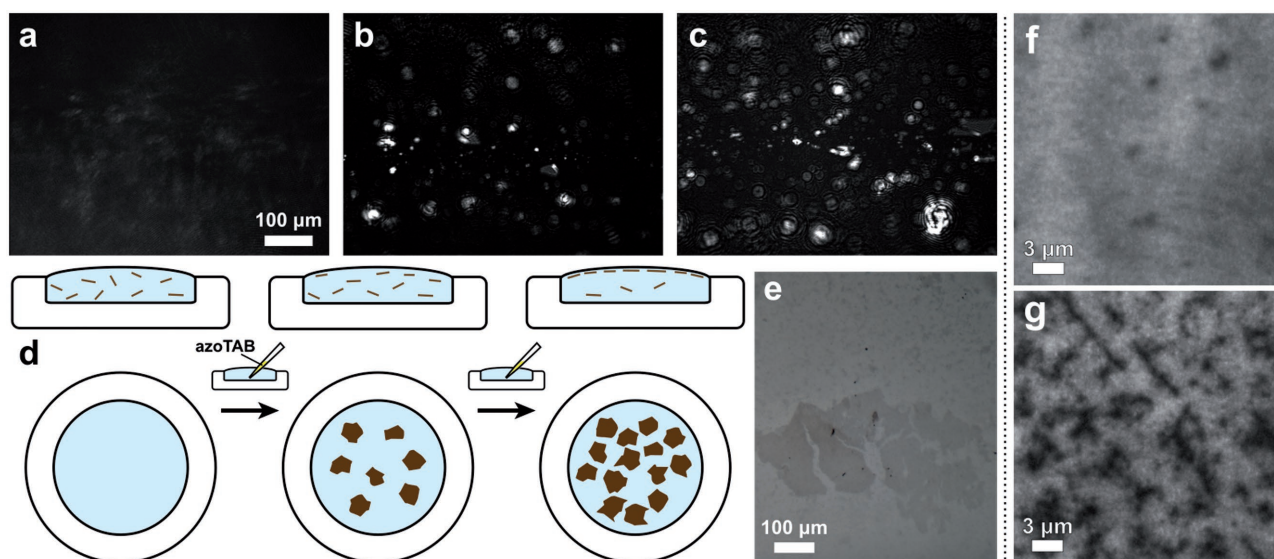


Figure 4. Brewster-angle microscopy images of the air–water interface for 0.1 mg mL^{−1} aqueous GO dispersion at a) pH 10, and after doping the same sample with *trans* azoTAB to concentrations of b) 0.05×10^{-3} M, and c) 0.1×10^{-3} M. d) Schematic showing the increased enrichment of GO at the air–water interface with each addition of azoTAB in cross-section (top row) and plan (bottom row) view. e) An optical micrograph of the air–water interface from a pH 10 solution of 0.1 mg mL^{−1} GO and 0.1×10^{-3} M azoTAB grafted onto a cover slip sputter-coated with copper. Wide-field fluorescence microscopy images of GO sheets deposited on glass by dip-coating a f) 0.1 mg mL^{−1} GO and g) 0.1 mg mL^{−1} GO with 0.1×10^{-3} M azoTAB solution at pH 10. Darker regions are indicative of fluorescence quenching by GO sheets.

As BAM utilizes optical objectives for imaging, the observed area is quite large on the scale of GO sheets, and hence their morphology is difficult to examine. Furthermore, the air–water interface is a dynamic system and thus in constant motion, making it difficult to capture a focused image with BAM. To obtain a more well-defined representation of the air–water interface, a glass slide sputtered with ≈ 20 nm copper (Quorum Q150T-S sputter coater) was gently placed flat on the surface of a sample containing 0.1 mg mL^{−1} GO and 0.1×10^{-3} M azoTAB and removed, creating a so-called “graft” of the interface. Subsequent imaging of the graft with conventional optical microscopy showed clearly defined sheet-like domains about the interface (Figure 4e), suggesting the adsorption of monolayer GO. These results were reinforced with wide-field fluorescence microscopy (WFM) using a sample preparation procedure adapted from Kim et al.^[28] The samples were prepared by dipping a glass slide in a similar 0.1 mg mL^{−1} GO and 0.1×10^{-3} M azoTAB sample at pH 10, as well as an equivalent GO sample without azoTAB, and pulling it back out through the interface, in theory extracting the material deposited there. The slide is then coated with a thin layer of fluoroscein and polyvinyl pyrrolidone, and then imaged using a fluorescence microscope. The GO quenches the fluorescence of the dye, and hence can be viewed as dark patches in the resultant image.^[28] Very little quenching can be observed for GO alone due to the sheets being predominately in the bulk rather than at the interface (Figure 4f). However with 0.1×10^{-3} M azoTAB present, the sample exhibits significant quenching, suggesting accumulation of GO at the interface (Figure 4g), again reinforcing the role of the surfactant.

Based on the significant differences in interfacial adsorption of GO/azoTAB observed when system pH was varied (Figure 1), it is clear that surface charge is a key factor underlying this

process. To more thoroughly investigate this idea, the effects of adding a simple electrolyte, in this case KCl, were examined for GO and azoTAB at pH 8.5 (Figure 5b), where adsorption of the materials was previously seen to be minimal owing to increased colloidal stability of the GO. Taking the 0.1 mg mL^{−1} GO with 0.1×10^{-3} M azoTAB ratio again, and measuring the surface tension over time for differing amounts of KCl, it was found that increasing the KCl concentration assisted in lowering the surface tension of the mixture (Figure 5a). In colloidal systems, neutral salts can serve to minimize repulsive forces between particles by compression of the electrical double-layer.^[29] Hence it is likely that the surface charge of the GO sheets is being partially screened by added KCl. As such, at pH 10 and above, where the amount of Na⁺ counterion becomes comparable with that of the GO and azoTAB ($>0.1 \times 10^{-3}$ M Na⁺), it is likely that these ions are interacting with the GO surface in tandem with surfactant, contributing to the pH effect. Screening of the surface charge is also reflected in the zeta potential analyses (Figure 5c), where the values appear to be less negative at the low surfactant concentrations compared to the equivalent samples at pH 8.5 without added salt (Figure 1e). Adsorption of the GO/azoTAB composite at the air–water interface was again indicated by XRR, showing a very similar scattering pattern as determined previously (thickness 56.9 Å). This pattern was also fit with a three layer model, confirming GO at the interface (Figure 5d,e).

It is also important to note that the air–water (and indeed oil–water) interfaces bear a negative surface potential on the order of tens of millivolts across the pH range explored.^[30–32] Therefore, the effect of charge neutralization of the GO sheets through surfactant addition as well as charge screening from counterions could be expected to reduce the repulsion from the interface itself, also facilitating GO enrichment. From the zeta

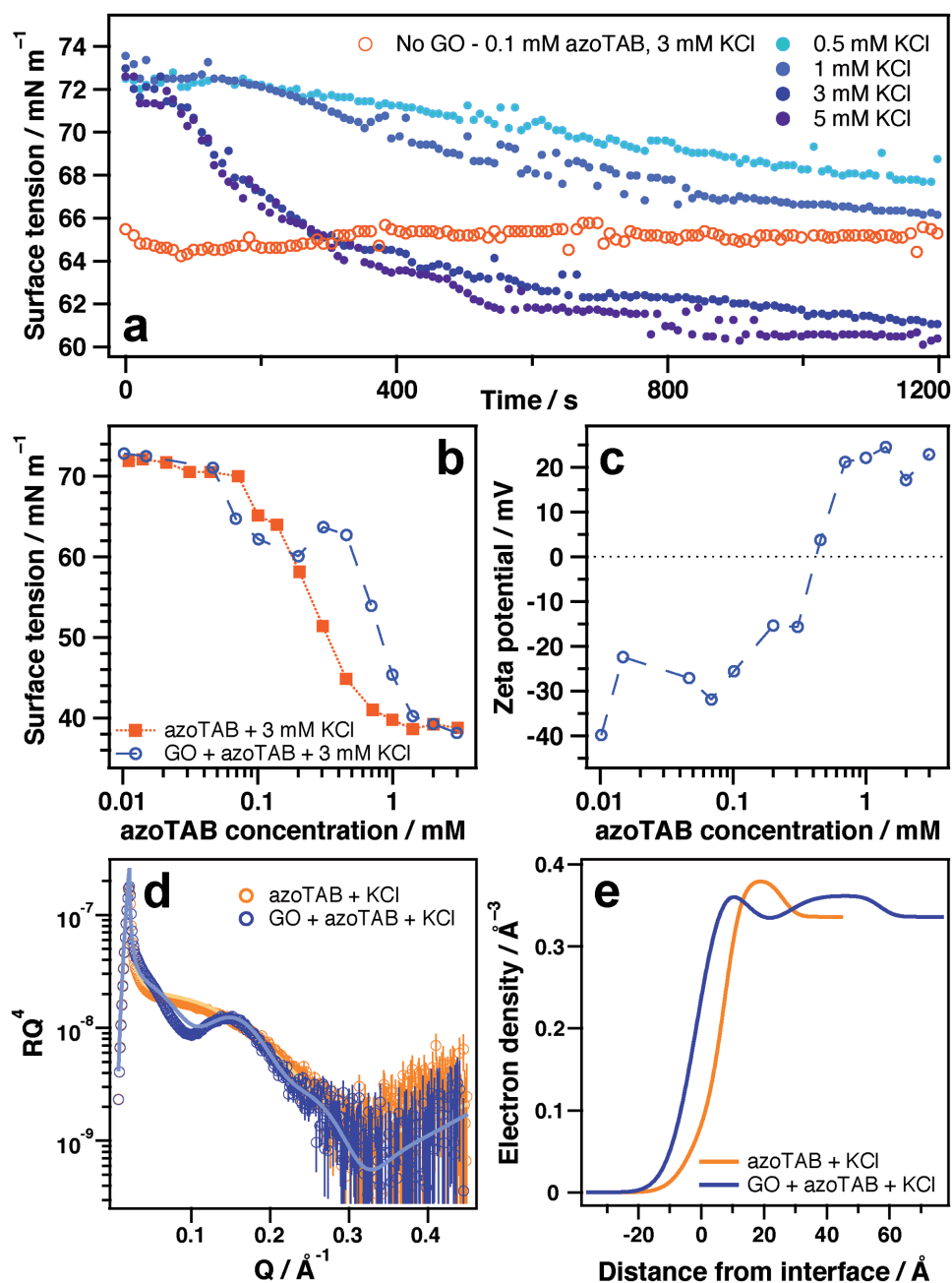


Figure 5. a) Changes in surface tension over time for samples containing 0.1 mg mL⁻¹ GO, 0.1 × 10⁻³ M azoTAB and the specified concentrations of KCl at pH 8.5. b) Equilibration tensiometry data for pure azoTAB and azoTAB with 0.1 mg mL⁻¹ GO, with 3 × 10⁻³ M KCl present. Samples are at pH 10 for the pure system and pH 8.5 for the mixed system. c) Zeta potentials of 0.1 mg mL⁻¹ GO with azoTAB in 3 × 10⁻³ M KCl at pH 8.5. d) X-ray reflectivity data comparing 0.1 × 10⁻³ M azoTAB and 5 × 10⁻³ M KCl with an equivalent sample also containing 0.1 mg mL⁻¹ of GO. The hollow symbols represent the experimental data and the solid lines are model fits. e) The corresponding electron density profiles for the results in (d). In all instances azoTAB is in the *trans*-dominated PSS.

potential measurements in Figures 2c and 5c, it is apparent that the GO is still negatively charged at the ratios where most adsorption occurs (around 0.1 mg mL⁻¹ GO with 0.1 × 10⁻³ M azoTAB). Hence the presence of a sufficient proportion of counterions from added electrolyte or base such as to provide additional screening of the surface charges would also enhance the adsorption of GO at the interface. Once the repulsion from the interface is sufficiently overcome, hydrophobic and van der

Waals interactions become the dominant forces driving adsorption. Moreover, it is also likely that at high surfactant concentrations (>0.7 × 10⁻³ M), the lack of adsorption of the now positively charged GO sheets may be due to repulsion from an interface now saturated with cationic surfactant molecules (Figure 3e).

Having determined that surfactant adsorption drives GO to the air–water interface, we further investigated the effects

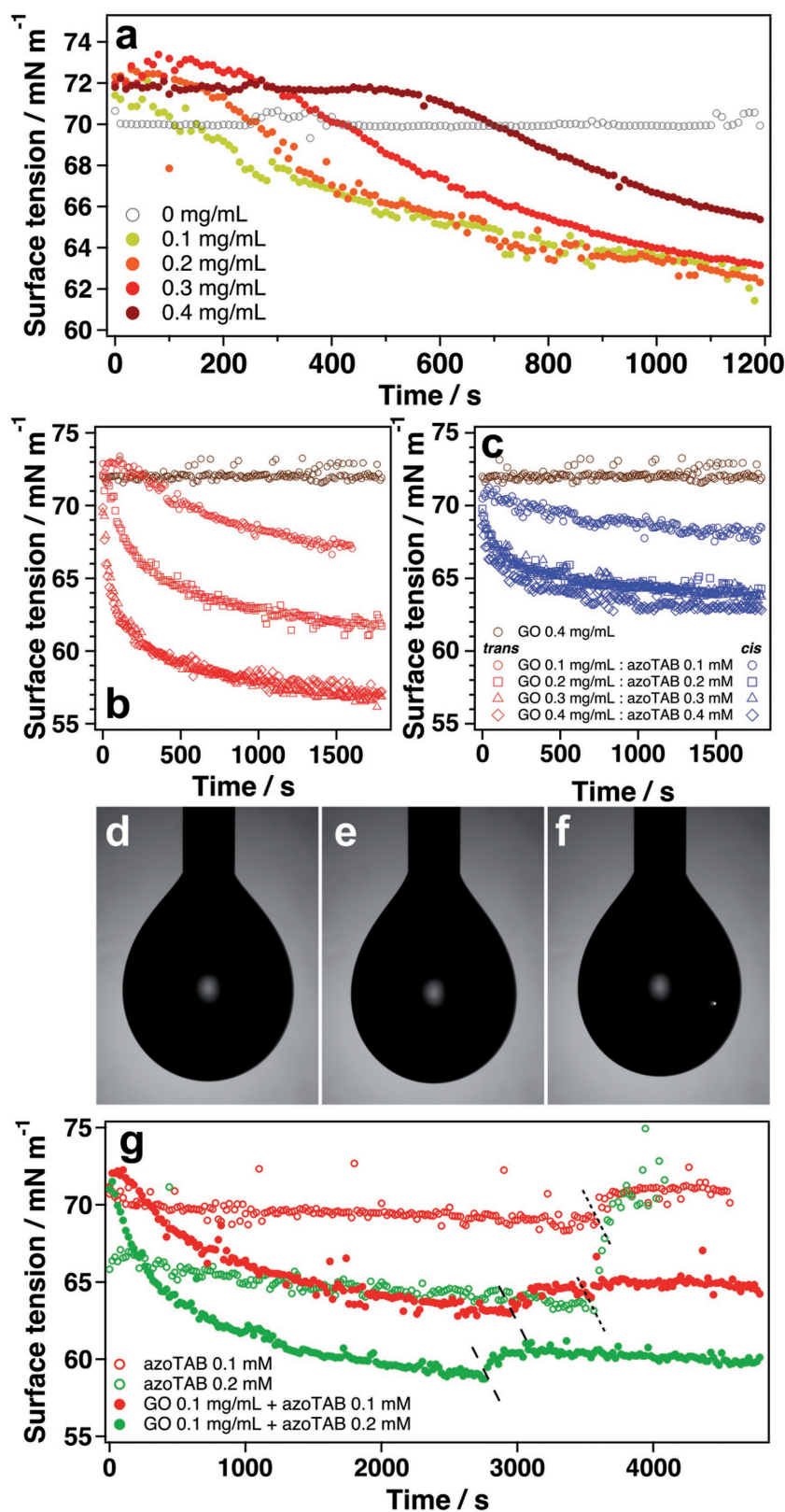


Figure 6. a) Changes in surface tension over time for GO and 0.1×10^{-3} M azoTAB. b,c) Dynamic surface tension measurements in which the azoTAB/GO ratio was kept constant but total concentration was increased. b) The surfactant is in the *trans*-dominated photostationary state and c) the surfactant is in the *cis*-dominated PSS. d–f) Images of pendant drops for 0.1 mg mL^{-1} GO

of tuning the surfactant/GO ratio as well as photoisomerization. Keeping a constant azoTAB concentration of 0.1×10^{-3} M, and incrementally increasing the GO concentration shows a gradually smaller decline in surface tension as well as the speed at which it declines (Figure 6a). This indicates that the amount of surfactant adsorbed to the GO is clearly significant, as at the 0.4 mg mL^{-1} GO concentration there is no apparent decline in surface tension for the first 600 seconds of the measurement. Whereas at 0.1 mg mL^{-1} GO, where the amount of adsorbed surfactant is much greater (≈ 4), the decline is almost instantaneous as the sheets are much more surface active (Figure 6a). An azoTAB/GO ratio of 0.1×10^{-3} M azoTAB to 0.1 mg mL^{-1} GO corresponds to a mass ratio of ≈ 0.4 mg azoTAB to 1 mg GO (calculated precisely for all samples in the Supporting Information). By taking this same ratio but increasing the loading of each material, it was found that the surface effects of GO and azoTAB could be accentuated by not only inducing a more rapid decrease in surface tension, but also by decreasing it to a greater extent ($\approx 57 \text{ mN m}^{-1}$ at equilibrium for the two higher loadings, Figure 6b). The faster diffusion of the materials to the interface at the higher loadings is in line with the law of mass transfer, however the additional lowering of surface tension suggests that at the smaller proportion (0.1×10^{-3} M azoTAB and 0.1 mg mL^{-1} GO), the interface is not fully saturated with materials at equilibrium (also apparent from the BAM images, Figure 4b,c).

Interestingly, when azoTAB is isomerized to the *cis* configuration, the drop in surface tension caused by the GO/azoTAB assembly is significantly smaller and does not appear to change noticeably beyond the proportion of 0.2×10^{-3} M azoTAB to 0.2 mg mL^{-1} GO (Figure 6c). These findings highlight that not only charge and surfactant ratio are key factors in governing the interfacial behavior of this system, but the nature of the surfactant is also integral. As *cis* azoTAB has a greater aqueous solubility than the *trans* isomer due

and 0.2×10^{-3} M azoTAB as in (g), over the course of the measurement. Images were taken d) at the beginning of the measurement, e) at equilibrium just before UV illumination, and f) at the end of the measurement following irradiation. g) Changes in surface tension over time for samples of GO and azoTAB at pH 10.5 in response to an external stimulus of 365 nm light after equilibration (dashed lines indicate commencement of UV irradiation).

to the much larger dipole moment of the tail-group, its affinity for the interface is significantly lower.^[33] As a result of this effect, the reduced surface activity observed for the GO/azoTAB complex could be for two possible reasons: either the amount of surfactant adsorbed to the GO surface is significantly less, or the sheets themselves are simply less surface active in spite of being coated with surfactant, stemming from the decreased hydrophobicity of the surfactant tail-groups. According to previously obtained adsorption isotherm data,^[23] the difference in the adsorbed amount of azoTAB surfactant on the GO should be negligible at these concentrations, regardless if the surfactant has been irradiated or not. Therefore the differences in surface tension for the surfactant/GO complex based on the structural configuration of azoTAB can be attributed predominately to the change in hydrophobicity. This indicates that the interfacial behavior of these materials is also innately related to the physical chemistry of the surfactant as well as the bulk solution conditions, providing additional and more subtle means for controlling the behavior.

To effect photo-induced control over the interfacial properties of the system in situ, dynamic surface tension was monitored for GO/azoTAB during which the response to UV illumination mid-measurement was also assessed (Figure 6g). Samples consisted initially of azoTAB in the *trans*-PSS with and without GO. For samples with GO, UV illumination (≈ 365 nm) was started when the sample appeared to be at equilibrium (i.e., when surface tension was no longer decreasing appreciably). For both concentrations measured (0.1×10^{-3} and 0.2×10^{-3} M azoTAB with 0.1 mg mL^{-1} GO), a small increase in surface tension of $\approx 2\text{--}3 \text{ mN m}^{-1}$ was observed immediately after illumination commenced (Figure 6g). These changes over time are also evident in the progressive droplet shapes corresponding to 0.1 mg mL^{-1} GO with 0.2×10^{-3} M azoTAB (Figure 6d,e), where at equilibrium (Figure 6e) there is a small additional deformation of the droplet compared to the initial drop profile (Figure 6c), which is then partially reversed following illumination with the UV light (Figure 6f). These outcomes are clearly a result of the photo-induced isomerization of azoTAB from the *trans* to the *cis* isomer, however they are significantly less prominent than would be expected based on the results in Figures 6b,c. Furthermore, irradiating the pure surfactant solution at 0.2×10^{-3} M almost instantly increases the surface tension dramatically to above $>70 \text{ mN m}^{-1}$. Because GO is macroscopic and a 2D material, the energy barrier to effect its desorption from the interface is likely to be significantly higher than the molecular surfactant (thousands of $k_B T$ for GO compared to typically only a few $k_B T$ for surfactant molecules). Hence the effects of photoisomerization may be insufficient to cause the GO to partition back into the bulk solution. Therefore, the observed effects of the UV light on the samples with GO are likely a result of free surfactant desorption from the interface, or the desorption of only smaller sheets.

To demonstrate the effectiveness of surfactant-enhanced adsorption of GO at fluid interfaces, we attempted to stabilize oil-in-water emulsions using the GO/azoTAB combination as the stabilizer, and toluene as the oil phase. To assist the emulsification process, samples were subjected to 30 s periods of sonication after which they were left overnight before imaging. Aqueous GO dispersion on its own at pH 10 (0.4 mg mL^{-1})

showed very little capability for emulsification, with only a very small layer of droplets forming (Figure 7a). As established due to the highly charged nature of GO, its dispersion in the bulk aqueous solvent is thermodynamically favored through stabilizing dipole interactions with water molecules, causing its adsorption to the air–water interface to be nonspontaneous, a fact that would also apply to the oil–water interface. Similarly, *trans* and *cis* azoTAB at 0.4×10^{-3} M (pH 10) also showed minimal capacity for emulsifying toluene (Figure 7a). The emulsion layer for the *trans* azoTAB sample appears to be marginally thicker than that of the *cis* sample, which coincides with the increased surface activity of the *trans* isomer causing it to partition more toward the interface than the bulk solution. The more vivid color of the *cis* azoTAB solution is a result of the diminished ability of the *cis* isomer to absorb light in the near UV region of the spectrum.^[34] Optical microscopy images of emulsion droplets formed in these samples can be viewed in the Supporting Information as well as the relative proportions of the samples that have been emulsified.

Significantly greater stabilization effects are observed when GO and azoTAB are used concurrently (Figure 7b,c). As confirmed by the tensiometry and reflectivity data, the dual system results in significantly more material at the interface, most importantly GO. Hence the capacity for emulsification is substantially higher when both materials are present in the system when compared to either one individually, again due to the synergistic effects of the two materials. The emulsion layer increases in size when the concentrations of each material are raised (Figure 7b,c), presumably because there is additional material available for stabilization. However observing the optical microscopy images of these emulsions and determining the droplet diameters reveals that for the *trans* azoTAB/GO system, the oil droplets become significantly smaller at the higher material loadings (Figure 7d–g), with the average diameter decreasing from 45.8 to $14.5 \mu\text{m}$ at the 0.1×10^{-3} M azoTAB: 0.1 mg mL^{-1} GO and 0.4×10^{-3} M azoTAB: 0.4 mg mL^{-1} GO ratios, respectively. As increasing the amount of interface requires energy, this result corresponds to an improved capacity for stabilization. The same effect is observed in the *cis* azoTAB/GO samples (Figure 7h–k), but to a much lower extent from 35.3 to $29.7 \mu\text{m}$ for the same concentrations. The peak widths were also found to shorten at the higher materials loadings, indicating a decrease in droplet polydispersity (see the Supporting Information). Because the *trans* isomer is more surface active, this property is likely mirrored in the self-assembled composite, hence the *trans* azoTAB/GO system will show a greater affinity for the oil–water interface, enhancing their capacity for dispersion of the oil compared to the equivalent *cis* system. These findings suggest that it is possible to control emulsion characteristics based on the choice of surfactant. Furthermore, the presence of nonspherical droplets also indicates that there are particles—in this case GO—located at the interface;^[5] such droplets cannot arise in emulsions stabilized by labile surfactants alone.^[35,36] The emulsions formed here can thus be thought to be of the Pickering or Ramsden type (i.e., particle stabilized).^[4,5] Samples below the optimal GO/azoTAB ratio where the surface activity of the sheets is too low, and above the optimal ratio where the sheets become positively charged are shown in the Supporting Information.

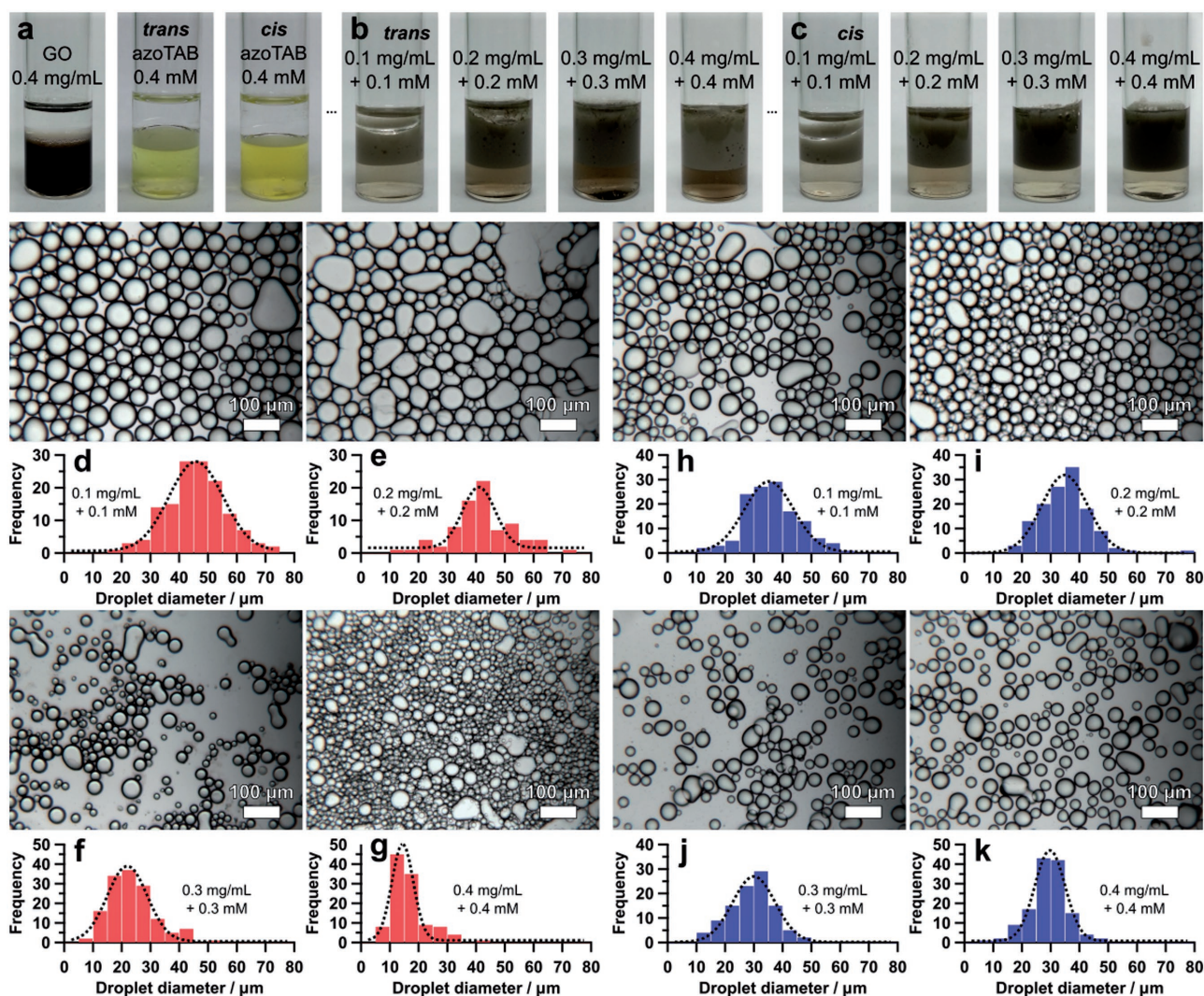


Figure 7. a) “Blank” emulsion samples containing an equal volume of toluene and the specified concentrations of GO, *trans* and *cis* azoTAB. Toluene-in-water emulsions in which the aqueous phase comprises the specified concentrations of GO and b) *trans* or c) *cis* azoTAB. Samples were sonicated for 30 s and left overnight before photographing. d–k) Optical microscopy images of toluene-in-water emulsion droplets with the corresponding histograms of droplet size shown below. (d)–(g) correspond to the *trans* azoTAB samples (red histograms) while (h)–(k) correspond to the *cis* azoTAB samples (blue histograms). All *cis* azoTAB solutions were irradiated with 365 nm light prior to incorporation of the GO. All samples (blanks included) were at pH \approx 10.

In both instances there was minimal emulsification of the toluene, again reaffirming the significance of the GO/azoTAB ratio. Additional images of emulsions and droplets as well as a full table of the parameters extracted from the Gaussian fits are presented in the Supporting Information.

The conversion of GO to reduced graphene oxide (rGO) did not appear to increase adsorption to the air–water interface, but instead seemed to inhibit the process (Figure 8a). Upon chemical reduction, GO loses much of its oxygen functionality which causes it to become more hydrophobic.^[37] A significant proportion of the oxidation is retained however, hence rGO still has a negative surface potential and can be dispersed in water, although its aqueous stability is greatly diminished.^[12] Therefore it was hypothesized that rGO with azoTAB would show even greater capacity for adsorbing at the air–water interface than the azoTAB/GO system. Performing similar

tensiometry measurements at high and low pH revealed that for all surfactant/rGO ratios, the equilibrium surface tension was higher than that of pure azoTAB at the same concentration (Figure 8a), suggesting that adsorption at the air–water interface was only occurring for free surfactant molecules and that adsorption to rGO in the bulk simply depletes the available surfactant concentration.

For differing concentrations of azoTAB, rGO displays similar surface charging behavior with only a minor decrease in the point of charge inversion to around $(0.1\text{--}0.2) \times 10^{-3}$ M azoTAB (Figure 8b). However the lack of adsorption of surfactant-coated rGO sheets as observed when GO was used is curious. We posit that this could be one of two factors both related to the increased hydrophobicity of rGO. It is possible that the surfactants are adsorbing to hydrophobic rGO sheets via their tail-groups, meaning the hydrophilic head-groups are in solution,

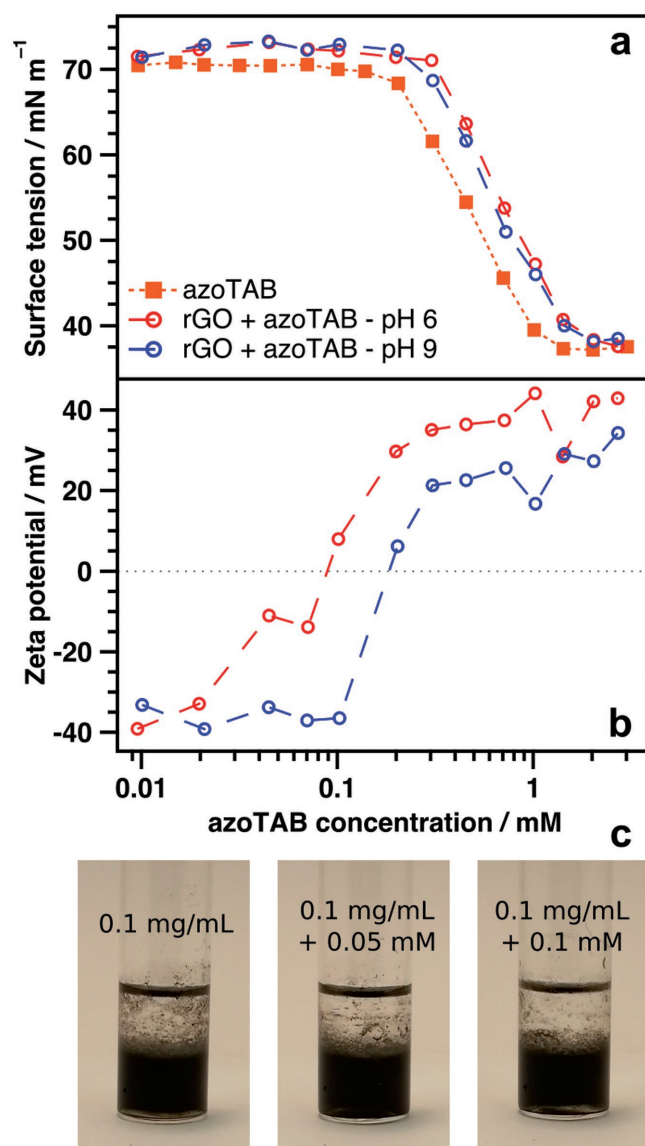


Figure 8. a) Equilibrium tensiometry data for pure azoTAB and azoTAB with 0.1 mg mL⁻¹ rGO at different values of pH. b) Zeta potentials of 0.1 mg mL⁻¹ rGO dispersion with azoTAB at different values of pH. In all instances azoTAB is in the *trans*-dominated PSS. c) Emulsion samples comprising an equal volume of toluene and the specified concentration of aqueous rGO + azoTAB, 12 h after mixing.

keeping the sheets solvated such that they remain preferentially in the bulk rather than the air–water interface. Alternatively, the sheets are largely crumpled in solution and even though the surfactant molecules can still adsorb to the rGO, the adsorption of the sheets themselves is inhibited by this morphology. Small-angle neutron scattering data also has shown that rGO with azoTAB exhibits fractal aggregation in solution,^[23] further affirming this theory. The rGO sheets may also simply be too hydrophobic to spontaneously adsorb to the interface. This behavior could be considered akin to protein folding, where the hydrophobic regions are also oriented to the interior of the structure to minimize interactions with the surrounding solvent.^[38] In either case, emulsification was attempted using

mixtures of rGO and azoTAB, and the results are shown in Figure 8c. In all samples with rGO present, little to no emulsion layer was apparent after samples had been left for 12 h, indicating that rGO and azoTAB are not effective interfacial stabilizers in the compositions used. Due to the apparent lack of interfacial adsorption and emulsification, further experiments were not conducted on rGO systems.

3. Conclusion

A simple and controllable method for enhancing adsorption of GO at air–water and oil–water interfaces is demonstrated whereby the addition of small amounts of a cationic surfactant are added to render the sheets more surface active. The ratio of surfactant to GO is key in driving this process, as too little surfactant does not sufficiently negate the surface charge of the GO, and too much causes overcharging or over-coating of the sheets, such that in both cases the GO remains in dispersion. By using a photoisomerizable surfactant as a mechanistic probe, subtle information on the system thermodynamics is obtained. Significant differences in system behavior are observed depending on the structure of the surfactant, with *cis* isomerization greatly diminishing the decline in surface tension over time, suggesting that hydrophobic forces are also playing a key role. Interestingly, these effects were not observed when substituting GO with rGO, which we suspect is due to significant crumpling of the rGO sheets in solution due to a much greater proportion of hydrophobic domains, thus inhibiting adsorption to the interface. Destabilization of the GO suspension counteracts adsorption at the interface, hence adjustment to moderately high pH (i.e., pH 10) greatly enhances the bulk stability of the system, offering a broader range of control with surfactant concentration. Adding a small quantity of neutral electrolyte (i.e., KCl) facilitates the adsorption process by partial screening of the surface charge. By using X-ray reflectivity, we were able to directly map changes in the air–water interface and attribute the physical effects observed with the apparent synergism between the surfactant and GO. Finally, the efficacy of the combined system was demonstrated in the stabilization of oil-in-water emulsions, whereby a substantial improvement in oil dispersion was seen versus either constituent independently. The system thus utilizes noncovalent self-assembly of the materials, overcoming the need for synthesizing difficult covalent composite materials and offering an easy method for achieving interfacial control and enhanced emulsification of the oil phase. The method is low energy, requires only very small quantities of materials, and constitutes an entirely new type of emulsion.

4. Experimental Section

GO was synthesized from graphite flakes (Sigma, +100 mesh) according to Marcano et al.^[39] Purification was modified slightly, with 3 cycles of centrifugation (4000 rpm) performed in ultrapure water only, followed by 1 week of dialysis using cellulose dialysis tubing (Sigma) to remove residual salt and acid. The product was kept and characterized as an aqueous suspension to maintain dispersion stability. Reduction of the GO followed Li et al.,^[12] with the resultant suspension also purified by

dialysis to remove the ammonia and any unreacted hydrazine. AzoTAB was synthesized as described previously.^[33,40] Characterization of these materials was performed previously and can be found in the Supporting Information of McCoy et al.^[23] Photoresponse of the surfactant for differing concentrations was assessed by UV–vis spectrophotometry on a Cary 60 instrument from Agilent Technologies (see the Supporting Information). Measurements were performed across the wavelength range of 200–550 nm using a 1 cm pathlength quartz cuvette.

All samples for analysis were prepared by adding of the colloidal material (i.e., GO or rGO) last to each mixture to avoid any potential equilibrium biasing. Adjusting of pH was performed by addition of sodium hydroxide solution (Merck, ≥99%), with the final pH values measured using a calibrated pH meter; pH was also measured individually for each sample using a HACH H135 minilab micro pH meter (see the Supporting Information). All salt addition experiments were performed using potassium chloride (Merck, ≥99.5%) as the electrolyte. As the properties and thus physical behavior of GO and rGO can differ markedly depending on their preparation routes, all samples were made using materials from the same synthesis or batch. Photoswitching was achieved using a 365 nm UV light source with a radiant power of 19.9 mW cm⁻²; samples were irradiated either prior to addition of the GO or during measuring as specified.

Tensiometry measurements were performed at room temperature (≈25 °C) using a custom-made pendant drop setup. Droplets were suspended from a blunt needle of accurately known diameter (0.8192 mm) to a sufficient size such as to cause deformation of the drop without it detaching before equilibrium was reached. All measurements were conducted in air, inside a cuvette to minimize evaporation. Drop analysis was completed using OpenDrop software.^[24] All pendant drop measurements were performed for a minimum of 20 min to allow system equilibration at the interface, and all reported equilibrium surface tension results (see the Supporting Information) were obtained by averaging the final 10 data points of each run. A box smoothing function had been applied to the data series in Figure 1b.

Zeta potentials for GO and rGO containing samples were determined by phase analysis light scattering (PALS) on a Brookhaven Nanobrook Omni. Light scattered by each sample in response to the applied voltage is detected to determine the electrophoretic mobilities, u_E , which are then used to calculate the zeta potentials, ζ , using the Smoluchowski equation

$$u_E = \frac{\nu_E}{E} = \frac{\zeta \epsilon}{\eta}$$

where ν_E is the electrophoretic velocity, E is the electric field strength, ϵ is the permittivity, and η is the viscosity of the medium. Samples were analyzed in 1 cm pathlength polystyrene cuvettes in which the palladium PALS electrode was carefully immersed. Each measurement involved 5 consecutive runs comprising 20 cycles at 25 °C.

XRR measurements of the air–water interface were performed using a PANalytical X-Pert PRO reflectometer (high tension = 45 kV, current = 40 mA) with a radiation wavelength (Cu K α) of 0.15418 nm. Measurements were 90 min in duration, during which the incident angle was increased from ≈0.01 to 0.99 Å⁻¹ (Q range). The specular reflectivity was thus observed as a function of the momentum transfer perpendicular to the sample surface. Samples were contained in 8 cm × 4 cm Langmuir troughs and sealed in a closed environment to minimize evaporation. The reflectometer enclosure temperature was ≈30 °C. All reflectivity data was modeled using MOTOFIT,^[26] a reflectivity analysis software package run from the IGOR Pro environment. Further details regarding modeling can be found in the Supporting Information.

BAM was performed on the air–water interface using an Accurion EP4 Imaging Ellipsometer system with a 10× objective lens (Nikon), and a 658 nm laser light source. Imaging was executed at an incident angle of 53° (i.e., the Brewster angle). An initial sample comprising a pH 10 aqueous dispersion of GO was imaged, following which two aliquots of azoTAB were incrementally added to the sample mixture to achieve

concentrations of 0.05×10^{-3} and 0.1×10^{-3} M. Imaging of the air–water interface was performed shortly after each addition to observe changes in adsorption with surfactant doping.

Samples imaged by WFM were prepared by dip-coating 22 mm² glass coverslips in sample solution. Coverslips were initially cleaned by immersing in chloroform and sonicating for 30 min to remove any polystyrene coating. The coverslips were then thrice washed with ultrapure water and dried prior to dipping. Samples comprised either 0.1 mg mL⁻¹ of GO or 0.1 mg mL⁻¹ of GO with 0.1×10^{-3} M azoTAB (both at pH 10), in which the prepared coverslips were vertically immersed ≈75% of the way for 2 min. The substrates were then slowly pulled up through the interface and gently shaken to remove extraneous liquid. Once dry the samples were prepared for WFM by a method adapted from Kim et al.,^[28] which involved spin-coating (1 min, 2000 rpm) either 10 or 20 μ L of a solution of 0.5 wt% PVP in ethanol with 1 mg of dissolved fluorescein. Imaging by WFM was then performed with an Olympus IX81 inverted fluorescence microscope fitted with a 100× 1.49 NA oil immersion TIRF objective lens. Samples were excited with 5 mW of 488 nm (blue) laser and the resulting fluorescence was detected on an Andor iXon EM-CCD. Regions of 25.6 μ m² were imaged for 500 ms with the gain held at 200.

Oil-in-water emulsions were prepared with an equal volume of toluene (Merck, ≥99.9%) and aqueous sample comprising GO, azoTAB or both at pH 10. The mixtures were then sonicated for 30 s using a Branson Digital Sonifier at an amplitude of 10% and left overnight. Samples for light microscopy were then prepared by extracting a small amount of mixture from the emulsion layer and depositing it on a glass slide. A coverslip was then carefully placed over the deposited material to create a plane of focus. Light microscopy images were taken using a CCD camera (Flea3, Point Grey, Richmond, BC, Canada) attached to a Kozo XJP 300 polarizing microscope with a 10× microscope objective lens. Size analysis of emulsion droplets was done using the ImageJ software and only performed on the images featured in the main article. Further details regarding data analysis can be found in the Supporting Information.

Supporting Information

Supporting Information is available from the Wiley Online Library or from the author.

Acknowledgements

The authors would like to acknowledge the Australian Centre for Neutron Scattering, Australian Nuclear Science and Technology Organisation, for use of their X-ray reflectivity and Brewster-angle microscopy instrumentation. The authors also thank the Australian Institute of Nuclear Science and Engineering for travel support (T.M.M.), as well as the Monash Centre for Atomically Thin Materials for additional funding. This work was supported in part by the grant of an ARC Future Fellowship (FT160100191) to R.F.T.

Conflict of Interest

The authors declare no conflict of interest.

Keywords

adsorption, air–water interface, graphene oxide, photosurfactants, pickering emulsions

Received: July 6, 2017
Revised: August 29, 2017
Published online: October 4, 2017

- [1] J. Kim, L. J. Cote, W. Kim, F. Yuan, K. R. Shull, J. Huang, *J. Am. Chem. Soc.* **2010**, 132, 8180.
- [2] D. R. Dreyer, S. Park, C. Bielawski, R. S. Ruoff, *Chem. Soc. Rev.* **2010**, 39, 228.
- [3] J.-J. Shao, W. Lv, Q.-H. Yang, *Adv. Mater.* **2014**, 26, 5586.
- [4] S. U. Pickering, *J. Chem. Soc., Trans.* **1907**, 91, 2001.
- [5] B. P. Binks, T. S. Horozov, *Colloidal Particles at Liquid Interfaces*, Cambridge University Press, Cambridge, UK **2006**.
- [6] B. P. Binks, S. O. Lumsdon, *Langmuir* **2001**, 17, 4540.
- [7] E. Vignati, R. Piazza, T. P. Lockhart, *Langmuir* **2003**, 19, 6650.
- [8] S. Biswas, L. T. Drzal, *Nano Lett.* **2009**, 9, 167.
- [9] Q. Liu, J. Shi, J. Sun, T. Wang, L. Zeng, G. Jiang, *Angew. Chem.* **2011**, 123, 6035.
- [10] D. Wu, F. Zhang, H. Liang, X. Feng, *Chem. Soc. Rev.* **2012**, 41, 6160.
- [11] B. Konkena, S. Vasudevan, *J. Phys. Chem. Lett.* **2012**, 3, 867.
- [12] D. Li, M. B. Muller, S. Gilje, R. B. Kaner, G. G. Wallace, *Nat. Nanotechnol.* **2008**, 3, 101.
- [13] F. Kim, L. J. Cote, J. Huang, *Adv. Mater.* **2010**, 22, 1954.
- [14] T. M. McCoy, M. J. Pottage, R. F. Tabor, *J. Phys. Chem. C* **2014**, 118, 4529.
- [15] Y. He, F. Wu, X. Sun, R. Li, Y. Guo, C. Li, L. Zhang, F. Xing, W. Wang, J. Gao, *ACS Appl. Mater. Interfaces* **2013**, 5, 4843.
- [16] C.-H. Chang, E. I. Franses, *Colloids Surf., A* **1995**, 100, 1.
- [17] A. Czajka, G. Hazell, J. Eastoe, *Langmuir* **2015**, 31, 8205.
- [18] T. M. McCoy, P. Brown, J. Eastoe, R. F. Tabor, *ACS Appl. Mater. Interfaces* **2015**, 7, 2124.
- [19] H. Kim, Y. R. Jang, J. Yoo, Y.-S. Seo, K.-Y. Kim, J.-S. Lee, S.-D. Park, C.-J. Kim, J. Koo, *Langmuir* **2014**, 30, 2170.
- [20] X. Liu, N. L. Abbott, *J. Colloid Interface Sci.* **2009**, 339, 1.
- [21] P. Brown, C. P. Butts, J. Eastoe, *Soft Matter* **2013**, 9, 2365.
- [22] B. A. Ciccirelli, J. A. Elia, T. A. Hatton, K. A. Smith, *Langmuir* **2007**, 23, 8323.
- [23] T. M. McCoy, A. C. Y. Liu, R. F. Tabor, *Nanoscale* **2016**, 8, 6969.
- [24] J. D. Berry, M. J. Neeson, R. R. Dagastine, D. Y. Chan, R. F. Tabor, *J. Colloid Interface Sci.* **2015**, 454, 226.
- [25] C.-J. Shih, S. Lin, R. Sharma, M. S. Strano, D. Blankschtein, *Langmuir* **2012**, 28, 235.
- [26] A. Nelson, *J. Appl. Crystallogr.* **2006**, 39, 273.
- [27] B. B. Luukkala, S. Garoff, R. M. Suter, *Phys. Rev. E* **2000**, 62, 2405.
- [28] J. Kim, L. J. Cote, F. Kim, J. Huang, *J. Am. Chem. Soc.* **2010**, 132, 260.
- [29] R. J. Hunter, *Foundations of Colloid Science*, 2 ed., Oxford University Press, Oxford **2001**.
- [30] M. Takahashi, *J. Phys. Chem. B* **2005**, 109, 21858.
- [31] P. Creux, J. Lachaise, A. Graciaa, J. K. Beattie, A. Djerdjev, *J. Phys. Chem. B* **2009**, 113, 14146.
- [32] R. F. Tabor, D. Y. C. Chan, F. Grieser, R. R. Dagastine, *Angew. Chem., Int. Ed.* **2011**, 50, 3454.
- [33] E. Chevallier, A. Mamane, H. A. Stone, C. Tribet, F. Lequeux, C. Monteux, *Soft Matter* **2011**, 7, 7866.
- [34] T. Shang, K. A. Smith, T. A. Hatton, *Langmuir* **2003**, 19, 10764.
- [35] R. F. Tabor, H. Lockie, D. Y. C. Chan, F. Grieser, I. Grillo, K. J. Mutch, R. R. Dagastine, *Soft Matter* **2011**, 7, 11334.
- [36] R. F. Tabor, F. Grieser, R. R. Dagastine, D. Y. C. Chan, *J. Colloid Interface Sci.* **2012**, 371, 1.
- [37] S. Stankovich, D. A. Dikin, R. D. Piner, K. A. Kohlhaas, A. Kleinhammes, Y. Jia, Y. Wu, S. T. Nguyen, R. S. Ruoff, *Carbon* **2007**, 45, 1558.
- [38] R. L. Baldwin, *Proc. Natl. Acad. Sci. USA* **1986**, 83, 8069.
- [39] D. C. Marcano, D. V. Kosynkin, J. M. Berlin, A. Sinitskii, Z. Sun, A. Slesarev, L. B. Alemany, W. Lu, J. M. Tour, *ACS Nano* **2010**, 4, 4806.
- [40] L. Yang, N. Takisawa, T. Hayashita, K. Shirahama, *J. Phys. Chem.* **1995**, 99, 8799.

SUPPORTING INFORMATION - Surfactant-Enhanced Adsorption of Graphene Oxide for Improved Emulsification of Oil in Water

Thomas M. McCoy,¹ Stephen A. Holt,² Ashley M. Rozario,¹
Toby D. M. Bell,¹ Rico F. Tabor^{1,*}

¹School of Chemistry,
Monash University, Clayton 3800, Australia

²Australian Centre for Neutron Scattering,
ANSTO, Lucas Heights, New South Wales 2234, Australia

*To whom correspondence should be addressed; E-mail: rico.tabor@monash.edu

During irradiation, the molecular symmetry of azoTAB becomes notably distorted such that the two nitrogen atoms are exposed, causing a significant increase in the compound's dipole moment (from *ca.* 0.4–3.5 D for the azobenzene group alone).¹ This is apparent in the UV spectra for azoTAB, where longer irradiation times significantly decrease the absorbance for the $\pi \rightarrow \pi^*$ transition (Figs. 1a-c). It is also evident in Figures 1a-c that longer irradiation time are required to fully isomerise an azoTAB solution at higher concentrations due the high absorption of the azobenzene chromophore.² Interactions with the surrounding aqueous solvent thus occur more readily, and the surfactant is thereby less driven to the interface.³

Moreover, azoTAB surfactant molecules in water are not entirely in one isomeric state or the other. Depending on the illumination conditions, the rate of photo-induced isomerisation to one isomer will eventually equal the rate of reversion to the other isomer and as such, the system reaches an equilibrium where the proportion of the first isomer can no longer be increased.⁴ The resultant equilibrium is referred to as a photostationary state which is composed of a specific mixture of both isomers.⁵ With this in mind it should be mentioned that when we refer to *trans* and *cis* we are implying their respective photostationary states which are 25% *cis* for the *trans*-dominated state and 95% *cis* for the *cis*-dominated state.⁶

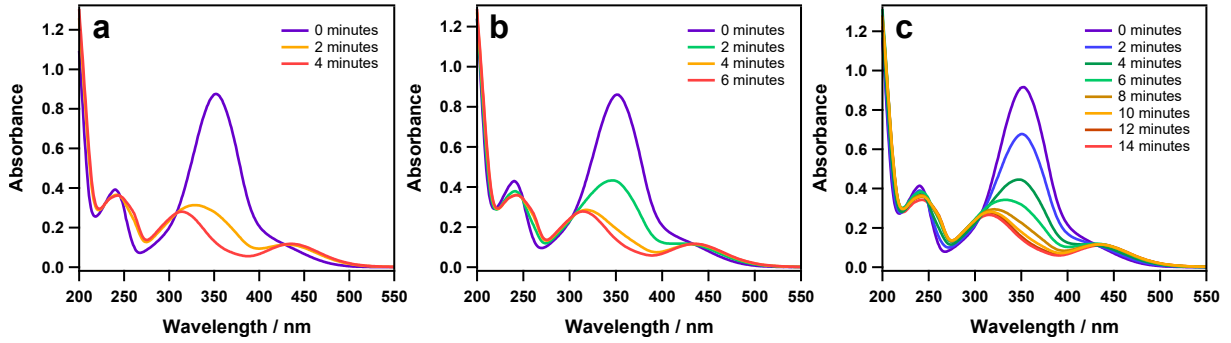


Figure S1: UV-visible spectra of a 1 mM (a), 2 mM (b) and 3 mM (c) azoTAB solution after irradiation with 365 nm light for the specified time periods.

Pendant drop tensiometry measurements involve photographing of a suspended droplet image profile in which the drop size and volume are determined by pixel correlation of the droplet against the needle diameter, and the surface tension is determined by solving the Young-Laplace equation for non-spheres (1) by iteratively fitting the drop profile:

$$\Delta P = \gamma \left(\frac{1}{R_1} + \frac{1}{R_2} \right)$$

where ΔP is the pressure differential across the interface, γ is the surface tension and R_1 and R_2 are the droplet radii. As all measurements performed with this technique were conducted in air as the continuous medium, interfacial tension can be substituted with surface tension.⁷

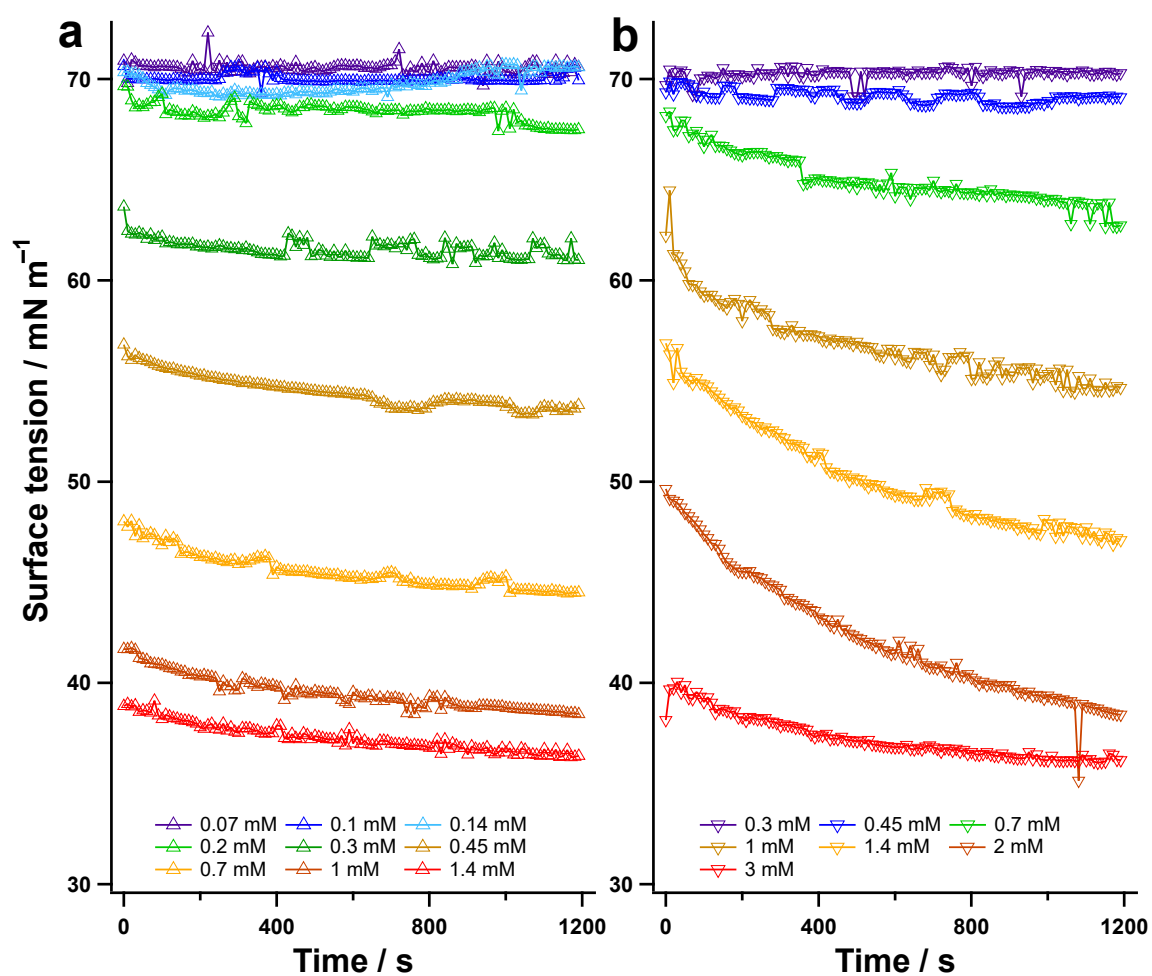


Figure S2: Surface tension data over time for the specified azoTAB concentrations in the *trans* (a) and *cis* (b) configurations.

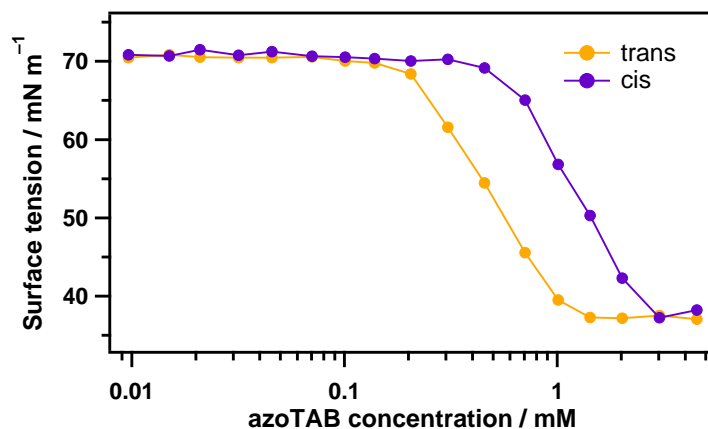


Figure S3: (a) Pendant drop tensiometry data of azoTAB photosurfactant before (*trans*) and after (*cis*) irradiation with 365 nm light.

Table 1: Raw data values for the mean surface tensions of azoTAB in water for the *trans* and *cis* isomers at various concentrations.

azoTAB concentration (mM)	Mean surface tension (mN/m)	
	<i>trans</i>	<i>cis</i>
0.010	70.5	70.8
0.015	70.8	70.7
0.021	70.5	71.5
0.032	70.5	70.8
0.046	70.5	71.2
0.070	70.6	70.6
0.101	70.0	70.5
0.139	69.8	70.3
0.205	68.4	70.0
0.306	61.6	70.2
0.456	54.5	69.1
0.706	45.6	65.0
1.012	39.5	56.8
1.426	37.3	50.3
2.019	37.2	42.3
3.025	37.5	37.2
4.530	37.1	38.2

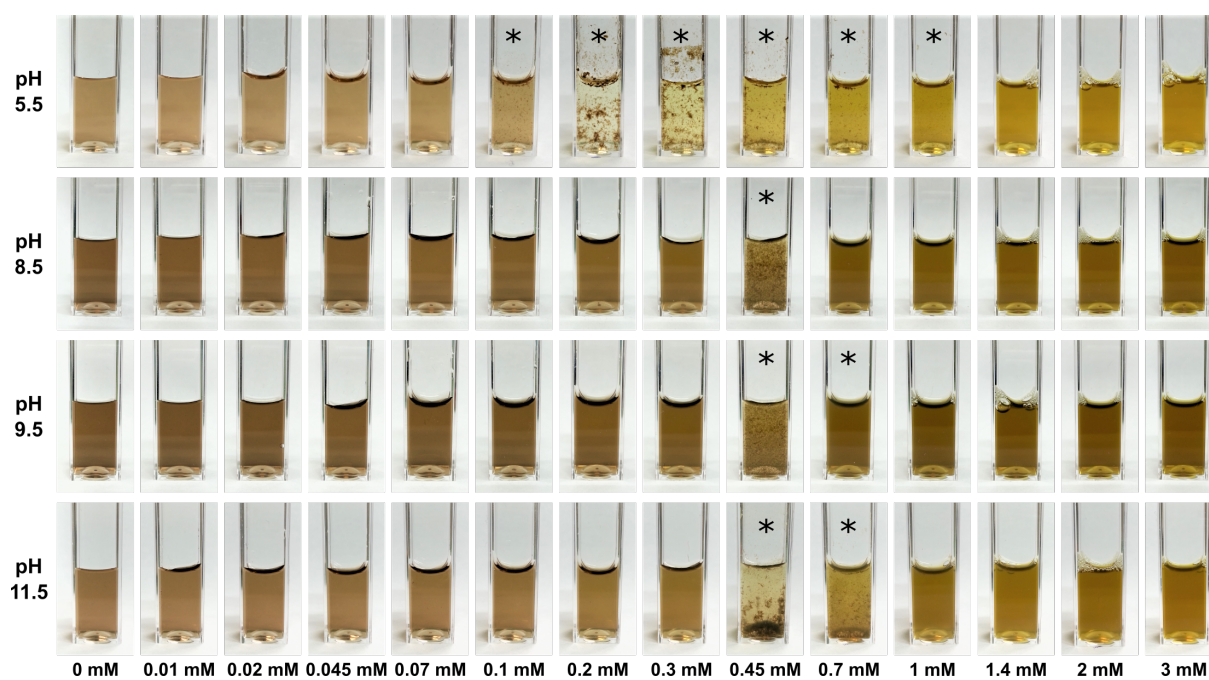


Figure S4: Samples containing 0.1 mg/mL of aqueous GO dispersion with the specified concentrations of *trans* azoTAB at approximately pH 5.5, 8.5, 9.5 and 11.5. Samples that are either unstable or metastable have been marked with an asterisk (*).

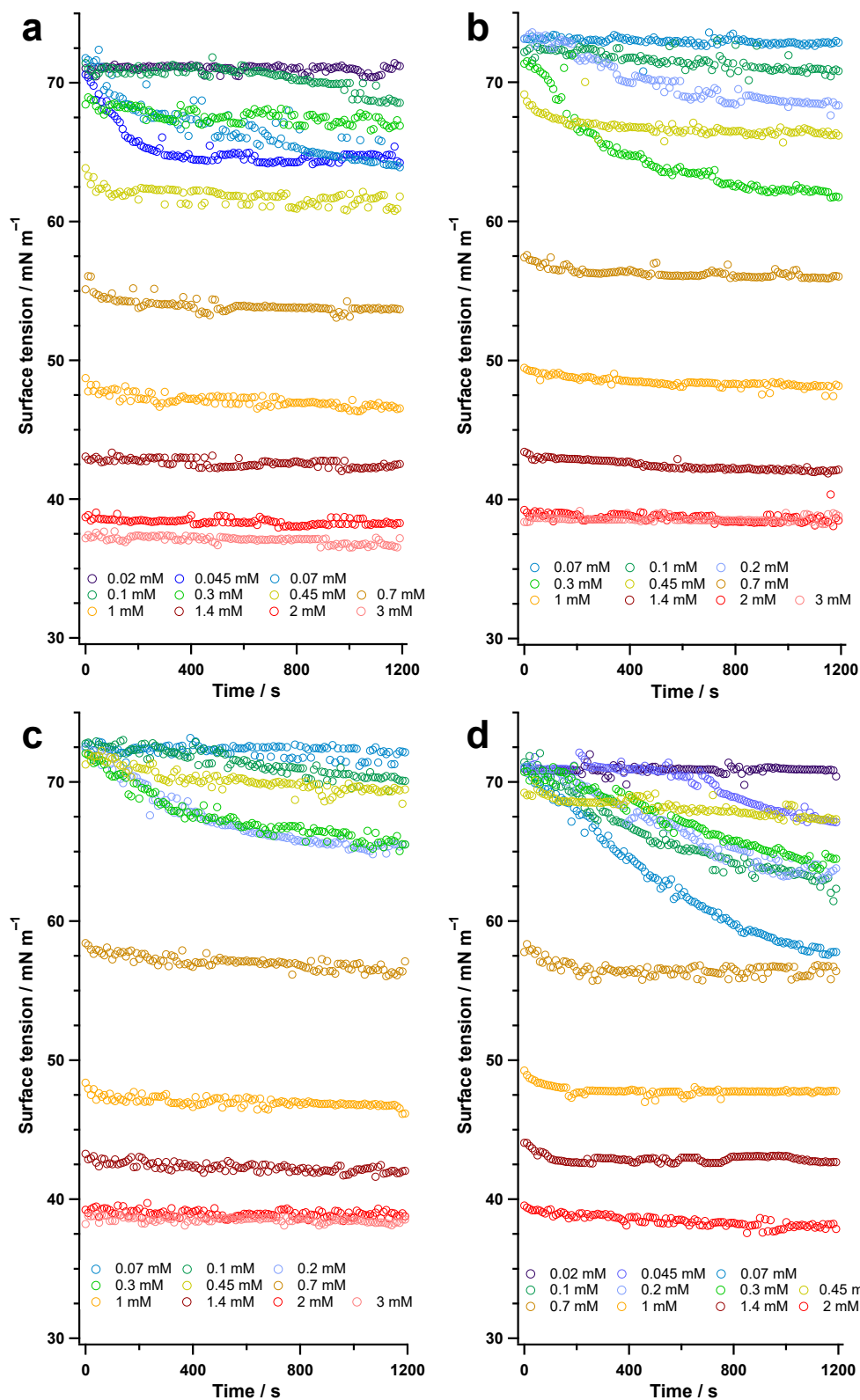


Figure S5: Pendant drop tensiometry data showing changes in surface tension over time for the samples shown in Fig. 4: 0.1 mg/mL GO dispersions in water with the specified concentrations of *trans* azoTAB at pH 5.5 (a), 8.5 (b), 9.5 (c) and 11.5 (d). The measurements span approximately 20 minutes.

Table 2: Raw data values for various measurements performed on samples containing 0.1 mg/mL of aqueous GO dispersion with the specified concentrations of *trans* azoTAB at approximately pH 5.5, *i.e.* with no added base.

azoTAB concentration (mM)	Mass ratio azoTAB:GO	Stability	Eq. surface tension (mN/m)	pH	Zeta potential (mV)	Conductance (μ S)
0	0	Stable	69.7	5.3	-38.20 ± 1.31	18
0.010	0.048	Stable	70.8	5.4	-24.68 ± 1.05	25
0.021	0.093	Stable	71.0	5.3	-24.02 ± 1.29	34
0.045	0.204	Stable	64.7	5.3	-18.77 ± 1.57	50
0.073	0.327	Stable	64.4	5.7	-11.29 ± 1.37	57
0.105	0.471	Unstable	68.8	5.9	-21.72 ± 0.78	75
0.202	0.904	Unstable	71.1	4.8	-0.23 ± 0.82	110
0.304	1.359	Unstable	67.1	5.5	15.08 ± 0.79	131
0.452	2.054	Unstable	61.4	5.2	28.14 ± 0.53	133
0.706	3.189	Unstable	53.7	5.7	30.85 ± 2.08	207
1.005	4.541	Unstable	46.7	5.3	43.82 ± 0.48	269
1.421	6.398	Stable	42.4	5.5	50.17 ± 0.46	329
2.036	9.138	Stable	38.2	5.9	43.78 ± 1.96	412
3.045	13.679	Stable	36.8	6.7	43.01 ± 2.32	528

Table 3: Raw data values for various measurements performed on samples containing 0.1 mg/mL of aqueous GO dispersion with the specified concentrations of *trans* azoTAB at approximately pH 8.5.

azoTAB concentration (mM)	Mass ratio azoTAB:GO	Stability	Eq. surface tension (mN/m)	pH	Zeta potential (mV)	Conductance (μ S)
0	0	Stable	71.4	8.5	-38.83 ± 1.16	242
0.011	0.052	Stable	71.4	8.5	-30.93 ± 0.87	250
0.021	0.097	Stable	73.2	8.3	-37.68 ± 0.97	251
0.047	0.215	Stable	73.5	8.6	-39.65 ± 1.11	249
0.075	0.336	Stable	72.8	8.5	-46.79 ± 0.56	271
0.109	0.494	Stable	68.4	8.7	-40.70 ± 0.75	270
0.203	0.915	Stable	62.2	8.6	-33.65 ± 1.97	299
0.305	1.371	Stable	66.3	8.4	-19.81 ± 1.98	306
0.455	2.003	Unstable	66.5	8.2	9.58 ± 1.30	352
0.702	3.087	Stable	56.0	8.4	31.73 ± 0.98	431
1.010	4.577	Stable	48.0	8.1	32.24 ± 1.15	509
1.404	6.353	Stable	42.0	8.3	31.46 ± 0.48	552
2.002	9.040	Stable	38.6	8.3	36.81 ± 0.36	653
3.023	13.62	Stable	38.6	8.3	39.95 ± 1.45	831

Table 4: Raw data values for various measurements performed on samples containing 0.1 mg/mL of aqueous GO dispersion with the specified concentrations of *trans* azoTAB at approximately pH 9.5.

azoTAB concentration (mM)	mass ratio azoTAB:GO	Stability	Eq. surface tension (mN/m)	pH	Zeta potential (mV)	Conductance (μ S)
0	0	Stable	70.6	9.62	-44.03 ± 0.74	393
0.01	0.043	Stable	72.2	9.69	-42.07 ± 1.64	377
0.022	0.097	Stable	72.4	9.63	-34.87 ± 2.12	368
0.048	0.217	Stable	71.6	9.76	-42.39 ± 1.42	386
0.071	0.32	Stable	72.0	9.68	-42.62 ± 1.56	379
0.099	0.445	Stable	70.0	9.23	-45.14 ± 0.92	410
0.2	0.87	Stable	65.4	9.55	-29.43 ± 2.76	413
0.303	1.342	Stable	65.6	9.6	-25.77 ± 0.78	428
0.452	2.035	Unstable	69.3	9.42	-3.01 ± 1.07	450
0.712	3.196	Metastable	56.4	9.28	16.57 ± 1.42	494
1.023	4.589	Stable	46.6	9.07	30.2 ± 1.28	562
1.404	6.301	Stable	42.0	8.89	36.75 ± 1.3	646
2.012	9.038	Stable	38.9	8.88	29.89 ± 1.84	744
2.982	13.448	Stable	38.3	8.93	39.15 ± 0.83	879

Table 5: Raw data values for various measurements performed on samples containing 0.1 mg/mL of aqueous GO dispersion with the specified concentrations of *trans* azoTAB at approximately pH 11.5.

azoTAB concentration (mM)	Mass ratio azoTAB:GO	Stability	Mean surface tension (mN/m)	pH	Zeta potential (mV)	Conductance (μ S)
0	0	Stable	70.9	11.8	-41.36 ± 0.73	3058
0.012	0.052	Stable	70.4	11.8	-34.37 ± 1.12	2838
0.022	0.099	Stable	70.8	11.8	-40.84 ± 0.70	3117
0.045	0.202	Stable	67.3	11.8	-40.37 ± 0.53	3085
0.072	0.325	Stable	57.9	11.7	-45.97 ± 0.85	2973
0.100	0.446	Stable	62.6	11.8	-41.91 ± 1.81	2954
0.204	0.913	Stable	63.6	11.7	-46.85 ± 0.50	2954
0.307	1.378	Stable	64.2	11.7	-37.92 ± 0.56	2788
0.453	2.028	Unstable	67.3	11.6	-8.45 ± 0.92	2679
0.709	3.172	Unstable	56.5	11.5	24.55 ± 0.74	2412
1.015	4.542	Stable	47.8	11.7	26.10 ± 0.86	2891
1.407	6.344	Stable	42.7	11.7	27.02 ± 0.74	2808
2.016	8.993	Stable	38.1	11.6	25.91 ± 1.24	2789
3.031	13.553	Stable	38.0	11.6	26.78 ± 1.09	2636

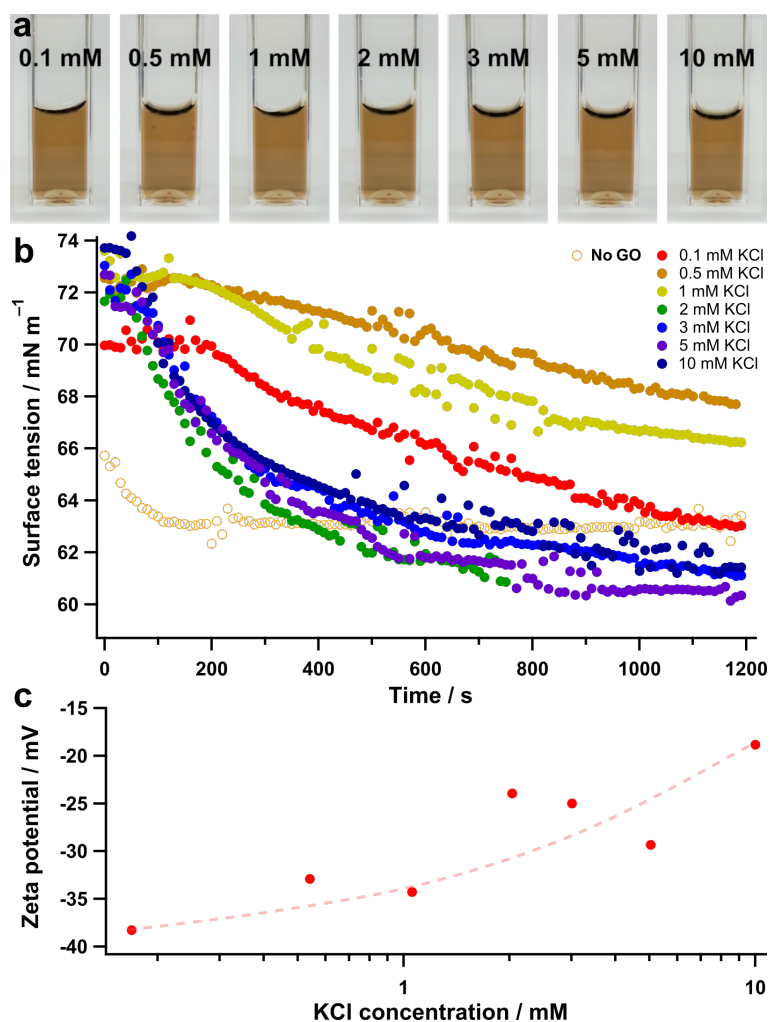


Figure S6: (a) Samples containing 0.1 mg/mL of aqueous GO dispersion and 0.1 mM of *trans* azoTAB with the specified concentrations of KCl at approximately pH 8.5. (b) Pendant drop tensiometry data showing changes in surface tension over time for the samples shown in (a). (c) Phase analysis light scattering data showing changes in zeta potential for the samples shown in (a), the dashed line has been added as a guide to the eye.

Table 6: Raw data values for various measurements performed on samples containing 0.1 mg/mL of aqueous GO dispersion and 0.1 mM of *trans* azoTAB with the specified concentrations of KCl at approximately pH 8.5.

GO concentration (mg/mL)	azoTAB concentration (mM)	KCl concentration (mM)	Stability	Eq. surface tension (mN/m)	Zeta potential (mV)	Conductance (μ S)
-	0.10	4.81	-	-	-	-
0.10	0.10	0.17	Stable	63.1	-38.28 ± 1.90	346
0.10	0.10	0.54	Stable	68.1	-32.93 ± 2.73	438
0.10	0.10	1.06	Stable	66.3	-34.29 ± 0.72	593
0.10	0.10	2.04	Stable	60.1	-23.97 ± 1.95	887
0.10	0.10	3.01	Metastable	61.2	-25.00 ± 3.34	1182
0.10	0.10	5.04	Metastable	60.5	-29.36 ± 1.50	1814
0.10	0.10	10.01	Metastable	61.6	-18.86 ± 2.01	2984

Table 7: Raw data values for the mean surface tensions of various concentrations of *trans* azoTAB in water with 3 mM of KCl present.

azoTAB concentration (mM)	Mean surface tension (mN/m)
0.011	71.9
0.014	72.1
0.021	71.7
0.031	70.5
0.045	70.5
0.072	70.0
0.100	65.1
0.139	64.0
0.204	58.1
0.303	51.4
0.453	44.8
0.711	41.0
0.995	39.8
1.414	38.6
2.010	39.2
3.032	38.7

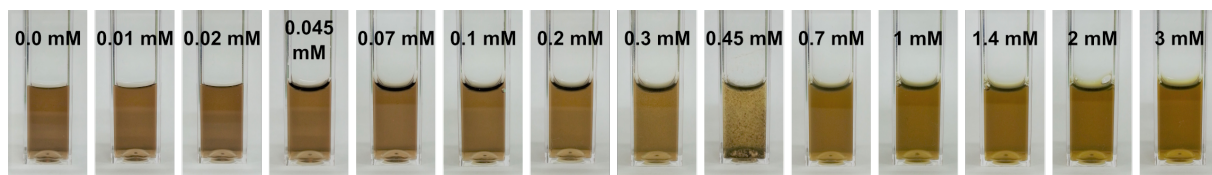


Figure S7: (a) Samples containing 0.1 mg/mL of aqueous GO dispersion and 3 mM of KCl with the specified concentrations of *trans* azoTAB at approximately pH 8.5.

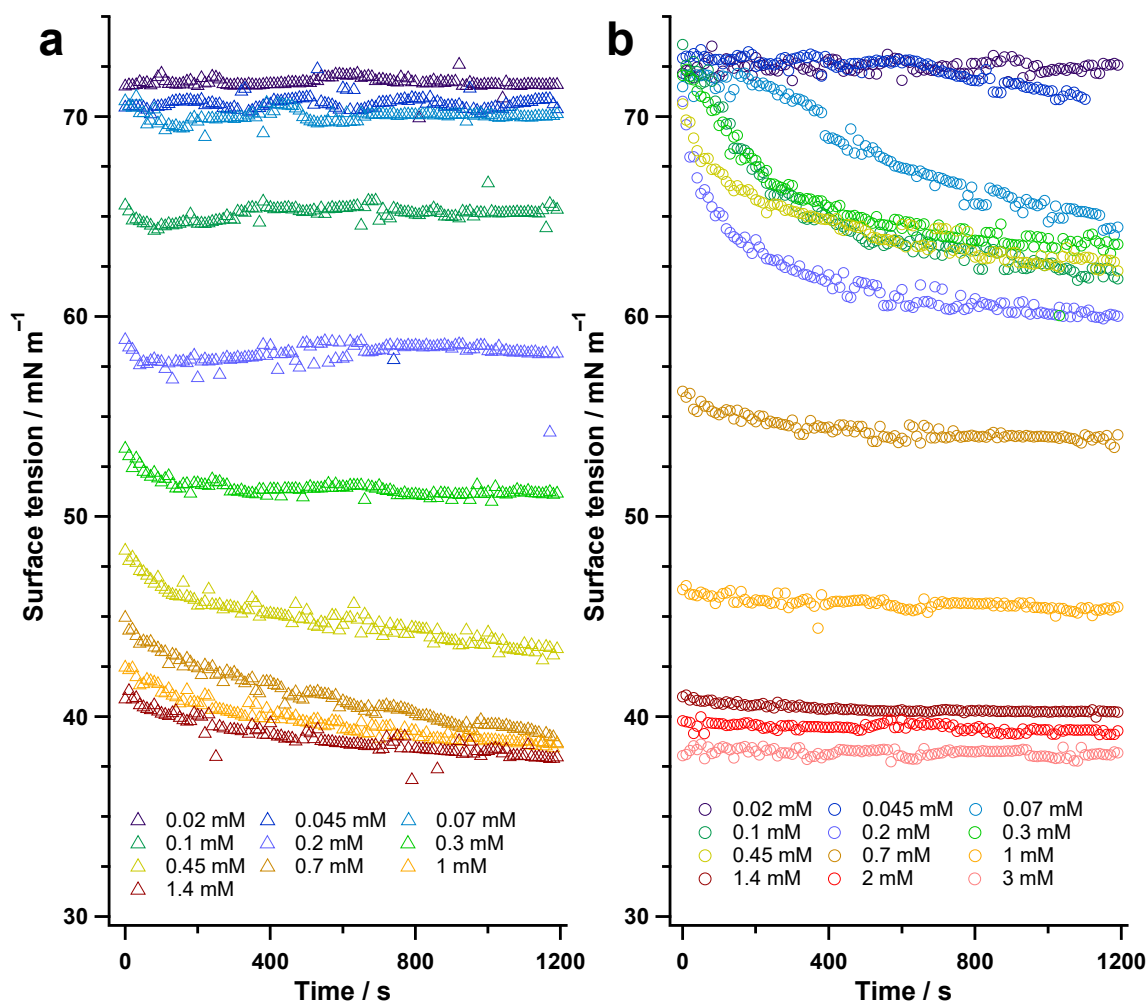


Figure S8: Pendant drop tensiometry data showing changes in surface tension over time for (a) *trans* azoTAB with 3 mM of KCl added and (b) the samples shown in Fig. 7. Concentrations featured in the legends refer to the amount of azoTAB.

Table 8: Raw data values for various measurements performed on samples containing 0.1 mg/mL of aqueous GO dispersion and 3 mM of KCl with the specified concentrations of *trans* azoTAB at approximately pH 9.

azoTAB concentration (mM)	mass ratio azoTAB:GO	KCl concentration (mM)	Stability	Eq. surface tension (mN/m)	pH	Zeta potential (mV)	Conductance (μ S)
0	0	3.020	Stable	73.1	9.1	-35.59 ± 1.38	1140
0.010	0.044	2.993	Stable	72.8	8.8	-39.82 ± 0.86	1213
0.015	0.067	3.020	Stable	72.5	8.8	-22.39 ± 1.00	1205
0.047	0.211	3.014	Stable	71.0	8.6	-27.11 ± 2.00	1254
0.069	0.309	3.013	Stable	64.7	9.0	-31.91 ± 0.76	1190
0.101	0.457	3.006	Stable	62.2	9.1	-25.57 ± 1.29	1209
0.200	0.900	3.019	Stable	60.1	8.6	-15.37 ± 1.56	1236
0.307	1.413	3.020	Unstable	63.7	8.7	-15.65 ± 1.13	1224
0.454	2.046	3.007	Unstable	62.7	9.0	3.77 ± 2.08	1212
0.696	3.148	3.009	Metastable	53.9	8.7	21.17 ± 1.19	1284
0.996	4.484	3.032	Stable	45.4	8.7	22.12 ± 1.13	1279
1.408	6.347	3.008	Stable	40.2	8.7	24.54 ± 0.98	1268
2.004	9.004	3.010	Stable	39.2	8.8	17.16 ± 1.60	1299
2.986	13.489	3.009	Stable	38.1	8.6	22.92 ± 0.77	1479

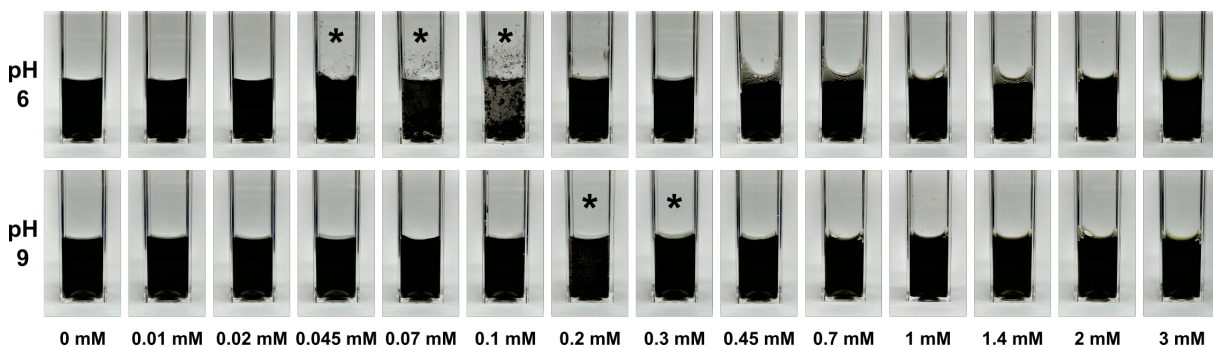


Figure S9: (a) Samples containing 0.1 mg/mL of aqueous rGO dispersion and the specified concentrations of *trans* azoTAB at approximately pH 6 and pH 9. Samples that are either unstable or metastable have been marked with an asterisk (*).

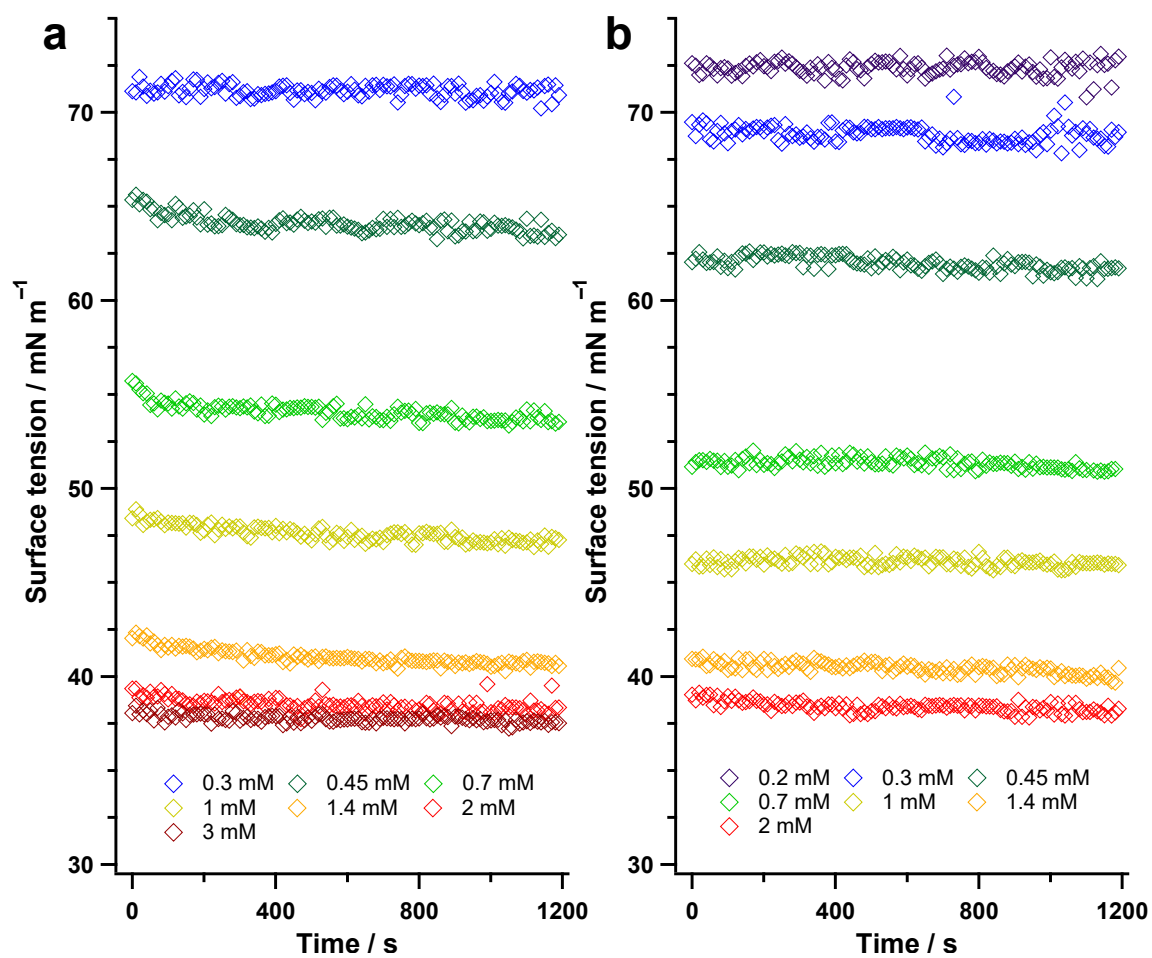


Figure S10: Pendant drop tensiometry data showing changes in surface tension over time for rGO with the specified concentrations of *trans* azoTAB at approximately pH 6 (a) and pH 9 (b).

Table 9: Raw data values for various measurements performed on samples containing 0.1 mg/mL of aqueous rGO dispersion with the specified concentrations of *trans* azoTAB at approximately pH 6.

azoTAB concentration (mM)	mass ratio azoTAB:GO	Stability	Eq. surface tension (mN/m)	pH	Zeta potential (mV)	Conductance (μ S)
0	0	Stable	72.3	6.1	-33.85 ± 0.89	26
0.010	0.044	Stable	71.5	5.5	-39.18 ± 1.41	30
0.020	0.088	Stable	72.3	5.7	-32.92 ± 0.96	37
0.045	0.200	Metastable	73.2	5.9	-11.06 ± 2.33	48
0.071	0.326	Unstable	72.4	6.1	-13.87 ± 0.97	58
0.101	0.453	Unstable	72.2	6.1	7.98 ± 0.39	72
0.199	0.898	Stable	71.4	5.5	29.70 ± 0.73	96
0.303	1.352	Stable	71.1	5.8	35.10 ± 0.65	113
0.455	2.040	Stable	63.6	5.7	36.41 ± 0.44	141
0.714	3.174	Stable	53.8	5.6	37.40 ± 1.55	190
1.025	4.613	Stable	47.2	6.3	44.14 ± 0.98	250
1.419	6.337	Stable	40.7	6.6	28.41 ± 1.68	336
2.034	9.069	Stable	38.4	7.1	42.13 ± 1.22	435
2.709	12.123	Stable	37.6	7.3	42.95 ± 1.37	521

Table 10: Raw data values for various measurements performed on samples containing 0.1 mg/mL of aqueous rGO dispersion with the specified concentrations of *trans* azoTAB at approximately pH 9.

azoTAB concentration (mM)	mass ratio azoTAB:GO	Stability	Eq. surface tension (mN/m)	pH	Zeta potential (mV)	Conductance (μ S)
0	0	Stable	71.7	9.4	-35.45 ± 1.10	206
0.010	0.045	Stable	71.4	9.2	-33.22 ± 2.09	212
0.021	0.095	Stable	72.9	9.3	-39.19 ± 1.09	215
0.045	0.201	Stable	73.3	9.4	-33.79 ± 1.96	227
0.070	0.314	Stable	72.3	9.5	-37.11 ± 0.68	228
0.103	0.461	Stable	72.9	8.4	-36.54 ± 1.06	226
0.203	0.906	Unstable	72.2	8.5	6.19 ± 0.89	250
0.307	1.380	Metastable	68.7	8.9	21.31 ± 0.53	273
0.455	2.032	Stable	61.6	8.7	22.60 ± 0.58	318
0.727	3.264	Stable	51.0	8.5	25.59 ± 0.97	329
1.028	4.601	Stable	46.0	8.3	16.73 ± 0.53	387
1.447	6.476	Stable	40.0	8.4	29.06 ± 0.98	474
2.038	9.116	Stable	38.1	8.5	27.33 ± 1.52	558
2.712	12.157	Stable	38.5	8.7	34.30 ± 0.87	634

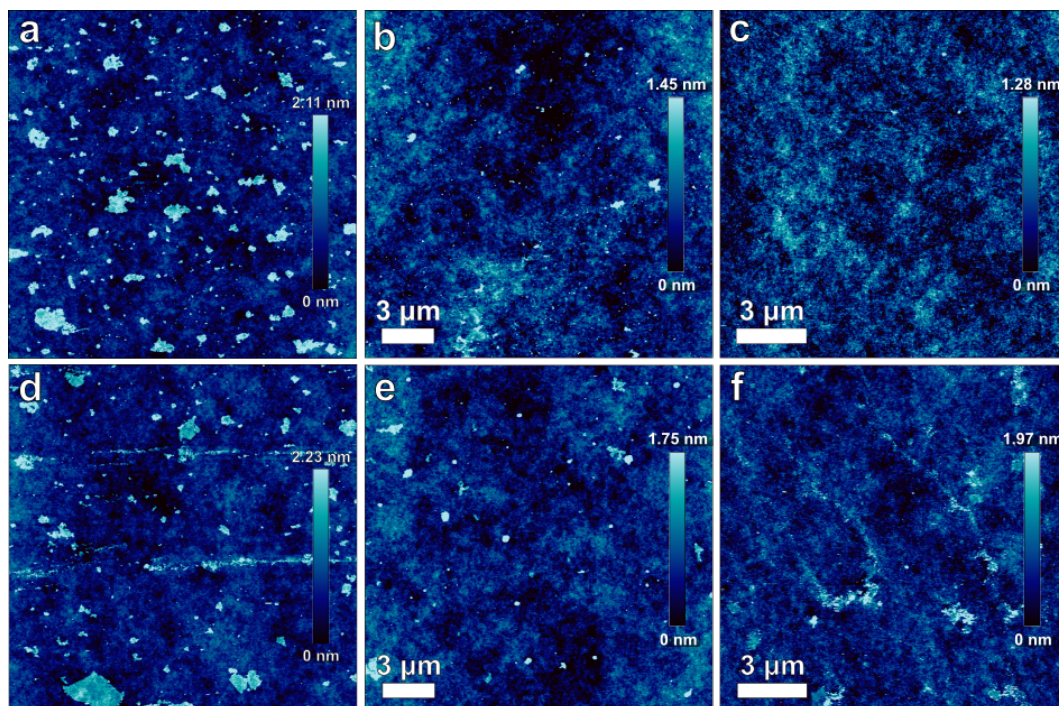


Figure S11: Atomic force microscopy images of GO sheets deposited on glass by dip-coating in an aqueous dispersion of 0.1 mg/mL GO (a-c) and 0.1 mg/mL GO with 0.1 mM *trans* azoTAB (d-f). Solutions were at approximately pH 9. Images were taken on various positions of the cover slips.

Images by atomic force microscopy (AFM) were gathered on a JPK NanoWizard 3. Imaging was performed in tapping mode using Bruker NCHV model cantilevers with spring constants of *ca.* 42 N/m and nominal resonant frequencies of *ca.* 350 kHz. Sample preparation was as described in the main text for wide-field fluorescence (without polymer coating).

From Figure 11, there is little apparent evidence of GO at the interface even when azoTAB is incorporated. As GO synthesis from bulk graphite flakes results in dispersions with high lateral polydispersity (submicron to multiple micron sheets), it is possible that upon addition of the surfactant, the larger sheets are preferentially adsorbing at the interface due to their lower edge to plane ratio and thus lower aqueous stability.⁸ This hypothesis is supported by the images in Figures 4b,c and e of the main paper, wherein large (>20 μm) GO sheets are predominantly observed at the interface. Therefore it is likely that the particles are on a size scale unsuitable for AFM analysis.

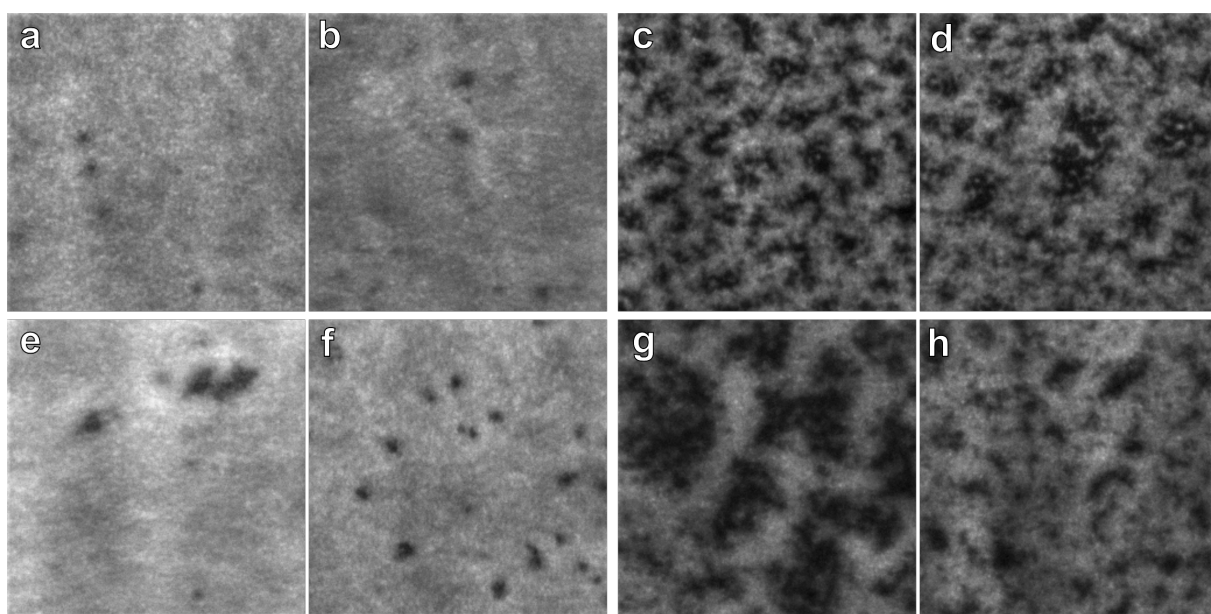


Figure S12: Additional FQM images of GO deposited onto glass cover slips by dip-coating in a 0.1 mg/mL dispersion of GO (a,b,e,f) and a 0.1 mg/mL dispersion of GO with 0.1 mM of *trans* azoTAB (c,d,g,h). Images a-d are of samples with 10 μ L of the fluorescent layer (see methods for details) spin-coated on the sample surface and images e-h are of samples with 20 μ L spun on. Solutions were at approximately pH 9 and the total area of each image is $25.6 \times 25.6 \mu\text{m}$.

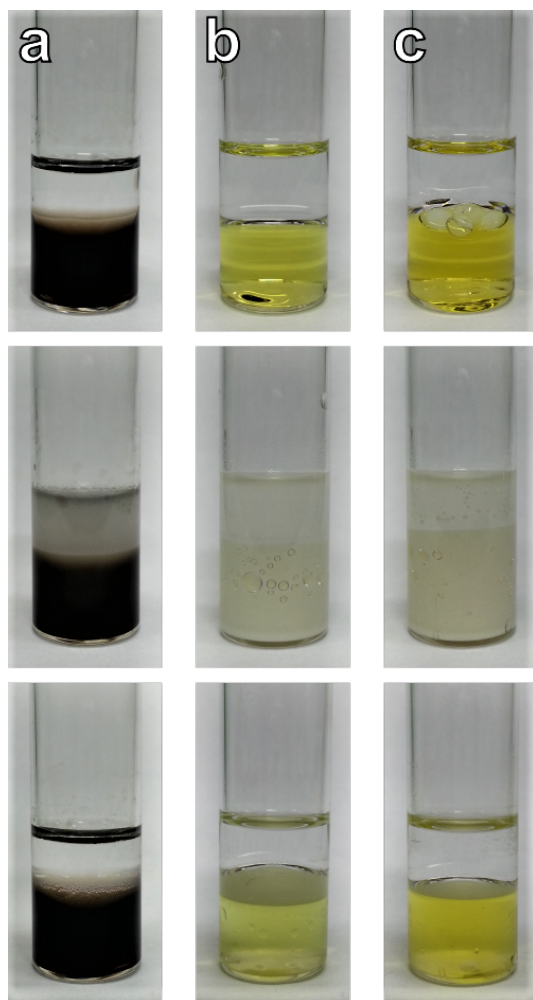


Figure S13: (a) Sample containing an equal volume of toluene and 0.4 mg/mL of aqueous GO dispersion at pH 10. (b) Sample containing an equal volume of toluene and 0.4 mM of *trans* azoTAB at approximately pH 10, (c) is a similar sample however the azoTAB has been irradiated with 365 nm light. The top row represents each sample prior to ultrasonication, the middle row is immediately after sonication and the bottom row is each sample after being left overnight.

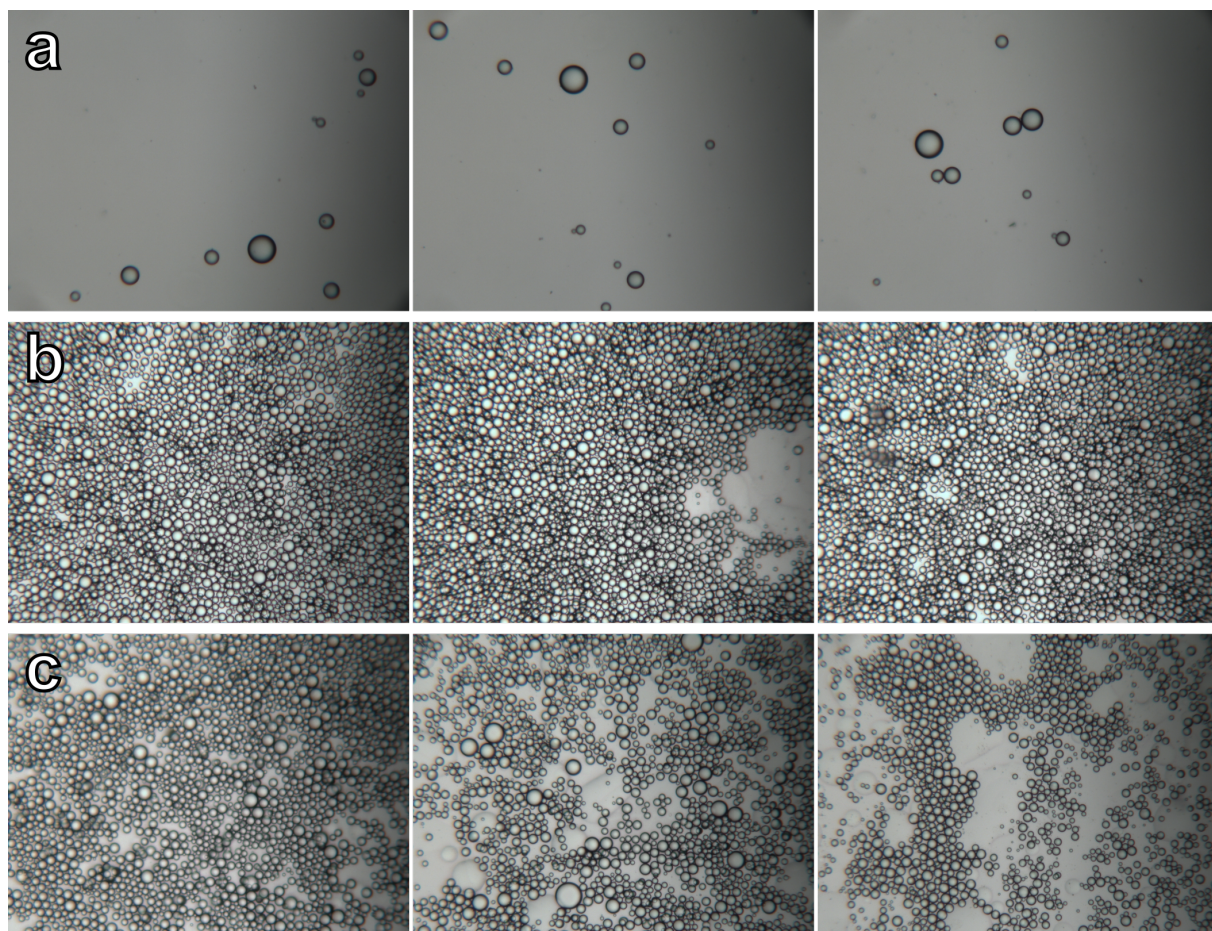


Figure S14: Optical microscopy images of toluene-in-water emulsion droplets stabilised by 0.4 mg/mL of aqueous GO dispersion (a), 0.4 mM of *trans* azoTAB (b) and 0.4 mM of *cis* azoTAB (c). From left to right images are of the same sample. All samples were at approximately pH 10 and image areas are image areas are 604.01 by 805.34 μm .

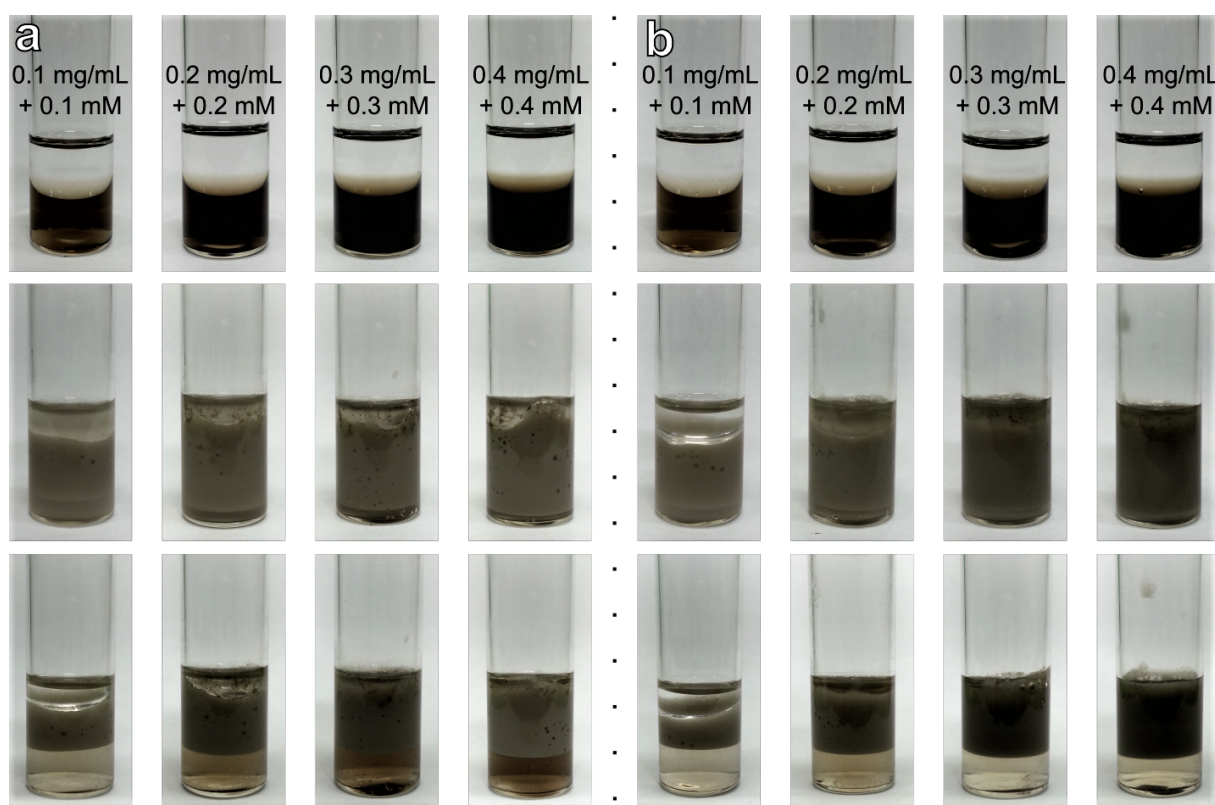


Figure S15: (a) Sample containing an equal volume of toluene and the specified concentrations of aqueous GO dispersion and *trans* azoTAB at pH 10. (b) Similar samples whereby the azoTAB solution was irradiated with 365 nm light prior to incorporation of the GO. The top row represents each sample prior to ultrasonication, the middle row is immediately after sonication and the bottom row is each sample after being left overnight.

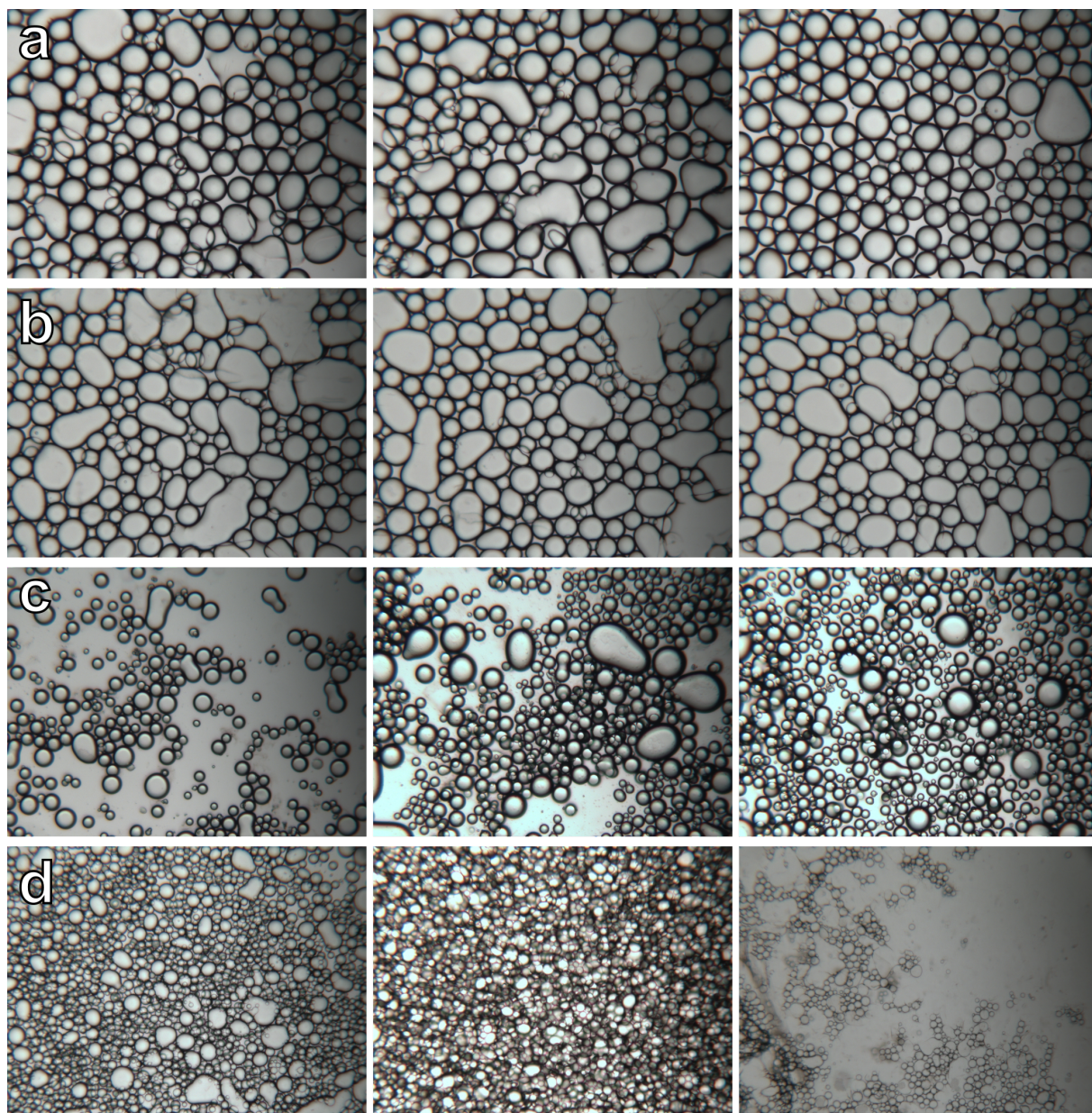


Figure S16: Optical microscopy images of toluene-in-water emulsion droplets stabilised by 0.1 mg/mL of aqueous GO dispersion and 0.1 mM of *trans* azoTAB (a), 0.2 mg/mL GO and 0.2 mM *trans* azoTAB (b), 0.3 mg/mL GO and 0.3 mM *trans* azoTAB (c) and lastly 0.4 mg/mL GO and 0.4 mM *trans* azoTAB (b). From left to right images are of the same sample. All samples were at approximately pH 10 and image areas are image areas are 604.01 by 805.34 μm .

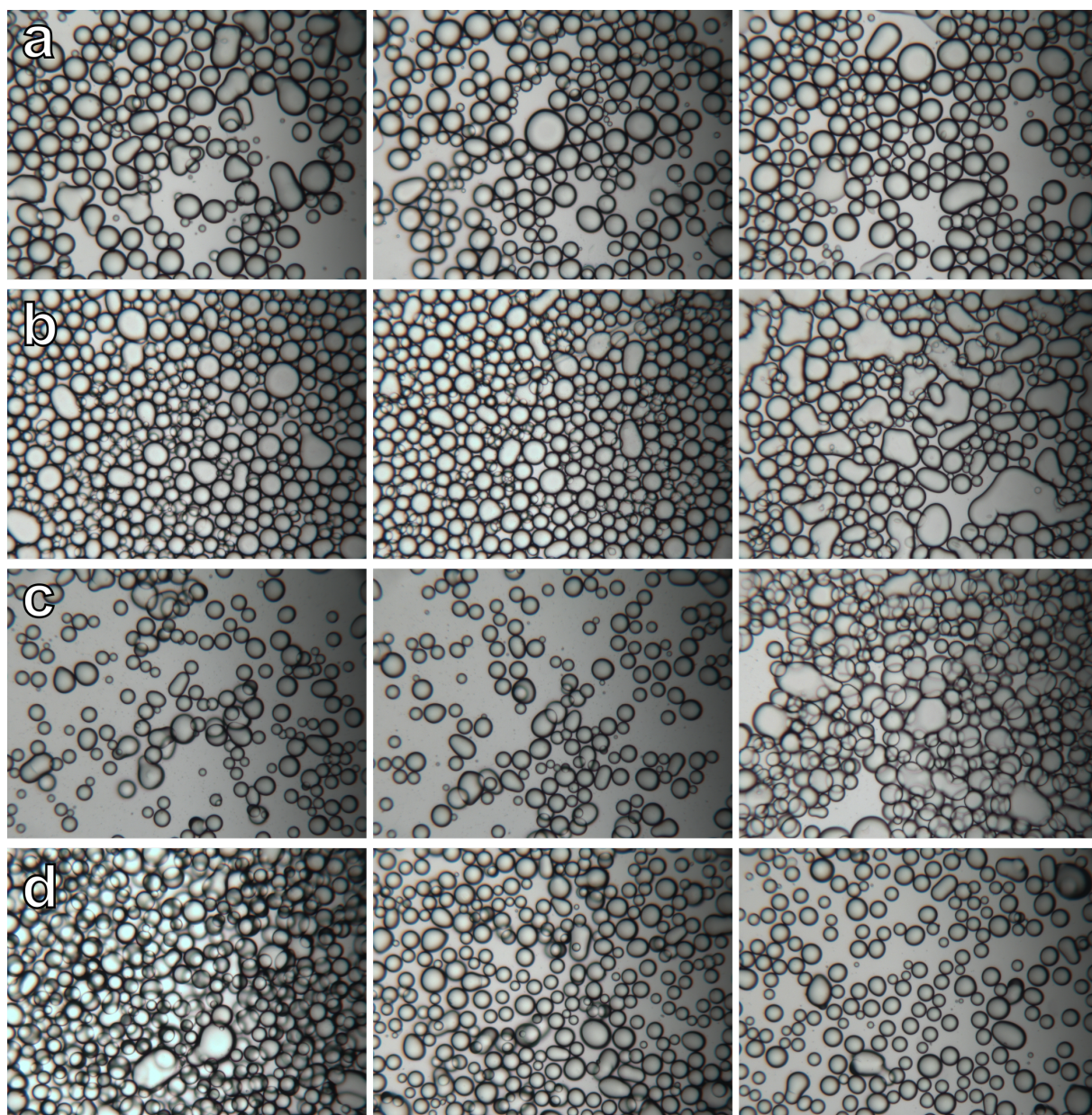


Figure S17: Optical microscopy images of toluene-in-water emulsion droplets stabilised by 0.1 mg/mL of aqueous GO dispersion and 0.1 mM of *cis* azoTAB (a), 0.2 mg/mL GO and 0.2 mM *cis* azoTAB (b), 0.3 mg/mL GO and 0.3 mM *cis* azoTAB (c) and lastly 0.4 mg/mL GO and 0.4 mM *cis* azoTAB (b). All azoTAB solution was irradiated with 365 nm light prior to incorporation of the GO. From left to right images are of the same sample. All samples were at approximately pH 10 and image areas are 604.01 by 805.34 μm .

Table 11: Average diameters of the emulsion droplets and the peak widths for specific surfactant/GO mixtures based on the Gaussian functions fit to the histograms in the main paper. Values are shown \pm one standard deviation.

Azo conc. (mM)	Isomer	GO conc. (mg/mL)	Average droplet diameter (μm)	Peak width (μm)	Emulsion volume /Total volume
-	-	0.4	-	-	0.06
0.4	<i>trans</i>	-	-	-	0.14
0.4	<i>cis</i>	-	-	-	0.07
0.1	<i>trans</i>	0.1	45.8 ± 0.49	13.3 ± 0.89	0.37
0.2	<i>trans</i>	0.2	41.0 ± 0.78	8.1 ± 1.21	0.52
0.3	<i>trans</i>	0.3	21.9 ± 0.36	9.8 ± 0.58	0.50
0.4	<i>trans</i>	0.4	14.5 ± 0.24	5.3 ± 0.43	0.61
0.1	<i>cis</i>	0.1	35.3 ± 0.61	12.1 ± 1.02	0.35
0.2	<i>cis</i>	0.2	34.9 ± 0.45	11.4 ± 0.75	0.53
0.3	<i>cis</i>	0.3	30.0 ± 0.41	10.5 ± 0.67	0.60
0.4	<i>cis</i>	0.4	29.7 ± 0.21	7.5 ± 0.33	0.65

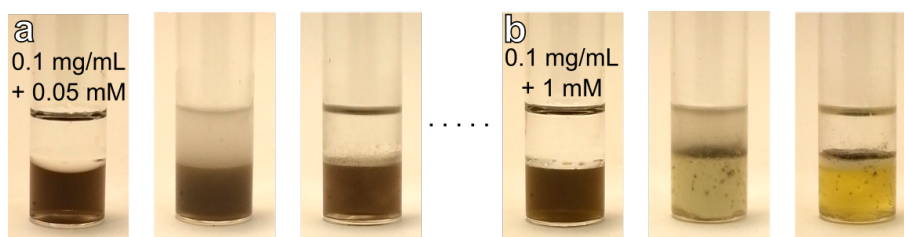


Figure S18: (a-b) Samples containing an equal volume of toluene and the specified concentrations of aqueous GO dispersion and *trans* azoTAB at pH 10. The left image of each series represents each sample prior to ultrasonication, the middle images are immediately after sonication and the right images are after being left overnight.

Table 12: Sample compositions and fitting parameters for all XRR samples where SLD is the scattering length density and BGD is background. Values are representative of the specified layer from the model.

azoTAB conc. (mM)	GO/rGO conc. (mg/mL)	KCl conc. (mM)	No. of layers	Thickness (Å)			Roughness (Å)			SLD			
				Layer 1	2	3	1	2	3	BGD	1	2	3
0.098	0	4.765	2	7.9	18.0		7.2	4.0		3.5	4.37	10.75	
0	0.100	0	1	4.6			2.5			4.5	7.96		
0	0.099	0	1	1.7			2.6			5.9	8.36		
0.045	0.115	0	1	2.4			6.5			2.7	2.14		
0.102	0	0	2	16.7	5.2		3.2	4.6		5.5	0.73	9.95	
0.103	0.094	0	3	24.6	8.1	8.9	5.8	5.3	6.3	7.7	4.15	13.94	12.57
0.103	0.101	5.252	3	10.7	17.7	29.0	7.9	6.5	6.4	3.8	13.92	9.12	10.19
1.350	0	0	2	10.5	18.3		3.0	7.9		7.6	5.39	13.60	
1.384	0.100	0	2	16.9	6.9		5.3	5.4		2.2	12.50	8.37	
1.347	0.098	0	2	17.3	3.9		5.9	5.4		5.4	13.46	6.18	
0	0.100	0	1	6.5			2.1			4.2	0.86		
0	0.099	0	1	4.1			5.0			7.0	12.68		

Table 13: Sample compositions and fitting parameters relating to the kinetics XRR measurements (Fig. 20) all XRR samples where SLD is the scattering length density and BGD is background. Values are representative of the specified layer from the model.

Time (minutes)	azoTAB conc. (mM)	GO conc. (mg/mL)	No. of layers	Thickness (\AA)		Roughness (\AA)		SLD			
				Layer 1	2	1	2	BGD	1	2	
90	0.209	0.100	2	21.4	15.3	2.8	7.3	4.1	1.18	10.85	
180	0.209	0.100	2	25.2	10.4	4.0	6.9	7.3	3.56	14.36	
270	0.209	0.100	2	22.3	8.7	4.2	6.1	6.9	4.17	6.14	

X-ray reflectivity

Taking a sample comprising 0.1 mg/mL of GO and 0.2 mM of *trans*-azoTAB at pH 10, the specular reflectivity of the air-water interface was monitored over time (Fig. 20a). To explore a full Q -range (0.01 - 0.99 \AA^{-1}) and achieve reasonable statistics, an individual measurement time was set at 90 minutes. Hence the measurements do not represent a true approximation of the adsorption kinetics of the GO/azoTAB, as from greater than *ca.* 0.3 \AA^{-1} almost all scattering was related to the background solvent.

From the initial measurement (90 minutes) to the second measurement (180 minutes), the depth of the fringe at *ca.* 0.16 \AA^{-1} becomes more pronounced indicating that there is more material at the interface (Fig. 20a). Modelling of the data revealed that the total thickness of this interfacial film was *ca.* 35.6 \AA (see Supporting Information). As azoTAB is only approximately 23 \AA in length, more than just a surfactant monolayer must be present at the interface. GO has a known thickness of approximately 1 nm ,⁹ which would account for the remainder of the thickness. A two layer model was also applied to these data series in which the top layer had an

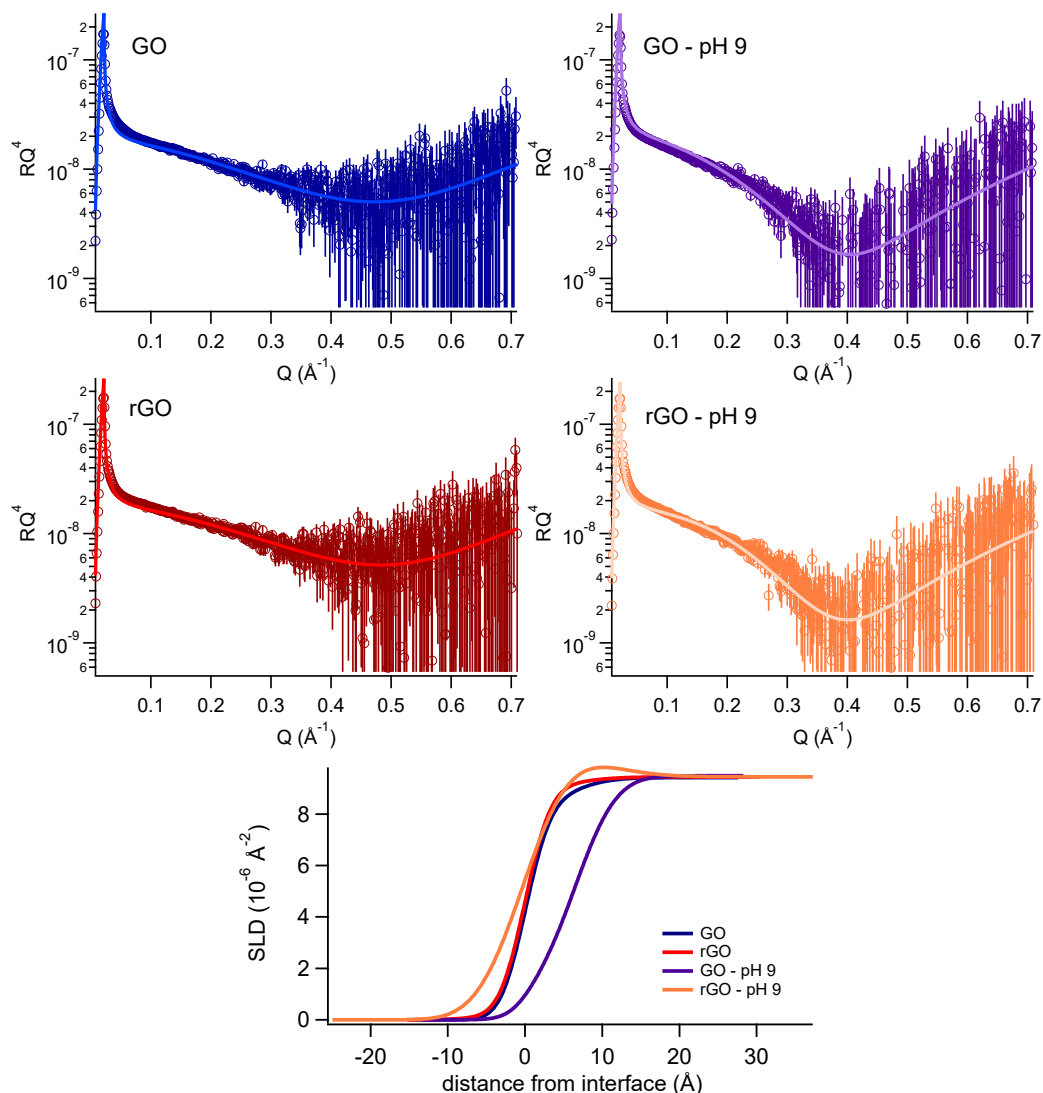


Figure S19: X-ray reflectivity data of a 0.1 mg/mL aqueous dispersions of GO and rGO with and without base. The corresponding electron density profiles for the results are shown in the bottom graph.

apparent thickness of *ca.* 25.2 \AA and the bottom layer *ca.* 10.4 \AA (see Supporting Information), lending credibility to the theory that the changes indeed result from surfactant-coated GO sheets at the interface. The sample was irradiated with 365 nm light prior to taking the final data series (270 minutes) and the film thickness was found to decrease slightly to *ca.* 31.0 \AA . As the azobenzene adopts a bent configuration in its *cis* form, the molecular length decreases, which would account for the change observed. This is also evident in the corresponding electron

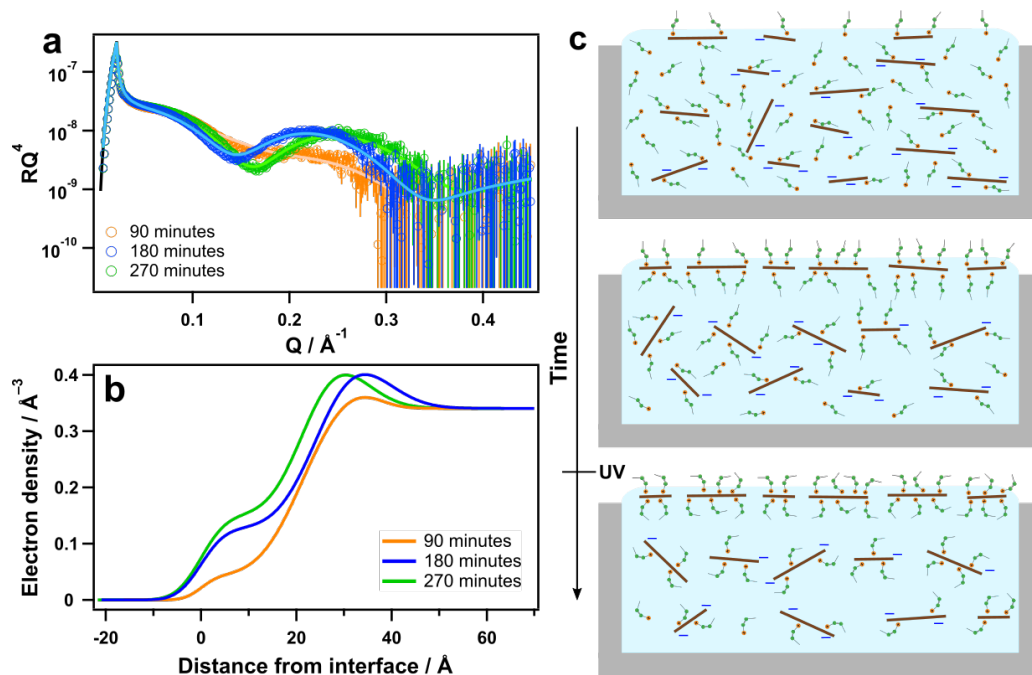


Figure S20: (a) X-ray reflectivity data of a 0.1 mg/mL GO dispersion with 0.2 mM *trans* azoTAB at pH 10 as a function of time. The sample was irradiated with 365 nm light for 5 minutes before commencing the final measurement (270 minutes). The hollow symbols represent the raw data points while the solid lines are model fits. (b) The corresponding electron density profiles for the results in (a). (c) Schematic representation of the reflectivity data, showing the increased adsorption of surfactant-coated GO sheets at the air-water interface over time, and finally conversion of the azoTAB molecules from the *trans* to the *cis* isomer upon irradiation with UV light.

density profile (Fig. 20b), however there does not appear to be desorption of material, based on the shape of the curve compared to the 180 minute data set. This is unsurprising as larger structures such as GO would require significantly more energy to desorb from the interface compared to surfactant molecules. These results are also represented schematically in Figure 20c, showing adsorption of the GO and azoTAB over time followed by photoisomerisation of the surfactant molecules.

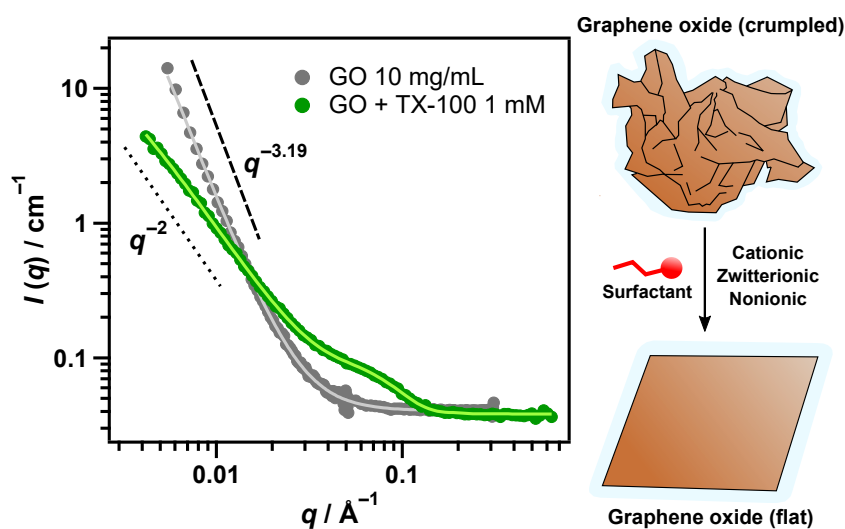
References

- [1] H. M. D. Bandara, S. C. Burdette. *Chem. Soc. Rev.* **2012**, *41*, 1809.
- [2] B. A. Ciccirelli, J. A. Elia, T. A. Hatton, K. A. Smith. *Langmuir* **2007**, *23*, 8323.
- [3] E. Chevallier, A. Mamane, H. A. Stone, C. Tribet, F. Lequeux, C. Monteux. *Soft Matter* **2011**, *7*, 7866.
- [4] J. Griffiths. *Chem. Soc. Rev.* **1972**, *1*, 481.
- [5] E. Fischer, M. Frankel, R. Wolovsky. *J. Chem. Phys.* **1955**, *23*, 1367.
- [6] T. Shang, K. A. Smith, T. A. Hatton. *Langmuir* **2003**, *19*, 10764.
- [7] J. D. Berry, M. J. Neeson, R. R. Dagastine, D. Y. Chan, R. F. Tabor. *J. Colloid Interface Sci.* **2015**, *454*, 226.
- [8] J. Luo, L. J. Cote, V. C. Tung, A. T. L. Tan, P. E. Goins, J. Wu, J. Huang. *J. Am. Chem. Soc.* **2010**, *132*, 17667.
- [9] L. J. Cote, F. Kim, J. Huang. *J. Am. Chem. Soc.* **2009**, *131*, 1043.

Chapter 6

Bulk properties of aqueous graphene oxide and reduced graphene oxide with surfactants and polymers: adsorption and stability

Published: Thomas M. McCoy, Liliana de Campo, Anna V. Sokolova, Isabelle Grillo, Ekaterina I. Izgorodina and Rico F. Tabor, Bulk properties of aqueous graphene oxide and reduced graphene oxide with surfactants and polymers: adsorption and stability. *Phys. Chem. Chem. Phys.*, 2018, **20**, 16801-16816.





Cite this: *Phys. Chem. Chem. Phys.*,
2018, 20, 16801

Bulk properties of aqueous graphene oxide and reduced graphene oxide with surfactants and polymers: adsorption and stability†

Thomas M. McCoy,^a Liliana de Campo,^b Anna V. Sokolova,^b Isabelle Grillo,^c
Ekaterina I. Izgorodina^a and Rico F. Tabor^{*a}

A diverse range of molecular surfactants and polymers have been incorporated into aqueous graphene oxide (GO) and reduced graphene oxide (rGO) dispersions in order to understand the complex relationship between surface chemistry, surface forces and interfacial thermodynamics of these materials with typical amphiphiles. Surfactant additives were systematically varied in terms of their charge and hydrophobicity to reveal important structure–function relationships affecting adsorption and interaction with GO and rGO surfaces. Small-angle (and ultra small-angle) neutron scattering was employed to examine and monitor the interactions and self-assembly in each system. Charge was found to be the overriding factor driving adsorption, as cationic surfactants very readily adsorbed to both GO and rGO, whereas anionic surfactants gave little to no evidence of adsorption despite possessing hydrophobic tail-groups. Molecules of neutral charge such as nonionic and zwitterionic surfactants as well as neutral polymers also showed strong affinities for GO and rGO, indicating that dispersion and dipole (induction polarisation) interactions also play a significant role in adsorption with these materials. Modelling the neutron data revealed in many cases a q^{-2} slope in the low q and ultra low q regions, indicating that scattering was occurring from large, flat surfaces (lamellae or bilayers), suggesting an effective flattening of the sheets in dispersion. The results presented thus help to form a roadmap for the behaviour of GO and rGO with surfactants and polymers, relevant to adsorption, stabilisation, formulation and coating in aqueous environments as adsorbent and functional materials.

Received 30th April 2018,
Accepted 3rd June 2018

DOI: 10.1039/c8cp02738b

rsc.li/pccp

1 Introduction

Graphene oxide (GO) and reduced graphene oxide (rGO) have continued to gain considerable research momentum in recent years owing to their great potential in a wide variety of fields and applications. Unlike pristine graphene, which is composed of pure carbon,^{1,2} GO and rGO have the useful benefit of being processable in aqueous solution due to their chemical functionalisation with oxygenated groups.^{3–5} This feature, combined with their exceptional surface area to mass ratio, make GO and rGO sheets ideal substrates in applications where adsorption is a central process.^{6–8} Such areas include emulsification,^{9–11} foaming,^{12–15} coating,^{16–18} self-assembly^{19–21} and adsorption/

decontamination;²² the findings put forward in this study are most significantly applicable to the latter two phenomena.

GO is highly compatible with water, and as such can form concentrated dispersions and even hydrogels.^{23,24} The aggressive oxidation of graphite using the improved Hummers' method (used in this work),²⁵ results in a large proportion of oxygen being introduced to the graphene sheets (up to 40% by mass), in the form of epoxy, hydroxy and carboxy groups.³ GO sheets are thus exceptionally hydrophilic and exhibit large negative surface potentials in water, readily resulting in their dispersion through favourable solvation and electrostatic repulsions.^{26,27} However, when reduced with hydrazine,⁵ aromaticity on the basal plains of the sheets is largely restored, and the oxygen content controllably decreases down to approximately 20% by mass, resulting in a material intermediate between graphene and GO in terms of electrical, mechanical and adsorption properties. Therefore, rGO sheets are inherently more hydrophobic, and only form stable suspensions up to 0.5 mg mL^{−1}, despite retaining significant negative surface charge.⁵ The effective hydrophilic–lipophilic balance of these materials is thus a significant factor influencing their dispersion and adsorption properties,²⁸ and realistically

^a School of Chemistry, Monash University, Clayton 3800, VIC, Australia.

E-mail: rico.tabor@monash.edu; Fax: +61 3 9905 4597; Tel: +61 3 9905 4558

^b Australian Centre for Neutron Scattering, ANSTO, Lucas Heights 2234, NSW, Australia

^c Institut Laue-Langevin, F-38042 Grenoble, France

† Electronic supplementary information (ESI) available: Contains further information on models, fitting parameters and sample characterisation. See DOI: 10.1039/c8cp02738b

limits the use of rGO in aqueous applications.²⁹ However, deposition of rGO from water has been found to be effective in technological processing, from anti-corrosion layers^{30,31} to supercapacitors^{32,33} and batteries.^{34–37}

In spite of substantial research into the applications and chemistry of GO and rGO as adsorbent materials,^{6–8,22} a clear understanding of their physical behaviour and interactions with small molecules in solution has not been obtained. For instance, contention exists surrounding the interfacial properties and surface activity of GO and rGO, specifically on whether their behaviour is more akin to that of molecular surfactants or amphiphilic particles, with most works suggesting the former.^{9,20,28,38} Theoretical chemistry computations, including molecular dynamics, density functional theory and *ab initio*, have been performed on model systems of GO and rGO to assist in understanding their electronic structure, surface chemistry, and wettability.^{27,39–42} However, the relationship between these important aspects of GO and rGO chemistry, and the way that these materials interact with myriad organic and inorganic compounds, remains poorly characterised. Further investigation of aqueous GO and rGO dispersions with molecular additives and the key criteria for adsorption are thus required before the commercialisation and application of these materials in areas such as industrial wastewater treatment and oil recovery becomes viable.

In this work, we directly examine the response of aqueous suspensions of GO and rGO to a variety of carefully selected molecular surfactants and polymers. Using a combination of small and ultra-small-angle neutron scattering (SANS and USANS), we have monitored *in situ* the interactions and assembly of these compounds with the carbon nanomaterials at nano and microscopic length scales. The surfactant additives vary in terms of their head-group chemistry, in order to understand the effects of charge sign and hydrophilicity, and tail-groups to control hydrophobicity and saturation (to explore π – π -stacking effects with GO/rGO basal plane). Through this systematic variation, the effects of electrostatic, polarisation and hydrophobic (dispersion forces) interactions on the adsorption and co-assembly of the surfactants with both GO and rGO can be compared. Thus, we are able to gain insight into the fundamental physicochemical phenomena underpinning the behaviour and basis for GO and rGO as aqueous adsorbents, so that predictions can be made, and more effective deployment of these materials in industrial applications can be achieved.

2 Experimental

Materials

Graphene oxide was synthesised from graphite flakes (Sigma, +100 mesh) by the improved method of Marcano *et al.*²⁵ Minor modifications to the procedure included an incremental addition of the potassium permanganate prior to heating the mixture, and purification by 3 cycles of centrifugation (4000 rpm), redispersing the particles in ultrapure water only, followed by dialysis for 1 week (cellulose dialysis tubing, 12 800 Da molecular weight

cut-off, Sigma). The product was kept and characterised as an aqueous suspension. Reduction of the GO followed Li *et al.*,⁵ with the product also purified by dialysis in ultrapure water. Characterisation of these materials has been performed previously and can be found in the Electronic Supplementary Information of McCoy *et al.*⁴³

Cetyltrimethylammonium bromide (CTAB, $\geq 99\%$) was from ChemSupply and dodecyltrimethylammonium bromide (DTAB, $\geq 98\%$) and tetradecyltrimethylammonium bromide (TTAB, $\geq 98\%$) were from Sigma. Hexaethylene glycol monododecyl ether ($C_{12}E_6$), pentaethylene glycol monododecyl ether ($C_{12}E_5$) and tetraethylene glycol monododecyl ether ($C_{12}E_4$), all $\geq 98\%$, were from Sigma. Triton X-100 (TX-100, $\geq 98\%$) and sodium dodecyl sulphate (SDS, 90%) were from ChemSupply. Sodium bis(2-ethylhexyl) sulfosuccinate (AOT, 96%) was from ACROS Organics. Each of these surfactants were used as received with the exception of SDS which was recrystallised once from hot ethanol. Erucyl amidopropyl betaine (EAPB) and oleyl amidopropyl betaine (OAPB) were synthesised and purified as described previously.^{44–46} Polyethylene glycol or oxide (PEG, $M_v = 400\,000\text{ g mol}^{-1}$) and Pluronic F-127 were from Sigma.

Methods

Small-angle neutron scattering (SANS) measurements were undertaken on two instruments: D11 (Institut Laue-Langevin, Grenoble, France) and Bilby⁴⁷ (Australian Centre for Neutron Scattering, Lucas Heights, Australia). Samples were prepared using D_2O as the solvent and measured in 2 mm path-length Hellma cells at room temperature (25°C). The radially isotropic raw counts from the detectors were reduced to radially averaged absolute intensity profiles as a function of the scattering vector, q , defined as

$$q = \frac{4\pi}{\lambda} \sin \frac{\theta}{2}$$

where θ is the scattering angle and λ is the wavelength of the incident neutrons. Bilby is a time-of-flight SANS instrument, hence the instrument utilises a range of wavelengths, in this case $\lambda = 2\text{--}20\text{ \AA}$, to obtain spatiotemporal information about the sample. The main detector was positioned 6 m from the samples while the four curtain detectors were 3 m (left and right detectors) and 4 m (top and bottom detector), giving a q -range of approximately $0.002\text{--}0.6\text{ \AA}^{-1}$. In the process of reduction, the raw data were normalised against a transmission measurement and the background was corrected using a blocked beam measurement. Scaling for absolute intensities was achieved by accounting for the sample thickness (2 mm) and using an empty beam measurement. Scattering from an empty cell (for pure surfactant samples) or D_2O sample (for samples containing GO or rGO) was subtracted prior to modelling data. The D11 SANS instrument was used to obtain the scattering of the pure GO dispersions (ILL data citation: DOI: 10.5291/ILL-DATA.9-10-1309). For D11, two configurations were used with $\lambda = 10\text{ \AA}$, with a wavelength spread defined by $\Delta\lambda/\lambda = 9\%$, and sample-detector distances of 1.2 and 8 m, with a detector offset to provide a q -range of $0.003\text{--}0.387\text{ \AA}^{-1}$.

Ultra-small-angle neutron scattering (USANS) measurements were made using the Kookaburra beamline^{48,49} at the Australian Centre for Neutron Scattering, ANSTO. The instrument features a Bonse–Hart setup in which two parallel arrays of quintuple-reflection channel-cut silicon crystals serve to monochromate and analyse the beam.⁵⁰ A wavelength of 4.74 Å was used in these measurements and depending on run time, could obtain data over a q -range of 0.00005–0.005 Å^{−1} (0.1–10 μm length scales). Desmearing of the data was then performed using a specially developed Igor Pro package⁵¹ before stitching with the relevant SANS data.

Modelling of scattering data was performed using the software ‘SasView’ (<http://www.sasview.org>). In some instances when combining SANS and USANS, a scale factor was applied to the USANS data in order to align with the corresponding SANS data, made necessary by fluctuations in incident beam intensity and desmearing effects. For all data presented throughout, symbols represent the raw experimental scattering data, and solid lines are model fits generated as described in the text. Vertical error bars are present in all data sets, but in most instances are too small to see. All fitting parameters from the models are presented in the ESI,[†] including further details on the models themselves and modelling procedures.

Atomic force microscopy (AFM) was performed using a JPK NanoWizard 3. Imaging was carried out in AC mode with Bruker NCHV model cantilevers with spring constants of *ca.* 42 N m^{−1} and nominal resonant frequencies of *ca.* 340 kHz. Samples were prepared by spin-coating (60 s, 2000 rpm) approximately 3–5 μL of 0.1 mg mL^{−1} GO or rGO onto freshly cleaved mica disks (ProSciTech). For samples with polymer, the 0.1 mg mL^{−1} GO or rGO dispersions also included 0.1 or 0.5 mg mL^{−1} of PEG or Pluronic F127. Images were refined using the JPK Data Processing software and lateral dimensions for GO and rGO sheets were measured using Gwyddion (<http://gwyddion.net>).⁵²

3 Results and discussion

Graphene oxide and reduced graphene oxide

Small-angle scattering is not a commonly exploited technique for examining and characterising two-dimensional carbon nanomaterials. Small-angle X-ray scattering (SAXS) has been used to characterise graphite oxide (3D stack) prepared by various known methods,⁵³ however the low electron densities of the elements make analysing dilute solutions of graphene oxide (GO, single layer) difficult by SAXS, and the very low proportion of hydrogen (<2%)³ also offers poor contrast using SANS with solvent contrast variation. In all SANS data sets presented in this work, 0.1 mg mL^{−1} of GO or rGO is used, and the observed scattering from the carbon nanomaterials themselves in each case is minimal (Fig. 1a). Atomic force microscopy (AFM) imaging (in air) revealed monolayer nanosheets (*≈*1 nm thickness) for both GO and rGO (Fig. 1b–e), with average lateral sizes of 0.338 and 0.407 μm respectively (Fig. 1f and g). These materials are therefore within the length regime accessible to SANS and USANS (1 nm–10 μm). The wrinkling of rGO (Fig. 1c) is

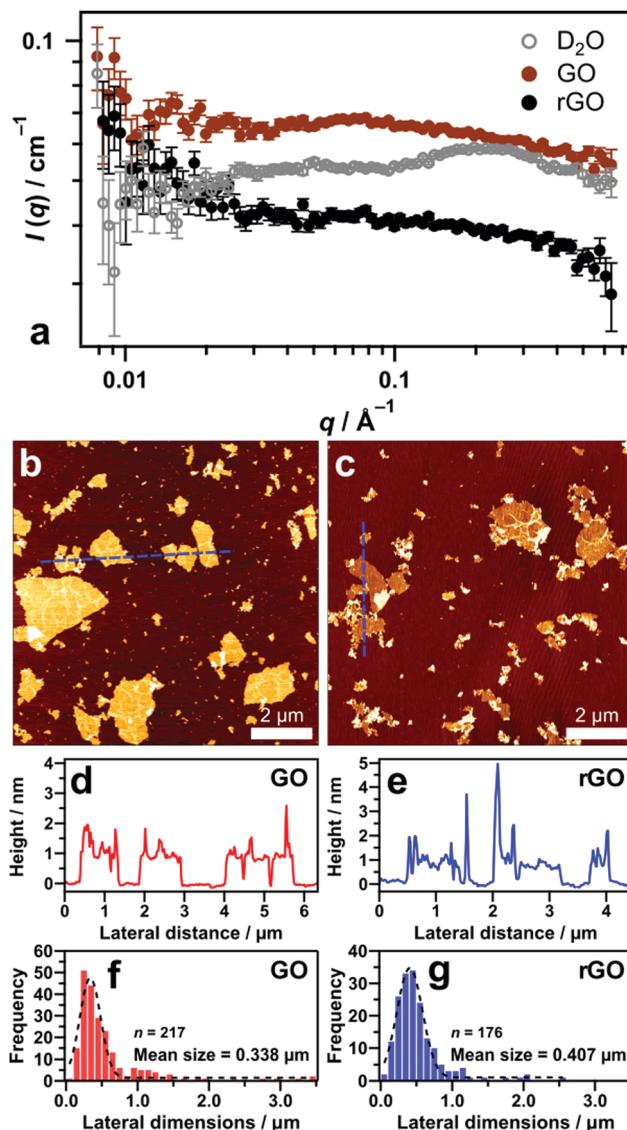


Fig. 1 (a) SANS data of 0.1 mg mL^{−1} GO and rGO following D₂O background subtractions. Note that the suspensions were diluted with D₂O from concentrated suspensions in H₂O. Hence, a D₂O background was subtracted from these data sets rather than an empty cell background, as the baseline scatter from GO and rGO samples were marginally higher due to containing approximately 3% H₂O. Data for D₂O has had scattering from an empty cell subtracted. Data for GO is offset by multiplication for clarity (*×*2). (b and c) AFM height images of GO and rGO dried on mica respectively. (d and e) Height profiles of GO and rGO respectively where each cross section corresponds to the dashed blue line on the image above. (f and g) Histograms of the lateral dimensions of GO and rGO sheets respectively. Data is binned to 100 nm and n is the total number of observations.

likely a result of the drying process for imaging. The increased hydrophobicity of rGO sheets causes them to fold and clump together through strong π – π -stacking interactions. Large clusters of rGO could also be observed in some regions of the AFM samples (see ESI,[†] Fig. S2).

In order to model the scattering for pure aqueous GO dispersions, a mass fractal model was employed (Fig. 2).⁵⁴ The mass fractal model approximates the scattering of spatially

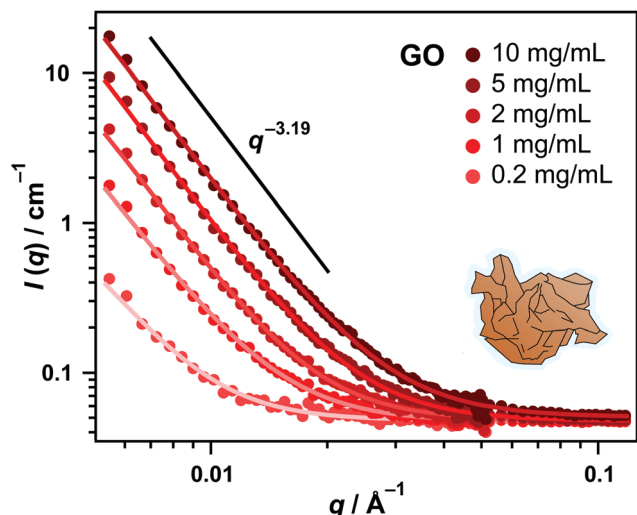


Fig. 2 SANS data of GO in D₂O at increasing concentrations. Symbols are raw data points and solid lines are the mass fractal model fits. Inset is the proposed 'crumpled' structure for GO sheet morphology in solution, as determined by the slope at low q .

inhomogeneous objects according to a power law, allowing determination of the fractal dimensionality D_m of the material. This provides a statistical index of how aggregated or structurally complex the material/assembly is over the measured length scale (higher fractal dimension corresponds to higher complexity).^{54,55} As carbon and oxygen have similar scattering length densities (6.65 and $5.80 \times 10^{-6} \text{ Å}^{-2}$ respectively) to that of D₂O ($6.34 \times 10^{-6} \text{ Å}^{-2}$), the scattering contrast for GO originates from the proportion of hydrogen which is only small in these materials (<2% by mass).³ Therefore, the hydrogen atoms serve as the scattering 'building blocks' or particle radius for the mass fractal structure, hence, this parameter is treated as negligible (see ESI† for fitting parameters). The modelling of the GO SANS data reveals mass fractal dimensions of approximately 2.8 (see ESI† Table S1), with the slopes at low q being around 3.2 (Fig. 2), indicating that the sheets have a semi-aggregated, crumpled morphology when dispersed on their own in aqueous solution.^{56–58}

As scattering from the GO sheets themselves becomes significantly greater at higher concentrations (Fig. 2), GO and rGO concentrations of 0.1 mg mL^{-1} were used in all subsequent measurements. In this case, scattering contrast for neutrons is thus expected to arise from the surfactant molecules added to the aqueous GO and rGO dispersions. The use of surfactants therefore not only gives insight into molecular interactions with these carbon nanomaterials for understanding adsorption, but also allows selective 'highlighting' of the sheets. Thus, their precise morphologies can be determined without convolution of the data from multiple scattering sources.

Interactions with cationic surfactants

Cationic magnetic surfactants have been shown to destabilise GO and form noncovalent magneto-responsive composites that can be used as recoverable materials in wastewater purification.⁵⁹ Likewise, a cationic photo-switchable surfactant can be used for

reversible, light-controllable separation and redispersion of rGO.⁴³ Cationic surfactants have also even been exploited to enhance the surface activity of GO sheets and facilitate their enrichment at interfaces,⁶⁰ resulting in improved capacity for emulsion stabilisation,⁶¹ and recovery by froth flotation.^{62,63} In all cases, the positively charged head-group ensures a strong electrostatic attraction with the negatively charged GO and rGO sheets, resulting in significant levels of adsorption. Therefore, we first explored the effects of cationic surfactants in aqueous dispersions of GO and rGO. For this, a classic and well characterised series of surfactants with trimethylammonium head-groups was chosen: cetyltrimethylammonium bromide (hexadecyltrimethylammonium bromide, CTAB), tetradecyltrimethylammonium bromide (TTAB) and dodecyltrimethylammonium bromide (DTAB). The lengths of the alkyl chains vary from 16, 14 and 12 carbons respectively (Fig. 4d), so that the hydrophobic contribution to the molecular interactions could also be assessed.

As cationic surfactants bear an opposing charge to GO and rGO sheets in solution, there is a propensity for the carbon materials to flocculate within a specific range of carbon nanomaterial : surfactant ratios due to reduction in magnitude of the interparticle repulsive forces.^{43,61} SANS measurements *in situ* may be ineffective or misleading when used on unstable or inhomogeneous systems. Therefore it was necessary to map the stability of the colloidal suspension across a broad range of concentration ratios to uncover where the system was stable/unstable, and thus determine which sample compositions were suitable for analysis by SANS.

Stability phase diagrams for DTAB, TTAB and CTAB with GO were determined (Fig. 3) in which a total of 20 different sample compositions were assessed for each surfactant (see ESI† Fig. S4–S6). Samples were deemed stable if no aggregation could be observed, metastable if partial aggregation and sedimentation over 24 hours could be observed, and unstable if the GO was completely flocculated (Fig. 3a). Depending on the surfactant, the initial onset of GO aggregation with increasing surfactant loading was found to occur at lower surfactant concentrations with increasing tail-group length (Fig. 3b–d, CTAB < TTAB < DTAB). This effect is likely due to the higher surface activity associated with the longer tail-groups causing adsorption onto the GO surfaces and subsequent destabilisation to occur more readily. In turn, colloidal restabilisation of the GO was also found to occur at lower surfactant concentrations for the longer chain molecules (Fig. 3b–d). Stability of the GO at increased surfactant loadings can be attributed to charge reversal of the sheets from adsorbed cationic surfactant, such that the materials are now stabilised through positive charge repulsions.⁶¹ As CTAB is more surface active than TTAB and DTAB, larger quantities adsorb to the GO sheets, hence the restabilisation effect is observed at lower surfactant concentrations with increasing tail-group length. The same can be said for TTAB when compared to DTAB. Interestingly, this effect also appears to coincide with the critical micelle concentrations (CMC) for each surfactant (see ESI† Fig. S3),^{64,65} reaffirming that the behaviour is a hydrophobic phenomenon. The phase behaviour indicates that hydrophobic

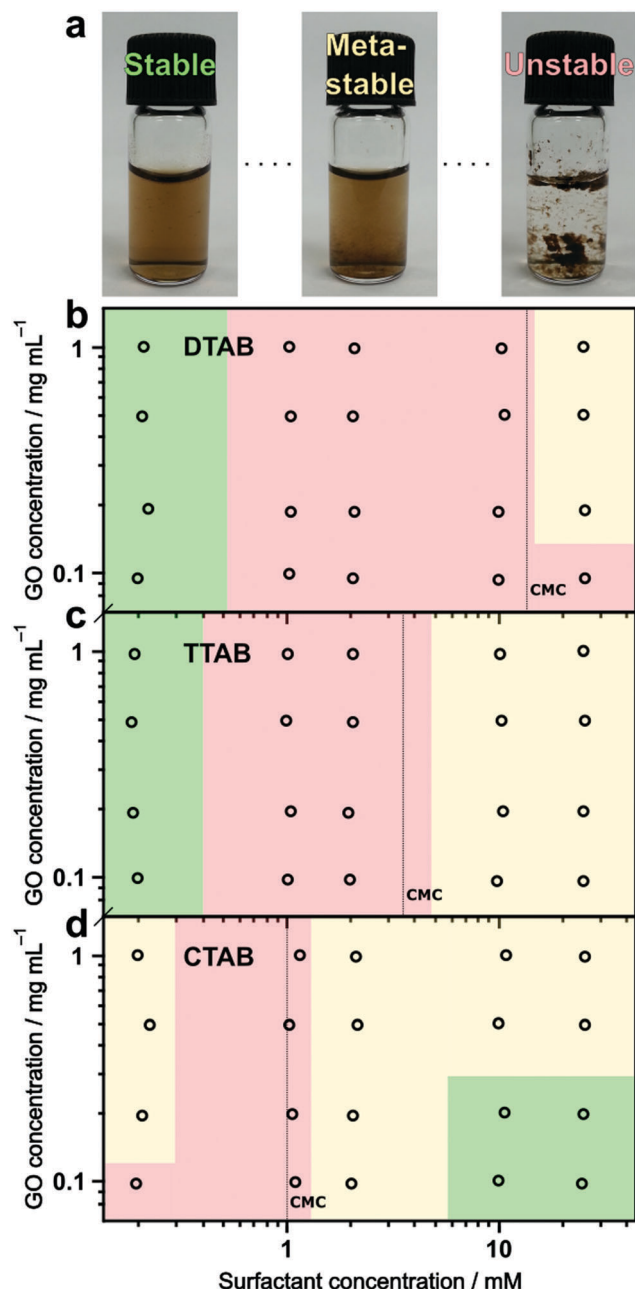


Fig. 3 (a) Samples of TTAB and GO with phase behaviour specified as stable, metastable and unstable. (b–d) Stability phase diagrams of aqueous graphene oxide dispersions with DTAB (b), TTAB (c) and CTAB (d). The green regions signify stable systems, while the yellow and red regions represent metastable (partially flocculated) and unstable (flocculated) systems. The circles signify specific individual samples (see ESI,† Fig. S4–S6) from which the borders between phases were estimated. The vertical dashed lines mark the approximate critical micelle concentrations (CMC) for each surfactant as determined from surface tension measurements (see ESI,† Fig. S3).

interactions (dispersion forces) also play a significant role in adsorption and interactions within these systems, and that charge is not the only factor governing the bulk and interfacial properties of GO in the presence of adsorbing molecules.

With these effects in mind, high DTAB, TTAB and CTAB concentrations (25 mM) were used with GO and rGO to ensure

that the samples remained stable for SANS. Samples with DTAB and TTAB at this concentration were regarded as metastable (Fig. 3b and c), however the sedimentation of the materials was slow enough that scattering measurements were still possible. SANS measurements from pure 25 mM solutions of DTAB, TTAB and CTAB (*i.e.* with no GO/rGO present), can be accurately modelled using an ellipsoid model⁶⁶ with Hayter–Penfold structure factor (Fig. 4a).^{67–71} The fitting yields equatorial radii of 1.7, 2.0 and 2.3 nm, and axial radii of 2.7, 3.2 and 3.8 nm for DTAB, TTAB and CTAB respectively (see ESI,† Table S3), concordant with literature values.⁷² The increases in micellar radii are due to the lengths of the surfactant tails,⁷³ and the greater structure factor contributions for CTAB and TTAB (peaks at medium q , 0.03 Å⁻¹) can be attributed to the larger volume fractions of micelles which will form more readily and at lower concentrations for these surfactants than DTAB (see ESI,† for details, Table S3).

When GO and rGO are incorporated with these surfactants (Fig. 4b and c), substantial differences in scattering in the low q region (0.003–0.02 Å⁻¹) can be observed compared to the pure surfactant solutions (Fig. 4a). As q is an inverse length scale, scattering at lower q values corresponds to larger objects, which in the context of these systems must be the GO and rGO sheets. This is a very clear indication of strong interaction between the surfactant molecules and carbon nanomaterials, as the scattering from the sheets themselves was found to be negligible at 0.1 mg mL⁻¹ (Fig. 1a). Furthermore, the scattering at low q conforms to a q^{-2} trend, which is indicative of scattering from flat, planar structures.^{74,75} Note that this is not seen in the scattering of pure GO dispersions at any concentration (Fig. 2), indicating that the surfactant has changed the sheet morphology. As this trend continues even through the USANS region (Fig. 4f), it is possible that the surfactants are serving to ‘flatten’ the sheets and render them rigid, as crumpling of the sheets would result in an increase in the fractal dimension, and a low q slope greater than q^{-2} , as was shown in Fig. 2. This phenomenon is dubbed ‘nano-ironing’ and could be useful in coatings or deposition applications where full exploitation of the GO and rGO surface area would be beneficial.

To model the scattering when both GO/rGO and surfactant are present, the same mass fractal model was employed to define the scattering in the low q regions.⁵⁴ Given that the scattering contrast in these systems is from the surfactant molecules, they will serve as the ‘building blocks’ for the mass fractal structure, and as their adsorption on the sheets will essentially be in a random arrangement, the mass fractal model is again an ideal representation for the GO and rGO sheet morphology. This has been used previously for similar GO/rGO systems with cationic photosurfactants.⁴³ At 25 mM however (Fig. 4b and c), the background concentration of micelles is still significant, therefore the model for the micelles must be included in the fitting algorithm to accurately fit the medium q region. Therefore the summation model (a step-wise addition of the fractal and micelle models) was used to produce the final fits for these systems (see ESI,† for more detail, Fig. S7). A final important consideration when modelling these data is the

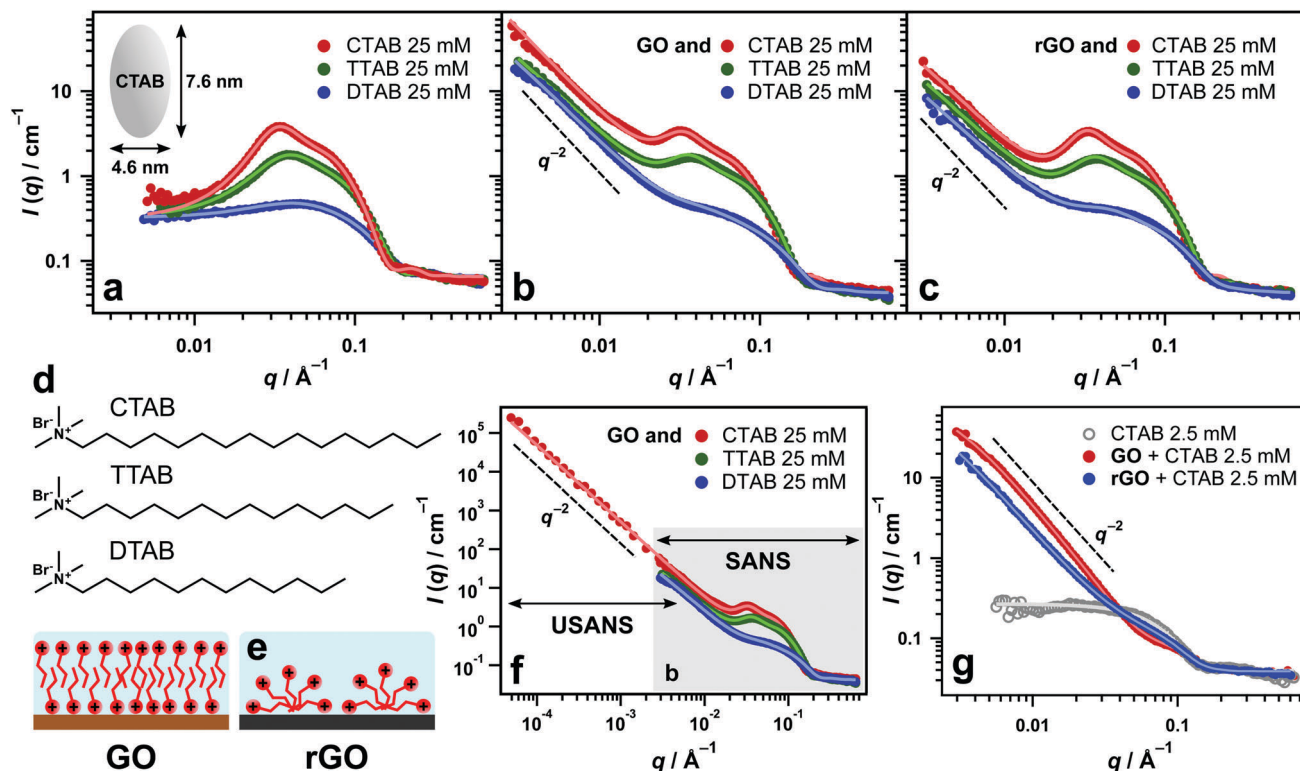


Fig. 4 (a–c) SANS data of DTAB, TTAB and CTAB surfactants at 25 mM without carbon nanomaterial present (a), and also with GO (b) and rGO (c). Concentrations for all carbon nanomaterials were 0.1 mg mL^{-1} . The inset in (a) represents a meridional cross-section of the CTAB micelles as determined from the fitting parameters. (d) Chemical structures of DTAB, TTAB and CTAB. (e) Schematics of cationic surfactant adsorption on GO and rGO. Bromide anions have been omitted for simplicity. (f) Inclusion of USANS region to GO/CTAB data in b (shaded area). (g) SANS data of 2.5 mM CTAB with GO and rGO.

charge contribution to the scattering from the sheets themselves. As GO and rGO are highly charged, a structure factor contribution arising from interactions between sheets and micelles could be expected. However at GO and rGO concentrations of 0.1 mg mL^{-1} (0.01 wt%), the volume fraction of the sheets is so low that this effect can be regarded as negligible.

Comparing the scattering of the individual surfactants with GO and rGO, higher scattering intensities are observed in the low q region as the length of the surfactant tail is increased (Fig. 4b and c). This observation concurs with the phase behaviour in Fig. 3, indicating that hydrophobicity influences the partitioning of the surfactants between the bulk aqueous phase and the sheet surfaces. Interestingly, when rGO is used, the overall scattering intensity in the fractal region is lower when compared to that of GO (Fig. 4b and c). This suggests that despite hydrophobicity of the surfactants serving to promote adsorption, a stronger affinity exists for GO than rGO, implying that electrostatic and dipole interactions are more significant for adsorption than hydrophobic interactions, as GO is more strongly charged and has a much greater proportion of oxygen-containing functional groups than rGO.^{5,26} This may also relate to the nature of the surfactant adsorption on both carbon nanomaterials. For GO it is possible that the surfactants are adsorbing *via* their head-groups with the tails protruding into solution. As this would unfavourably result in the tail-groups being exposed to the bulk aqueous solution, another monolayer

of surfactant adsorbs with the head-groups now on the exterior of the structure to overcome the reorganisational entropy of water, collectively resulting in a surfactant bilayer on the surfaces of the GO sheets (Fig. 4e). Conversely for rGO, because it is hydrophobic, the surfactants most likely adsorb flat on the surfaces of the sheets, resulting in adsorbed hemispherical micelles (Fig. 4e). The adsorption mechanisms cannot be explicitly determined from the scattering data, however, the precedent for this theory has been asserted in many adsorption studies and reviews on quaternary ammonium surfactants at aqueous solid-liquid interfaces.^{76–80} Therefore, a larger amount of surfactant molecules would be adsorbing to GO, resulting in greater scatter. The fractal dimensions for the rGO systems are also lower (< 2) than the corresponding GO samples (see ESI,† Table S3), further emphasising that the interactions are weaker with rGO. It is therefore likely that GO could be superior to rGO as an aqueous adsorbent, even for certain hydrophobic materials. Similar behaviour for GO and CTAB has been predicted previously by small-angle X-ray scattering.⁸¹ In all cases, the bromide counter-ions are likely to be within the vicinity of the surfactant head-groups either as undissociated moieties or as loosely bound counter-ions.⁸² Hence, their contribution to the assembly and thus scattering, is expected to be minimal.

Reducing the surfactant concentration to 2.5 mM, DTAB and TTAB destabilised GO and rGO, however CTAB mixtures were stable (Fig. 3b–d). At the lower concentration, the structure

factor contribution from the CTAB micelles becomes negligible due to the lesser volume fraction (Fig. 4g), and they can be modelled with a simple ellipsoid model (see ESI,† Table S4). Without obstruction from the large structure factor peak, the effects of the GO and rGO sheets become clearer, and it can be seen that scattering with a continuous slope of q^{-2} through medium q is apparent (Fig. 4g). The presence of the sheets results in depletion of the surfactants available for micellisation, and adsorption instead occurs along the flat, rigid GO/rGO surfaces. Again, the intensity through the low q region is higher for the GO/CTAB system than the rGO/CTAB system, showing stronger adsorption to the GO. The small shoulders around 0.07 \AA^{-1} are due to a low concentration of CTAB micelles in each mixture. Unfortunately, even at 2.5 mM CTAB, the presence of a non-negligible number of background micelles in the GO and rGO/CTAB mixtures means that a lamellar model could not be reliably employed to determine the thickness of the aggregates (see ESI,† for further explanation, Fig. S8), and the hypothesised adsorption mechanism in the two systems is therefore still only speculative at this stage.

Interactions with anionic surfactants

Similarly to the cationic surfactants analysed, sodium dodecyl sulphate (SDS) and sodium bis(2-ethylhexyl) sulfosuccinate or Aerosol-OT (AOT) form ellipsoidal micelles, with large Hayter-Penfold structure factor peaks being caused by the overall charge of the aggregates. Hence, data for SDS and AOT were modelled similarly (see ESI†). However being anionic, SDS and AOT exhibit the same surface charge as GO and rGO and hence, are likely to experience charge-based repulsions from the sheets. Modelling the SANS data for pure SDS and AOT at 25 mM (Fig. 5a) gave equatorial radii of 1.8 and 1.2 nm, and axial radii of 2.7 and 2.6 nm respectively (see ESI,† Table S5), similar to literature values.^{83–85} The shorter tail-lengths of AOT account for the lower equatorial radius of the micelles.

The equivalent SANS patterns with GO and rGO included show very little difference in the scattering to those of the blank micelles (Fig. 5b and c). Modelling these data was achieved using very similar fitting parameters (see ESI,† Table S5),

indicating that the micellar compositions of the samples did not notably change with the addition of GO or rGO. Therefore, little to none of the surfactant molecules are apparently adsorbed to the sheets, and are instead forming bulk micelles. The effect of same charge repulsion is likely the overriding factor dictating system behaviour here, as the surfactants could potentially adsorb to the sheets *via* hydrophobic interactions through their tail-groups, however the scattering suggests that the apparent adsorption is minimal, indicating that surface charge is the more dominant force. As charge interactions are longer in range,⁸⁶ this is to be expected. Small increases in scattering intensity are observable in the low q region for the GO and rGO samples with both surfactants (Fig. 5b and c), meaning that perhaps very small quantities of surfactant are adsorbing. This small effect appears larger in magnitude for AOT than SDS, which could be due to AOT having a higher surface activity. Note that the scattering at low q increases appreciably for pure 25 mM AOT (Fig. 5a). The maximum aqueous solubility of AOT at room temperature is approximately 44 mM,⁸⁵ therefore this increase is likely due to critical scatter from inter-micellar attractions/clustering.

It is also important to note that sulfonate groups have substantial solvation shells allowing them to interact with water very strongly.^{87,88} Therefore, SDS and AOT micelles may be further stabilised against disaggregation by their hydration from the bulk water, further inhibiting their adsorption to the GO and rGO surfaces. The lack of adsorption is thus, likely a culmination of charge repulsion and strong solvation effects. As with bromide in the case of the cationic surfactants, the dissociated sodium counter-ions are presumed to form an equilibrium between full solvation in the bulk water and weak electrostatic interactions with the SDS/AOT micelles and GO/rGO sheets. Hence, their influence in these systems is likely to be insignificant.

Interactions with nonionic surfactants

When considering nonionic surfactants, the head-groups are uncharged, so the effects of charge-based interactions with GO and rGO become negligible. Hence, samples were found to be

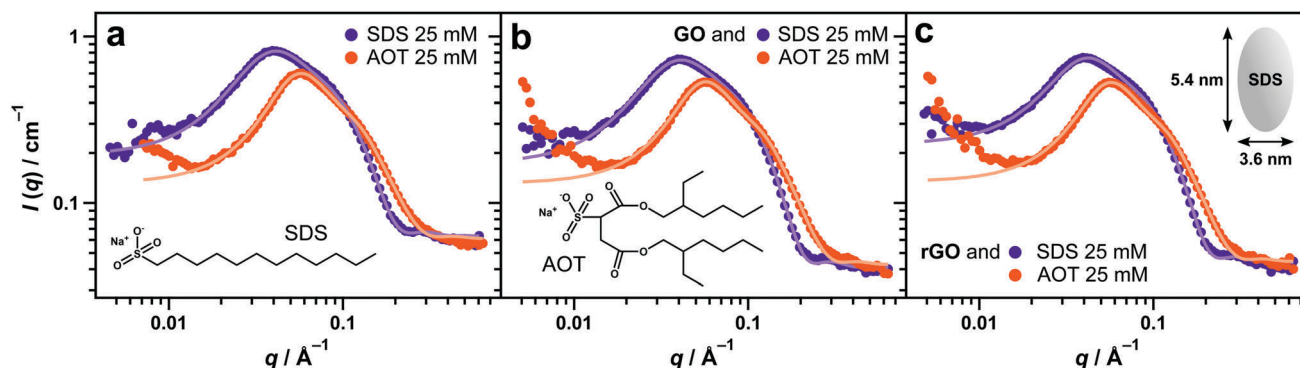


Fig. 5 SANS data for SDS and AOT surfactants at 25 mM without carbon nanomaterial present (a) and with GO (b) and rGO (c). Concentrations for all carbon nanomaterials were 0.1 mg mL^{-1} . Insets in (a) and (b) are the chemical structures for both surfactants. The inset in (c) represents the meridional cross-section of the SDS micelles as determined from the fitting parameters.

stable irrespective of the surfactant loadings. Triton X-100 (TX-100) is a well-known and widely utilised nonionic surfactant with a distribution of 1–20 ethylene oxide units in the head-group where the mean ethylene oxide number is 9.5, and a phenyl ring and branching in the tail-group (Fig. 6c, inset). In water at 10 mM, TX-100 forms squat cylindrical micelles (Fig. 6a) approximately 8.8 nm in length and 2.1 nm in radius (see ESI,† Table S6). At the same concentration with GO and rGO present, the form factor of the TX-100 micelles is still prevalent, indicating a high presence of background micelles remaining in the system. Modelling of these systems was therefore achieved using an additive fit of cylinder and mass fractal models (see ESI†). As with the cationic surfactants, an increase in scattering at low q is observed (Fig. 6b). This result can again be interpreted as surfactant adsorption to the sheets, as when reducing the concentration of TX-100 from 10 mM to 1 mM, where the micellar contribution to the scattering is significantly lower, a clear, unmasked increase in scattering intensity for the systems with GO and rGO can be seen even in the medium q region (Fig. 6c). The scattering slopes conform to q^{-2} , again indicating scattering from flat surfaces (*i.e.* the GO and rGO sheets). The trend continues into the USANS region indicating large structures, with an additional increase in slope order to q^{-3} at ultra-low q , most likely from surfactant critical scatter (Fig. 6a).

Interestingly, there are very few differences in scattering when using GO *versus* rGO with TX-100 (Fig. 6b and c). TX-100 has an aromatic phenyl ring, therefore it is likely to experience strong π -stacking interactions with rGO due to the large restoration of the aromaticity of the basal plane from the reduction process.⁵ The π -stacking interactions with GO will be comparatively weak, however the polarisation interactions between the TX-100 head-group and GO is much stronger than for rGO. Consequently, summing the overall interactions for both materials could result in the net surfactant adsorption reaching similar levels, accounting for the lack of difference in scattering for the two materials with TX-100. It is also possible that for both materials, adsorption is dominated by head-groups interactions, and as TX-100 is polydisperse, occurs according to the preferred

head-group lengths (*i.e.* molecules with shorter ethylene oxide chains adsorb to rGO and those with longer chains adsorb to GO).

Therefore, to more systematically investigate the interactions of nonionic surfactants with GO and rGO, SANS was used to examine systems in which monodisperse C_nE_m surfactants were used. These surfactants have a specific number (m) of ethylene oxide units for the head-group and a specific number of carbon atoms (n) in their tail-group. For these measurements, three C_nE_m surfactants were chosen: hexaethylene glycol monododecyl ether ($C_{12}E_6$), pentaethylene glycol monododecyl ether ($C_{12}E_5$) and tetraethylene glycol monododecyl ether ($C_{12}E_4$) (Fig. 7a). The tail-group length (12 carbons) is the same for all three molecules, however the number of ethylene glycol units varies by one, significantly altering the hydrophilicity across the series.

The most hydrophilic surfactant of this series, $C_{12}E_6$, was found to form cylindrical micelles (Fig. 7b), with an average radius of 2.1 nm and length of 10.6 nm (see ESI,† Table S7), concurrent with literature SANS values.^{89,90} $C_{12}E_5$ was found to form long, flexible cylinders (or worms) (Fig. 7c),⁹¹ 2.1 nm in radius and $C_{12}E_4$ formed vesicles (Fig. 7d),⁹² with average radii of 25.2 nm at 10 mM and 38.3 nm at 1 mM (see ESI,† Table S12). The sharper form factor resolution for $C_{12}E_4$ at 1 mM compared to that at 10 mM is due to the difference in polydispersity for the vesicle radii of each mixture, which were 27.8 and 36.5% respectively (see ESI,† Table S12). Given that the micelle morphologies and scattering intensities vary so drastically for each of these surfactants, it is difficult to draw clear distinctions between the adsorption and interactions with GO and rGO when altering the surfactant chemistry. However, for these surfactants, significant differences are evident when comparing the scattering of mixtures with GO against mixtures with rGO, an effect which was not observed for TX-100 (Fig. 6).

At 10 mM, $C_{12}E_6$ exhibits similar scattering with GO and rGO to that of TX-100, where there appears to be a high concentration of background cylindrical micelles, and an increase in intensity at low q due to surfactant adsorbed to the sheets (Fig. 7b). However unlike TX-100, noticeably higher scattering occurs in the low q region for the GO system than the rGO system.

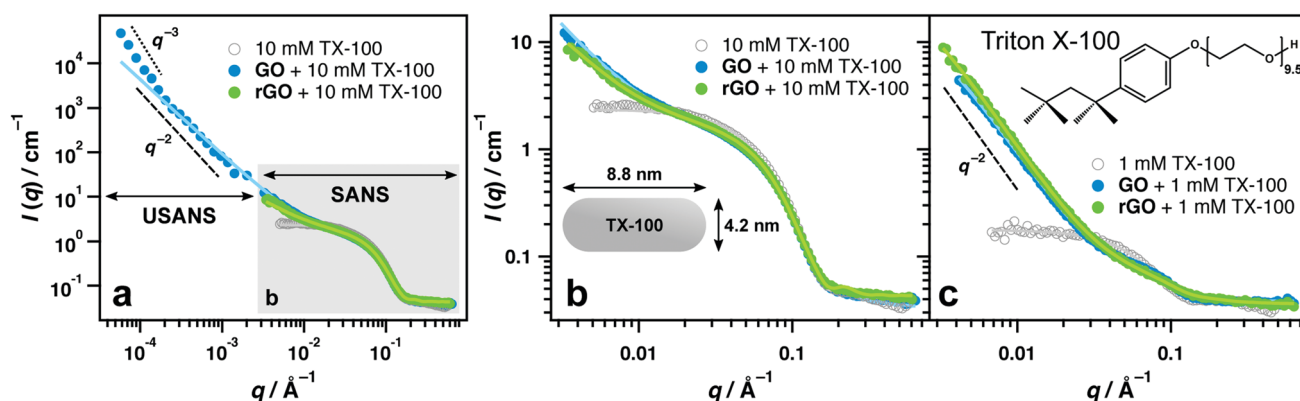


Fig. 6 (a) SANS and USANS data of blank 10 mM TX-100 and 10 mM TX-100 with GO and rGO. (b) SANS region of the data represented by the shaded area in a. (c) Blank 1 mM TX-100 and 1 mM TX-100 with GO and rGO. The inset in (b) represents the meridional cross-section of the TX-100 cylindrical micelles as determined from the fitting parameters. Concentrations for all carbon nanomaterials were 0.1 mg mL⁻¹.

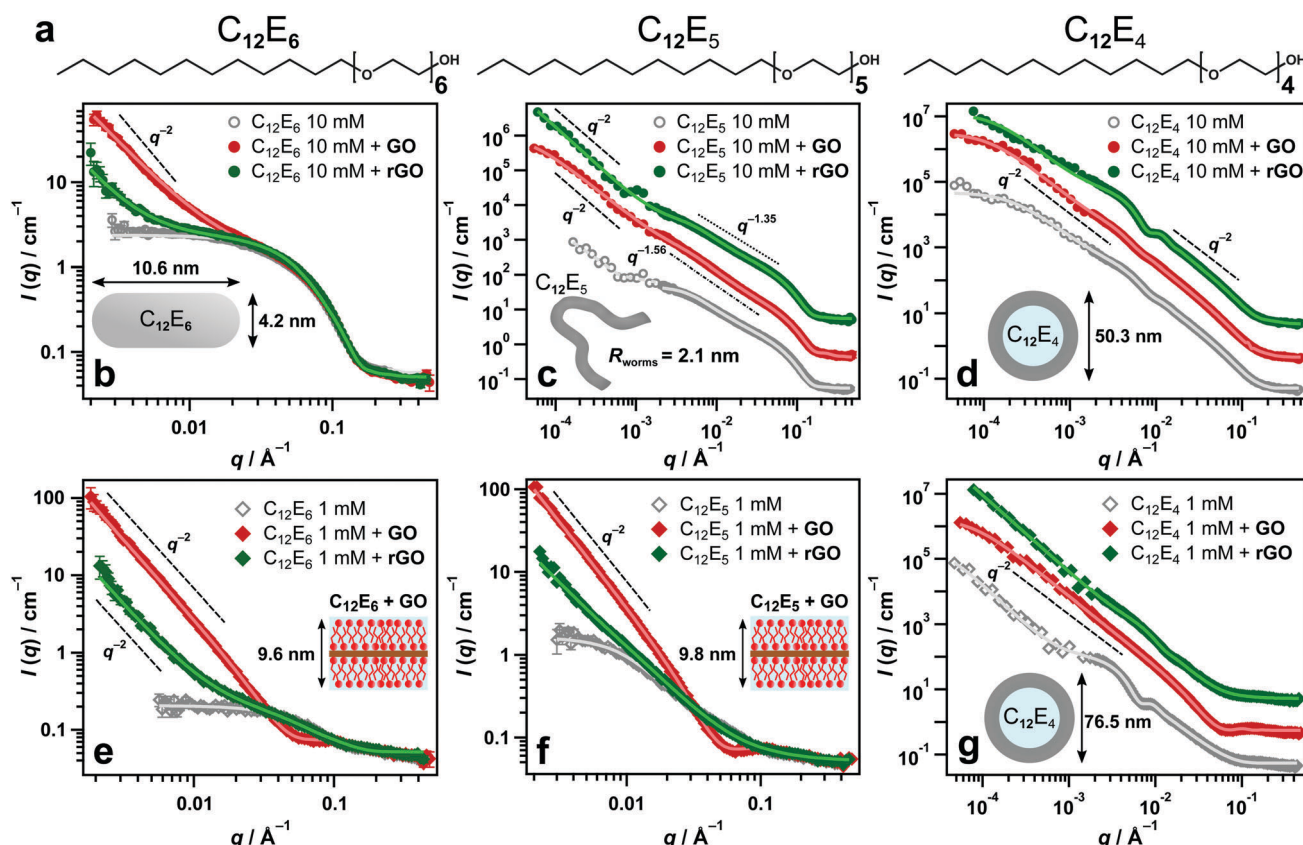


Fig. 7 (a) Chemical structures of $C_{12}E_6$, $C_{12}E_5$ and $C_{12}E_4$. (b–d) SANS data of $C_{12}E_6$, $C_{12}E_5$ and $C_{12}E_4$ surfactants (respectively) at 10 mM with and without GO and rGO (b). (e–g) SANS data of $C_{12}E_6$, $C_{12}E_5$ and $C_{12}E_4$ surfactants (respectively) at 1 mM with and without GO and rGO (b). The data in (c), (d) and (g) include the USANS region. Concentrations for all carbon nanomaterials were 0.1 mg mL^{-1} . The insets in (b), (c), (d) and (g) represent the blank micelle structures for each surfactant as determined from the fitting parameters while the insets in (e) and (f) are schematics for the lamellar aggregates of the GO/surfactant systems as determined from the fitting. Data in figures (c), (d) and (g) have been offset by multiplication for clarity: $\times 10$ for GO data and $\times 100$ for rGO data.

There is therefore a significantly greater amount of $C_{12}E_6$ adsorbed to GO than rGO, suggesting that as with the cationic surfactants, polarisation interactions contribute more strongly to the adsorption of these molecules than do the hydrophobic (dispersion) interactions from the surfactant tail-groups. This effect would also be thermodynamically driven by freeing water entropy associated with the unfavourable solvation of hydrocarbons^{93,94} (*i.e.* the surfactant tails and exclusive carbon domains of the GO and rGO, which are more substantial for rGO). Reducing the concentration of $C_{12}E_6$ to 1 mM, the difference in scattering becomes even more marked, as the system with rGO appears to conform to the same form factor as the blank micelle sample at medium q values, whereas the system with GO has a very different shape, sharply increasing in intensity at q values below 0.05 \AA^{-1} (Fig. 7b). The low q scattering in all instances again follows a slope of q^{-2} , highlighting the flattened, sheet-like structure of the GO and rGO nanosheets. This again reinforces that the surfactants are acting to flatten the sheets, which is not observed in the naked GO and rGO dispersions (see ESI,† Table S7). When using 1 mM $C_{12}E_5$, the overall scattering is very similar to that of $C_{12}E_6$, with higher adsorption occurring on GO than rGO (Fig. 7f).

Changes in hydrophobicity therefore have little impact on molecular interactions of nonionics with GO or rGO. These findings also reinforce the clear significance of the π -stacking interaction in the case of TX-100 with rGO. At 10 mM $C_{12}E_5$, the scattering from the blank micelles was so large that it obscured the data with GO and rGO, even in the low q region, hence it is difficult to draw clear conclusions from the raw scattering. However, modelling the GO and rGO systems with 10 mM $C_{12}E_5$ revealed a scattering medium q slope for GO ($q^{-1.56}$) than rGO ($q^{-1.35}$). As this is the length scale in which wormlike micelles appear to be locally cylindrical (q^{-1}),⁹⁵ these power laws suggest greater deviation from the wormlike structure in the GO system, which would occur if $C_{12}E_5$ adsorption was occurring more readily to GO than rGO.

The enormous difference in surfactant adsorption on GO *versus* rGO can again be justified by the proposed packing mechanism for the surfactants on each surface (first described in the cationic section, Fig. 4e). As rGO represents a more hydrophobic interface, it is feasible to presume the surfactants may lie flat on the surfaces of the sheets to balance hydrophobic interactions with van der Waals forces and free water entropy.⁹⁴ Conversely, because GO is predominantly hydrophilic, the

surfactants are likely to be adsorbing primarily *via* their polar head-groups, allowing for a much denser packing arrangement in the form of surfactant bilayers.^{96,97} This hypothesis is supported further by modelling the results for C₁₂E₆ and C₁₂E₅ at 1 mM with GO and rGO (see ESI†, Tables S8 and S11). In the cases with GO, the background micelle concentrations are clearly tiny, therefore modelling these data using exclusively a lamellar model becomes possible because there is now a well-defined upturn in the sample scattering in line with the background scattering (high q , 0.2–0.4 Å⁻¹). The lamellar model allows determination of the average thicknesses of the aggregates based on this upturn,⁷⁴ which for GO/C₁₂E₆ and GO/C₁₂E₅ were found to be 9.6 and 9.8 nm respectively (Fig. 7e and f). These thicknesses are much greater than the 1 nm thickness for GO sheets confirmed by AFM (Fig. 1b and d), and given that the molecular length for C₁₂E₆ is approximately 3.9 nm,⁹⁸ suggests a structure comprised of a GO sheet sandwiched between two surfactant bilayers, with significant overlap occurring between the tail-group regions (Fig. 7e and f insets). The lack of any Bragg peaks corresponding to bilayer spacings also indicates that these aggregates contain only a single sheet, and are thus, not multiply stacked. However, stacking of this nature may be possible at higher loadings of GO, and is also more credible for nonionic surfactants due to the absence of electrostatic repulsions, which would occur in the cases of the cationic surfactants. In the equivalent cases with rGO, the amount of surfactant forming micelles is apparently still too high to allow meaningful use of the lamellar model (Fig. 7e and f), and were therefore fit with additive models of micelles and mass fractals (see ESI†). This also concurs with the hypothesis for surfactant adsorption mechanism, as if the surfactants adsorbed lying down on the rGO surfaces to form hemispherical micelles (Fig. 4e), the amount of surfactant adsorbed would be much lower and the scattering would be weaker, as is evident. In addition, subsequent stacking between multiple rGO sheets as is predicted for GO, would be geometrically unfavourable.

Lastly in the C_nE_m series, the interactions of C₁₂E₄ with GO and rGO were analysed by SANS (Fig. 7d and g). C₁₂E₄ is known to form large multilamellar vesicles,^{92,99} and therefore the scattering from these mixtures was very strong, even for the pure surfactant samples. Hence, clear differences in the intensity of the scattering for these systems are difficult to interpret unambiguously. However, differences in the scattering form factors are apparent and give some physical insight into the interactions. These data, including the blank surfactants (which likely contain a mixture of vesicles, evidenced by the SANS data, and lamellae, evidenced by the USANS data),^{100,101} were modelled using the addition of mass fractal and vesicle models (see ESI†). At 10 mM C₁₂E₄, the pure surfactant solution has only a subtle vesicle form factor due to a high degree of polydispersity in the radius of the vesicles (see ESI†). However, with rGO incorporated in the system, the polydispersity decreases significantly from 36.5% to 22.4%, resulting in a much sharper peak at 0.01 Å⁻¹ (Fig. 7d). This effect is interpreted as a depletion in the amount of surfactant available for micellisation due to adsorption on the rGO sheets, as decreasing the

concentration of the pure C₁₂E₄ solution to 1 mM also resulted in a much more well-defined vesicle form factor (Fig. 7g). For GO with C₁₂E₄ at 10 mM (Fig. 7d), the co-assembly of the surfactants and sheets may also be resulting in stacked bilayers as was inferred for GO with C₁₂E₆ and C₁₂E₅. In this case, the aggregates may dominate the scattering, masking the form factor for the vesicles.

At 1 mM C₁₂E₄, the clear vesicle form factor observed in the pure surfactant solution is almost totally lost when GO and rGO are added, indicating adsorption of the majority of surfactant molecules onto the sheets (Fig. 7g). However, the vesicle form factor is still slightly apparent in the rGO scattering, but not in the GO scattering, suggesting that a larger proportion of molecules are adsorbing in the case of GO. This is an interesting result, as the hydrophilicity of C₁₂E₄ is significantly lower than that of C₁₂E₆ and C₁₂E₅. However, the effect of dipole interactions and packing arrangement on the sheet surfaces still appear to be more significant contributors to adsorption than surfactant hydrophobicity. Scattering again conforms to a slope of q^{-2} , indicating flat surfaces (Fig. 7g). Nonionic surfactants may therefore offer useful alternatives for GO and rGO ‘nano-ironing’, as well as the spontaneous assembly of lamellar liquid crystals based on carbon nanomaterials which may be useful in optical applications and nano-templating.

Interactions with zwitterionic surfactants

Zwitterionic surfactants also have an overall charge of zero, however unlike nonionic surfactants, there are formal charge groups associated with the surfactant heads. Erucyl amidopropyl betaine (EAPB) and oleyl amidopropyl betaine (OAPB) are environmentally friendly zwitterionic surfactants that have 22 and 18 carbons in their alkyl chains respectively (Fig. 8a).^{46,95} These types of surfactants form complex fluids, stemming from their ability to spontaneously self-assemble into viscoelastic wormlike micelles,⁹⁵ and hence are commonly used in personal care products also because of their biocompatibility.¹⁰² SANS data from the pure, 10 mM surfactant solutions (Fig. 8b) were thus fit using a flexible cylinder model,^{103,104} revealing ‘worm’ radii of 2.9 and 2.2 nm for EAPB and OAPB respectively (see ESI†, Table S13). The higher surface activity of EAPB from the longer tail-group results in a lower CMC, and hence, a higher volume fraction of worms compared to OAPB. Therefore, scattering intensity is greater for EAPB (Fig. 8b). Furthermore, the larger scattering volume/cross-section of the C22 chain would also significantly contribute to the greater intensity.

The one-dimensional elongation of wormlike micelles results in a low q scattering slope of q^{-1} for the pure surfactant solutions (Fig. 8b).⁶⁶ However, with GO and rGO added, the low q slope in all cases becomes approximately q^{-2} (Fig. 8c and d), indicating the wormlike system has evolved to a planar morphology. Therefore, as in the previous instances with cationic and nonionic surfactants, it appears that the zwitterionic betaine surfactants also have a high affinity for the sheet-like materials, and are adsorbing to the planar faces of the GO and rGO. The trend continues well into the USANS region (Fig. 8e), showing continuous aggregation of the surfactants on the

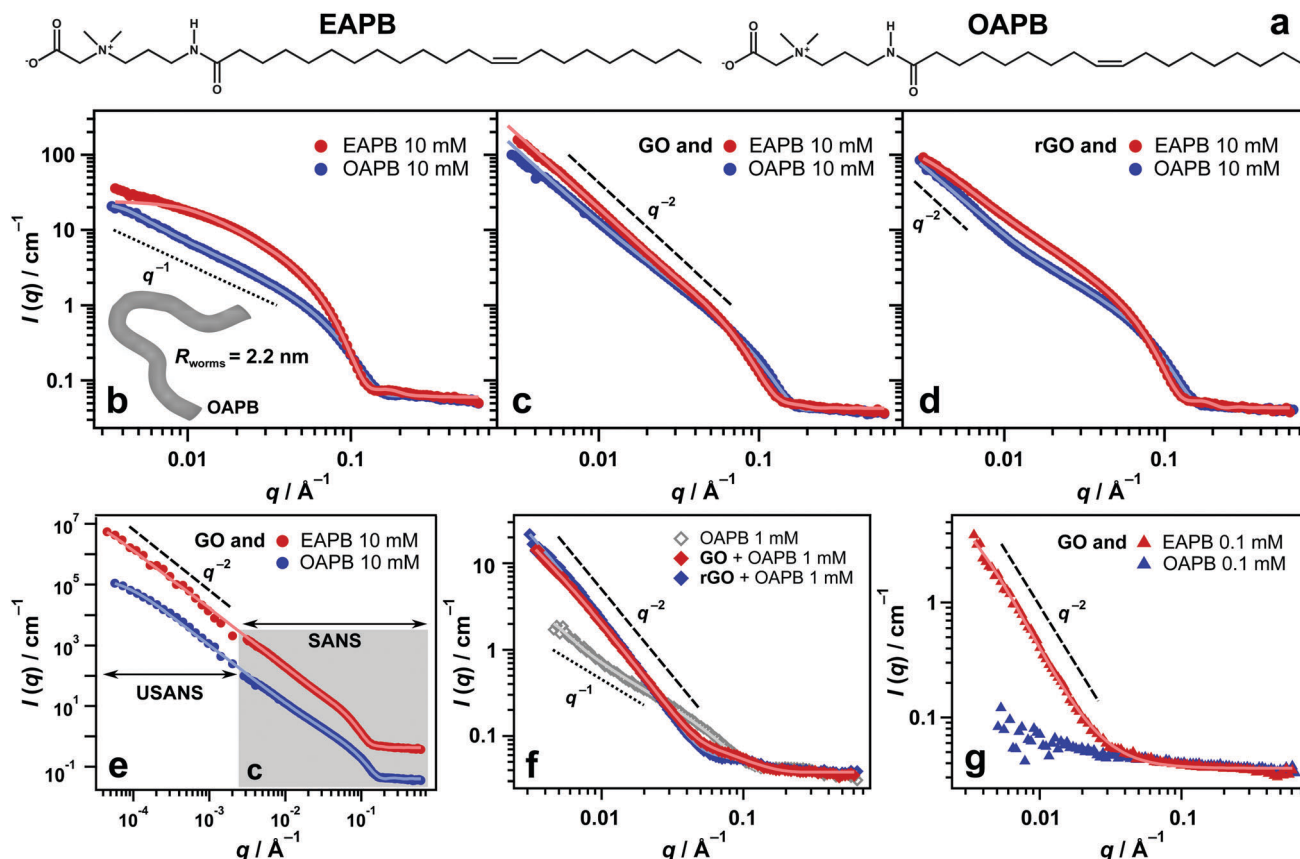


Fig. 8 (a) Chemical structures of erucyl amidopropyl betaine (EAPB) and oleyl amidopropyl betaine (OAPB). (b–d) SANS data for EAPB and OAPB surfactants at 10 mM without carbon nanomaterial present (b), and also with GO (c) and rGO (d) at 0.1 mg mL^{−1}. The inset in (b) represents the OAPB wormlike micelles as determined by the fitting parameters. (e) Inclusion of USANS region to GO/betaine data in (c), i.e. the shaded area. Data in this figure have been offset by multiplication (EAPB ×10) for clarity (f) SANS data of pure 1 mM OAPB, and also with GO and rGO present at 0.1 mg mL^{−1}. (g) SANS data of GO with 0.1 mM EAPB and OAPB.

surfaces of the sheets. At 10 mM EAPB and OAPB, for both GO and rGO, the adsorption appears to be slightly stronger for EAPB than OAPB. This is likely due to the higher surface activity of EAPB causing it to partition more to the interface with GO and rGO, however the difference is only minor and likely also relates to the scattering length densities of the surfactants, which will be lower for EAPB, giving higher contrast with D₂O (neutron scattering length densities for protium *ca.* −3.74 and deuterium *ca.* 6.67 × 10^{−6} Å^{−2}).

Moreover, the differences in the scattering of GO and rGO with both surfactants seem insignificant (Fig. 8c and d). The likely explanation for the lack of difference for the two materials may reside in the chemical complexity of these particular surfactants as well as the fact that the extra long tail-groups render them very hydrophobic. Being zwitterionic, the effects of the charge groups become reduced due to self-screening, however they, along with the amide group further towards the center of the molecule (Fig. 8a), will still experience strong polar interactions with their surroundings. In addition, these surfactants have an unsaturated group in their alkyl tails, meaning that similar to TX-100, π -stacking interactions may also contribute. Coupling the π -stacking interactions with the long 18 and 22 carbon tail-groups, these molecules will exhibit much stronger

hydrophobic interactions than the previous surfactants examined. Therefore overall, the attractive forces arising from both the dipole and very strong hydrophobic interactions mean that surfactant-surfactant interactions dominate in the case of these long-chain betaines.^{105,106} Hence, these surfactants readily form bilayers and can be considered lipid-like molecules. As a result, these surfactants are likely to form bilayers on both GO and rGO irrespective of their chemical nature because of overriding surfactant-surfactant interactions.

When reducing the concentration of OAPB to 1 mM, differences in the amount of scattering when mixed with GO and rGO were also negligible (Fig. 8f). As one might expect the partitioning between bulk and adsorbed surfactant to be different at lower concentrations, this outcome reinforces the hypothesis that for these lipid-like surfactants, intermolecular interactions between surfactant molecules are likely dominating. Bilayer formation on the GO and rGO surfaces is thus the favourable adsorption assembly, and therefore the effects of the carbon nanomaterials become less significant. Equivalent samples with EAPB at 1 mM were unstable, possibly because at this concentration the amount of surfactant is not enough to form bilayers on the sheets, and they instead become hydrophobic, resulting in aggregation. Hence, these samples were

not amenable to analysis with SANS. A comparison between the two surfactants could however be made when reducing the surfactant concentration to 0.1 mM (Fig. 8g). The scattering with GO was found to be substantially stronger for EAPB than OAPB, showing that hydrophobicity does have a notable contribution to the interactions and adsorption of small molecules with these carbon nanomaterials.

Interactions with polymers

Block co-polymers have been used with GO to enhance surface activity,^{107,108} as well as assist with dispersion of carbon nanotubes.^{109,110} For the final additive class of this study, the interactions of two model polymers with aqueous dispersions of GO and rGO were explored using SANS. Two common polymers were chosen: polyethylene glycol (PEG) and Pluronic F127, which is a widely used triblock co-polymer (structures shown in Fig. 9a). Dispersed in water on their own, PEG and Pluronic F127 give fairly weak scattering, however the scattering of PEG is stronger than the scattering of Pluronic F127 (Fig. 9a). The reason behind this result is that the PEG chains are much larger, and in solution follow an essentially 'random walk' or Gaussian coil,¹¹¹ whereas Pluronic F127 self-assembles into loosely aggregated, highly hydrated spherical micelles.^{112,113} These patterns were fit with unified power models to determine their radii of gyration (for polymers, this relates to the interactions between chains and monomers as well as size),^{114,115} which were 22.2 and 4.0 nm for PEG and Pluronic F127 respectively (see ESI,† Table S14), indicating that PEG units are more dispersed with longer contour lengths. Both polymers are intrinsically hydrophilic, however Pluronic F127 is also amphiphilic because of its methylated central block, driving micellisation. Therefore, the scattering data for Pluronic F127 in Fig. 9a can also be fit with a spheres model (see ESI,† Fig. S11),¹¹⁶ revealing spherical micelles of approximately 4.0 nm in radius (see ESI,† Table S15), the same as the radius of gyration, which is to be expected for spheres.

For both polymers, the scattering intensities increased with the inclusion of GO and rGO. This increase was only very slight with GO (Fig. 9b), indicating minimal interactions between the materials. However contrary to any of the surfactant systems,

both polymers displayed a significantly higher affinity for rGO (Fig. 9c). The unified power model also gives good approximation for the scattering from fractal aggregates (such as GO and rGO sheets),¹¹¹ therefore is also valid for the combined polymer/GO and rGO systems. The radius of gyration for PEG and Pluronic F127 with rGO increased to 36.3 and 26.7 nm respectively (see ESI,† Table S14), which translates to a 567.5% increase for Pluronic F127. Pluronic F127 is therefore most likely changing from spherical micelles in the pure polymer solution to unravelled, adsorbed polymer chains on the surfaces of the sheets. These effects are most likely thermodynamically driven, and can be explained by the solvation of these materials by water molecules. As both polymers are hydrophilic and GO is also hydrophilic, there is little entropic gain in their co-assembly with regards to the solvent water molecules, as both the polymers and GO have favourable polar interaction sites with which water can interact. Therefore, the materials will mostly remain solvated in the bulk rather than adsorbing to each other. However, because rGO is hydrophobic, the adsorption of the polymers (especially Pluronic F127) will serve to free water molecules that are unfavourably oriented at the interfaces with the rGO sheets.¹¹⁷ This outcome would correspond to an increase in entropy, and hence would be thermodynamically favoured. The adsorption of the polymer onto rGO is thus greater, accounting for the higher scattering of the rGO/polymer systems compared to the GO/polymer systems.

To corroborate the scattering data and the conclusions drawn from them, atomic force microscopy (AFM) imaging was performed on these systems to see if physical evidence for the adsorption of the polymers could be observed. Without GO or rGO added, PEG appeared to form small aggregates when dried onto the surface of mica, whereas Pluronic F127 appeared to spread over the mica surface (Fig. 10a and d). These results suggest a higher adsorption affinity for Pluronic F127 than PEG on mica. With GO and rGO added, the deposited materials do appear to show adsorbed polymer on the surfaces of the sheets (Fig. 10b, c, e and f). In the samples with rGO, almost all of the polymer material appears to be co-located on to the sheets

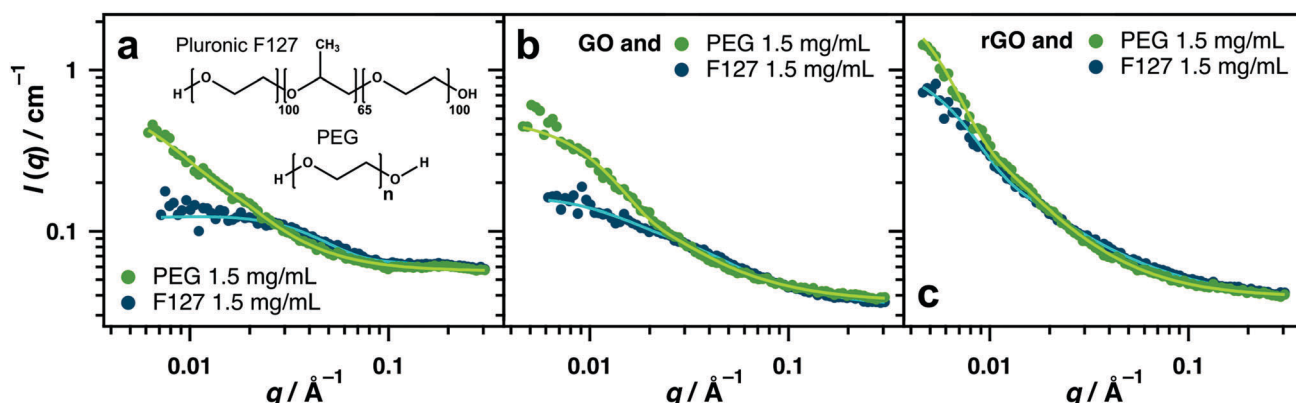


Fig. 9 SANS data for PEG ($M_n = 400\,000$ g mol⁻¹) and Pluronic F127 at 1.5 mg mL⁻¹ without carbon nanomaterial present (a) and with GO (b) and rGO (c). Concentrations for all carbon nanomaterials were 0.1 mg mL⁻¹. Insets to (a) are chemical structures of each polymer.

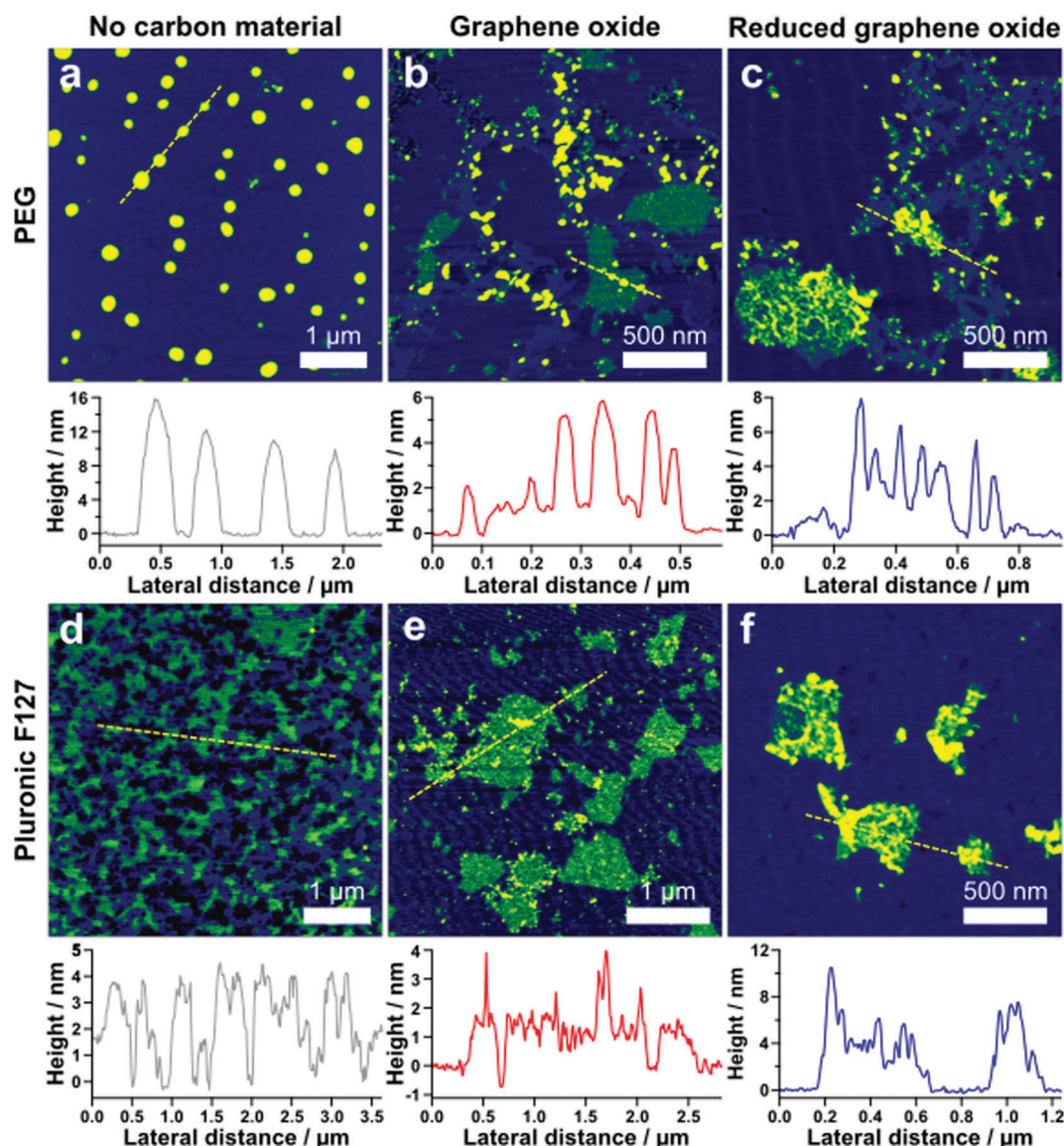


Fig. 10 AFM images of 0.1 mg mL^{-1} of polymer with or without 0.1 mg mL^{-1} GO or rGO in dispersion: (a–c) AFM height images of PEG (a) with GO (b) and rGO (c). (d–f) AFM height images of Pluronic F127 (d) with GO (e) and rGO (f). Height profiles corresponding to the dashed yellow cross sections are shown below each respective image. Samples were dried onto mica substrate.

rather than the background mica (Fig. 10c and f), reasserting the strong co-assembly indicated by the scattering with rGO and both polymers (Fig. 9c). While some polymer adsorption is evident for the samples with GO, the effect is not quite as clear, especially in the case of Pluronic F127 (Fig. 10b and e), again supporting the scattering data (Fig. 9b). When increasing the amount of polymer in these mixtures by a factor of 5 and imaging by AFM, it was found that the addition of rGO completely disrupted the fractal aggregation exhibited by the pure polymers at this loading, whereas GO caused only partially disrupted aggregation (see ESI,† Fig. S12). This again indicates stronger interactions with rGO than GO, and suggests that the design of composite materials comprising polymers and carbon nanomaterials may be more effective when rGO is used. It must be noted that as these are dried samples, they are only

indicative of the solution behaviour and must be interpreted with caution.

4 Conclusions

A range of surfactants that were systematically varied in specific physical properties such as charge and hydrophobicity were added to aqueous dispersions of monolayer graphene oxide (GO) and reduced graphene oxide (rGO). Small and ultra-small-angle neutron scattering (SANS and USANS) were used to monitor the self-assembly within these systems, giving insight into the adsorption and interactions between the surfactants and carbon nanomaterials. Electrostatic interactions were found to be the most dominant forces in these systems, as

cationic surfactants showed very high affinity for GO and rGO, whereas anionic surfactants exhibited almost no adsorption. Nonionic and zwitterionic surfactants also adsorbed strongly to both materials, suggesting however that charge is not the sole factor driving adsorption, and that dipole and hydrophobic interactions are also strong contributors to their assembly. Lastly, two neutral polymers, one of which was completely hydrophilic and the other amphiphilic, were mixed with GO and rGO, both showing moderate or weak interactions that were apparently entropic in origin as evidenced by higher adsorption to rGO than GO. This indicates that additives do not have to be amphiphilic in order to adsorb to aqueous carbon nanomaterials, and in certain circumstances is thermodynamically driven.

Interestingly, when comparing the behaviour of GO and rGO, in most cases, greater scattering was evident in systems with GO, indicating higher levels of adsorption. This suggests that dipole interactions are typically more significant than hydrophobic effects with relation to adsorption of amphiphiles on these materials. To account for this observation, we propose a differing adsorption mechanism for surfactants on GO *versus* rGO. With GO, we believe that surfactants are adsorbing *via* their head-groups due to the stronger dipole interactions, and as a result, form a densely packed surfactant bilayer along the surface of the GO sheets. This structure is clearly apparent when using nonionic surfactants, and these bilayers could then stack with multiple sheets to form lamellae (liquid crystals) due to the absence of charge repulsion between surfactant layers. For rGO however, because the sheets are inherently more hydrophobic, the surfactants are more likely to lie flat on the surface because of stronger hydrophobic interactions (*i.e.* entropic effects arising from water structuring),⁹⁴ resulting in hemispherical micelles.^{78,79} Thus, the amount of surfactant adsorbed to GO is greater due to the denser packing arrangement. Surfactants that were more hydrophobic also appeared to adsorb more readily than equivalent surfactants with shorter tail-groups, presumably due to increased surface active partitioning.

Where surfactant adsorption was evident, the scattering at low q (the fractal region) often followed a trend of q^{-2} , indicating scattering from flat surfaces. The surfactants therefore were effectively flattening the GO and rGO sheets in solution (nano-ironing). Hence, these composite systems could also be useful in materials coatings where the surfactants serve to maximise the carbon nanomaterial surface area. The overall results collectively provide a broader understanding of the nature of molecular interactions with aqueous GO and rGO nanosheets, and may assist with the effective utilisation of these materials in adsorption, stabilisation and environmental applications where synergism can be used to enhance effectiveness and develop new routes to diverse, chemically functional systems.

Conflicts of interest

There are no conflicts to declare.

Acknowledgements

We would like to acknowledge the Australian Centre for Neutron Scattering, Australian Nuclear Science and Technology Organisation,

for beam-time. We also thank the Australian Institute of Nuclear Science and Engineering for travel support (T. M. M.), as well as the Monash Centre for Atomically Thin Materials for additional funding. This work was supported in part by the grant of an ARC Future Fellowship (FT160100191) to R. F. T. We would lastly like to thank Gregory Warr, Yachin Cohen and Stuart Prescott for insightful discussions on scattering phenomena.

References

- 1 K. S. Novoselov, A. K. Geim, S. V. Morozov, D. Jiang, Y. Zhang, S. V. Dubonos, I. V. Grigorieva and A. A. Firsov, *Science*, 2004, **306**, 666–669.
- 2 J. C. Meyer, A. K. Geim, M. I. Katsnelson, K. S. Novoselov, T. J. Booth and S. Roth, *Nature*, 2007, **446**, 60.
- 3 D. R. Dreyer, S. Park, C. Bielawski and R. S. Ruoff, *Chem. Soc. Rev.*, 2010, **39**, 228–240.
- 4 S. Stankovich, D. A. Dikin, R. D. Piner, K. A. Kohlhaas, A. Kleinhammes, Y. Jia, Y. Wu, S. T. Nguyen and R. S. Ruoff, *Carbon*, 2007, **45**, 1558–1565.
- 5 D. Li, M. B. Muller, S. Gilje, R. B. Kaner and G. G. Wallace, *Nat. Nanotechnol.*, 2008, **3**, 101–105.
- 6 G. K. Ramesha, A. V. Kumara, H. B. Muralidhara and S. Sampath, *J. Colloid Interface Sci.*, 2011, **361**, 270–277.
- 7 G. Zhao, J. Li, X. Ren, C. Chen and X. Wang, *Environ. Sci. Technol.*, 2011, **45**, 10454–10462.
- 8 K. Gupta and O. P. Khatri, *J. Colloid Interface Sci.*, 2017, **501**, 11–21.
- 9 J. Kim, L. J. Cote, W. Kim, F. Yuan, K. R. Shull and J. Huang, *J. Am. Chem. Soc.*, 2010, **132**, 8180–8186.
- 10 Y. He, F. Wu, X. Sun, R. Li, Y. Guo, C. Li, L. Zhang, F. Xing, W. Wang and J. Gao, *ACS Appl. Mater. Interfaces*, 2013, **5**, 4843–4855.
- 11 T. M. McCoy, M. J. Pottage and R. F. Tabor, *J. Phys. Chem. C*, 2014, **118**, 4529–4535.
- 12 Y. He, N. Zhang, F. Wu, F. Xu, Y. Liu and J. Gao, *Mater. Res. Bull.*, 2013, **48**, 3553–3558.
- 13 Y. Lei, F. Chen, Y. Luo and L. Zhang, *Chem. Phys. Lett.*, 2014, **593**, 122–127.
- 14 Z. Niu, J. Chen, H. H. Hng, J. Ma and X. Chen, *Adv. Mater.*, 2012, **24**, 4144–4150.
- 15 Y. He, Y. Liu, T. Wu, J. Ma, X. Wang, Q. Gong, W. Kong, F. Xing, Y. Liu and J. Gao, *J. Hazard. Mater.*, 2013, **260**, 796–805.
- 16 D. A. Dikin, S. Stankovich, E. J. Zimney, R. D. Piner, G. H. B. Dommett, G. Evmenenko, S. T. Nguyen and R. S. Ruoff, *Nature*, 2007, **448**, 457–460.
- 17 Y. Su, V. Kravets, S. Wong, J. Waters, A. Geim and R. Nair, *Nat. Commun.*, 2014, **5**, 4843.
- 18 J. Hong, Y. S. Kang and S. W. Kang, *Ind. Eng. Chem. Res.*, 2011, **50**, 3095–3099.
- 19 F. Kim, L. J. Cote and J. Huang, *Adv. Mater.*, 2010, **22**, 1954–1958.
- 20 L. J. Cote, J. Kim, Z. Zhang, C. Sun and J. Huang, *Soft Matter*, 2010, **6**, 6096–6101.

- 21 M. Krueger, S. Berg, D. Stone, E. Strelcov, D. A. Dikin, J. Kim, L. J. Cote, J. Huang and A. Kolmakov, *ACS Nano*, 2011, **5**, 10047–10054.
- 22 G. Z. Kyzas, E. A. Deliyanni and K. A. Matis, *J. Chem. Technol. Biotechnol.*, 2014, **89**, 196–205.
- 23 H. Bai, C. Li, X. Wang and G. Shi, *J. Phys. Chem. C*, 2011, **115**, 5545–5551.
- 24 A. Akbari, P. Sheath, S. T. Martin, D. B. Shinde, M. Shaibani, P. C. Banerjee, R. Tkacz, D. Bhattacharyya and M. Majumder, *Nat. Commun.*, 2016, **7**, 10891.
- 25 D. C. Marciano, D. V. Kosynkin, J. M. Berlin, A. Sinitskii, Z. Sun, A. Slesarev, L. B. Alemany, W. Lu and J. M. Tour, *ACS Nano*, 2010, **4**, 4806–4814.
- 26 B. Konkena and S. Vasudevan, *J. Phys. Chem. Lett.*, 2012, **3**, 867–872.
- 27 C.-J. Shih, S. Lin, R. Sharma, M. S. Strano and D. Blankschtein, *Langmuir*, 2012, **28**, 235–241.
- 28 T. D. Gamot, A. R. Bhattacharyya, T. Sridhar, F. Beach, R. F. Tabor and M. Majumder, *Langmuir*, 2017, **33**, 10311–10321.
- 29 I. Chowdhury, N. D. Mansukhani, L. M. Guiney, M. C. Hersam and D. Bouchard, *Environ. Sci. Technol.*, 2015, **49**, 10886–10893.
- 30 D. Kang, J. Y. Kwon, H. Cho, J.-H. Sim, H. S. Hwang, C. S. Kim, Y. J. Kim, R. S. Ruoff and H. S. Shin, *ACS Nano*, 2012, **6**, 7763–7769.
- 31 F. A. Ghauri, M. A. Raza, M. S. Baig and S. Ibrahim, *Mater. Res. Express*, 2017, **4**, 125601.
- 32 L. L. Zhang, X. Zhao, M. D. Stoller, Y. Zhu, H. Ji, S. Murali, Y. Wu, S. Perales, B. Clevenger and R. S. Ruoff, *Nano Lett.*, 2012, **12**, 1806–1812.
- 33 Y. Chen, X. Zhang, D. Zhang, P. Yu and Y. Ma, *Carbon*, 2011, **49**, 573–580.
- 34 X. Zhu, Y. Zhu, S. Murali, M. D. Stoller and R. S. Ruoff, *ACS Nano*, 2011, **5**, 3333–3338.
- 35 B. Qu, C. Ma, G. Ji, C. Xu, J. Xu, Y. S. Meng, T. Wang and J. Y. Lee, *Adv. Mater.*, 2014, **26**, 3854–3859.
- 36 N. Li, M. Zheng, H. Lu, Z. Hu, C. Shen, X. Chang, G. Ji, J. Cao and Y. Shi, *Chem. Commun.*, 2012, **48**, 4106–4108.
- 37 B. Wang, X. Li, X. Zhang, B. Luo, M. Jin, M. Liang, S. A. Dayeh, S. Picraux and L. Zhi, *ACS Nano*, 2013, **7**, 1437–1445.
- 38 L. J. Cote, J. Kim, V. C. Tung, J. Luo, F. Kim and J. Huang, *Pure Appl. Chem.*, 2010, **83**, 95–110.
- 39 N. Lu and Z. Li, *Quantum Simulations of Materials and Biological Systems*, Springer, 2012, ch. Graphene Oxide: Theoretical Perspectives, pp. 69–84.
- 40 N. Wei, C. Lv and Z. Xu, *Langmuir*, 2014, **30**, 3572–3578.
- 41 M. Zokaie and M. Foroutan, *RSC Adv.*, 2015, **5**, 39330–39341.
- 42 H. Tang, D. Liu, Y. Zhao, X. Yang, J. Lu and F. Cui, *J. Phys. Chem. C*, 2015, **119**, 26712–26718.
- 43 T. M. McCoy, A. C. Y. Liu and R. F. Tabor, *Nanoscale*, 2016, **8**, 6969–6974.
- 44 D. Feng, Y. Zhang, Q. Chen, J. Wang, B. Li and Y. Feng, *J. Surfactants Deterg.*, 2012, **15**, 657–661.
- 45 G. A. Gaynanova, A. R. Valiakhmetova, D. A. Kuryashov, N. Y. Bashkirtseva and L. Y. Zakharova, *J. Surfactants Deterg.*, 2015, **18**, 965–971.
- 46 V. T. Kelleppan, J. E. Moore, T. M. McCoy, A. V. Sokolova, L. d. Campo, B. L. Wilkinson and R. F. Tabor, *Langmuir*, 2017, **34**, 970–977.
- 47 A. Sokolova, J. Christoforidis, A. Eltobaji, J. Barnes, F. Darmann, A. E. Whitten and L. de Campo, *J. Neutron Res.*, 2016, **27**, 9–13.
- 48 C. Rehm, A. Brûlé, A. K. Freund and S. J. Kennedy, *J. Appl. Crystallogr.*, 2013, **46**, 1699–1704.
- 49 C. Rehm and L. de Campo, *J. Neutron Res.*, 2016, **27**, 30–32.
- 50 C. Rehm, L. d. Campo, A. Brûlé, F. Darmann, F. Bartsch and A. Berry, *J. Appl. Crystallogr.*, 2018, **51**, 1–8.
- 51 S. R. Kline, *J. Appl. Crystallogr.*, 2006, **39**, 895–900.
- 52 D. Nečas and P. Klapetek, *Open Phys.*, 2012, **10**, 181–188.
- 53 G. Titelman, V. Gelman, S. Bron, R. Khalfin, Y. Cohen and H. Bianco-Peled, *Carbon*, 2005, **43**, 641–649.
- 54 D. F. R. Mildner and P. L. Hall, *J. Phys. D: Appl. Phys.*, 1986, **19**, 1535–1545.
- 55 G. Bushell, Y. Yan, D. Woodfield, J. Raper and R. Amal, *Adv. Colloid Interface Sci.*, 2002, **95**, 1–50.
- 56 J. D. Ramsay, S. W. Swanton and J. Bunce, *J. Chem. Soc., Faraday Trans.*, 1990, **86**, 3919–3926.
- 57 P. W. Schmidt, *J. Appl. Crystallogr.*, 1991, **24**, 414–435.
- 58 A. Y. Cherny, E. Anitas, V. Osipov and A. Kuklin, *J. Appl. Crystallogr.*, 2014, **47**, 198–206.
- 59 T. M. McCoy, P. Brown, J. Eastoe and R. F. Tabor, *ACS Appl. Mater. Interfaces*, 2015, **7**, 2124–2133.
- 60 H. Kim, Y. R. Jang, J. Yoo, Y.-S. Seo, K.-Y. Kim, J.-S. Lee, S.-D. Park, C.-J. Kim and J. Koo, *Langmuir*, 2014, **30**, 2170–2177.
- 61 T. M. McCoy, S. A. Holt, A. M. Rozario, T. D. M. Bell and R. F. Tabor, *Adv. Mater. Interfaces*, 2017, **4**, 1700803.
- 62 M. Abdolkarimi-Mahabadi and M. Manteghian, *J. Dispersion Sci. Technol.*, 2015, **36**, 924–931.
- 63 T. M. McCoy, H. C. W. Parks and R. F. Tabor, *Carbon*, 2018, **135**, 164–170.
- 64 S. P. Moulik, M. E. Haque, P. K. Jana and A. R. Das, *J. Phys. Chem.*, 1996, **100**, 701–708.
- 65 Z. Adamczyk, G. Para and P. Warszyński, *Langmuir*, 1999, **15**, 8383–8387.
- 66 L. Feigin, D. I. Svergun and G. W. Taylor, *Structure analysis by small-angle X-ray and neutron scattering*, Springer, 1987, pp. 25–55.
- 67 J. B. Hayter and J. Penfold, *Mol. Phys.*, 1981, **42**, 109–118.
- 68 J. B. Hayter and J. Penfold, *J. Chem. Soc., Faraday Trans. 1*, 1981, **77**, 1851–1863.
- 69 J.-P. Hansen and J. B. Hayter, *Mol. Phys.*, 1982, **46**, 651–656.
- 70 J. B. Hayter and J. Penfold, *Colloid Polym. Sci.*, 1983, **261**, 1022–1030.
- 71 C. Wu, D. Y. Chan and R. F. Tabor, *J. Colloid Interface Sci.*, 2014, **426**, 80–82.
- 72 V. Aswal and P. Goyal, *Physica B*, 1998, **245**, 73–80.
- 73 S. Berr, *J. Phys. Chem.*, 1987, **91**, 4760–4765.
- 74 J. Berghausen, J. Zipfel, P. Lindner and W. Richtering, *J. Phys. Chem. B*, 2001, **105**, 11081–11088.
- 75 N. Kučerka, J. F. Nagle, J. N. Sachs, S. E. Feller, J. Pencer, A. Jackson and J. Katsaras, *Biophys. J.*, 2008, **95**, 2356–2367.

- 76 P. Somasundaran, T. W. Healy and D. Fuerstenau, *J. Phys. Chem.*, 1964, **68**, 3562–3566.
- 77 S. Manne and H. E. Gaub, *Science*, 1995, **270**, 1480–1482.
- 78 G. G. Warr, *Curr. Opin. Colloid Interface Sci.*, 2000, **5**, 88–94.
- 79 R. Atkin, V. Craig, E. J. Wanless and S. Biggs, *Adv. Colloid Interface Sci.*, 2003, **103**, 219–304.
- 80 R. Atkin, V. Craig and S. Biggs, *Langmuir*, 2000, **16**, 9374–9380.
- 81 W. Meng, E. Gall, F. Ke, Z. Zeng, B. Kopchick, R. Timsina and X. Qiu, *J. Phys. Chem. C*, 2015, **119**, 21135–21140.
- 82 K. Eskilsson and V. Yaminsky, *Langmuir*, 1998, **14**, 2444–2450.
- 83 S. Hayashi and S. Ikeda, *J. Phys. Chem.*, 1980, **84**, 744–751.
- 84 M. Bergstrom and J. S. Pedersen, *Phys. Chem. Chem. Phys.*, 1999, **1**, 4437–4446.
- 85 S. Nave, J. Eastoe, R. K. Heenan, D. Steytler and I. Grillo, *Langmuir*, 2000, **16**, 8741–8748.
- 86 S. Bhatia, J. Barker and A. Mourchid, *Langmuir*, 2003, **19**, 532–535.
- 87 K. A. Mauritz and R. B. Moore, *Chem. Rev.*, 2004, **104**, 4535–4586.
- 88 Q. Zhao, P. Majsztrik and J. Benziger, *J. Phys. Chem. B*, 2011, **115**, 2717–2727.
- 89 R. Zielinski, E. Kaler and M. Paulaitis, *J. Phys. Chem.*, 1995, **99**, 10354–10358.
- 90 J. Gapinski, J. Szymanski, A. Wilk, J. Kohlbrecher, A. Patkowski and R. Hołyst, *Langmuir*, 2010, **26**, 9304–9314.
- 91 A. Bernheim-Groswasser, E. Wachtel and Y. Talmon, *Langmuir*, 2000, **16**, 4131–4140.
- 92 F. Nettesheim, J. Zipfel, P. Lindner and W. Richtering, *Colloids Surf., A*, 2001, **183–185**, 563–574.
- 93 B.-Y. Zhu and T. Gu, *Adv. Colloid Interface Sci.*, 1991, **37**, 1–32.
- 94 R. F. Tabor, F. Grieser, R. R. Dagastine and D. Y. C. Chan, *Phys. Chem. Chem. Phys.*, 2014, **16**, 18065–18075.
- 95 T. M. McCoy, A. Valiakhmetova, M. J. Pottage, C. J. Garvey, L. de Campo, C. Rehm, D. A. Kuryashov and R. F. Tabor, *Langmuir*, 2016, **32**, 12423–12433.
- 96 F. Tiberg, J. Brinck and L. Grant, *Curr. Opin. Colloid Interface Sci.*, 1999, **4**, 411–419.
- 97 R. Zhang and P. Somasundaran, *Adv. Colloid Interface Sci.*, 2006, **123**, 213–229.
- 98 W. Brown, R. Johnsen, P. Stilbs and B. Lindman, *J. Phys. Chem.*, 1983, **87**, 4548–4553.
- 99 H. Kunieda, K. Nakamura, H. Davis and D. F. Evans, *Langmuir*, 1991, **7**, 1915–1919.
- 100 W. Richtering, *Optical Methods and Physics of Colloidal Dispersions*, Springer, 1997, pp. 90–96.
- 101 R. Weigel, J. Läger, W. Richtering and P. Lindner, *J. Phys. II*, 1996, **6**, 529–542.
- 102 J. E. Hunter and J. F. Fowler, *J. Surfactants Deterg.*, 1998, **1**, 235–239.
- 103 J. S. Pedersen and P. Schurtenberger, *Macromolecules*, 1996, **29**, 7602–7612.
- 104 W.-R. Chen, P. D. Butler and L. J. Magid, *Langmuir*, 2006, **22**, 6539–6548.
- 105 J. N. Israelachvili, D. J. Mitchell and B. W. Ninham, *J. Chem. Soc., Faraday Trans.*, 1976, **72**, 1525–1568.
- 106 J. N. Israelachvili, D. J. Mitchell and B. W. Ninham, *Biochim. Biophys. Acta*, 1977, **470**, 185–201.
- 107 Z. Sun, T. Feng and T. P. Russell, *Langmuir*, 2013, **29**, 13407–13413.
- 108 D. Chen, Z. Sun, T. P. Russell and L. Jin, *Langmuir*, 2017, **33**, 8961–8969.
- 109 G. Ciofani, V. Raffa, V. Pensabene, A. Menciassi and P. Dario, *Fullerenes, Nanotubes, Carbon Nanostruct.*, 2009, **17**, 11–25.
- 110 M. Granite, A. Radulescu and Y. Cohen, *Langmuir*, 2012, **28**, 11025–11031.
- 111 G. Beaucage, *J. Appl. Crystallogr.*, 1996, **29**, 134–146.
- 112 K. Mortensen and Y. Talmon, *Macromolecules*, 1995, **28**, 8829–8834.
- 113 M. Bohorquez, C. Koch, T. Trygstad and N. Pandit, *J. Colloid Interface Sci.*, 1999, **216**, 34–40.
- 114 G. Beaucage and D. Schaefer, *J. Non-Cryst. Solids*, 1994, **172**, 797–805.
- 115 G. Beaucage, *J. Appl. Crystallogr.*, 1995, **28**, 717–728.
- 116 A. Guinier, G. Fournet and C. Walker, *Small angle scattering of X-rays*, J. Wiley & Sons, New York, 1955.
- 117 P. Somasundaran and S. Krishnakumar, *Colloids Surf., A*, 1997, **123**, 491–513.

Electronic Supplementary Information - Bulk properties of aqueous graphene oxide and reduced graphene oxide with surfactants and polymers: adsorption and stability

Thomas M. McCoy,^a Liliana de Campo,^b Anna V. Sokolova,^b
Isabelle Grillo,^c Ekaterina I. Izgorodina,^a Rico F. Tabor^{a,*}

^aSchool of Chemistry, Monash University, Clayton 3800, Australia

^bAustralian Centre for Neutron Scattering, ANSTO, Lucas Heights, New South Wales 2234, Australia

^cInstitut Laue Langevin, F-38042 Grenoble, France

*To whom correspondence should be addressed; E-mail: rico.tabor@monash.edu

This document contains additional figures used for interpretation as well as analysis for the findings presented in the main paper. All fitting parameters used in modelling the SANS/USANS data presented in the main paper are shown as well as explanations for model choice, alternative model considerations and model equations.

Table S1: Mass fractal fitting parameters for graphene oxide (GO) at different concentrations.

GO concentration mg/mL	Scale	Radius	Mass fractal dimension	Cutoff length nm
0.2	1.38×10^{-7}	-	2.85	37.6
1	7.76×10^{-7}	-	2.81	46.3
2	1.40×10^{-6}	-	2.87	41.7
5	3.39×10^{-6}	-	2.85	46.5
10	6.69×10^{-6}	-	2.85	46.2

Aqueous graphene oxide (GO) suspensions were modelled with the mass fractal approximation developed by Mildner and Hall:¹

$$I(q) = scale \times P(q)S(q) + background$$

$$P(q) = F(qR)^2$$

$$F(x) = \frac{3[\sin(x) - x\cos(x)]}{x^3}$$

$$S(q) = \frac{\Gamma(D_m - 1)\zeta^{D_m-1}}{[1 + (q\zeta)^2]^{(D_m-1)/2}} \frac{\sin[(D_m - 1)\tan^{-1}(q\zeta)]}{q}$$

The parameter, R , represents the scattering building blocks for the fractal and D_m is the mass fractal dimension, which must be a value between 0 and 6, and depicts the fractal complexity of the aggregate. The parameter, ζ , is the cut-off length which relates to the overall size of the structures. A more detailed description of the mass fractal model and why it was chosen is discussed in the main paper.

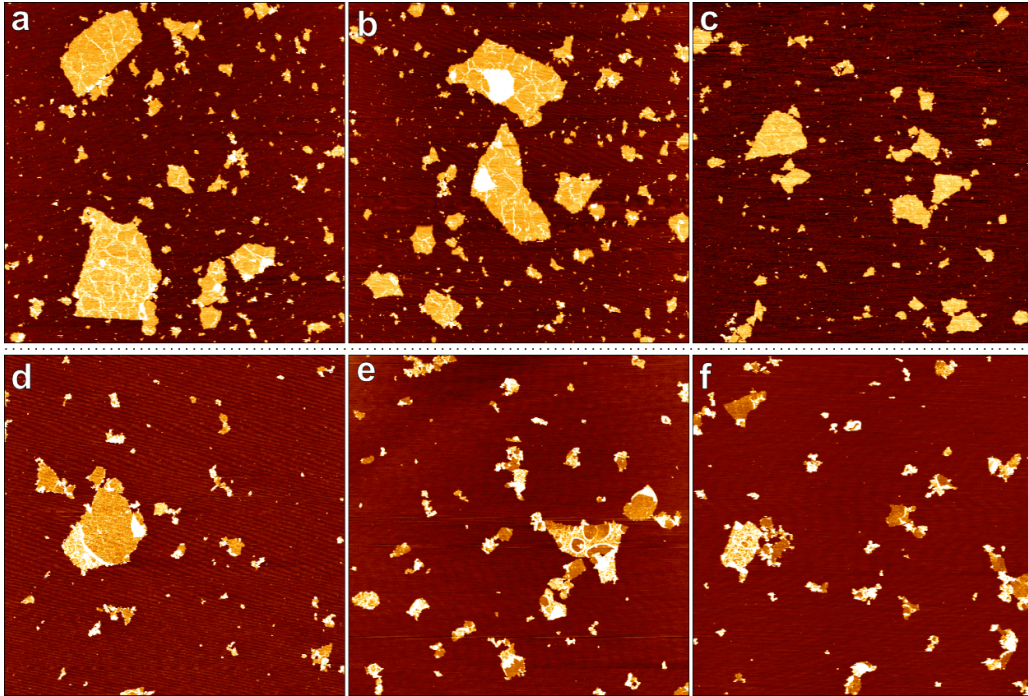


Figure S1: Additional AFM height images of GO (a-c) and rGO (d-f) dried on mica.

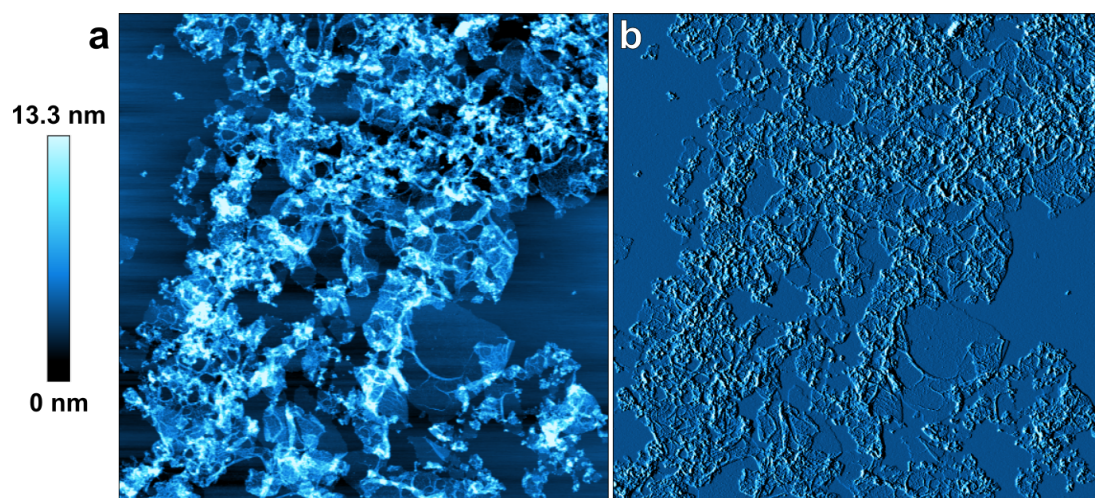


Figure S2: (a) AFM height image of a cluster of rGO dried on mica. (b) The corresponding AFM amplitude image.

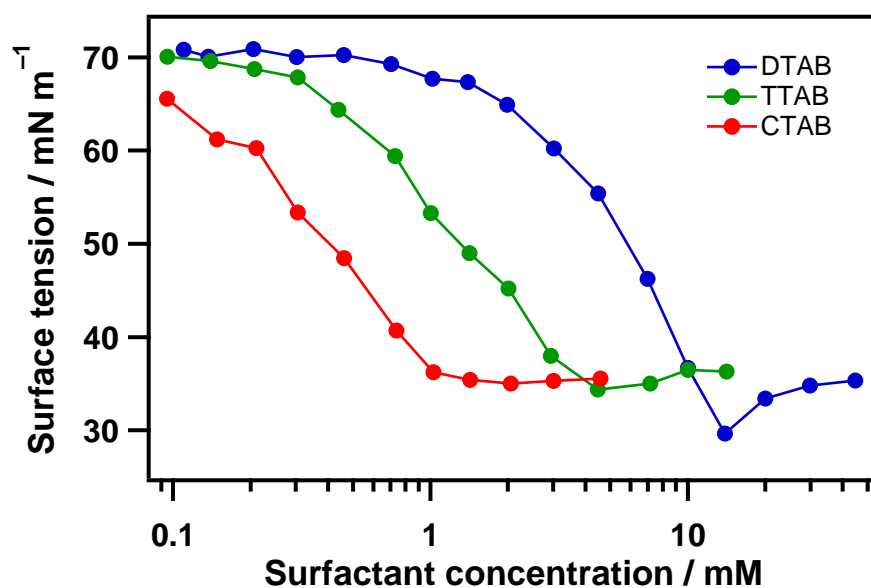


Figure S3: Surface tension data for the cationic surfactants dodecyltrimethylammonium bromide (DTAB), tetradecyltrimethylammonium bromide (TTAB) and cetyltrimethylammonium bromide (CTAB). Measurements were carried out on a custom-made pendant drop apparatus using OpenDrop analysis software.²

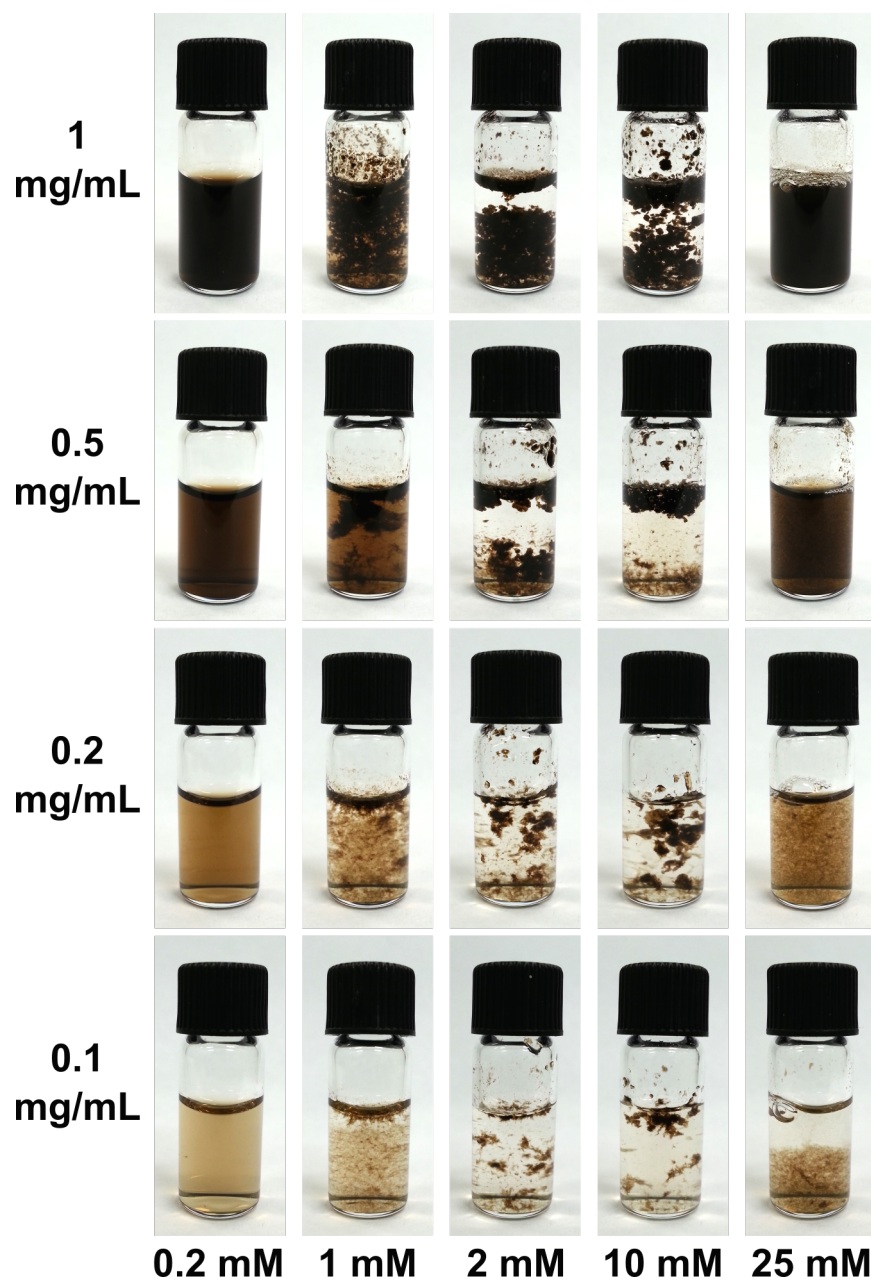


Figure S4: Sample images of GO at various concentrations with the specified concentrations of DTAB added. Used in determining stability phase diagram in main paper.

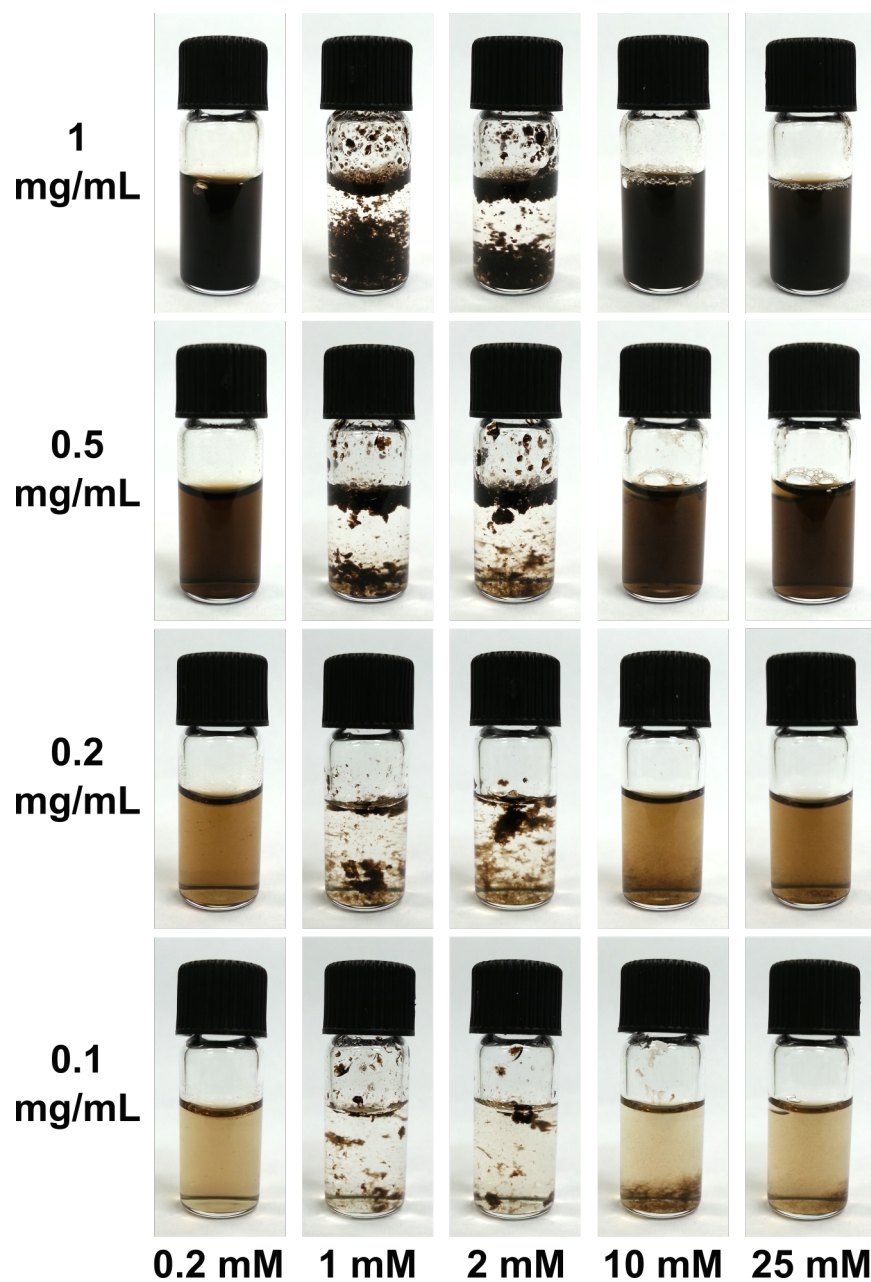


Figure S5: Sample images of GO at various concentrations with the specified concentrations of TTAB added. Used in determining stability phase diagram in main paper.

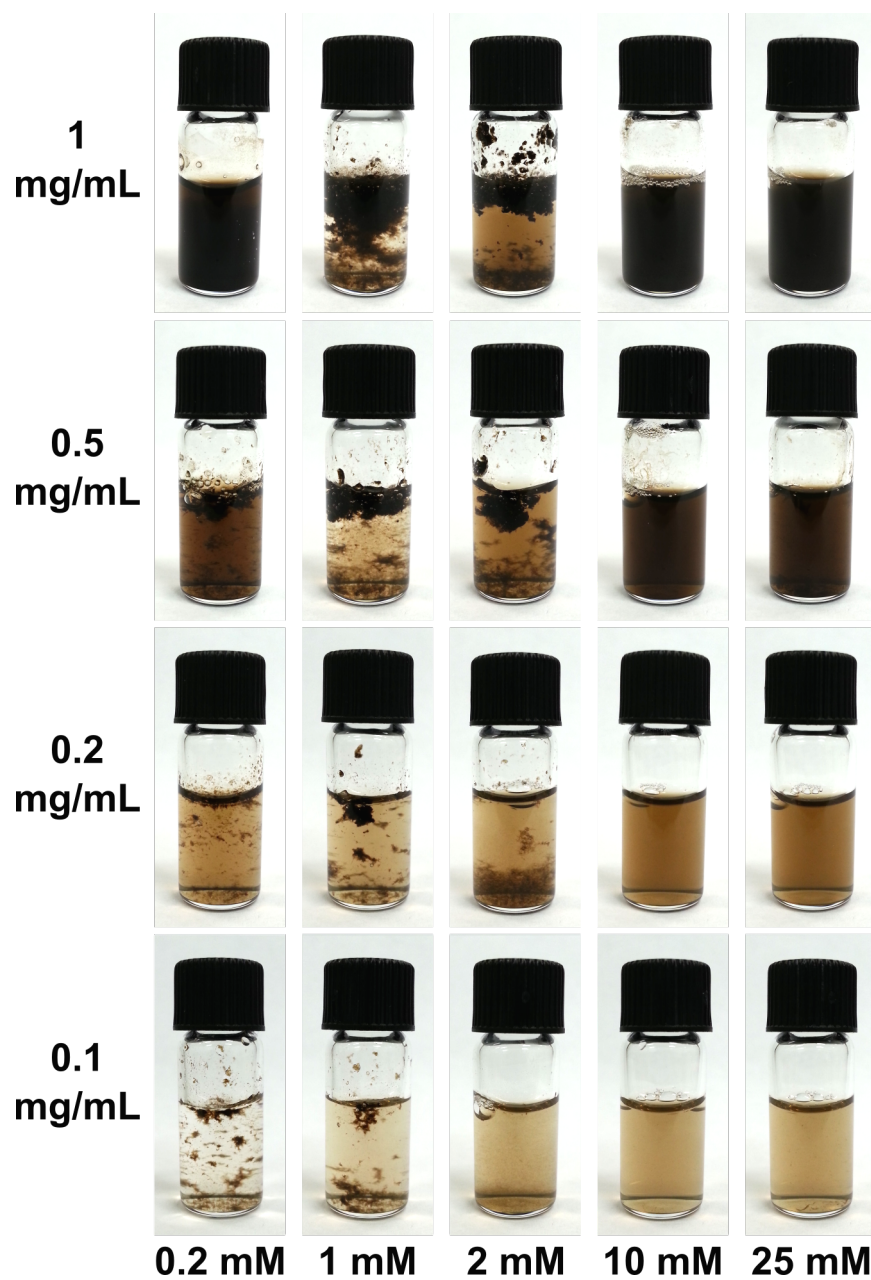


Figure S6: Sample images of GO at various concentrations with the specified concentrations of CTAB added. Used in determining stability phase diagram in main paper.

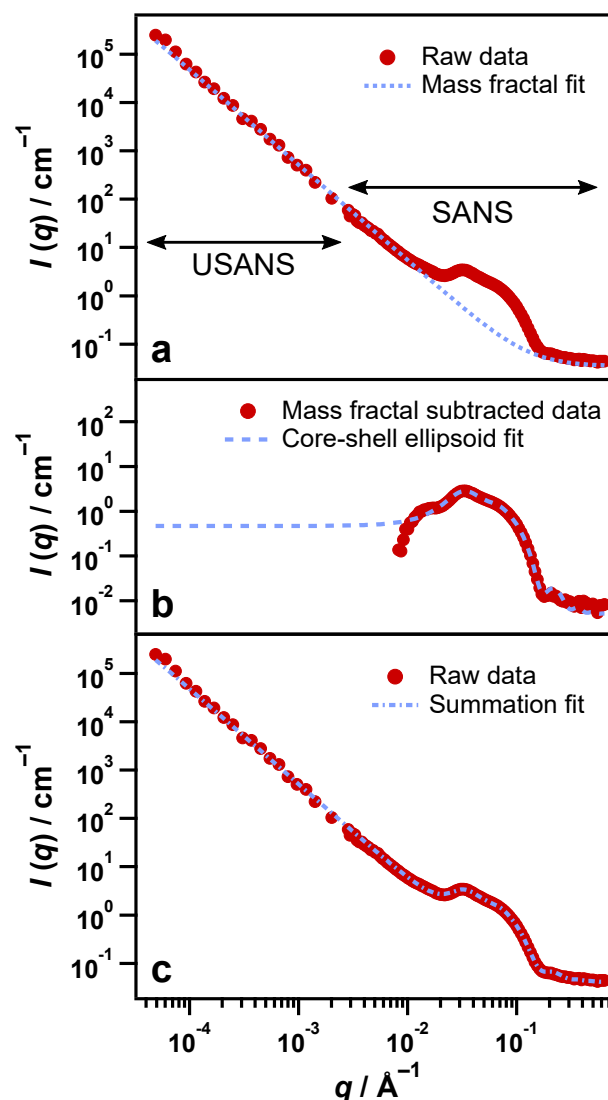


Figure S7: Step-wise process to fitting a summation model to a data set; in this example 25 mM CTAB with 0.1 mg/mL GO: (a) Mass fractal model fit to original SANS/USANS data (low q , fractal region). (b) The mass fractal fit is subtracted from the data and a core-shell ellipsoid model with Hayter-Penfold structure factor is used to fit the new data set (medium q , micelle region). (c) The sum of the mass fractal and ellipsoid models represents the final fit for the original data.

Modelling of systems with cationic and anionic surfactant was done using a core-shell ellipsoid model^{3,4} with inclusion of a Hayter-Penfold structure factor for charged particles.⁵⁻⁹ A core-shell rather than a solid model was used, as in SasView, the core-shell model performed more

accurately in tandem with the structure factor than did the solid ellipsoid model.¹⁰ The core-shell model differs in that there are separate terms for the distances from the micelle core to inner shell boundary, and the inner shell boundary to the outer shell boundary (*i.e.* interface with solvent), each of which have their own respective scattering length densities. The addition of these two lengths would equal the particle radius for the solid ellipsoid model. Note that in all data modelling using the core-shell ellipsoid model, the thickness of the shell was set to 0, hence the model was made to behave the same as the solid ellipsoid model, which is as follows:

$$P(q, \alpha) = \frac{scale}{V} f^2(q) + background$$

where

$$f(q) = \frac{3(\Delta\rho)V \sin[qr(R_a, R_b, \alpha)] - qr \cos[qr(R_a, R_b, \alpha)]}{[qr(R_a, R_b, \alpha)]^3}$$

and

$$r(R_a, R_b, \alpha) = [R_b^2 \sin^2 \alpha + R_a^2 \cos^2 \alpha]^{1/2}$$

The two radii, R_a and R_b , represent the radius along the perpendicular rotational and longitudinal axes of the cylinder ellipsoid respectively. α is the angle between the ellipsoidal axis and the scattering vector q . The Hayter-Penfold structure factor, $S(q)$, is used in conjunction with the ellipsoid form factor and approximates the effects of charge-based interactions between the micelles, where the q vector is defined as:

$$q = \sqrt{q_x^2 + q_y^2}$$

For all cationic systems with structure factor contributions, the summation model method involving the addition of a mass fractal model for the low q region, and the core-shell ellipsoid fit with Hayter-Penfold structure factor for the medium q (micelle) region, to define the overall scattering (Fig. S7). This is because the SasView environment does not have the capacity to simultaneously manage two models as well as a structure factor contribution.

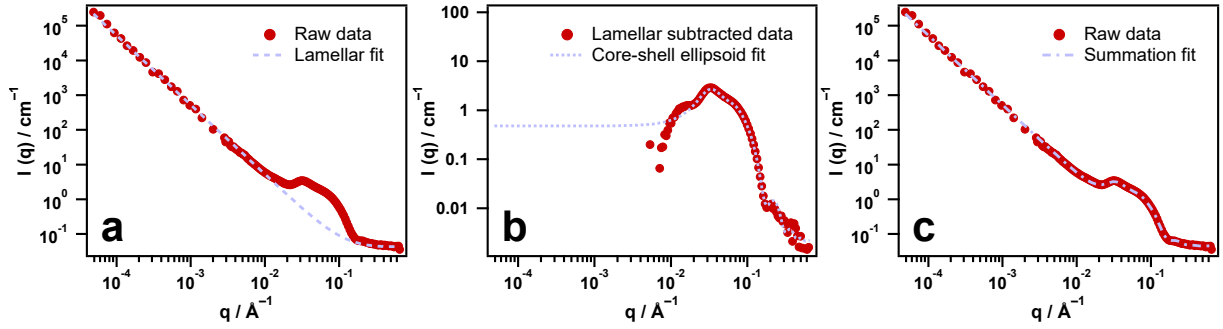


Figure S8: Similar step-wise process as presented for fitting a summation model to the 25 mM CTAB with 0.1 mg/mL GO data set, however in this case we substitute the mass fractal model with a lamellar model. (a) Lamellar model fit to original SANS/USANS data. (b) The lamellar fit is subtracted from the data and a core-shell ellipsoid model with Hayter-Penfold structure factor is used to fit the new data set (medium q , micelle region). (c) The sum of the lamellar and ellipsoid models represents the final fit for the original data.

Because the scattering in the low and ultra-low q region conforms to a slope of q^{-2} , indicating flat surfaces, a lamellar or bilayers model can also be used to define this region (Fig. S8). The lamellar model is from Berghausen.¹¹ The scattering intensity is given by the following equation:

$$I(q) = 2\pi \frac{P(q)}{\delta q^2}$$

where the form factor is given by:

$$P(q) = \frac{2\Delta\rho^2}{q^2}(1 - \cos(q\delta))$$

In both equations, δ is the bilayer thickness in Å. For all modelling, the scattering length density (\AA^{-2}) of the scatterer and solvent are taken into account and are represented in the equations as ρ , with the difference or ‘contrast’ being $\Delta\rho$. Unfortunately however, use of the lamellar model does not generate reliable parameters from the modelling of these systems due to the contribution of micelle form and structure factor to the scattering being so prominent. This effect thus masks the true thickness of the aggregates, defined by the point of upturn in the scattering from the background to q^{-2} , meaning the lamellar modelling for low q becomes a balancing exchange between the input scale factor and thickness. Note the error margin for thickness in the provided fit is 2.5 nm, greater than the calculated thickness of 1.1 nm (Table S2). Therefore the lamellar model can not be meaningfully used in systems where a significant

concentration of background micelles are present, and the mass fractal model thus provides a more useful representation of the data.

Table S2: Fitting parameters for the lamellar and core-shell ellipsoid models applied to the 25 mM CTAB with 0.1 mg/mL GO data set (Fig. S8).

Surfactant	Concentration mM	Scale	Bilayer thickness nm	$R_{Eq.}$ nm	$R_{Ax.}$ nm	Volume fraction %	Charge e^{-}	Salt concentration mM
CTAB	25	2.80×10^{-3}	1.1 ± 2.5	2.4	3.7	0.73	49.0	5.24

Table S3: Fitting parameters for cationic surfactants. Aside from pure surfactant solutions, all data are fit using a combination of mass fractal and ellipsoid models with Hayter-Penfold structure factor. $R_{eq.}$ and $R_{ax.}$ are the equatorial and axial radii of the micelles respectively. Scattering length densities of the solvent (D_2O) and micelles were kept constant at 6.3 and $1 \times 10^{-6} \text{ \AA}^{-2}$ respectively.

Carbon nanomaterial	Surfactant	Concentration mM	Scale	Mass fractal dimension	Cutoff length nm	$R_{eq.}$ nm	$R_{ax.}$ nm	Volume fraction %	Charge e^{-}	Salt concentration mM
-	DTAB	25	-	-	-	1.7	2.7	0.34	9.4	5.34
-	TTAB	25	-	-	-	2.0	3.2	0.79	14.6	1.20
-	CTAB	25	-	-	-	2.3	3.8	0.96	21.6	0.12
GO	DTAB	25	4.45×10^{-4}	1.87	1500	1.9	1.5	0.43	7.2	0.02
GO	TTAB	25	8.38×10^{-4}	1.77	2000	2.1	2.8	0.60	24.1	1.43
GO	CTAB	25	5.95×10^{-4}	1.98	100000	2.4	3.6	0.72	49.1	4.83
rGO	DTAB	25	4.00×10^{-4}	1.71	4000	2.2	1.2	0.44	10.8	1.37
rGO	TTAB	25	4.84×10^{-4}	1.76	3000	2.1	2.8	0.64	18.1	0.12
rGO	CTAB	25	6.04×10^{-4}	1.79	5652.2	2.4	3.4	0.80	25.9	0.17

Table S4: Fitting parameters for 2.5 mM CTAB samples. Aside from blank 2.5 mM CTAB, all data are fit using a sum of mass fractal and ellipsoid models. At this surfactant concentration, no structure factor was required. $R_{eq.}$ and $R_{ax.}$ are the equatorial and axial radii of the micelles respectively. Scattering length densities of the solvent (D_2O) and micelles were kept constant at 6.3 and $1 \times 10^{-6} \text{ \AA}^{-2}$ respectively.

Carbon nanomaterial	Surfactant	Concentration mM	Scale 1	Particle radius nm	Mass fractal dimension	Cutoff length nm	Scale 2	$R_{Eq.}$ nm	$R_{Ax.}$ nm
-	CTAB	2.5	-	-	-	-	1.09×10^{-3}	3.1	1.8
GO	CTAB	2.5	2.74×10^{-4}	5.1	2.14	39.1	1.11×10^{-3}	2.7	1.0
rGO	CTAB	2.5	1.66×10^{-4}	4.8	2.07	63.7	1.03×10^{-3}	3.0	1.4

Table S5: Ellipsoid model fitting parameters with Hayter-Penfold structure factor for anionic surfactants. $R_{eq.}$ and $R_{ax.}$ are the equatorial and axial radii of the micelles respectively. Scattering length densities of the solvent (D_2O) and micelles were kept constant at 6.3 and $1 \times 10^{-6} \text{ \AA}^{-2}$ respectively.

Carbon Nanomaterial	Surfactant	Concentration mM	$R_{eq.}$ nm	$R_{ax.}$ nm	Volume fraction %	Charge e^-	Salt concentration mM
-	SDS	25	1.8	2.7	0.52	12.6	1.16
-	AOT	25	1.2	2.6	0.81	14.9	1.86
GO	SDS	25	1.7	2.6	0.48	12.2	1.35
GO	AOT	25	1.2	2.5	0.73	19.7	6.15
rGO	SDS	25	1.7	2.7	0.49	17.4	1.98
rGO	AOT	25	1.2	2.5	0.72	20.0	6.56

Table S6: Fitting parameters for Triton X-100. Aside from the pure surfactant samples, all data are fit using a sum of mass fractal and cylinder models. $R_{eq.}$ and $R_{ax.}$ are the equatorial and axial radii of the micelles respectively. Scattering length densities of the solvent (D_2O) and micelles were kept constant at 6.3 and $1 \times 10^{-6} \text{ \AA}^{-2}$ respectively.

Carbon nanomaterial	Surfactant	Concentration mM	Scale 1	Particle radius nm	Mass fractal dimension	Cutoff length nm	Scale 2	Radius nm	Length nm
-	Triton X-100	10	-	-	-	-	6.23×10^{-3}	2.1	8.8
GO	Triton X-100	10	6.93×10^{-4}	-	1.68	20000.0	4.59×10^{-3}	2.2	7.4
rGO	Triton X-100	10	5.30×10^{-4}	1.0	1.70	100.0	4.80×10^{-3}	2.3	7.4
-	Triton X-100	1	-	-	-	-	4.06×10^{-4}	2.3	7.4
GO	Triton X-100	1	8.32×10^{-5}	7.0	2.03	50.0	4.23×10^{-4}	2.7	2.8
rGO	Triton X-100	1	6.53×10^{-5}	4.8	2.11	53.7	1.94×10^{-3}	2.8	0.5

The rod/cylinder (or ellipsoid) model used in modelling data with TX-100 was from Feigin and Svergun,¹⁰ follows the same principles as the ellipsoid model and is explained in detail above.

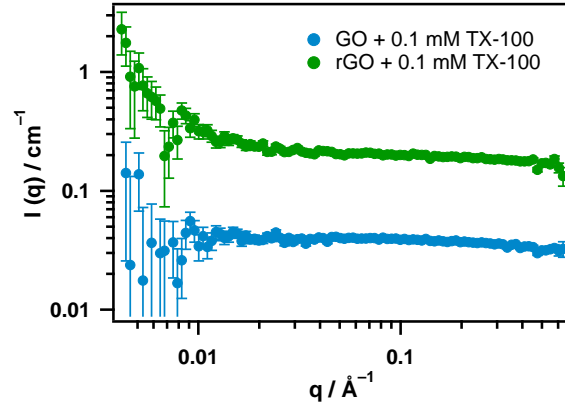


Figure S9: SANS data for 0.1 mg/mL GO and rGO with 0.1 mM Triton X-100. The data for rGO has been offset for clarity.

Table S7: Fitting parameters for $C_{12}E_6$ with GO and rGO. These data were fit using cylinder models for the pure surfactant samples, and a sum of mass fractal and cylinder models where carbon nanomaterials and surfactants were present. Scattering length densities of the solvent (D_2O) and micelles were kept constant at 6.3 and $1 \times 10^{-6} \text{ \AA}^{-2}$ respectively.

Carbon nanomaterial	Surfactant	Concentration mM	Scale 1	Particle radius nm	Mass fractal dimension	Cutoff length nm	Scale 2	Radius nm	Length nm
-	$C_{12}E_6$	10	-	-	-	-	5.61×10^{-3}	2.1	10.6
GO	$C_{12}E_6$	10	1.19×10^{-3}	1.5	1.73	1000.0	4.94×10^{-3}	3.0	3.2
rGO	$C_{12}E_6$	10	5.05×10^{-5}	1.7	1.98	9845.0	6.27×10^{-3}	2.0	8.9
-	$C_{12}E_6$	1	-	-	-	-	6.51×10^{-4}	1.8	8.5
rGO	$C_{12}E_6$	1	4.15×10^{-5}	-	1.99	2118	5.33×10^{-4}	1.6	9.2

Table S8: Fitting parameters for 1 mM $C_{12}E_6$ with GO. This data set was fit using a sum of lamellar and cylinder models. Scattering length densities of the solvent (D_2O) and micelles were kept constant at 6.3 and $1 \times 10^{-6} \text{ \AA}^{-2}$ respectively.

Carbon nanomaterial	Surfactant	Concentration mM	Scale 1	Radius nm	Length nm	Scale 2	Thickness nm
GO	$C_{12}E_6$	1	7.02×10^{-3}	0.4	3.5	1.59×10^{-4}	9.6

Table S9: Flexible cylinder fitting parameters for pure C₁₂E₅ samples. At 10 mM, a two-power law model was also used to fit the USANS region. Scattering length densities of the solvent (D₂O) and micelles were kept constant at 6.3 and $1 \times 10^{-6} \text{ \AA}^{-2}$ respectively.

Surfactant	Concentration mM	Scale 1	Lower q power	Higher q power	Crossover point \AA^{-1}	Scale 2	Radius nm	Length nm	Kuhn length nm
C ₁₂ E ₅	10	5.48×10^{-4}	1.64	0.41	6.30×10^{-4}	5.47×10^{-3}	2.1	207.9	26.9
C ₁₂ E ₅	1	-	-	-	-	5.12×10^{-4}	1.8	103.3	11.7

The flexible cylinder or ‘worm’ model is presented in Pederson *et al.*¹²

$$I_{WC}(q, L, b, R_{CS}) = c \Delta \rho_m^2 M S_{WC}(q, L, b) P_{CS}(q, R_{CS})$$

Where c is the surfactant concentration, M is the molecular weight of the micelles and $S_{WC}(q, L, b)$ represents the scattering function of a semi-flexible chain without volume effects in which L/b is the number of statistical segments in the chain:

$$S_{WC}(q, L, b) = [(1 - \chi(q, L, b)) S_{chain}(q, L, b) + \chi(q, L, b) S_{rod}(q, L)] \Gamma(q, L, b)$$

Chen *et al* included corrections to the formula by accounting for intermicellar interactions by including the parameter in the following equation,¹³ which is currently used in modelling flexible cylinders in SasView:

$$f_{corr}(q) w(q R_G) [1.22(q R_G)^{-1/0.585} + 0.4288(q R_G)^{-2/0.585} - 1.651(q R_G)^{-3/0.585}]$$

Table S10: Fitting parameters for C₁₂E₅ with GO and rGO. Data were fit using a sum of mass fractal and flexible cylinder models. Scattering length densities of the solvent (D₂O) and micelles were kept constant at 6.3 and $1 \times 10^{-6} \text{ \AA}^{-2}$ respectively.

Carbon nanomaterial	Surfactant	Concentration mM	Scale 1	Particle radius nm	Mass fractal dimension	Cutoff length nm	Scale 2	Radius nm	Length nm	Kuhn length nm
GO	C ₁₂ E ₅	10	7.21×10^{-4}	-	1.88	2217.2	4.01×10^{-3}	2.1	269.1	20.5
rGO	C ₁₂ E ₅	10	6.50×10^{-5}	-	2.12	6000.0	5.22×10^{-3}	2.1	165.4	28.6
rGO	C ₁₂ E ₅	1	4.64×10^{-4}	-	1.64	625.5	1.63×10^{-5}	3.9	100.0	6.8

Table S11: Fitting parameters for 1 mM C₁₂E₅ with GO. This data set was fit using a sum of lamellar and flexible cylinder models. Scattering length densities of the solvent (D₂O) and micelles were kept constant at 6.3 and $1 \times 10^{-6} \text{ \AA}^{-2}$ respectively.

Carbon nanomaterial	Surfactant	Concentration mM	Scale 1	Radius nm	Length nm	Scale 2	Thickness nm
GO	C ₁₂ E ₅	1	2.61×10^{-3}	0.8	1.5	2.18×10^{-4}	9.8

Table S12: Fitting parameters for C₁₂E₄ with GO and rGO. All data including pure surfactant samples were fit using a sum of mass fractal and vesicle models. Scattering length densities of the solvent (D₂O) and micelles were kept constant at 6.3 and $1 \times 10^{-6} \text{ \AA}^{-2}$ respectively.

Carbon nanomaterial	Surfactant	Concentration mM	Scale 1	Particle radius nm	Mass fractal dimension	Cut off length nm	Volume fraction %	Radius nm	Polydispersity of radius %	Thickness nm
-	C ₁₂ E ₄	10	1.83×10^{-3}	1.6	2.02	466.1	0.12	25.1	36.5	4.8
GO	C ₁₂ E ₄	10	1.39×10^{-3}	2.7	2.12	832.9	0.38	30.8	47.2	1.4
rGO	C ₁₂ E ₄	10	5.45×10^{-4}	-	2.16	719.9	0.31	33.0	22.4	3.5
-	C ₁₂ E ₄	1	4.41×10^{-6}	-	2.41	2948.6	0.04	38.3	27.8	3.8
GO	C ₁₂ E ₄	1	3.51×10^{-4}	8.3	2.10	1281.6	0.07	4.1	10.4	0.4
rGO	C ₁₂ E ₄	1	4.35×10^{-5}	4.2	2.36	3892.2	0.11	15.5	47.1	0.6

The model providing the form factor, $P(q)$, for a unilamellar vesicle is from Guinier and Fournet,¹⁴ and is represented by the following:

$$P(q) = \frac{scale}{V_{shell}} \left[\frac{3V_1(\rho_1 - \rho_2)J_1(qR_1)}{(qR)_1} + \frac{3V_2(\rho_2 - \rho_{solv})J_1(qR_2)}{(qR)_2} \right]^2 + background$$

Where V_{shell} is the volume of the shell, V_1 is the volume of the core and V_2 is the total volume. R_1 is the radius of the core and R_1 is the radius from the core to the shell in \AA . $J_1 = (\sin x - x \cos x)/x^2$. Polydispersity for vesicle radius was also included in the fitting algorithm for C₁₂E₄ systems.

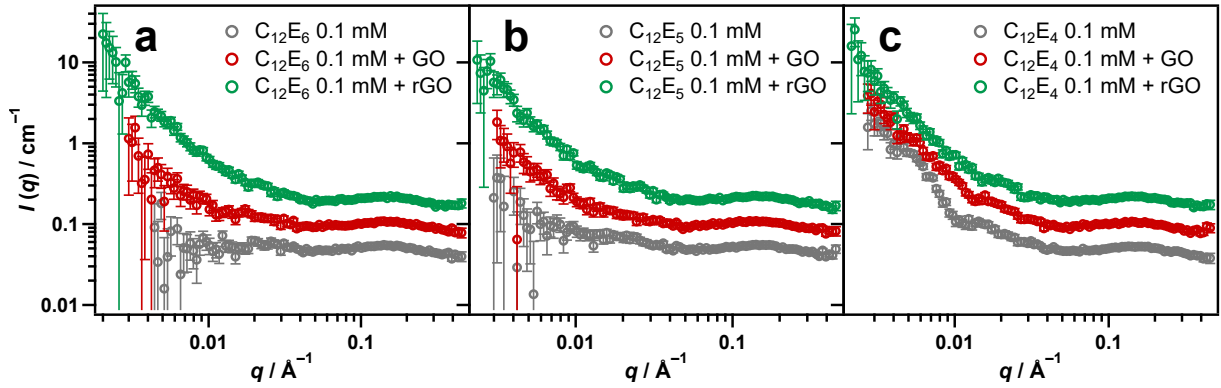


Figure S10: SANS data for 0.1 mM $C_{12}E_6$ (a), 0.1 mM $C_{12}E_5$ (b) and 0.1 mM $C_{12}E_4$ (c) with 0.1 mg/mL GO and rGO. The data for GO and rGO has been offset by multiplication for clarity.

Table S13: Fitting parameters for erucyl amidopropyl betaine (EAPB) and oleyl amidopropyl betaine (OAPB). Aside from the pure surfactant samples, all data are fit using a sum of mass fractal and flexible cylinder models. Radius is the cross-sectional radius of the wormlike micelles and Kuhn length is the apparent length over which the wormlike structures appear rigid. Scattering length densities of the solvent (D_2O) and micelles were kept constant at 6.3 and $1 \times 10^{-6} \text{ \AA}^{-2}$ respectively.

Carbon nanomaterial	Surfactant	Concentration mM	Scale 1	Particle radius nm	Mass fractal dimension	Cutoff length nm	Scale 2	Radius nm	Kuhn length nm	Length nm
-	OAPB	10	-	-	-	-	5.00×10^{-3}	2.2	74.6	126.3
-	EAPB	10	-	-	-	-	9.43×10^{-3}	2.9	38.5	34.9
GO	OAPB	10	9.52×10^{-4}	2.6	2.0	1341.4	3.24×10^{-3}	1.9	59.8	847.3
rGO	OAPB	10	3.02×10^{-4}	1.0	2.0	500.0	3.58×10^{-3}	2.2	29.3	4,626.1
GO	EAPB	10	1.37×10^{-3}	2.0	2.0	4264.8	1.54×10^{-3}	2.8	15.6	10000.0
rGO	EAPB	10	8.17×10^{-4}	1.8	2.0	44.6	3.22×10^{-3}	2.9	61.3	245.0
-	OAPB	1	-	-	-	-	4.02×10^{-4}	2.4	54.6	218.6
GO	OAPB	1	1.82×10^{-4}	6.5	2.0	79.0	4.82×10^{-4}	1.4	34.0	136.0
rGO	OAPB	1	2.15×10^{-4}	6.6	2.0	200.0	6.74×10^{-4}	0.9	39.2	100.3
GO	OAPB	0.1	-	-	-	-	-	-	-	-
GO	EAPB	0.1	7.47×10^{-6}	-	2.4	35.8	-	-	-	-

Modelling for samples with EAPB and OAPB was carried out using the same flexible cylinder model as for $C_{12}E_5$.

Table S14: First level unified power model fitting parameters for polyethylene glycol (PEG) and Pluronic F127 polymer samples. R_g is the radius of gyration of the aggregates while power, B_i and G_i are parameters of the Debye equation.

Carbon Nanomaterial	Polymer	Concentration mg/mL	R_g nm	Power	B_i cm^{-1}	G_i cm^{-1}
-	PEG	1.5	22.2	1.80	0.008	59.5
-	Pluronic F127	1.5	4.0	0.10	1.787	2.7
GO	PEG	1.5	15.2	1.37	0.007	8.1
GO	Pluronic F127	1.5	10.7	1.34	0.032	8.0
rGO	PEG	1.5	36.3	1.54	0.036	547.1
rGO	Pluronic F127	1.5	26.7	1.20	0.094	124.2

For polymer and GO/rGO systems, a unified power model was employed to approximate the scattering of the mass fractal clusters (*i.e.* the GO and rGO sheets) and random coils (*i.e.* the polymers) *in situ*.^{15,16} This model uses multiple exponential or power laws (referred to as levels) to define the scattering of a variety of particle types and is ideal for mass fractal systems. The function for calculating scattering intensity is:

$$I(q) = \text{background} + \sum_{i=1}^N \left[G_i \exp\left(-\frac{q^2 R_{gi}^2}{3}\right) + B_i \exp\left(-\frac{q^2 R_{g(i+1)}^2}{3}\right) \left(\frac{1}{q_i^*}\right)^{P_i} \right]$$

where

$$q_i^* = q \left[\text{erf}\left(\frac{q R_{gi}}{\sqrt{6}}\right) \right]^{-3}$$

Each level is represented by one of the following parameters: G_i , R_{gi} , B_i and P_i .

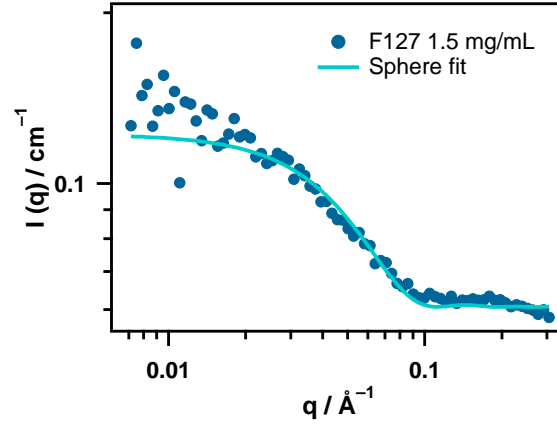


Figure S11: SANS data for pure 1.5 mg/mL Pluronic F127 modelled using a spheres model instead of a unified power model.

Table S15: Sphere model fitting parameters for pure Pluronic F127 polymer. Scattering length densities of the solvent (D_2O) and micelles were kept constant at 6.3 and $1 \times 10^{-6} \text{ \AA}^{-2}$ respectively.

Carbon Nanomaterial	Polymer	Concentration mg/mL	Radius nm
-	Pluronic F127	1.5	4.0

Details for the sphere model used to fit 1.5 mg/mL Pluronic F127 is from Guinier and Fournet.¹⁴ The equation for the scattering intensity, $I(q)$, as a function of the scattering vector, q , for spheres is as follows:

$$I(q) = \frac{scale}{V} \left[\frac{3V(\Delta\rho)(\sin(qr) - qr \cos(qr))}{(qr)^3} \right]^2 + background$$

Where V is the volume of the scatterer, r is the radius of the sphere in \AA , $scale$ is the volume fraction, $\Delta\rho$ is the contrast (difference in scattering length density between the solvent and scatterer) and the background is in cm^{-1} .

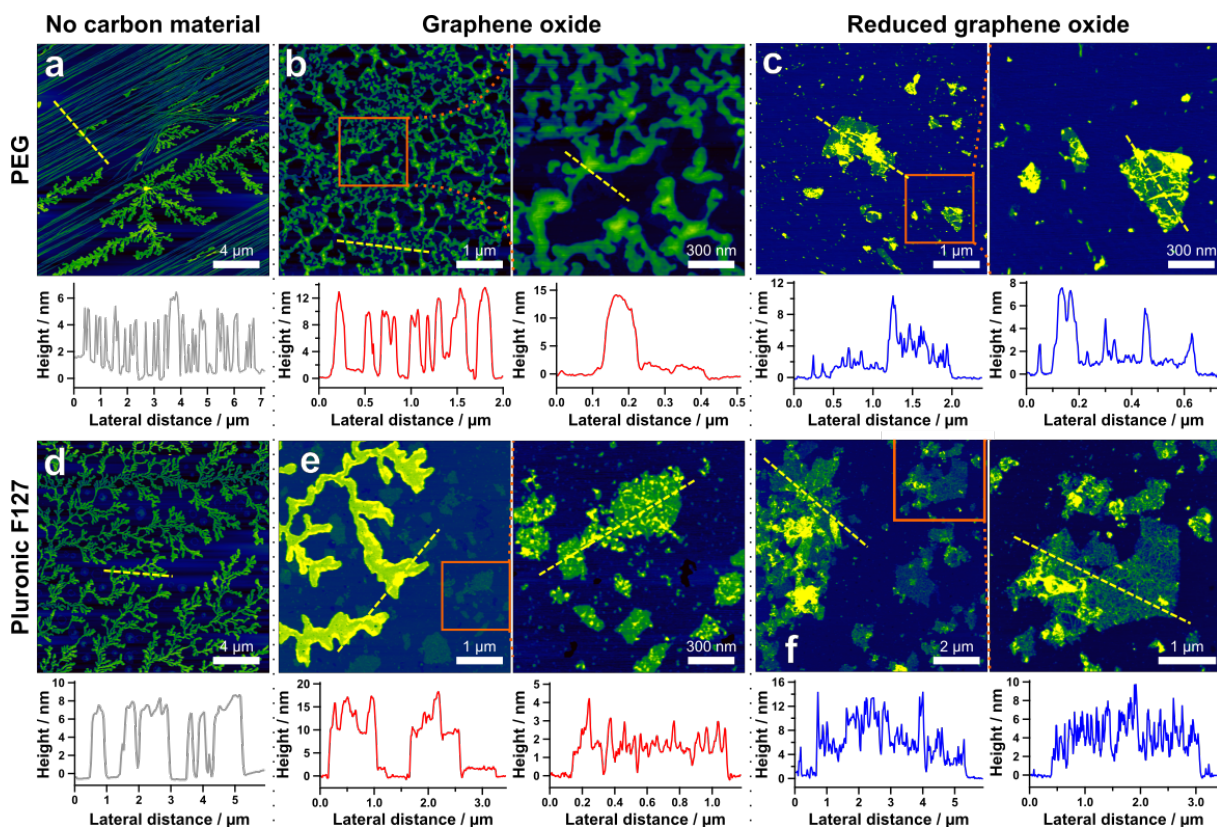


Figure S12: AFM images of 0.1 mg/mL of polymer with or without 0.1 mg/mL GO or rGO dispersions: (a) AFM height images of PEG (a) with GO (b) and rGO (c). AFM height images of pluronic F127 (d) with GO (e) and rGO (f). Height profiles corresponding to the dashed yellow cross sections are shown below each respective image. Higher magnification images correspond to the area inside the orange boxes. Samples are dried on mica substrate.

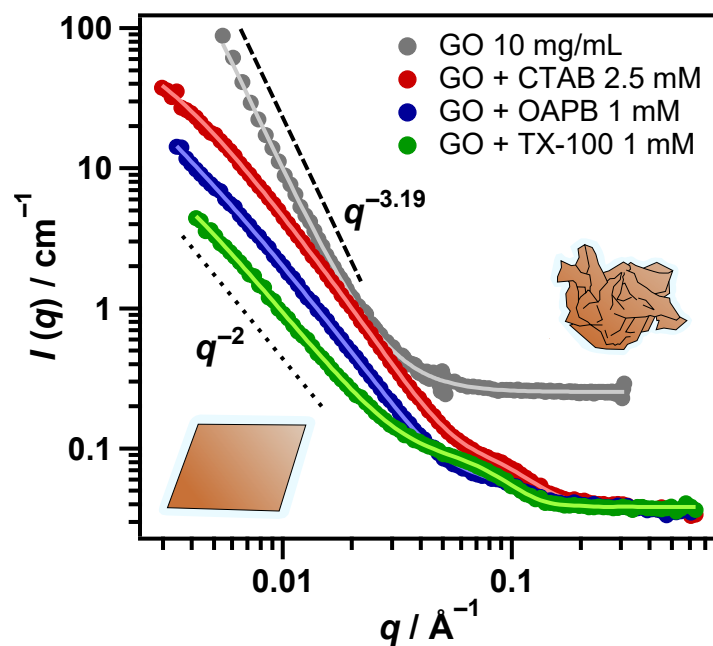


Figure S13: SANS data demonstrating the change in slope from q^{-3} (crumpled fractal sheets) for pure aqueous GO dispersion at 10 mg/mL to q^{-2} (flat surfaces) with the inclusion of either a cationic (CTAB), zwitterionic (OAPB) or nonionic (TX-100) surfactant. Concentration of GO in samples with surfactant is 0.1 mg/mL. The data set with 10 mg/mL GO has been offset by multiplication ($\times 5$) for clarity.

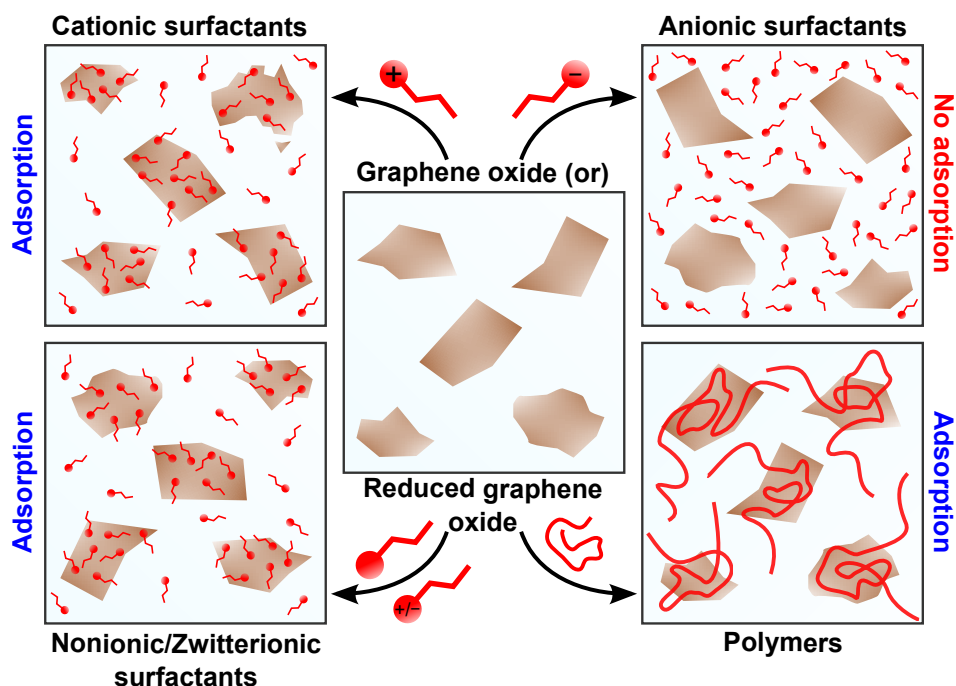


Figure S14: Schematic summarising adsorption interactions of graphene oxide and reduced graphene oxide with each surfactant class and polymers investigated in this study.

References

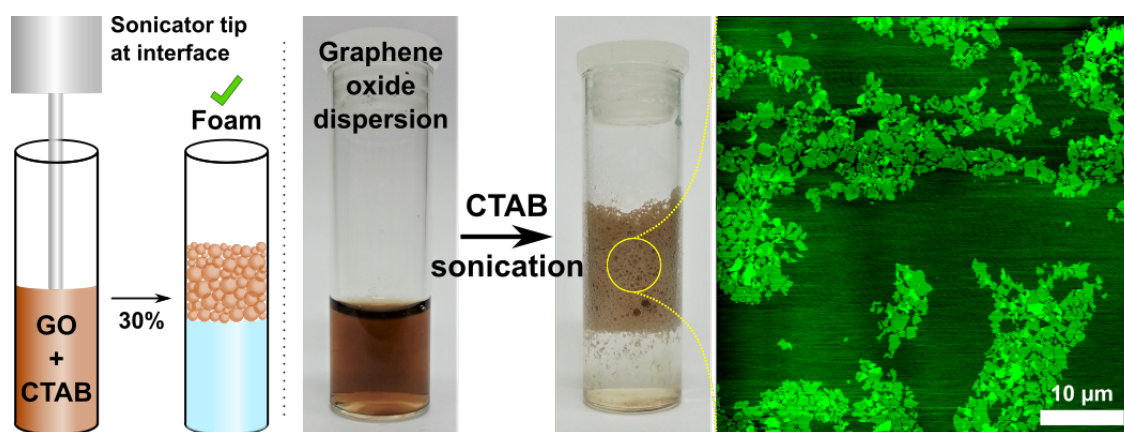
- [1] Mildner, D. F. R., Hall, P. L. Small-angle scattering from porous solids with fractal geometry. *J. Phys. D: Appl. Phys.* **1986** *19*, 1535–1545.
- [2] Berry, J. D., Neeson, M. J., Dagastine, R. R., Chan, D. Y., Tabor, R. F. Measurement of Surface and Interfacial Tension using Pendant Drop Tensiometry. *J. Colloid Interface Sci.* **2015** *454*, 226 – 237.
- [3] Kotlarchyk, M., Chen, S.-H. Analysis of small angle neutron scattering spectra from polydisperse interacting colloids. *J. Chem. Phys.* **1983** *79*, 2461–2469.
- [4] Berr, S. Solvent isotope effects on alkytrimethylammonium bromide micelles as a function of alkyl chain length. *J. Phys. Chem.* **1987** *91*, 4760–4765.
- [5] Hayter, J. B., Penfold, J. An analytic structure factor for macroion solutions. *Mol. Phys.* **1981** *42*, 109–118.

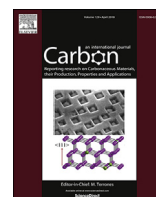
- [6] Hayter, J. B., Penfold, J. Self-consistent Structural and Dynamic Study of Concentrated Micelle Solutions. *J. Chem. Soc., Faraday Trans. I* **1981** *77*, 1851–1863.
- [7] Hansen, J.-P., Hayter, J. B. A rescaled MSA structure factor for dilute charged colloidal dispersions. *Molecular Physics* **1982** *46*, 651–656.
- [8] Hayter, J. B., Penfold, J. Determination of Micelle Structure and Charge by Small-Angle Neutron Scattering. *Colloid Polym. Sci.* **1983** *261*, 1022–1030.
- [9] Wu, C., Chan, D. Y., Tabor, R. F. A simple and accurate method for calculation of the structure factor of interacting charged spheres. *J. Colloid Interface Sci.* **2014** *426*, 80–82.
- [10] Feigin, L., Svergun, D. I., Taylor, G. W. General principles of small-angle diffraction. In *Structure analysis by small-angle X-ray and neutron scattering*. Springer, **1987**, pages 25–55.
- [11] Berghausen, J., Zipfel, J., Lindner, P., Richtering, W. Influence of water-soluble polymers on the shear-induced structure formation in lyotropic lamellar phases. *J. Phys. Chem. B* **2001** *105*, 11081–11088.
- [12] Pedersen, J. S., Schurtenberger, P. Scattering Functions of Semiflexible Polymers with and without Excluded Volume Effects. *Macromolecules* **1996** *29*, 7602–7612.
- [13] Chen, W.-R., Butler, P. D., Magid, L. J. Incorporating intermicellar interactions in the fitting of SANS data from cationic wormlike micelles. *Langmuir* **2006** *22*, 6539–6548.
- [14] Guinier, A., Fournet, G., Walker, C. Small angle scattering of X-rays. *J. Wiley & Sons, New York* **1955** .
- [15] Beaucage, G. Approximations leading to a unified exponential/power-law approach to small-angle scattering. *J. Appl. Crystallogr.* **1995** *28*, 717–728.
- [16] Beaucage, G. Small-angle scattering from polymeric mass fractals of arbitrary mass-fractal dimension. *J. Appl. Crystallogr.* **1996** *29*, 134–146.

Chapter 7

Highly efficient recovery of graphene oxide by froth flotation using a common surfactant

Published: Thomas M. McCoy, Huw C. W. Parks and Rico F. Tabor, Highly efficient recovery of graphene oxide by froth flotation using a common surfactant. *Carbon*, 2018, **135**, 164-170.





Highly efficient recovery of graphene oxide by froth flotation using a common surfactant

Thomas M. McCoy^a, Huw C.W. Parks^{a, b}, Rico F. Tabor^{a, *}

^a School of Chemistry, Monash University, Clayton, 3800, Australia

^b School of Chemistry, Cardiff University, Cardiff, CF10 3AT, United Kingdom

ARTICLE INFO

Article history:

Received 26 January 2018

Received in revised form

24 March 2018

Accepted 14 April 2018

Available online 17 April 2018

Keywords:

Graphene oxide

Flotation

Foam

Cetyltrimethylammonium bromide

ABSTRACT

In this work, it is shown that graphene oxide (GO) sheets can be effectively recovered from aqueous solution by a simple froth flotation method. Small amounts of cetyltrimethylammonium bromide (CTAB) are added to assist with flocculating and driving the GO to the air–water interface, then ultrasonication is employed to form a foam that entrains the GO. The surfactant is essential in this process by firstly destabilising the GO dispersion through surface charge neutralisation, allowing the particles to aggregate. Furthermore, the hydrophobic component of the adsorbed surfactant molecules enhances adsorption of the GO at the air–water interface. Positioning the sonicator tip precisely at the air–water interface is crucial for foam formation by ensuring air bubbles are entrained into the sample. The nature of the foam can also be manipulated by altering the sonication intensity or by incorporating additional surfactant additives. At ideal GO:CTAB ratios, almost full removal (>99%) of the GO from an aqueous dispersion is achieved, with minimal overall change in the particle size distribution of the GO. It is shown that this process can also be used when GO is employed as an adsorbent for removing toxic metals and organic species from aqueous solution.

© 2018 Elsevier Ltd. All rights reserved.

1. Introduction

Froth flotation is an efficient and low energy separation technique that is widely used in industry for the selective removal of materials from water, being commonly employed in areas such as minerals processing [1,2] and wastewater treatment [3]. This technique involves bubbles rising through an aqueous mixture, and exploits differences in the attachment efficiencies of the materials at the air–water interface, to enable their selective separation [4,5]. Froth flotation can be used on a broad variety of materials, from molecules to colloidal particles, and is exceptional in its ability to deal with large industrial fluid volumes. The fact that bubbles are of low density and rise rapidly means that fast, low energy mixing and separation occur within a vessel [6]. Furthermore, the entrainment of materials in a concentrated froth or foam that floats on top of the aqueous subphase enables easy collection simply by skimming or spilling over of the froth, unlike separation of particulates through sedimentation. Hence froth flotation is a comparatively efficient and effective separation technique with excellent economical value

[7].

Likewise, the interest surrounding graphene oxide (GO), an atomically thin material derived from the graphite carbon lattice, has soared in recent years [8]. Unlike pristine graphene, GO has a rich composition of oxygen-containing functional groups which serve to make the material hydrophilic [9,10], hence GO has potential in aqueous applications such as adsorbents for water treatment or mineral extraction where the use of pristine graphene would be impractical. However, of paramount importance to its deployment is the efficient removal of the GO itself from water for its use as an adsorbent to be industrially viable; a method such as froth flotation to enable this would be ideal. Membrane filtration could also be a useful method for recovering GO from water, as filters with nanoscale pore sizes are commercially ubiquitous and would easily capture large GO sheets. However, filters for the industrial scale do not typically have pore sizes below 1 μm, due to significant decreases in the rate of diffusion [11]. As such it is possible that the majority of sub-micron sheets may not be captured by the membrane. Furthermore, particles with potentially large lateral dimensions like GO sheets can very quickly result in pore blocking, which may render the filter ineffective [12]. Accumulation of matter on the membrane can also eventually lead to

* Corresponding author.

E-mail address: rico.tabor@monash.edu (R.F. Tabor).

fouling which can negatively impact the performance of the filter and reduce its lifespan [13]. Membrane filters therefore have the disadvantage of requiring constant upkeep, whereas froth flotation relies only on the surface chemistry.

GO sheets have been shown to exhibit surfactant-like properties and adsorb at a variety of interfaces including air–liquid [14]. This effect has been attributed to the amphiphilic character of the sheets, with the hydrophobicity being greater on their basal plane [15–18]. Therefore the entrainment of GO particles within a foam should be readily achievable. However, GO sheets in water exhibit a strong negative surface potential as a result of readily deprotonated carboxylic groups around their periphery, thus the sheets are highly stabilised against aggregation through electrostatic inter-particle repulsions [19,20]. Because of this effect, we have shown recently that clean GO sheets do not spontaneously adsorb at interfaces, and remain favourably solvated in the bulk water [14]. Therefore, GO must be rendered surface active, which can be achieved by employing a surface active ‘collector’ [14], such as a surfactant molecule, to enhance the foamability of GO and facilitate its recovery via froth flotation.

The addition of surfactants to colloidal dispersions of hydrophilic silica particles has been identified as a pathway to boosting the foamability of the particles [21–24]. The physical basis for this phenomenon is that the surfactant molecules adsorb to the surfaces of the particles, increasing their hydrophobicity such that the particles and surfactants then collectively adsorb to the air–water interface [25,26]. Foams stabilised by solid particles are known as ‘Pickering’ [27] (or ‘Ramsden’) [28] foams, and are a well established commodity in colloid science. As GO sheets are microscopic in size (and particulate in nature), foams stabilised by GO are of the Pickering variety [29]. Particle-stabilised foams show unprecedented stability due to their high desorption energy from the surfaces of the bubbles [30,31]; this effect is amplified when high aspect ratio nanosheets are used [32,33]. Therefore, utilising GO in the stabilisation of foams can be expected to offer enhanced stability to coalescence or collapse of the foam. The process of stabilising a foam however, as with emulsions, relies on the presence of a surface active or surface adsorbed component, hence the importance of surfactant inclusion in the case of GO systems.

In this work, we develop and explore a recovery method for GO from aqueous solution by capturing the sheets within a foam network. Cetyltrimethylammonium bromide (CTAB) surfactant is incorporated to facilitate this process, and the synergistic effects of the two components are investigated to understand the key factors driving foam formation. Previous work has reported the separation of carbon nanoribbons by froth flotation [34]; however, the focus was on statistical analysis and modeling of the separation. Our work focuses on the fundamental physical chemistry of the foaming phenomenon for GO nanosheets, and optimising the recovery process such that maximal capture is achieved in the most efficient way. CTAB has been used as an aid for GO synthetic procedures [35,36]. Other studies on foam preparation using two-dimensional carbon nanomaterials involve high energy and low yielding techniques such as freeze drying [37,38], chemical vapour deposition [39] and electrochemistry [40], therefore a facile and thermodynamically driven foaming process may improve the feasibility of GO use at larger scales.

2. Experimental

Graphene oxide was synthesised from graphite flakes (Sigma, +100 mesh) according to the improved Hummers’ method of Marciano et al. [41] Changes to the procedure include an incremental addition of the potassium permanganate prior to heating the mixture, and purification by dialysis for 1 week (cellulose dialysis

tubing, 14 kDa molecular weight cutoff, Sigma) after an initial 3 cycles of centrifugation (4000 rpm), in which redispersion of the GO in ultrapure water was undertaken. The product was kept and characterised in aqueous suspension at all times.

Flotation and foaming of the GO was achieved by ultrasonication using a Branson 450 Digital Sonifier (20 kHz frequency, 400 W max power). A specified concentration of cetyltrimethylammonium bromide (ChemSupply, ≥95%) was added to the GO dispersion then mixed initially by gentle shaking. For froth flotation, the tip of the ultrasonic probe was then positioned precisely at the air–liquid interface of each sample. Sonication amplitudes were then varied between 10%, 30% and 50% of the maximum amplitude for the microtip used, corresponding to energy inputs of 0.79, 2.55 and 4.05 W/cm³ for this instrument (see [Supplementary Data](#) for calculations), and the total sonication time kept constant at 30 s. Characterisation of the resultant foams by light microscopy imaging was conducted using a Kozo XJP-300 polarizing microscope with a 4× magnification microscope objective lens and an attached CCD camera (Flea3, Point Grey, Richmond, BC, Canada). Foam material was moved by spatula onto a glass slide after which a cover slip was gently mounted to create an even plane of focus for imaging. Cocamidopropyl betaine (CAPB) was obtained from Aussie Soap Supplies as a 35% solution in water by mass.

Zeta potentials of GO/CTAB systems were measured by phase analysis light scattering using a Brookhaven Nanobrook Omni. Data points were averaged from 5 measurements for each sample with each measurement comprising 20 phase cycles at 25 °C. The palladium electrode was immersed carefully to ensure no bubbles were created and cuvettes were made from polystyrene with pathlengths of 1.0 cm. Zeta potentials, ζ , were determined according to the Smoluchowski approximation:

$$u_E = \frac{v_E}{E} = \frac{\zeta \epsilon}{\eta}$$

where u_E is the electrophoretic mobility, v_E is the electrophoretic velocity, E is the electric field strength, ϵ is the permittivity and η is the viscosity of the medium.

Atomic force microscopy characterisation of the GO before and after being subjected to the flotation process was performed using a JPK NanoWizard 3. Samples were prepared by spin coating a small aliquot (< 5 μ L) of diluted GO dispersion (0.1 mg/mL) onto a freshly cleaved mica disk (ProSciTech) for 1 min (2000 rpm). Images were 50 μ m² in area and obtained in tapping mode with a set-point value around 0.6 V and a line rate of less than 0.5 Hz. Cantilevers were Bruker NCHV model with nominal spring constants of 20–80 N/m and resonant frequencies around 320 kHz. The images were refined using the JPK data processing software, however analysis of individual sheet lateral dimensions were performed using Gwyddion software [42]. Post-flotation GO was purified of surfactant by initially redispersing the foam in 1 M HCl and centrifuging at 8000 rpm for 15 min. The GO was then washed twice in a 50/50 mixture of water and ethanol with further centrifugation to remove as much CTAB as possible. Final redispersion of the GO was in ultrapure water only.

Quantification of cadmium chloride (BDH Chemicals, ≥99.5%) removal was performed using atomic absorption spectroscopy (AAS) on a GBC Scientific Equipment XplorAA with an air–acetylene flame ionisation detector. The instrument was fitted with a Cadmium element lamp and analysis was performed at a wavelength of 228.8 nm with a slit width of 0.5 nm. Caffeine (Sigma, ≥99.5%) removal was monitored by UV–visible spectrophotometry on a Cary 60 instrument from Agilent Technologies in 1 cm path-length quartz cuvettes across the wavelength range 200–350 nm. All samples were prepared by adding the specific

adsorbate to the GO dispersion followed by CTAB, and then performing the flotation step. The remaining liquid beneath the foam was then filtered (0.4 μm syringe filters) to remove any large aggregates or GO, and diluted as required before measuring. The precise quantities of cadmium and caffeine remaining in solution were then calculated by comparing the results with the determined calibration curves for each compound (see [Supplementary Data](#)).

3. Results and discussion

The process of froth flotation relies on the attachment of materials to bubbles in order to cause their separation from a bulk aqueous solution or dispersion. Therefore, as GO is intrinsically hydrophilic and stable to aggregation through strong electrical double-layer repulsions, the simple act of bubbling a gas through a GO suspension does not result in the formation of a GO-stabilised foam [18]. Therefore, a change to the system is required to drive the GO to the air–water interface. As has been previously shown, a cationic photosurfactant (azoTAB) with a trimethylammonium headgroup has a very strong affinity for GO sheets through opposite charge attraction and can induce their flocculation [43]. Addition of the same surfactant was also found to result in spontaneous adsorption of the GO sheets at air–water and oil–water interfaces due to enhanced surface activity from GO/surfactant synergism [14]. Therefore, cetyltrimethylammonium bromide (CTAB), a common and inexpensive cationic surfactant and analogue of azoTAB, was chosen to mediate the removal of GO from aqueous systems by froth flotation. Strong interactions and self-assembly between CTAB and GO have also been proven by Meng and co-workers [44].

We started by exploring different ratios of CTAB and GO to find the optimum concentration range in which to perform flotation. CTAB has been previously found to cause gelation of GO at small CTAB additions when GO is at 5 mg/mL [45]. Therefore, to properly assess the phase behaviour of the two materials and avoid gelation, two constant GO concentrations of 0.2 and 1 mg/mL were examined as a function of different CTAB concentrations. It was found that bulk effects such as flocculation for a given amount of surfactant changed when comparing the two GO concentrations, and are therefore not arbitrarily defined. Rather, a specific mass ratio of GO to CTAB was required to induce flocculation, indicating an adsorption phenomenon and shown clearly by the differing crossover points for GO zeta potentials at both concentrations (Fig. 1c). Below GO:CTAB mass ratios of 5:1 w/w (see [Supplementary Data](#)), the amount of CTAB present is insufficient to cause complete destabilisation of the GO dispersion (Fig. 1a). The zeta potential measurements indicate that the surface is still negatively charged at these concentrations (Fig. 1c), hence the GO will remain in dispersion by electrostatic repulsion, instead of assembling at the air–water interface. Above GO:CTAB mass ratios of 1:2.5 w/w, the amount of CTAB added is high enough to invert the charge on the GO such that it is now stabilised by net positive charge repulsions, again confirmed by zeta potential measurements (Fig. 1c), an effect which was also noted previously for the azoTAB photosurfactant with GO dispersions [14,43].

Flocculation of GO appears to be central to successful foam formation, as only within the specified mass ratios of 5:1 and 1:2.5 w/w (GO:CTAB), where the colloidal materials had an overall charge near zero, was flotation successfully achieved (Fig. 1a). Outside of this range, the vast majority of GO remained in dispersion; however, within this region, close to full recovery (>99%) of the GO was obtained post-sonication (Fig. 1b). The results suggest that the efficacy of GO foam stabilisation is predicated on the GO sheets being able to densely pack at the air–water interface and inhibit the escape of gas molecules, which is a reasonable conclusion given the much faster diffusion rate of gases compared to oils

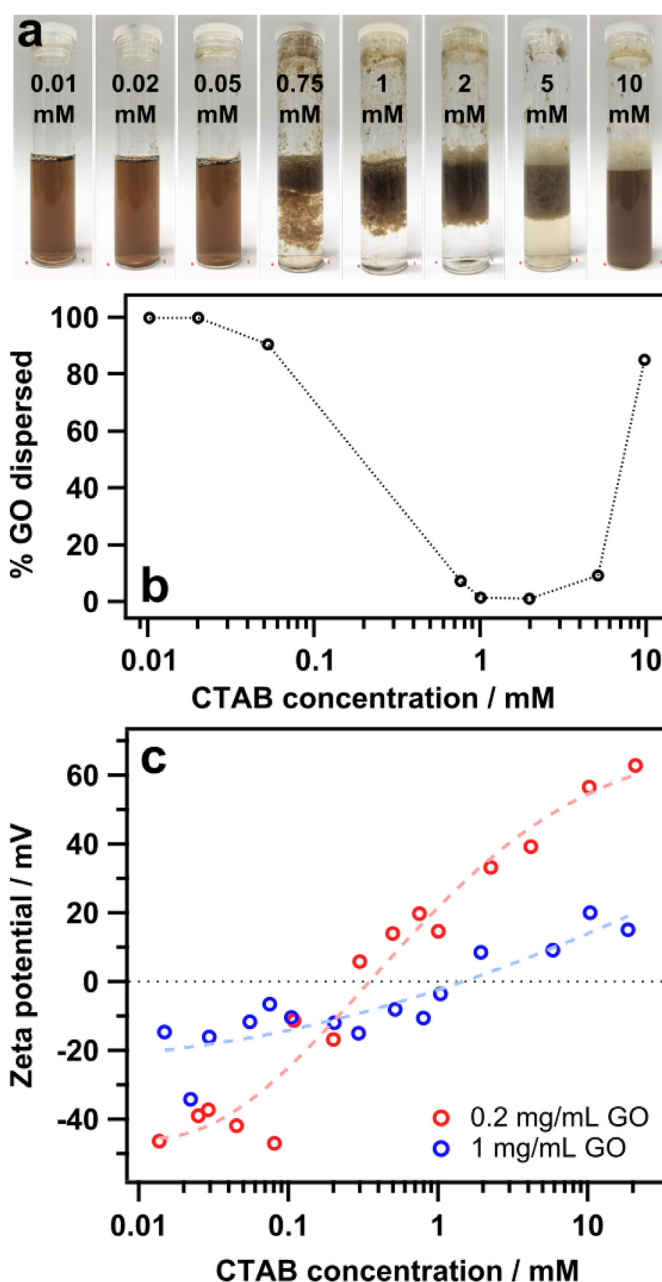


Fig. 1. (a) Samples containing 1 mg/mL GO and the specified concentrations of CTAB after ultrasonication for 2×30 s at 10% amplitude. (b) UV–visible spectrophotometry data of the bulk solution for these samples showing the percentage of GO still in dispersion. (c) Phase analysis light scattering data for the two fixed concentrations of GO with varying concentrations of CTAB. The dashed lines have been added as guides to the eye. (A colour version of this figure can be viewed online.)

in emulsion droplets. Conversely, aggregation of the GO alone does not appear to be adequate for foam formation to occur, as attempting the same experiment when destabilising the GO with 500 mM NaCl did not result in a stable foam (see [Supplementary data](#)). This observation emphasises the importance of the hydrophobicity imparted by the adsorbed surfactant molecules as well as charge neutralisation, and that the surface activity of the GO itself is insufficient when it comes to foam formation. A similar observation was made for silica nanoparticle/surfactant mixtures, with flocculated materials of increased hydrophobicity from adsorbed surfactant resulting in the best foams [25]. Flocculation was also found to be a prerequisite for the noncovalent magnetic recovery of GO

from water, again with cationic materials added in order to overcome the electrostatic stabilisation of the GO sheets, allowing their capture from solution using a magnet [46,47].

The sonication step is vital in the GO recovery process and fulfils two essential functions: firstly it generates air–water interface in the form of microscopic air bubbles that the GO/CTAB can adsorb to, but secondly it shears the GO aggregates and in doing so promotes higher surface area, allowing the sheets to more effectively stabilise the interfaces present within the foam network. It is important to note that in the samples from Fig. 1a, ultrasonication has assisted in causing the GO/CTAB composites to float by producing an adequate amount of entrapped microbubbles within the flocculated materials; however, they are not actually in the form of a conventional foam. This is because an ultrasonication amplitude of 10% (with the Branson 450 Digital Sonifier) is not energetically sufficient to bring about the evolution of a genuine (macroscopic) foam.

Upon increasing the sonication intensity to 30% (defined in Experimental), for an optimal GO/CTAB ratio (1 mg/mL GO, 2 mM CTAB), a distinct foam layer above the bulk solution can be observed (Fig. 2a). This outcome highlights that shearing of the GO is essential in forming a foam, as it is again clear that when sonicating a similar sample at an intensity of 10%, the GO sheets have not been adequately disaggregated (Fig. 2a). Thus, the material has remained in the solution as a hydrophobic agglomerate. Increasing the intensity further to 50% caused the volume of the foam to approximately double, most likely because the higher energy input forces more air through the system (Fig. 2a). The likely explanation for the differences in foam volume fractions with increasing sonication intensities is that the higher shear energies not only create more interface, but also aid in overcoming the high energy barrier for adsorption of these particles, a factor that has also been observed in Pickering emulsification with GO [48,49].

From obtained light microscopy images (Fig. 2c–f), it is clear that dense clusters of particulate matter comprising aggregated GO sheets are accumulating at the foam lamellae, preventing thin film drainage and rupture of the intervening liquid layer. This reinforces the effectiveness of the system as an interfacial stabiliser and exemplifies the significantly improved surface activity of the GO sheets when the surfactant is present. One limitation of this system lies in the toxic nature of CTAB [50,51], which would likely prevent its use in environmental applications, therefore other eco-friendly surfactants should be considered for the commercial viability of this methodology. Cocamidopropyl betaine (CAPB) is one of the most commonly used surfactants in personal care products due to its excellent foaming properties [52], and here we incorporate it into our GO/CTAB system to explore potential alternatives as well as probe further physical mechanisms underlying the behaviour of the system.

With 1 mM CAPB added to the same GO/CTAB mixture, little difference is observed for the foams with the naked eye (Fig. 2b). However, by light microscopy, significantly smaller bubbles are observed within the foam for the 30% sonication amplitude (Fig. 2d). This outcome indicates a significant enhancement in the stabilising capacity of the system, as the Young–Laplace pressure inside smaller bubbles is substantially greater, which usually causes them to ‘ripen’ into larger bubbles [53,54]. This result suggests that there may be additional synergism between the two surfactants and the GO. The CAPB is likely further lowering the surface tension of the system, giving increased capacity for foam stabilisation. In contrast, at 50% amplitude (Fig. 2f), the bubbles are much larger and the difference compared to the equivalent sample with GO/CTAB only (Fig. 2e) is negligible. It is possible that at the higher intensity, the energy input is too large such that even with the CAPB present, smaller bubbles can not be stabilised due to the increased volume of air being pushed through the sample. The results do suggest

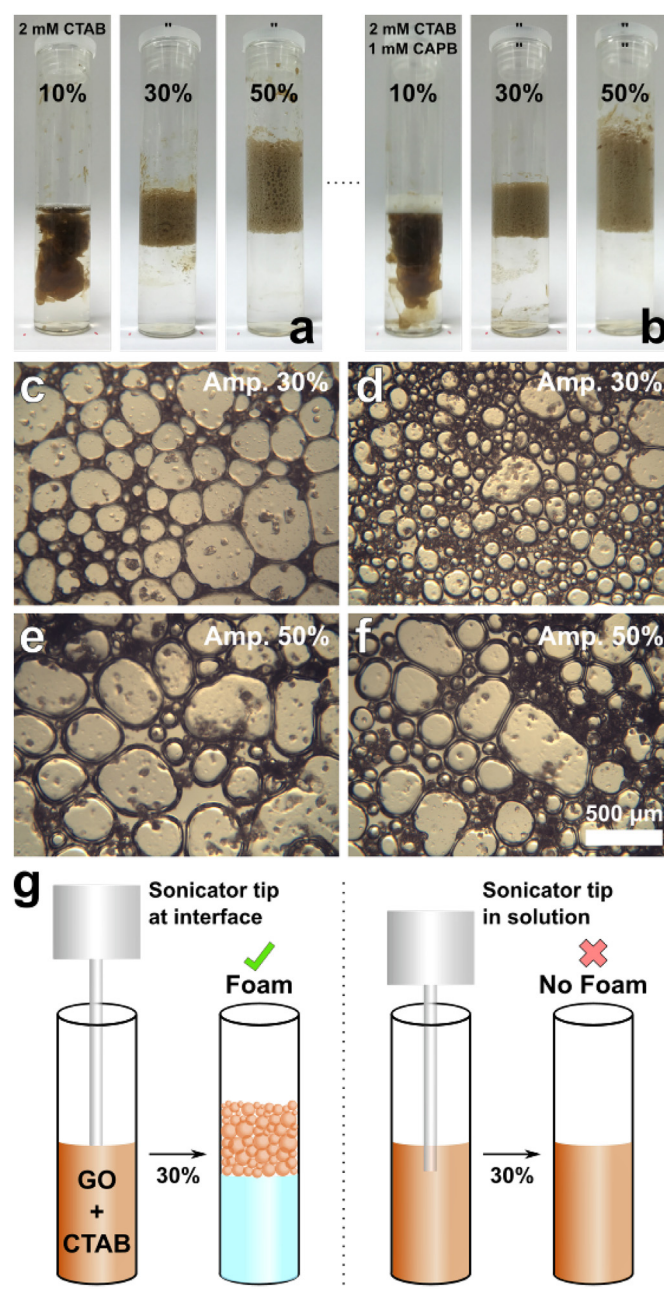


Fig. 2. (a) Samples containing 2 mM CTAB and 1 mg/mL GO after being subjected to 10, 30 and 50% amplitudes (defined in Experimental section) of ultrasonication. (b) Similar samples with 1 mM CAPB also added. (c–f) Light microscopy images of the foam layers formed after sonication: (c) 2 mM CTAB at 30%, (d) 2 mM CTAB with 1 mM CAPB at 30%, (e) 2 mM CTAB at 50% and (f) 2 mM CTAB with 1 mM CAPB at 50%. (g) Schematic showing ideal tip position for GO foam formation via ultrasonication. (A colour version of this figure can be viewed online.)

however that surfactant choice as well as surfactant mixtures may offer grounds for control of GO/surfactant foam properties as well as enhanced foam stability.

It is critical to note that foaming of the GO/CTAB is strongly dependent on the position of the sonicator tip within the sample. When the sonicator tip is arranged precisely at the air–water interface, air from the atmosphere is entrained into the sample, providing the gas–liquid interface with which the GO/CTAB composites can interact. If the probe is immersed too far below the surface of the sample, the shear field generated by from the tip will

only serve to mix the sample without incorporating bubbles, leaving the GO in the solution. This effect is shown schematically in Fig. 2g.

With ultrasonication being a high energy and potentially destructive technique, the question is raised as to whether the GO sheets are still intact following the recovery process. Atomic force microscopy was used to image directly the sheets before (Fig. 3b) and after (Fig. 3d) froth flotation. For the sample before ultrasonication, the GO was extracted from the pure dispersion (Fig. 3a). For the sample after ultrasonication, the GO was mixed with CTAB at the optimal ratio (1 mg/mL GO, 2 mM CTAB) and subjected to ultrasonication at 50% (Fig. 3c). The foam was then manually

removed and the GO isolated by washing out the CTAB (see Experimental section). The much larger GO sheets ($> 5 \mu\text{m}$) did appear to become fragmented during the sonication process; however, the average sheet width only decreased marginally from $1.86 \mu\text{m}$ to $1.33 \mu\text{m}$, indicating that the GO can be recovered in a reusable form. Moreover, the comminution of the GO could also be expected to be much lower using a sonication amplitude of 30% (or a shorter sonication time) which was also adequate for foam formation (Fig. 2a and b), instead of the 50% used in this analysis. A higher magnification AFM image is available for Fig. 3d in the [Supplementary Data](#), which clearly shows no disruption of the two-dimensional sheet morphology from the sonication process.

The size reduction of the sheets following froth flotation does imply that the adsorbed CTAB may be allowing the sheets to fragment more easily, perhaps by making them more rigid such that they are less able to accommodate the mechanical stresses induced by the sonication step. However, this does not appear to be the case as sonicating pure suspensions of GO also resulted in the larger sheets being fragmented into smaller sheets (see [Supplementary Data](#)). This effect was even observed at 10% sonication amplitude, indicating that the larger sheets are incredibly fragile and adsorption of the CTAB is neither inhibiting nor promoting sheet fragmentation. Ultrasonication has in fact been used as a method for controlling lateral sizes of GO sheets [55,56]. Interestingly, in the AFM image taken after foaming (Fig. 3d), the sheets have deposited in an adjoining fashion which is not seen in the images where the GO dispersions were sonicated without CTAB (see [Supplementary Data](#)). This is likely due to the charge neutralisation effects of the surfactant, and reinforces why the combined system is essential for foam stabilisation and flotation.

Lastly, as an initial test of the potential for this recovery method to be used in environmental applications, the GO/CTAB system was utilised in the decontamination of a model inorganic and organic toxin from water. GO has been found to be a highly effective adsorbent material for toxic metal ions in water as these ions are believed to have a strong affinity for GO due to their opposing charge [39,57]. Divalent metal ions are also thought to complex with the peripheral carboxylate groups on GO via a bidentate chelation mechanism [58,59]. For this study, cadmium ions were added to GO/CTAB mixtures (1 mg/mL GO, 2 mM CTAB) and then the flotation procedure was carried out at a 30% sonication intensity (Fig. 4c). The amount of Cd^{2+} ions removed was proportionally similar regardless of the initial concentration, with approximately 32.9 ppm removed from the sample with the lowest doping (1 mM) and 109.9 ppm removed from the sample with the highest doping (3 mM) (Fig. 4e). Lowering the amount of CTAB to 1 mM resulted in an increase in the amount removed in all instances (137.5 ppm of Cd^{2+} at higher doping). This suggests that the CTAB molecules and Cd^{2+} ions are competing for adsorption sites on the GO surface. As both bear a positive charge, it is likely that this arises from competition for the peripheral carboxylate groups. A small decrease in the volume of the foams was also observed upon halving the CTAB concentration (Fig. 4a,c). Furthermore, the incorporation of cadmium did not appear to impede the formation of the foams.

The removal of a model organic compound, caffeine, was also attempted using GO/CTAB (1 mg/mL GO, 1 or 2 mM CTAB) and employing froth flotation as the recovery mechanism (Fig. 4b,d). Caffeine displayed a fairly weak adsorption affinity for GO, with only as much as 95.2 ppm being removed at the highest caffeine doping (Fig. 4f). In addition, no improvement was observed for the lower CTAB concentration, suggesting a different adsorption mechanism to cadmium. Caffeine is a highly water soluble and neutrally charged compound, therefore, its interaction with GO is likely to be weak, via polar and van der Waals forces. Caffeine also

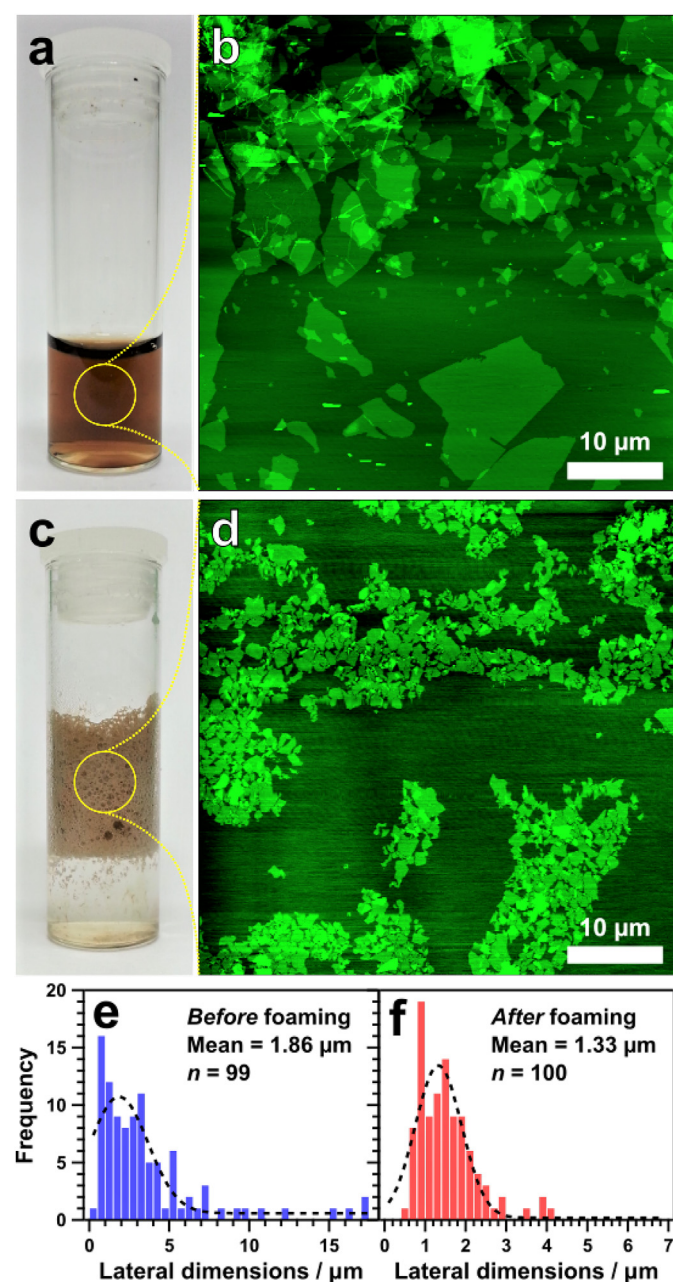


Fig. 3. (a) A 1 mg/mL aqueous dispersion of GO. (b) An AFM height image of GO prepared from the clean GO dispersion in (a). (c) A 1 mg/mL sample of GO with 2 mM CTAB after being ultrasonicated for 30 s at 50% amplitude. (d) An AFM height image of the GO extracted from the foam in (c). (e & f) Histograms of the lateral size dimensions of GO before (e) and after (f) foaming with ultrasonication. (A colour version of this figure can be viewed online.)

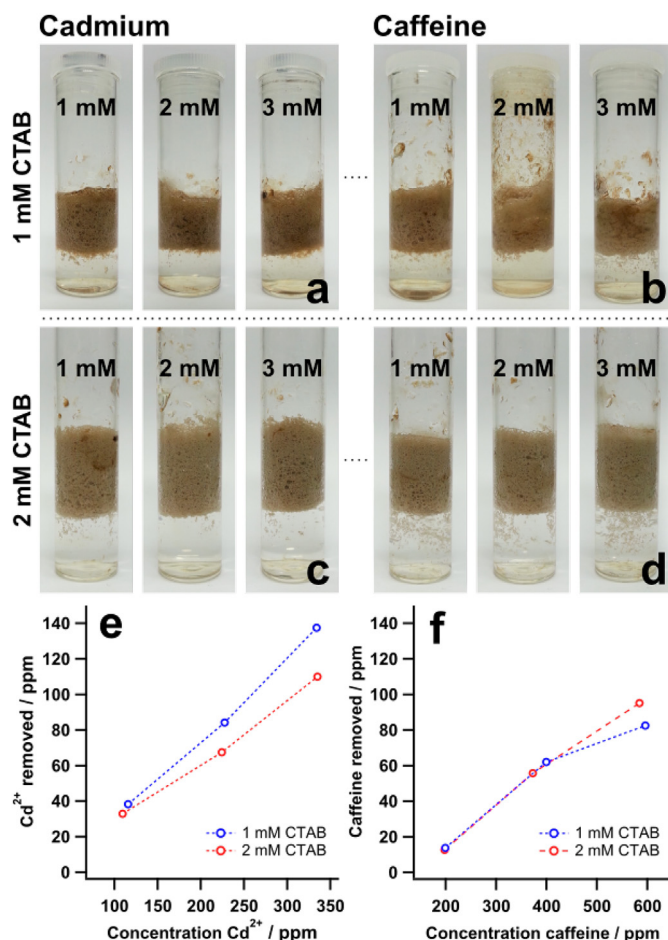


Fig. 4. (a & b) Flotation samples containing the specified concentrations of cadmium (a) and caffeine (b) and 1 mM CTAB. (c & d) Similar samples but with 2 mM CTAB. All samples contained 1 mg/mL GO. (e & f) The amounts (in ppm) of cadmium (e) and caffeine (f) removed from these samples by froth flotation. (A colour version of this figure can be viewed online.)

did not hinder the foaming of the GO/CTAB composites. While the amounts of captured cadmium and caffeine presented here are quite modest, the results still show potential for the use of this system in environmental decontamination as well as revealing important information regarding which toxins are feasible for capture. Optimising the materials loadings as well as the adsorption time could improve the results dramatically.

4. Conclusion

Graphene oxide nanosheets can be easily separated from aqueous solution using a facile froth flotation method involving the addition of CTAB surfactant and ultrasonication. As the adsorption of GO sheets at the air–water interface is non-spontaneous due to their high negative surface charge, the surfactant plays a critical role in the recovery of GO by neutralising the charge of the sheets, and promoting surface activity through GO/surfactant synergism. The surfactant-coated GO sheets then possess a much greater affinity for the air–water interface and as such can be entrained in a concentrated foam above the bulk solution. Ultrasonication of sufficient intensity applied directly at the surface of the suspension facilitates foam formation by shearing the GO and forcing air bubbles through the liquid which are then stabilised by the GO/CTAB composites. Flocculation is essential in this process by

allowing adequate packing of GO at the interface, hence the ratio of CTAB to GO must be optimised for foamability. Too little CTAB will not destabilise the GO suspension, and too much CTAB causes restabilisation by overcharging such that in both instances the GO remains in dispersion. At optimal ratios, almost full recovery of the GO is attained and thus, this system represents an easy and potentially industrially viable procedure for capturing GO from water, or making GO-stabilised foams without complex instrumentation or extreme system conditions.

These results indicate that low-energy separation of GO from aqueous systems can be achieved at low cost using ‘conventional’ technologies, provided suitable optimisation and additives (collectors) are used. This process can be used to recover GO when it is employed as an adsorbent for capturing toxic metals or organic species, again indicating future potential for GO in low-cost, large-scale treatment of water.

Acknowledgements

We thank the Australian Institute of Nuclear Science and Engineering and the Monash Centre for Atomically Thin Materials for scholarship funding (T.M.M.). This work was supported in part by the grant of an ARC Future Fellowship (FT160100191) to R.F.T. We also thank Rodney Hall for his assistance with atomic absorption spectroscopy. Lastly, we would like to acknowledge that authors Thomas M. McCoy and Huw C. W. Parks contributed equally to the progression and publication of this work.

Appendix A. Supplementary data

Supplementary data related to this article can be found at <https://doi.org/10.1016/j.carbon.2018.04.032>.

References

- [1] C. Nutt, Froth flotation: the adhesion of solid particles to flat interfaces and bubbles, *Chem. Eng. Sci.* 12 (2) (1960) 133–141.
- [2] T. Subrahmanyam, E. Forssberg, Froth stability, particle entrainment and drainage in flotation – a review, *Int. J. Miner. Process.* 23 (1) (1988) 33–53.
- [3] J. Rubio, M. Souza, R. Smith, Overview of flotation as a wastewater treatment technique, *Miner. Eng.* 15 (3) (2002) 139–155.
- [4] S.R. Rao, *Surface Chemistry of Froth Flotation: Volume 1: Fundamentals*, Springer Science & Business Media, 2013.
- [5] T. Chau, W. Bruckard, P. Koh, A. Nguyen, A review of factors that affect contact angle and implications for flotation practice, *Adv. Colloid Interface Sci.* 150 (2) (2009) 106–115.
- [6] R. Lemlich, *Adsorptive Bubble Separation Techniques*, Elsevier, 2012.
- [7] M.C. Fuerstenau, G.J. Jameson, R.-H. Yoon, *Froth Flotation: a Century of Innovation*, SME, 2007.
- [8] J. Kim, L.J. Cote, J. Huang, Two dimensional soft material: new faces of graphene oxide, *Acc. Chem. Res.* 45 (8) (2012) 1356–1364.
- [9] D.R. Dreyer, S. Park, C. Bielawski, R.S. Ruoff, The chemistry of graphene oxide, *Chem. Soc. Rev.* 39 (2010) 228–240.
- [10] K.A. Mkhoyan, A.W. Contryman, J. Silcox, D.A. Stewart, G. Eda, C. Mattevi, S. Miller, M. Chhowalla, Atomic and electronic structure of graphene-oxide, *Nano Lett.* 9 (3) (2009) 1058–1063.
- [11] N. Bolong, A. Ismail, M.R. Salim, T. Matsuura, A review of the effects of emerging contaminants in wastewater and options for their removal, *Desalination* 239 (1–3) (2009) 229–246.
- [12] L. Song, Flux decline in crossflow microfiltration and ultrafiltration: mechanisms and modeling of membrane fouling, *J. Membr. Sci.* 139 (2) (1998) 183–200.
- [13] P. Xu, J.E. Drewes, C. Bellona, G. Amy, T.-U. Kim, M. Adam, T. Heberer, Rejection of emerging organic micropollutants in nanofiltration–reverse osmosis membrane applications, *Water Environ. Res.* 77 (1) (2005) 40–48.
- [14] T.M. McCoy, S.A. Holt, A.M. Rozario, T.D.M. Bell, R.F. Tabor, Surfactant-enhanced adsorption of graphene oxide for improved emulsification of oil in water, *Adv. Mater. Interfaces* 4 (23) (2017), 1700803–n/a.
- [15] L.J. Cote, J. Kim, V.C. Tung, J. Luo, F. Kim, J. Huang, Graphene oxide as surfactant sheets, *Pure Appl. Chem.* 83 (1) (2010) 95–110.
- [16] J.-J. Shao, W. Lv, Q.-H. Yang, Self-assembly of graphene oxide at interfaces, *Adv. Mater.* 26 (2014) 5586–5612.
- [17] J. Kim, L.J. Cote, W. Kim, F. Yuan, K.R. Shull, J. Huang, Graphene oxide sheets at interfaces, *J. Am. Chem. Soc.* 132 (2010) 8180–8186.

- [18] F. Kim, L.J. Cote, J. Huang, Graphene oxide: surface activity and two-dimensional assembly, *Adv. Mater.* 22 (2010) 1954–1958.
- [19] B. Konkana, S. Vasudevan, Understanding aqueous dispersibility of graphene oxide and reduced graphene oxide through pK_a measurements, *J. Phys. Chem. Lett.* 3 (2012) 867–872.
- [20] D. Li, M.B. Muller, S. Gilje, R.B. Kaner, G.G. Wallace, Processable aqueous dispersions of graphene oxide nanosheets, *Nat. Nanotechnol.* 3 (2008) 101–105.
- [21] T.N. Hunter, E.J. Wanless, G.J. Jameson, R.J. Pugh, Non-ionic surfactant interactions with hydrophobic nanoparticles: impact on foam stability, *Colloids Surf., A* 347 (1) (2009) 81–89.
- [22] X. Dong, J. Xu, C. Cao, D. Sun, X. Jiang, Aqueous foam stabilized by hydrophobically modified silica particles and liquid paraffin droplets, *Colloids Surf., A* 353 (2) (2010) 181–188.
- [23] A.J. Worthen, S.L. Bryant, C. Huh, K.P. Johnston, Carbon dioxide-in-water foams stabilized with nanoparticles and surfactant acting in synergy, *AIChE J.* 59 (9) (2013) 3490–3501.
- [24] Y. Zhu, J. Jiang, Z. Cui, B.P. Binks, Responsive aqueous foams stabilised by silica nanoparticles hydrophobised in situ with a switchable surfactant, *Soft Matter* 10 (2014) 9739–9745.
- [25] B.P. Binks, M. Kirkland, J.A. Rodrigues, Origin of stabilisation of aqueous foams in nanoparticle-surfactant mixtures, *Soft Matter* 4 (2008) 2373–2382.
- [26] H. Heinz, C. Pramanik, O. Heinz, Y. Ding, R.K. Mishra, D. Marchon, R.J. Flatt, I. Estrela-Lopis, J. Llop, S. Moya, R.F. Ziolo, Nanoparticle decoration with surfactants: molecular interactions, assembly, and applications, *Surf. Sci. Rep.* 72 (1) (2017) 1–58.
- [27] S.U. Pickering, Emulsions, *J. Chem. Soc. Trans.* 91 (1907) 2001–2021.
- [28] W. Ramsden, Separation of solids in the surface—layers of solutions and ‘suspensions’ (observations on surface—membranes, bubbles, emulsions, and mechanical coagulation) — preliminary account, *Proc. R. Soc. Lond.* 72 (477–486) (1904) 156–164.
- [29] J. Texter, Graphene oxide and graphene flakes as stabilizers and dispersing aids, *Curr. Opin. Colloid Interface Sci.* 20 (5–6) (2015) 454–464.
- [30] Z. Du, M.P. Bilbao-Montoya, B.P. Binks, E. Dickinson, R. Ettelaie, B.S. Murray, Outstanding stability of particle-stabilized bubbles, *Langmuir* 19 (8) (2003) 3106–3108.
- [31] A. Stocco, W. Drenckhan, E. Rio, D. Langevin, B.P. Binks, Particle-stabilised foams: an interfacial study, *Soft Matter* 5 (11) (2009) 2215–2222.
- [32] J.S. Guevara, A.F. Mejia, M. Shuai, Y.-W. Chang, M.S. Mannan, Z. Cheng, Stabilization of pickering foams by high-aspect-ratio nano-sheets, *Soft Matter* 9 (2013) 1327–1336.
- [33] K. Hu, X. Xie, M. Cerruti, T. Szkopek, Controlling the shell formation in hydrothermally reduced graphene hydrogel, *Langmuir* 31 (20) (2015) 5545–5549.
- [34] M. Abdolkarimi-Mahabadi, M. Manteghian, Quantitative separation of graphene oxide nanoribbon by froth flotation, *J. Dispersion Sci. Technol.* 36 (7) (2015) 924–931.
- [35] K. Kakaei, K. Hasanpour, Synthesis of graphene oxide nanosheets by electrochemical exfoliation of graphite in cetyltrimethylammonium bromide and its application for oxygen reduction, *J. Mater. Chem. A* 2 (2014) 15428–15436.
- [36] E. Vaghri, D. Dorrnanian, M. Ghoranneviss, Effects of ctac concentration on the quality of graphene oxide nanosheets produced by green laser ablation, *Mater. Chem. Phys.* 203 (2018) 235–242.
- [37] Y. He, N. Zhang, F. Wu, F. Xu, Y. Liu, J. Gao, Graphene oxide foams and their excellent adsorption ability for acetone gas, *Mater. Res. Bull.* 48 (9) (2013) 3553–3558.
- [38] Z. Wang, Z. Tang, Z. Han, S. Shen, B. Zhao, J. Yang, Effect of drying conditions on the structure of three-dimensional n-doped graphene and its electrochemical performance, *RSC Adv.* 5 (26) (2015) 19838–19843.
- [39] Y. Lei, F. Chen, Y. Luo, L. Zhang, Synthesis of three-dimensional graphene oxide foam for the removal of heavy metal ions, *Chem. Phys. Lett.* 593 (2014) 122–127.
- [40] M. Favaro, F. Carraro, M. Cattelan, L. Colazzo, C. Durante, M. Sambì, A. Gennaro, S. Agnoli, G. Granozzi, Multiple doping of graphene oxide foams and quantum dots: new switchable systems for oxygen reduction and water remediation, *J. Mater. Chem. A* 3 (2015) 14334–14347.
- [41] D.C. Marcano, D.V. Kosynkin, J.M. Berlin, A. Sinitskii, Z. Sun, A. Slesarev, L.B. Alemany, W. Lu, J.M. Tour, Improved synthesis of graphene oxide, *ACS Nano* 4 (2010) 4806–4814.
- [42] D. Nečas, P. Klapetek, Gwyddion: an open-source software for spm data analysis, *Open Phys.* 10 (1) (2012) 181–188.
- [43] T.M. McCoy, A.C.Y. Liu, R.F. Tabor, Light-controllable dispersion and recovery of graphenes and carbon nanotubes using a photo-switchable surfactant, *Nanoscale* 8 (2016) 6969–6974.
- [44] W. Meng, E. Gall, F. Ke, Z. Zeng, B. Kopchick, R. Timsina, X. Qiu, Structure and interaction of graphene oxide–cetyltrimethylammonium bromide complexation, *J. Phys. Chem. C* 119 (36) (2015) 21135–21140.
- [45] H. Bai, C. Li, X. Wang, G. Shi, On the gelation of graphene oxide, *J. Phys. Chem. C* 115 (13) (2011) 5545–5551.
- [46] T.M. McCoy, P. Brown, J. Eastoe, R.F. Tabor, Noncovalent magnetic control and reversible recovery of graphene oxide using iron oxide and magnetic surfactants, *ACS Appl. Mater. Interfaces* 7 (2015) 2124–2133.
- [47] G. Hazell, M. Hinojosa-Navarro, T.M. McCoy, R.F. Tabor, J. Eastoe, Responsive materials based on magnetic polyelectrolytes and graphene oxide for water clean-up, *J. Colloid Interface Sci.* 464 (2016) 285–290.
- [48] Y. He, F. Wu, X. Sun, R. Li, Y. Guo, C. Li, L. Zhang, F. Xing, W. Wang, J. Gao, Factors that affect pickering emulsions stabilized by graphene oxide, *ACS Appl. Mater. Interfaces* 5 (2013) 4843–4855.
- [49] M. Ali, T.M. McCoy, I.R. McKinnon, M. Majumder, R.F. Tabor, Synthesis and characterization of graphene oxide–polystyrene composite capsules with aqueous cargo via a water–oil–water multiple emulsion templating route, *ACS Appl. Mater. Interfaces* 9 (21) (2017) 18187–18198.
- [50] B. Isomaa, J. Reuter, B.M. Djupsund, The subacute and chronic toxicity of cetyltrimethylammonium bromide (ctab), a cationic surfactant, in the rat, *Arch. Toxicol.* 35 (2) (1976) 91–96.
- [51] P. Pinnaduwa, L. Schmitt, L. Huang, Use of a quaternary ammonium detergent in liposome mediated dna transfection of mouse l-cells, *Biochim. Biophys. Acta* 985 (1) (1989) 33–37.
- [52] E.S. Basheva, D. Ganchev, N.D. Denkov, K. Kasuga, N. Satoh, K. Tsujii, Role of betaine as foam booster in the presence of silicone oil drops, *Langmuir* 16 (3) (2000) 1000–1013.
- [53] W. Ostwald, Blocking of ostwald ripening allowing long-term stabilization, *Phys. Chem.* 37 (1901) 385.
- [54] P.W. Voorhees, The theory of ostwald ripening, *J. Stat. Phys.* 38 (1) (1985) 231–252.
- [55] C. Botas, A.M. Pérez-Mas, P. Álvarez, R. Santamaría, M. Granda, C. Blanco, R. Menéndez, Optimization of the size and yield of graphene oxide sheets in the exfoliation step, *Carbon* 63 (2013) 576–578.
- [56] X. Qi, T. Zhou, S. Deng, G. Zong, X. Yao, Q. Fu, Size-specified graphene oxide sheets: ultrasonication assisted preparation and characterization, *J. Mater. Sci.* 49 (4) (2014) 1785–1793.
- [57] G. Zhao, J. Li, X. Ren, C. Chen, X. Wang, Few-layered graphene oxide nanosheets as super sorbents for heavy metal ion pollution management, *Environ. Sci. Technol.* 45 (2011) 10454–10462.
- [58] R. Sitko, E. Turek, B. Zawisza, E. Malicka, E. Talik, J. Heimann, A. Gabor, B. Feist, R. Wrzalik, Adsorption of divalent metal ions from aqueous solutions using graphene oxide, *Dalton Trans.* 42 (16) (2013) 5682–5689.
- [59] D. Gu, J.B. Fein, Adsorption of metals onto graphene oxide: surface complexation modeling and linear free energy relationships, *Colloids Surf., A* 481 (2015) 319–327.

SUPPLEMENTARY DATA - Highly efficient recovery of graphene oxide by froth flotation using a common surfactant

Thomas M. McCoy,¹ Huw C. W. Parks,² Rico F. Tabor^{1,*}

¹School of Chemistry,
Monash University, Clayton 3800, Australia

²School of Chemistry,
Cardiff University, Cardiff CF10 3AT, United Kingdom

*To whom correspondence should be addressed; E-mail: rico.tabor@monash.edu

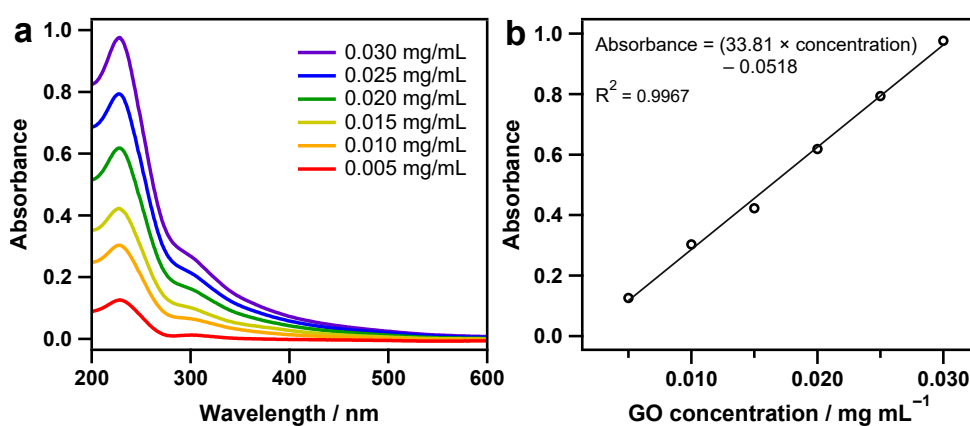


Figure S1: (a) UV-visible spectrophotometry data of aqueous graphene oxide dispersions at the specified concentrations. (b) Calibration curve corresponding to the data in (a). Absorbance values are taken at the wavelength of maximum absorption (228 nm).

Table 1: Calorimetric measurements for determination of the sonication power delivered by the Branson 450 Digital Sonifier at the programmed instrument amplitudes of 10%, 30% and 50%, for 3 mL foam samples.

Sonication amplitude	Mass H ₂ O (g)	T _{initial} (°C)	T _{final} (°C)	ΔT (°C)	Sonication time (s)	Total power (W)	Power delivered (W/cm ³)
10%	3.0196	23.7	29.4	5.7	30	2.40	0.79
30%	3.0236	23.7	42.0	18.3	30	7.71	2.55
50%	3.0194	23.7	52.8	29.1	30	12.24	4.05

Exemplar calculation for the power delivered by the Branson 450 Digital Sonifier at the 50% sonication amplitude:

$$Q = \frac{mc\Delta T}{t} \div V$$

$$Q = \frac{3.0194 \times 4.18 \times 29.1}{30} \div 3.0194 = 4.05 \text{ W/cm}^3$$

where Q is the heat energy, m is the sample mass, c is the specific heat capacity of water, ΔT is the change in temperature, t is the sonication time and V is the sample volume.

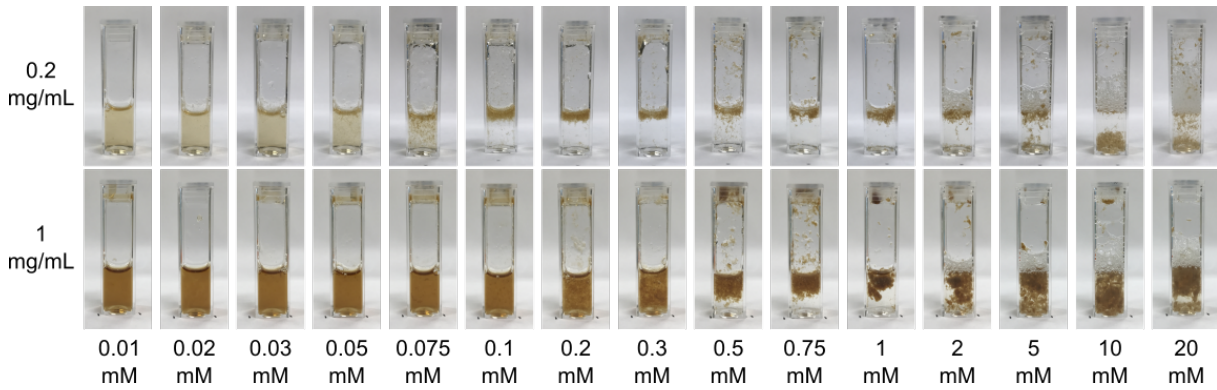


Figure S2: Samples containing 0.2 and 1 mg/mL of GO and varying concentrations of CTAB used for phase analysis light scattering.

Table 2: Compositions and PALS results for 0.2 mg/mL samples in Fig. S2.

CTAB concentration	GO:CTAB	Zeta potential	Conductance
mM	mg:mg	mV	μS
0.014	39.492	-46.5 ± 1.2	324
0.025	21.599	-39.1 ± 2.3	313
0.029	18.445	-37.4 ± 2.1	329
0.045	11.588	-41.9 ± 1.0	324
0.081	6.869	-47.1 ± 1.8	328
0.109	5.033	-11.4 ± 0.7	233
0.200	2.742	-16.8 ± 0.4	433
0.300	1.801	5.7 ± 0.5	460
0.498	1.096	14.0 ± 1.7	356
0.750	0.732	19.7 ± 1.5	492
1.005	0.541	14.6 ± 0.6	516
2.244	0.243	33.1 ± 0.3	595
4.161	0.132	39.2 ± 0.5	723
10.236	0.053	56.4 ± 1.6	902
20.851	0.026	62.8 ± 2.1	1264

Table 3: Compositions and PALS results for 1 mg/mL samples in Fig. S2.

CTAB concentration	GO:CTAB	Zeta potential	Conductance
mM	mg:mg	mV	μS
0.015	179.296	-14.7 ± 1.1	766
0.022	120.884	-34.2 ± 3.6	775
0.030	89.170	-16.2 ± 0.9	1085
0.055	47.838	-11.7 ± 0.8	1131
0.075	35.909	-6.6 ± 1.0	1068
0.105	25.279	-10.5 ± 0.6	1087
0.203	12.903	-12.0 ± 0.9	1137
0.295	9.027	-15.1 ± 1.2	948
0.516	5.227	-8.2 ± 0.6	1275
0.796	3.365	-10.7 ± 1.0	1501
1.040	2.566	-3.7 ± 0.6	1628
1.928	1.388	8.5 ± 1.2	682
5.851	0.414	9.1 ± 0.4	1873
10.345	0.257	20.0 ± 1.3	2217
18.537	0.137	15.0 ± 1.2	2545

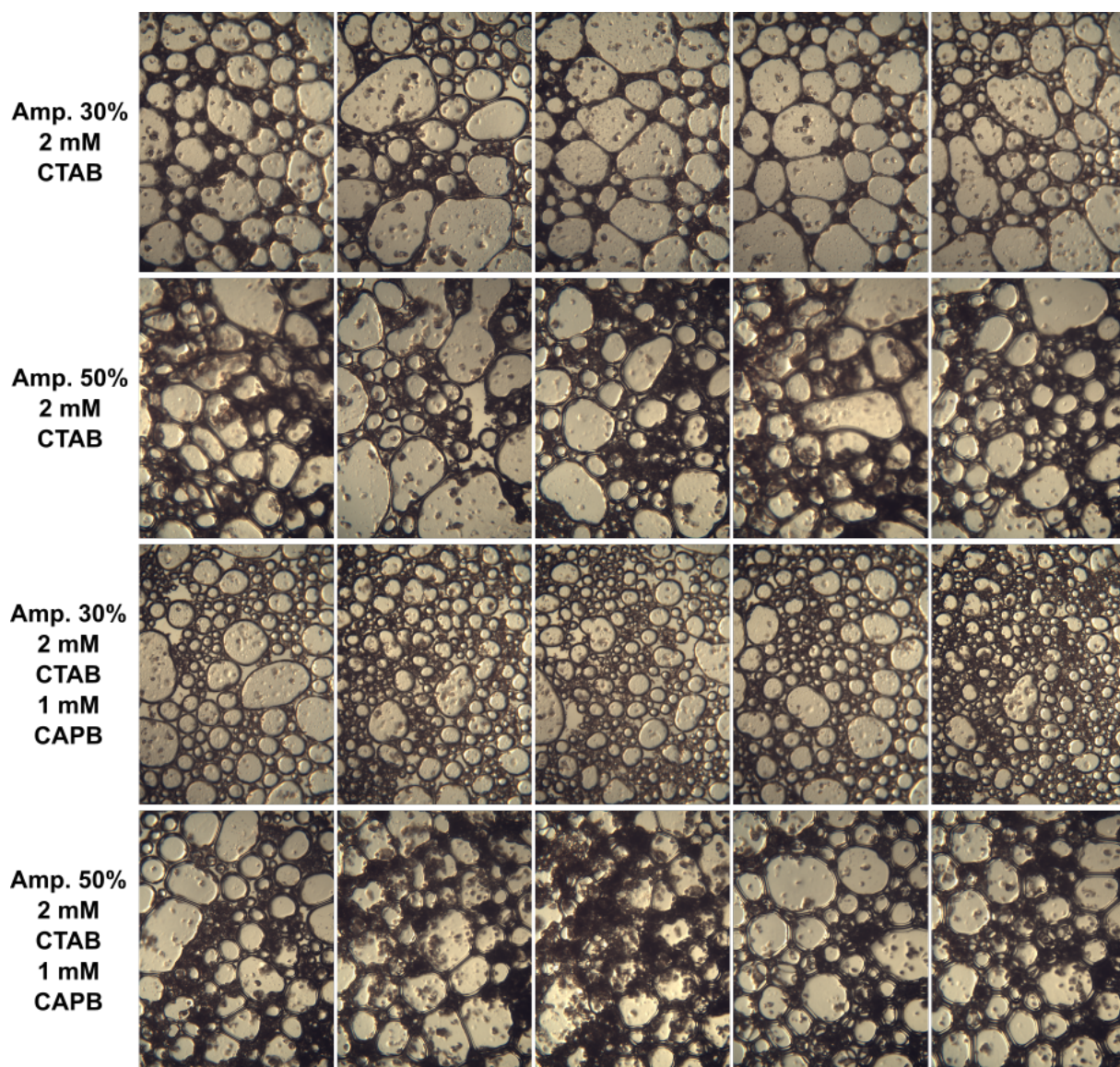


Figure S3: Additional light microscopy images of GO/CTAB foams at different sonication intensities with and without CAPB ($\times 4$ magnification objective).

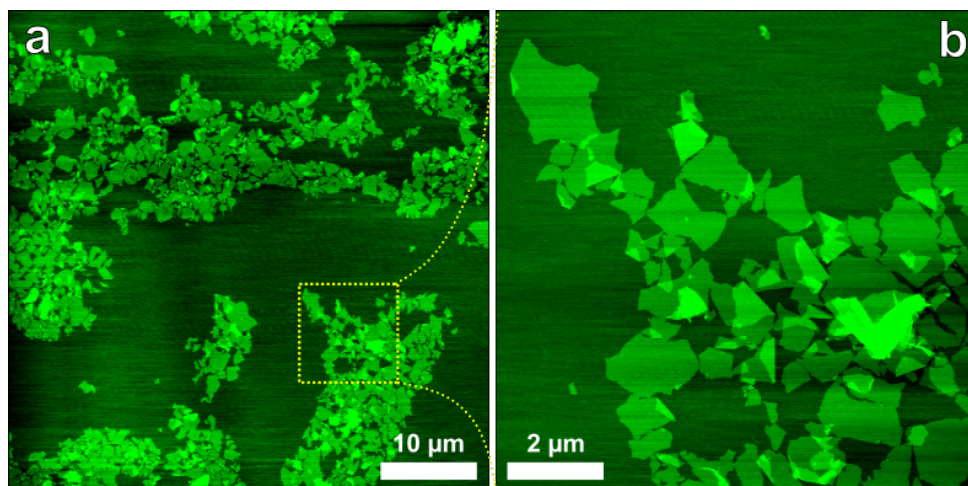


Figure S4: (a) AFM height image of GO sheets after recovery by foam entrainment (from the main paper). (b) Higher magnification AFM image of the area within the yellow box, more clearly showing the retained two-dimensional morphology of the sheets post-sonication.

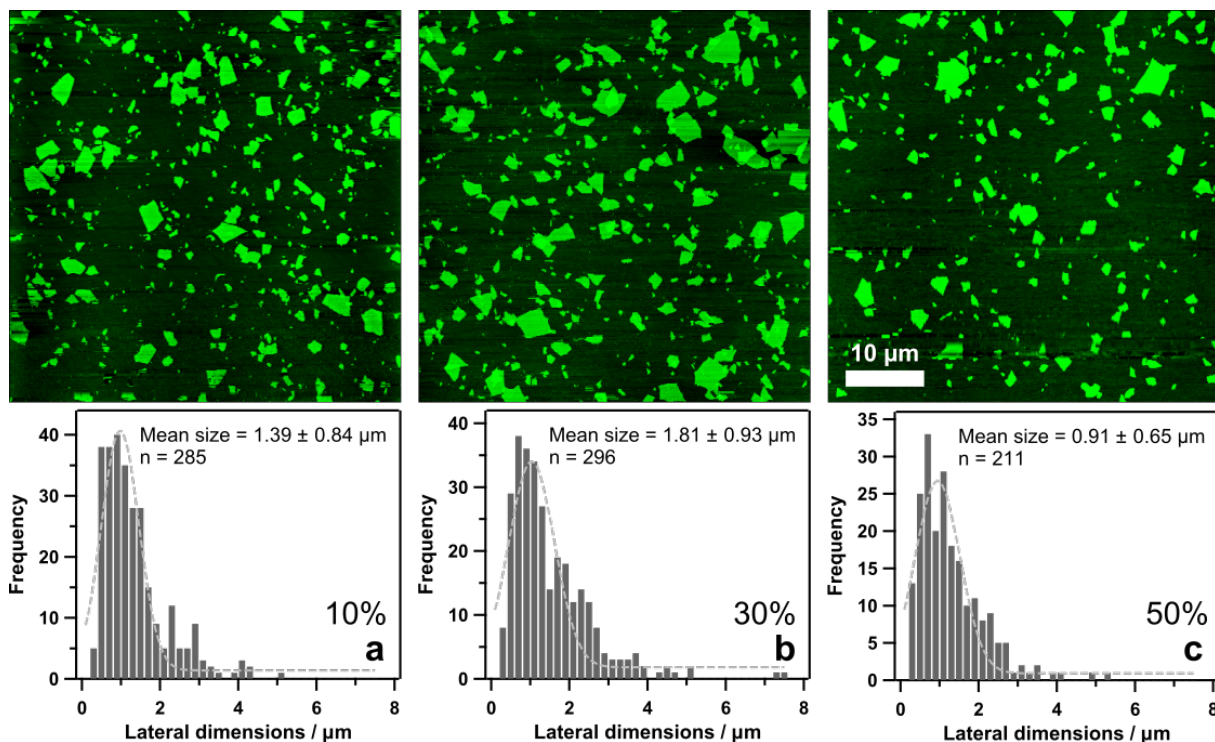


Figure S5: (a-c) AFM height images of GO sheets dried onto mica after sonication at 10% (a), 30% (b) and 50% (c) amplitudes on the Branson Digital Sonifier, with corresponding size histograms shown below. Mean size values were determined from the Gaussian fits and n represents the number of sheets analysed. All images are $50 \times 50 \mu\text{m}$.

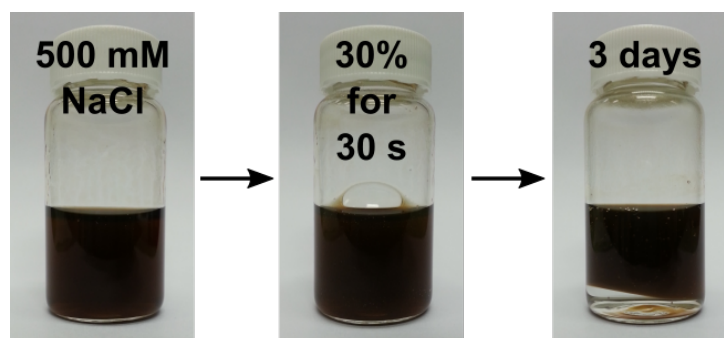


Figure S6: Sample containing 1 mg/mL GO and 500 mM NaCl after attempting froth flotation. Sonication was performed at an amplitude of 30% for 30 seconds.

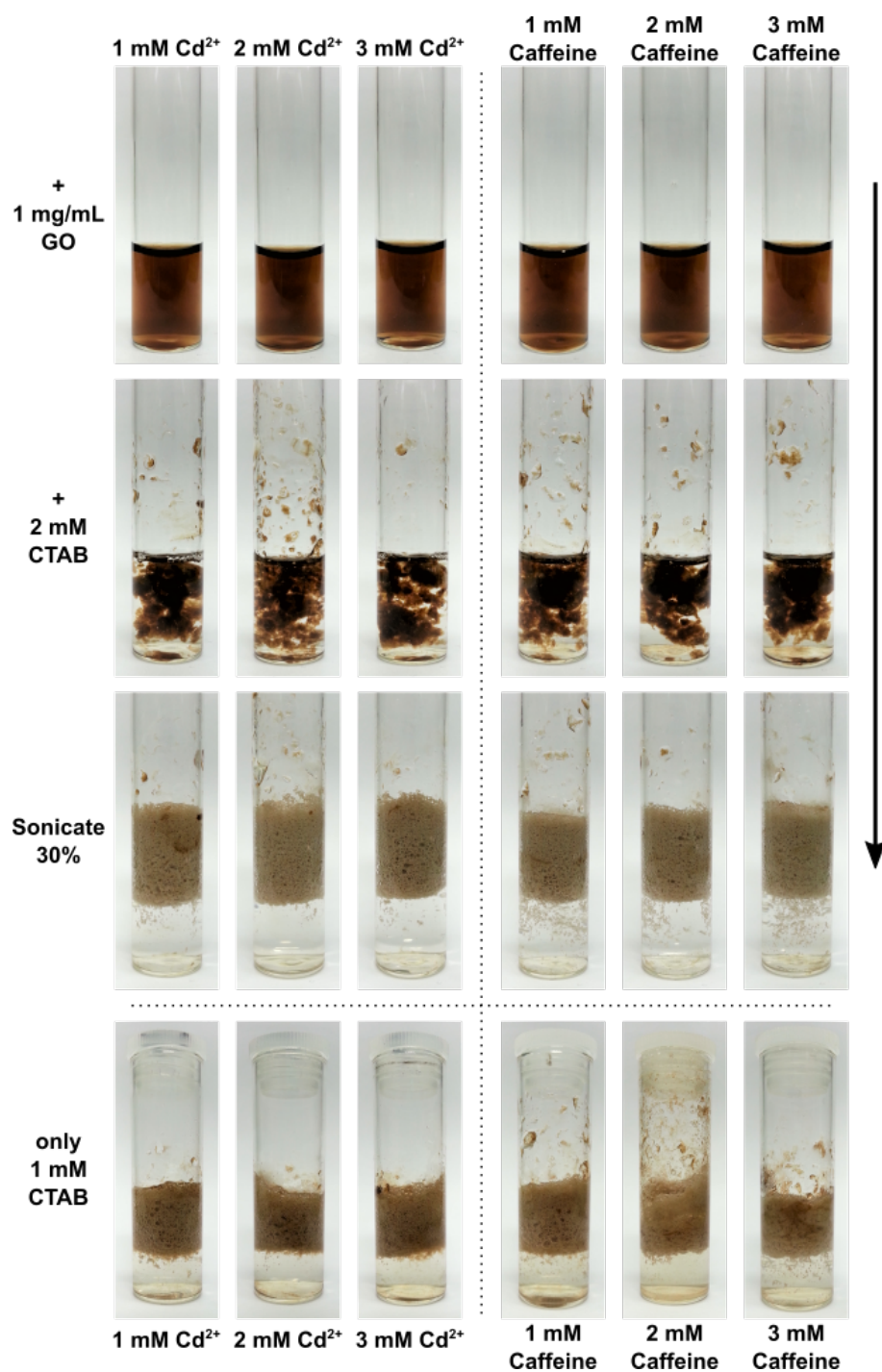


Figure S7: Flotation samples with varying concentrations of cadmium and caffeine at different stages of the recovery process.

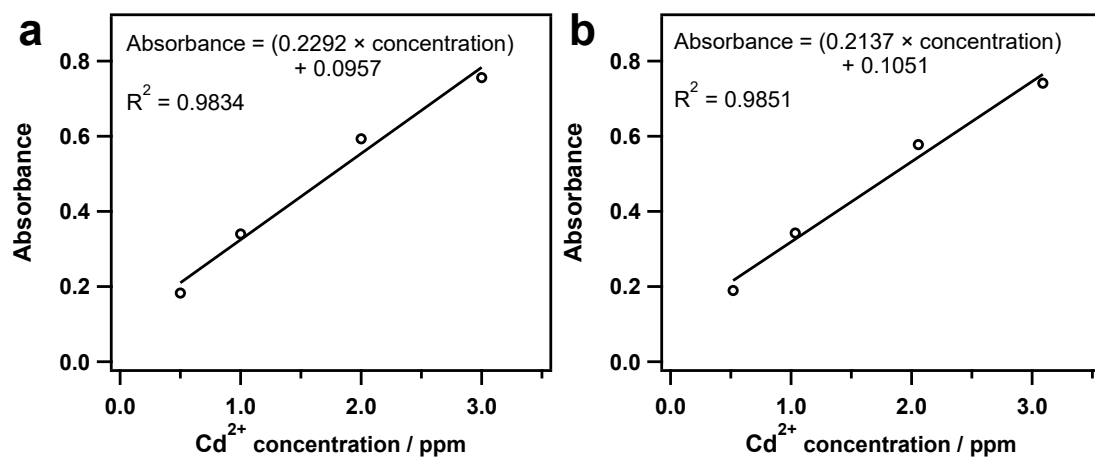


Figure S8: (a & b) Atomic absorption spectroscopy calibration data used for determining unknown quantities of cadmium in solution.

Table 4: Samples compositions and amount of Cd^{2+} removed as measured by AAS.

Conc. GO mg/mL	Conc. CTAB mM	Conc. Cd^{2+} ppm	Cd^{2+} removed ppm	% Cd^{2+} removed
0.93	1.91	109.5	32.9	30.0
0.98	1.99	224.4	67.4	30.0
0.98	1.99	335.1	109.9	32.8
0.98	0.98	115.8	38.3	33.0
1.00	1.00	227.6	84.1	37.0
1.00	0.98	334.1	137.5	41.1

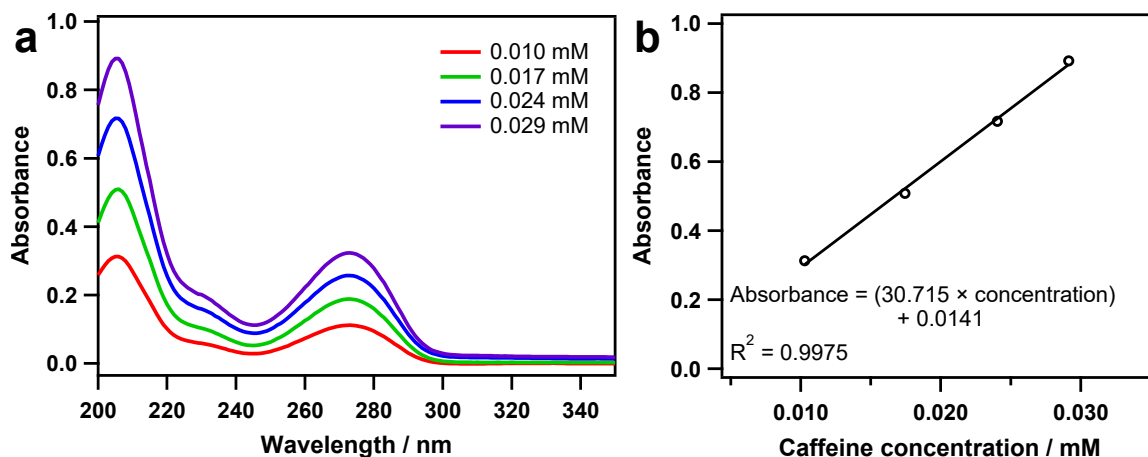


Figure S9: (a) UV-visible spectrophotometry calibration data of caffeine in aqueous solution. (b) The corresponding calibration curve for the data in (a), used for determining unknown quantities of caffeine in solution.

Table 5: Samples compositions and amount of caffeine removed as measured by spectrophotometry.

Conc. GO mg/mL	Conc. CTAB mM	Conc. Caffeine ppm	Caffeine removed ppm	% Caffeine removed
1.00	2.01	197.7	12.7	6.4
1.02	1.88	373.0	55.7	14.9
0.98	1.92	584.8	95.2	16.3
0.97	0.91	199.3	13.8	6.9
0.99	0.99	399.5	62.0	15.5
0.99	1.15	596.3	82.5	13.8

Chapter 8

Conclusions and future directions

This project has explored a significant number of aqueous systems comprising graphene oxide (GO) or reduced graphene oxide (rGO) with surfactants. The research focuses on understanding and controlling the bulk dispersion properties and adsorption of these materials at interfaces, in order to develop new and improved methods for the control and application of carbon nanomaterials in aqueous systems. To achieve these outcomes, novel systems of GO and rGO with a variety of surfactants that differ in fundamental physical properties, such as charge and hydrophobicity, were formulated and investigated to develop important structure–function relationships for these materials. The use of both GO and rGO, as well as the careful selection of surfactant molecules, allowed the key factors affecting stability of the graphene oxides as aqueous dispersions, as well as their adsorption at interfaces in response to surfactant additives, to be addressed.

A large combination of techniques were utilised in the project, so that a conceptual link between the observed behaviour for these systems and the underlying physical chemistry governing that behaviour could be obtained. Small-angle neutron scattering, zeta potential measurements and adsorption isotherms provided key insight into interactions, assembly and stability of the materials in bulk aqueous phases. In contrast, X-ray reflectivity and surface tension measurements gave information on adsorption at the air–water interface, so that clear distinctions relating to interfacial phenomena could be drawn. Finally, the use of imaging techniques such as atomic force microscopy and optical microscopy provided complementary, physical characterisation of the materials.

Cationic surfactants were found to readily adsorb to GO and rGO sheets in solution by electrostatic attraction. Above critical surfactant concentrations, the sheets are seen to aggregate in solution due to insufficient charge repulsion between sheets to maintain stability. The pH of the solution plays a significant role in this phenomenon, with larger surfactant concentrations required to destabilise the suspensions at high pH compared to low pH. This is explained by basic conditions facilitating deprotonation of the GO and rGO carboxylic groups, thus resulting in greater negative surface potentials. Further addition of cationic surfactant can cause restabilisation of the sheets by reversing the charge to a great enough magnitude that they now experience stabilising positive charge repulsions.

By using a photoswitchable cationic surfactant, it was possible to directly probe how the hydrophilic–hydrophobic nature of the surfactant molecules influenced their adsorption to GO and rGO. Photoswitching the surfactant from the *trans* isomer to the more hydrophilic *cis* isomer resulted in a significantly smaller proportion of the surfactants adsorbing to the sheets, indicating that electrostatics are not the only interactions contributing to adsorption in these systems. This photoswitching mechanism can be used to reversibly capture and redisperse the carbon nanomaterials by altering the adsorbed amount of surfactant; the method is more effective for rGO than GO due to its much more sharply defined stability boundary in water (arising from its greater hydrophobicity), which provides a more distinct boundary between dispersed and flocculated states.

Nonionic and zwitterionic surfactant also adsorb readily to GO and rGO, confirming the significance of polarisation and hydrophobic interactions in these systems. Anionic surfactants appear to be the only surfactant class that does not appreciably adsorb to these materials, owing to their like charge repulsions with GO and rGO. This suggests that long-range electrostatics are the dominant forces influencing the adsorption of small molecules with GO and rGO. In all cases where surfactant adsorption is apparent irrespective of surfactant class, small-angle neutron scattering measurements imply that the adsorption mechanism is likely different on GO sheets compared to rGO sheets, given that significantly greater scattering intensities are observed for GO/surfactant systems compared to equivalent rGO/surfactant systems. With GO sheets, the surfactant molecules are believed to adsorb via their head-groups due to strong polarisation interactions with the oxygen-containing moieties. At high surfactant loadings, this results in the formation of surfactant bilayers on the surfaces of the GO sheets in order to prevent solvation of the tail-groups. With rGO however, the surfactants are presumed to adsorb lying flat so that the tail-groups can interact with the hydrophobic domains, resulting in hemispherical micelles on the surfaces of rGO. Therefore, the surfactant adsorption capacity for rGO compared to GO is much lower, explaining the differences in scattering. Interestingly, the scattering patterns also indicate that surfactant adsorption on these materials changes the morphology of the sheets in solution from crumpled to flat; a phenomenon we have dubbed ‘nano-ironing’.

The same cationic photosurfactant mentioned earlier can also be used to effect the spontaneous adsorption of GO at the air–water interface. This behaviour arises due to the surfactant molecules adsorbing to the GO sheets, progressively neutralising the surface charge and rendering the sheets more hydrophobic. As a result, the dispersion of GO in the bulk solution becomes less favourable, and the sheets are thermodynamically driven to the interface where they experience more favourable interactions. This behaviour lowers the surface tension of water by significantly greater margins than the pure surfactant solutions, implying that the combined adsorption of the surfactant-coated GO sheets results in greater concentrations at the interface. The ratio between the surfactant and GO is the major parameter controlling this behaviour, as too little surfactant does not enhance the surface activity of the sheets sufficiently to drive them to the interface, and too much surfactant causes either aggregation or charge reversal of the sheets. In these instances, the GO remains in the bulk solution rather than migrating to the surface.

Interestingly, allowing GO sheets coated with the photosurfactant to adsorb at the air–water interface and then irradiating them with UV light to make the surfactant molecules more hydrophilic does not result in desorption and redispersion of the sheets back into the bulk aqueous phase. This demonstrates the high adsorption energy of GO at the interface, reinforcing the appeal for using high aspect ratio nanosheets to stabilise interfaces with greater efficacy. For interfacial applications, GO is found to be far more effective than rGO, as surfactant addition to aqueous dispersions of rGO does not promote interfacial activity. As rGO is significantly more hydrophobic than GO, it is hypothesised that the different surfactant adsorption mechanism on rGO as well as their greater propensity to crumple in solution may be the main factors hindering its adsorption at interfaces.

This synergistic surface activity is also exhibited in GO systems with nonionic and zwitterionic surfactants, but not anionic surfactants. Again, surfactant to GO ratio is found to be the overriding criterion influencing adsorption of the composite materials at the interface, with excess surfactant serving to inhibit the adsorption of GO at the interface. This is believed to arise from the hypothesised adsorption mechanism for surfactants on GO, whereby at high surfactant loadings the molecules assemble into organised bilayers at the surfaces of the sheets. This fully internalises the hydrophobic regions of the surfactant molecules, and subsequently, the composite material changes from hydrophobic back to hydrophilic. Thus it thermodynamically favours the bulk solution over the interface.

The addition of small quantities of salt to GO/surfactant mixtures, especially in systems where nonionic surfactants are being used, significantly enhances the adsorption of the composite material at the interface. Mechanistically this occurs because the salt ions in solution act to screen the surface charge of the GO sheets, reducing their colloidal stability and allowing them to pack more readily and densely at the air–water interface. The hydrophobicity of the surfactant is also found to greatly increase interfacial activity, as GO composites produced with long-chain betaine surfactants exhibited the highest interfacial activity at the lowest loadings of materials. These results offer many avenues via which to control the interfacial properties of GO in aqueous systems.

Having established the physical basis for achieving spontaneous adsorption of GO sheets at the air–water interface using surfactants, the combined and optimised systems are then used to create emulsions and foams with enhanced stability. The composite materials show significantly greater capacities for stabilising oil–in–water emulsions than the GO or surfactants alone at similar loadings, clearly demonstrating the synergism between the two types of materials. GO sheets flocculated by surfactants can also be efficiently recovered from aqueous solution by froth flotation due to their capacity to stabilise foams. Again the increased surface activity of the sheets brought about by the adsorbed surfactant molecules is the essential factor enabling this outcome. Overall, the results provide broad insight into the physical chemistry and thermodynamics of two-dimensional carbon nanomaterials as both stabilisers and adsorbent materials. The findings can be used to inform the design and formulation of novel, noncovalent composite materials mediated by surfactants, that are

capable of stabilising emulsions and foams with improved efficiency.

Further research to consolidate the bulk properties and self-assembly aspects of GO and rGO behaviour could involve additional small-angle scattering measurements at higher concentrations of the carbon nanomaterials and surfactants. All measurements performed so far contained only 0.1 mg/mL of GO or rGO in water (0.01% by weight), *i.e.* very dilute dispersions. Therefore, significantly increasing the concentrations may yield liquid crystalline character by causing stacking between surfactant-coated sheets. This type of aggregation would be evident in the scattering data as a distinct peak, characteristic of the spacing between sheets. Such an observation would also reassert the importance of the surfactant-induced flattening (nano-ironing) of GO and rGO sheets in solution, as this effect would enhance stacking.

To understand more fundamentally the interactions between molecular surfactants with GO and rGO surfaces, theoretical simulations incorporating a combination of density functional theory and *ab initio* calculations could shed light on the dominant forces and preferred surfactant orientations. This may also allow an understanding of how the specific functional groups of GO and rGO influence surfactant adsorption, and could help inform surfactant choice for improving the surface activity of the materials. A thorough study of specific ion effects on aqueous dispersions of GO and rGO should be performed, using a combination of simple and hydrophobic salts. This may clarify whether these materials follow Schulze-Hardy and Hofmeister behaviour with regards to their aggregation in solution, and could more clearly elucidate the effects of surfactant head-group chemistry when designing composite materials.

The use of additional surface techniques could also be exploited to complement the results of the bulk scattering measurements by more precisely examining the adsorption mechanisms of surfactant molecules on GO and rGO. These measurements would have to be performed *in situ*, and would involve the deposition of a film of GO or rGO on a surface, then immersing it in surfactant solutions of varying concentrations. Neutron reflectivity measurements could then be performed to see if differences in the adsorbed surfactant layer are present when using GO versus rGO, as neutrons would provide sufficient contrast for hydrogenated surfactants in solution. In addition, atomic force microscopy (AFM) imaging of similar samples in water could confirm the physical nature of the surfactant adsorption, whether it takes the form of a continuous bilayer or adsorbed micelles. Force-mapping and repeating images with increased tip force (set-point) could provide complementary information about the surfactant layer and breakthrough forces, to understand surfactant packing and rigidity.

The key to obtaining reliable results for these measurements will be ensuring that deposition of the GO and rGO films on the substrate is uniform. As surfactant layers are typically quite thin (on the order of nanometers), surface roughness of the film must be minimal in order to obtain meaningful data. Furthermore, this would allow larger areas to be imaged using the AFM, as defects or large changes in height of the surface would also mask observation of the adsorbed surfactant.

Optimisation of this process would likely be necessary by trialling various substrates on which to deposit the GO and rGO, such as gold, mica or glass, then characterising the surface before the surfactant solution is added. This may uncover the preferred substrate for conformal (flat) deposition of the sheets, making reflectivity and AFM measurements feasible.

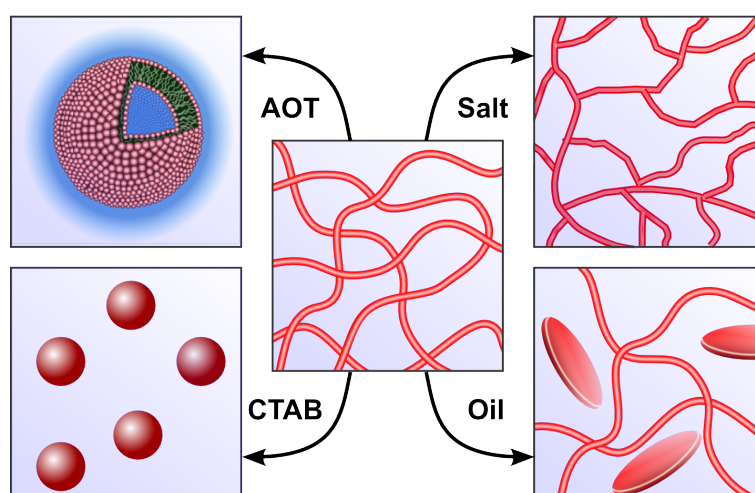
The scope of this thesis has focused primarily on more fundamental physical and chemical aspects of these materials at interfaces and in the bulk aqueous phase. To develop this work further, attempts to utilise these composite materials for industrial applications would also be valuable. Applications that would benefit from the high surface area and water dispersibility of GO and rGO, as well as their enhanced surface activity when mixed with surfactant molecules could include encapsulation and coating phenomena. Encapsulation for the recovery of oil and processing of minerals are possible areas of use for these systems, given their ability to effectively stabilise emulsions and foams. The testing and optimisation of GO/surfactant composites in the emulsification of crude oil would be essential for oil recovery. For minerals processing, the capture of metal ions would need to be investigated, as well as mechanisms for their release. Therefore, in addition to the photo-switchable surfactant examined in this work, surfactants that are responsive to other stimuli such as temperature, pH and shear should also be investigated. Here, GO could potentially provide an additional, practical means for modifying the system stability. Such findings would provide new opportunities for the development of ‘smart’ colloidal materials, and aid in the application of aqueous systems based around GO, rGO and surfactants.

Appendices

Appendix A

Structural Evolution of Wormlike Micellar Fluids Formed by Erucyl Amidopropyl Betaine with Oil, Salts, and Surfactants

Published: Thomas M. McCoy, Alsu Valiakhmetova, Matthew J. Pottage, Christopher J. Garvey, Liliana de Campo, Christine Rehm, Dmitry A. Kuryashov and Rico F. Tabor, Structural Evolution of Wormlike Micellar Fluids Formed by Erucyl Amidopropyl Betaine with Oil, Salts, and Surfactants. *Langmuir*, 2016, **32**, 12423-12433.



Structural Evolution of Wormlike Micellar Fluids Formed by Erucyl Amidopropyl Betaine with Oil, Salts, and Surfactants

Thomas M. McCoy,[†] Alsu Valiakhmetova,[‡] Matthew J. Pottage,[†] Christopher J. Garvey,[§] Liliana de Campo,[§] Christine Rehm,[§] Dmitry A. Kuryashov,[‡] and Rico F. Tabor^{*,†}

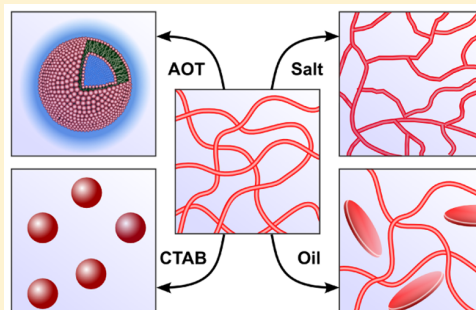
[†]School of Chemistry, Monash University, Clayton 3800, Australia

[‡]Oil and Petroleum Chemistry Department, Kazan National Research Technological University, Kazan, Russia

[§]Australian Centre for Neutron Scattering, ANSTO, Lucas Heights, New South Wales 2234, Australia

Supporting Information

ABSTRACT: Solutions of extended, flexible cylindrical micelles, often known as wormlike micelles, have great potential as the base for viscoelastic complex fluids in oil recovery, drilling, and lubrication. Here, we study the morphology and nanostructural characteristics of a model wormlike micellar fluid formed from erucyl amidopropyl betaine (EAPB) in water as a function of a diverse range of additives relevant to complex fluid formulation. The wormlike micellar dispersions are extremely oleo-responsive, with even as little as 0.1% hydrocarbon oil causing a significant disruption of the network and a decrease in zero-shear viscosity of around 100-fold. Simple salts have little effect on the local structure of the wormlike micelles but result in the formation of fractal networks at larger length scales, whereas even tiny amounts of small organic species such as phenol can cause unexpected phase transitions. When forming mixtures with other surfactants, a vast array of self-assembled structures are formed, from spheres to ellipsoids, lamellae, and vesicles, offering the ultimate sensitivity in designing formulations with specific nanostructural characteristics.



INTRODUCTION

Complex fluids are multicomponent materials generally containing a mixture of surfactants, polymers, and/or particles and exhibiting nonlinear viscosity behavior. The complex internal nano- and microstructures present, along with the interactions experienced by the different colloids, result in fluid mixtures with unique rheology, generally resulting in both viscous and elastic regimes, i.e., viscoelasticity.¹ Because of their ability to change viscosity depending on flow or shear conditions, complex fluids have found many applications in the energy industry, including drilling and fracking fluids.²

An especially important class of complex fluids are based upon wormlike (or threadlike) micellar solutions. These structures arise from the elongation of micelles due to favorable packing conditions whereby the spontaneous curvature of the end caps is significantly higher than that of the cylindrical body of the micelle.³ Growth of the micelle is thus thermodynamically more favored in the longitudinal axis in order to minimize the number of end caps, resulting in long, flexible, cylindrical structures (worms).³ These structures are sometimes considered to be equivalent to dynamic noncovalent polymers as a result of their structure and properties. Beyond a particular concentration, c^* , wormlike micelles form an entangled network (not unlike conventional macromolecular polymers past their overlap concentration) with viscoelastic properties.⁴ Factors that contribute to forming aggregates of this nature

include the molecular geometry of the amphiphiles involved, addition of salt to screen interheadgroup repulsion,⁵ and the addition of hydrotropes that intercalate between surfactant monomers.^{6,7} These micellar materials have been studied extensively, with several recent reviews covering their phase behavior and structural and rheological properties.^{3,8–10}

A particularly interesting and industrially relevant class of surfactants that are known to form wormlike micelles are the zwitterionic betaine surfactants, which contain quaternary ammonium and carboxylate ions in the surfactant headgroup and are commonly used in personal care products owing to their nonhazardous and biodegradable nature.¹¹ Wormlike micelles arising from solutions of long-alkyl-tail betaine surfactants have been explored previously, notably by the groups of Raghavan and Feng.^{12–14} Thus, although the rheology of these micelles has been thoroughly investigated, questions remain about their microstructure, particularly in mixed systems. Kumar and co-workers investigated the internal structure and rheology of a particular long-chain betaine, erucyl amidopropyl betaine (EAPB), as a pure surfactant and also as a

Special Issue: Tribute to Toyoki Kunitake, Pioneer in Molecular Assembly

Received: May 6, 2016

Revised: June 24, 2016

Published: September 3, 2016

function of organic salt additives, characterizing the fluids as elastic gels at and near room temperature.¹² Their investigation included the rheology of low-concentration systems (0.8–25 mM, 0.04–1.2 wt %) along with small-angle neutron scattering (SANS) of EAPB in water at higher concentrations of 2.4–7.2 wt %, where fully developed wormlike micelles are seen. However, these data did not include a sufficient q range to determine the persistence length of the micelles, the apparent length over which the micelles appear rigid, and so some fundamental questions remain.

Central to complex fluid research and its implementation is the ability to control the viscosity and flow properties. A particularly appealing characteristic for complex fluids based on wormlike micelles is the opportunity to induce a response to an internal or external stimulus.¹⁵ Examples of materials that exhibit temperature-,^{16,17} CO₂-,^{18–20} light-,^{21–23} or pH-responsive^{24,25} rheological properties have been shown, with zwitterionic surfactants exhibiting the latter. Furthermore, the effect of particulate additives such as silica nanoparticles on wormlike micellar fluids has been investigated and was found to increase the system viscosity and lower the entanglement concentration.^{26,27} Such particles can also be used as tracer probes to analyze the microrheology of complex fluids.^{1,28,29} Also, Shibaev and co-workers elegantly demonstrated that the addition of oil to a wormlike micelle solution of potassium oleate micelles facilitated the evolution to a microemulsion state, with an accompanying decrease in viscosity.³⁰ However, a more thorough investigation of how different types of additives can affect wormlike systems is needed to unearth new ways of controlling and fine-tuning these materials.

Here, we explore the internal nano- and microstructural properties of complex fluids based on solutions of erucyl amidopropyl betaine (docosen-13-yl amidopropyldimethyl betaine, EAPB, Figure 1a) when additives comprising a model oil, small organic molecules, and various salts and surfactants are incorporated. These materials are chosen to cover a diverse range of molecular geometries and chemistries in order to probe the fundamental self-assembly phenomena associated with the wormlike aggregation of betaine surfactants. A combination of small-angle and ultra-small-angle neutron scattering (SANS and USANS) are used along with viscometry to uncover the structural reasons for the unique behavior of these materials and the evolution of their internal nanostructure and self-assembly.

MATERIALS AND METHODS

Materials. Erucyl amidopropyl betaine (docosen-13-yl amidopropyldimethyl betaine, EAPB, Figure 1a) was synthesized and purified as described previously.^{14,31} The molecule as synthesized has a molar mass of 480.76 g/mol. Toluene and phenol (spectroscopic grade) were from Merck (Darmstadt, Germany) and used as received. Deuterium oxide (D₂O, 99.8 atom % D) was from Merck and used as received. All salts (sodium chloride, calcium chloride dihydrate, and tetra-*n*-butylammonium bromide) were ACS reagent grade from Merck and used as received. Sodium acetate was also used but was from BDH Chemicals (≥98%). Finally, surfactants sodium dodecylsulfate, cetyltrimethylammonium bromide, poly(ethylene glycol)-*p*-(1,1,3,3-tetramethylbutyl)-phenyl ether (Triton X-100), and sodium bis(ethylhexyl) sulfosuccinate (Aerosol-OT), all laboratory grade (≥90%), were from ChemSupply, Australia and used as received.

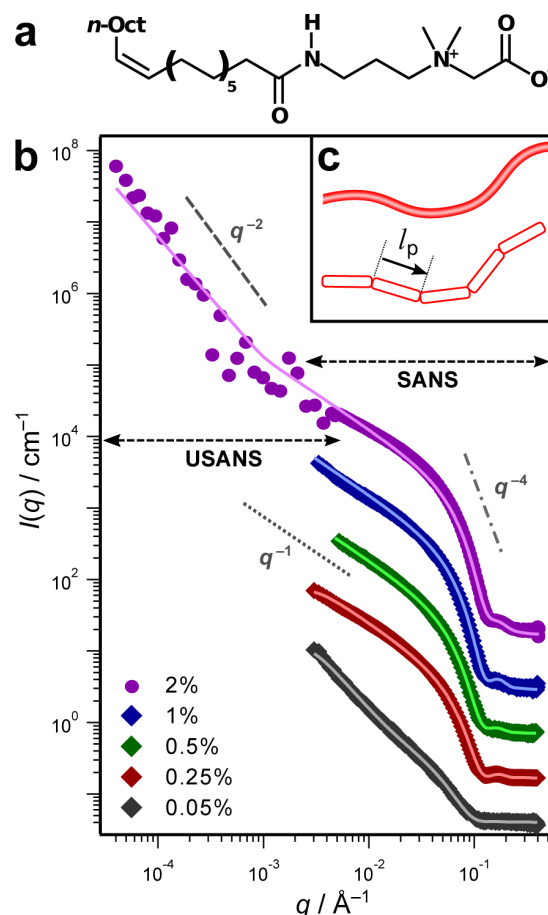


Figure 1. (a) Chemical structure of erucyl amidopropyl betaine (docosen-13-yl amidopropyldimethyl betaine, EAPB). (b) SANS and USANS spectra for solutions of EAPB in D₂O at the specified concentrations (by mass). Symbols are experimental scattering data, and solid lines are model fits generated as described in the text. Data sets are vertically offset by multiplication for clarity. The dotted, dashed, and dotted–dashed lines represent characteristic slopes of q^{-1} , q^{-2} , and q^{-4} respectively. (c) Schematic representation of the physical meaning of the persistence length, l_p , when applied to wormlike micelles.

Methods. **SANS.** Small-angle neutron scattering (SANS) measurements were made on the Quokka beamline at the Australian Centre for Neutron Scattering, Australian Nuclear Science and Technology Organisation (ANSTO), Lucas Heights, NSW, Australia.³² Samples were prepared using D₂O as the solvent and transferred to 2-mm path-length cells with 1-mm-thick quartz windows for analysis. Temperature control was achieved using a recirculating water bath with a characteristic precision of ± 0.05 °C. Throughout the measurements, temperature was recorded using a thermocouple placed in one of the sample holders to ensure accuracy at the sample position in the instrument. Data were reduced from the raw counts over a two-dimensional area detector to a radially averaged absolute intensity versus the scattering vector q , assuming radially isotropic scattering, where q is defined as

$$q = \frac{4\pi}{\lambda} \sin \frac{\theta}{2} \quad (1)$$

wherein λ is the wavelength of the incident neutron beam and θ is the scattering angle. The q range is defined by the instrument configurations and the size of the detector. For these experiments, an incident neutron wavelength of $\lambda = 5 \text{ \AA}$ ($\Delta\lambda/\lambda = 10$) was used as obtained by a mechanical velocity selector, with two sample–detector distances of 2 and 14 m, giving a q range of $0.005\text{--}0.400 \text{ \AA}^{-1}$. To reduce the raw counts on the detector to a normalized intensity, the response of each detector pixel was calibrated to the signal from a flat isotropic scatterer, and then the scattering from an empty quartz SANS cell was subtracted. The radial average of the intensity expressed as a function of q could then be obtained using the instrument configuration and detector response. The absolute intensity scaling was obtained by normalizing for the sample thickness (2 mm) and comparing the intensity to that of an empty beam measurement.

USANS. Ultra-small-angle neutron scattering (USANS) measurements were made on the Kookaburra beamline at the Australian Centre for Neutron Scattering, ANSTO.³³ This instrument is a Bonse-Hart configuration rocking-axis neutron spectrometer using two sets of identical, five-reflection, channel-cut silicon single crystals that act as the monochromator and analyzer. The crystals are arranged in a nondispersive parallel geometry such that they experience Bragg reflection conditions. For these experiments, an incident neutron wavelength of 4.74 \AA was used. Rocking curve profiles were obtained by rotating the analyzer crystal away from the aligned peak position (in which the undeviated neutrons are reflected directly into the detector) and measuring the neutron intensity as a function of the scattering vector, q , as defined above. The total available q range was $\sim 10^{-5} \text{ \AA}^{-1} < q < 10^{-2} \text{ \AA}^{-1}$, although in practice this was limited at high q by the intensity of sample scattering for certain samples. USANS data were desmeared in Igor Pro using the macro package for this purpose developed by Kline.³⁴

SANS and USANS data were combined and concurrently fitted using the SASView software (<http://www.sasview.org>). Details regarding the models and their equations as well as fitting parameters can be viewed in the [Supporting Information](#).

Viscometry. Viscometry measurements were performed using a RheoStress 6000 rheometer (Thermo Scientific HAAKE, Germany) equipped with a double-gap coaxial cylinder measuring system (outer cylinder diameter 21.7 mm, inner cylinder diameter 18 mm, height 55 mm).

RESULTS AND DISCUSSION

Wormlike EAPB Solutions in Water. Previous investigations of EAPB in water have focused on the rheology of the systems as a function of concentration and additives, with small-angle scattering conducted at high concentrations (2.4 wt % and greater).¹² Here, we explore lower concentrations to understand the behavior of EAPB at low loadings and the structural evolution of the micellar fluid. Scattering data of EAPB as a function of concentration is shown in [Figure 1b](#). Interestingly, at even the lowest concentration measured (0.05 wt %, 1 mM), wormlike micelles are produced with a radius of approximately 2.9 nm ([Supporting Information](#)), which correlates well with the length of a 22-carbon erucyl chain (2.93 nm from the Tanford equation³⁵). This is readily detected from the tendency toward a slope of q^{-1} at intermediate q values, before a change in slope to $\sim q^{-2}$ at low q values.^{36,37} For higher concentrations, this change in slope is lower in q than can be detected by SANS, indicating an

increase in the persistence length and thus scattering from one-dimensional extended objects.³⁶ The slope and functional form of the scattering at lower q values is obtained from ultra-small-angle neutron scattering (USANS) of the sample. Unfortunately, the lowest concentrations are not amenable to USANS because of their low scattering cross-section, and the contour lengths for these aggregates at higher concentration are too large to even be accurately measured by USANS. This implies overall sizes greater than the maximum accessible by USANS, which in these experiments is $d = 2\pi/q_{\min} \approx 15 \text{ \mu m}$.

However, at concentrations of 1 wt % and above, USANS can be performed, obtaining data with reasonable statistics ([Figure 1b](#)) showing a characteristic steepening in slope at a specific q value. This value is generally understood to correspond to the persistence length (Kuhn length), that is, the length scale at which the scattering switches from representing essentially rigid rods (at high q) to a flexible chain more akin to a polymer solution at low q .^{36,37} For EAPB at a concentration of 2 wt %, the point at which the slope changes indicates an apparent Kuhn length of around 150 nm, a surprisingly large value indicating rather rigid micelles. However, at 0.05 wt %, the scattering curve conforms to the steeper slope at much higher values of q indicating that the value of the persistence length is lower and the micelles are more flexible. This result is not unexpected because it has been found previously using a variety of experimental techniques that the persistence length tends to increase significantly with surfactant concentration.^{37,38} For ionic surfactants whose micelles can be rendered wormlike through the addition of salt (such as cetyltrimethylammonium bromide in the presence of potassium bromide),^{5,39} the rigidity of the micelles and hence the Kuhn length is intimately linked to the amount of salt added and generally takes values of 30–60 nm. However, for the zwitterionic surfactant used here, the relationship between solution conditions such as ionic strength and salt valency is less clear. These data can be modeled using a theory for flexible cylindrical micelles,³⁶ and this model was updated by Chen et al.³⁷ to incorporate intermicellar interactions. However, it is notable for the scattering data for EAPB at 2 wt % that the slope fit at low q is not perfect, indicating a departure from the structure predicted by this model. Chen et al. noted that the slope at low q and the crossover point were most sensitive to surfactant concentration and solution conditions for the systems they studied, and in general their systems had much lower Kuhn lengths than appear to be predicted in the present work.³⁷ It is therefore possible that the change in slope for these data is in fact indicative of a change to a gel-like regime,⁴⁰ which is discussed in detail in the sections below.

Mixtures of Wormlike EAPB Solutions with Oil. The addition of even very small amounts of an aromatic hydrocarbon oil, toluene, causes a significant change in the properties and microstructure of EAPB in water. For only 0.1 wt % oil added to a 1 wt % EAPB solution, the small-angle scattering data show an increase in slope at low q compared to the pure surfactant system ([Figure 2a](#)). This appears to indicate a significant amount of surface scattering without phase separation, indicating areas of bilayer-like aggregation.⁴¹ This is consistent with the formation of thin, flat, disklike micellar structures in which the thickness is typically a few nanometers (5–10 nm) and the length, which appears to be concentration-dependent, is greater than 100 nm ([Supporting Information](#)). For these samples, the USANS proves crucial because the lowest q scattering indicates that in fact at low oil volume

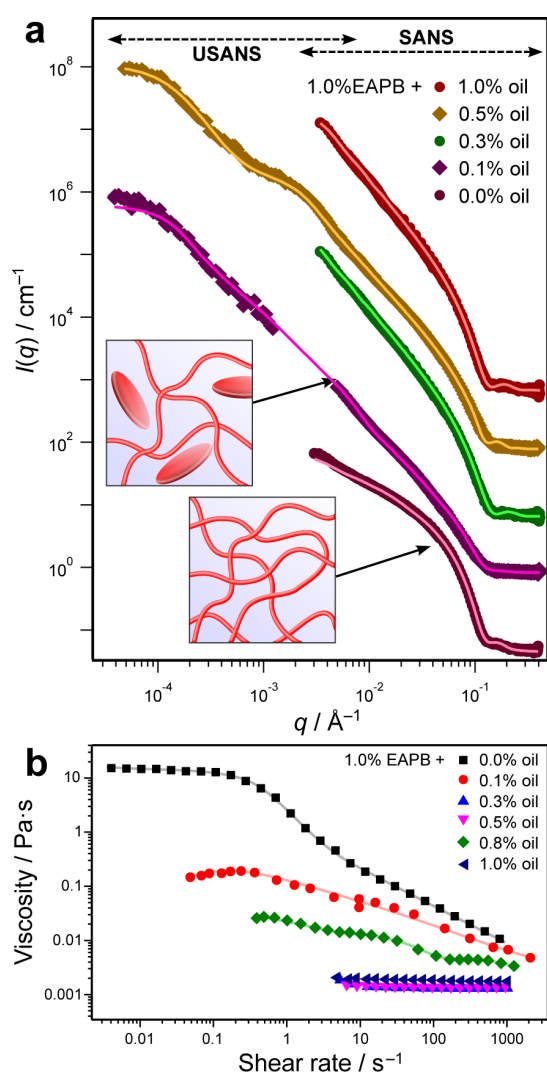


Figure 2. (a) SANS and USANS spectra for 1 wt % EAPB with different concentrations of a model oil (toluene) added, in D_2O . Symbols are experimental scattering data, and solid lines are model fits generated as described in the text. Data sets are vertically offset by multiplication for clarity. (b) Dynamic viscosity data for solutions of EAPB (1 wt %) with a model oil (toluene) added. It should be noted that eventual phase separation occurred for samples with more than 0.5% added oil.

fractions the addition of oil results in the emergence of a binary aggregate system, comprising worms as well as these small disclike structures. Hence the data can be fit using a linear combination of flexible cylinders plus disclike micelles (Supporting Information), with an approximately equal volume ratio at 0.1 wt % added toluene. At a higher oil loading of 0.5 wt %, the ratio of discs is much higher (82% by volume), and at 1 wt % added oil, the sample underwent very slow microphase separation to eventually reject excess oil as droplets that were stabilized as a fine emulsion.

Unsurprisingly, this abrupt microstructural change is accompanied by a significant decrease in fluid viscosity (Figure 2b), even with very small amounts of oil added (0.1%). In line with previous studies, we find that EAPB solutions have shear-dependent viscosity, and the addition of 0.1 wt % toluene results in a nearly 100-fold decrease in the apparent zero-shear

viscosity when compared to that of pure EAPB at the same concentration. This effect is presumably a result of the system switching from an entangled wormlike network to a mixture of worms and discs in which the remaining worms are below their entanglement concentration. Once 0.3 wt % oil has been added, the viscosity is close to that of water and is essentially independent of shear rate, indicating a dispersion of (comparatively) small micelles. Interestingly, at higher oil loadings, the viscosity increases again. This behavior is also consistent with the formation of phase-separated (macro)-emulsion droplets; complex emulsions are known to have higher viscosities than their parent liquids and experience shear-dependent viscous behavior.⁴²

Because toluene is an aromatic hydrocarbon, it is expected to partition into the hydrophobic micelle interior. Here it may intercalate between surfactant chains, potentially experiencing favorable stacking interactions with the π bonding orbitals of the unsaturated *cis* double bond within the EAPB tail group. This intercalation would result in an increase in the effective tailgroup volume (equally interpreted as an increase in surfactant critical packing parameter), driving the formation of lower-curvature surfaces, in this case, disclike micelles. A similar structural evolution for a different wormlike system was recently noted by Shibaev and co-workers, where worms transitioned into classical spherical microemulsion droplets upon addition of a linear hydrocarbon oil.³⁰ However, in the case of EAPB, the emulsification results in discs instead of droplets, which are a considerably rarer form of surfactant self-assembly.⁴³ This unique pathway presumably results from the packing conditions and the specific location of toluene within the self-assembled structure. Disc formation has been seen previously in dual-surfactant systems wherein a mixture of single-chain cationic and anionic surfactants formed disclike aggregates whereby the high curvature at the edges required for discs was facilitated by having one of the surfactants present in slight excess.⁴³ The excess surfactant invariably forms the edges of the micelles, with intermolecular spacing between headgroups increasing as a result of electrostatic repulsion, which in turn allows for much greater curvature. However, where both surfactants coexist, the structure is flat as a result of denser packing. Therefore, it is likely that toluene impacts the assembly of EAPB in a similar way, with excess oil accumulating at the edges. This is also supported by the fact that the proportion of discs in the system increased with the addition of toluene whereas the lateral length of the discs decreased (Supporting Information) so as to promote the formation of more edge regions.

Phenol is structurally rather similar to toluene and is widely used in industrial fluids and biological extractions.⁴⁴ The addition of small amounts of phenol to EAPB wormlike micellar fluids was found to transform the wormlike aggregates present in pure EAPB systems into lamellar or bilayer aggregates (Figure 3). Small-angle scattering from lamellar structures gives a well-defined characteristic slope of q^{-2} that continues to increase in intensity, indicating scattering from the surface of flat, two-dimensional “sheets”.⁴¹ This is apparent in the scattering data for EAPB with phenol where even at ultralow q the data conforms to this slope. At very small added amounts of phenol (0.1 wt %), the SANS data show significant deviation from the pure wormlike signature, suggesting a mixed system comprising both worms and bilayers. However, because of the inherently challenging nature of fitting mixed systems where a simple additive relationship between two models does

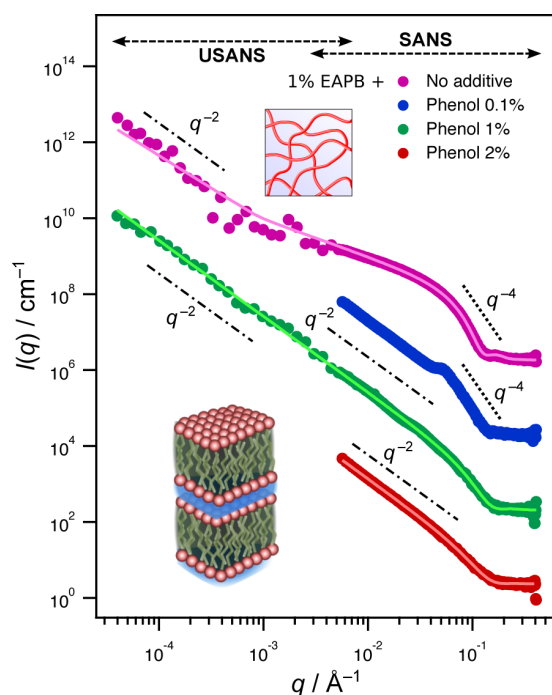


Figure 3. SANS and USANS spectra for solutions with 1% EAPB in D_2O and the specified concentrations of added phenol (by mass). Symbols are experimental scattering data, and solid lines are model fits generated as described in the text. Data sets are vertically offset by multiplication for clarity. The dotted–dashed and dotted lines have been added to indicate the characteristic slopes of each pattern and represent q^{-2} and q^{-4} , respectively. The schematic insets have been added to show the structural evolution of the system from pure worms to pure bilayers; the precise location of phenol within the structures is not indicated.

not appear to be obeyed, these data have not been fitted. When increasing the additive loading of phenol to equal and higher weight percentages to that of EAPB ($\geq 1\%$), the data appears to be indicative of a pure lamellar system and can be accurately fit using a model for noninteracting bilayer sheets. Note the absence of a characteristic Bragg peak in these data, suggesting unoriented bilayer fragments rather than a paracrystalline stack.⁴⁵

Previously it was found that doping aqueous solutions of the cationic surfactant cetyltrimethylammonium bromide (CTAB) with *p*-ethyl phenol resulted in the structural evolution of the system from spheres to worms and other structures.⁴⁶ However, transition to a lamellar phase from a pre-existing solution of wormlike micelles may be useful in templating layered materials or the design of modifiable synthetic bilayer membranes based on complex fluids.^{47,48} Because the phenol molecules are neutral and only sparingly surface-active, they will likely partition into the interior of the micelles as with toluene, significantly increasing the volume of the hydrophobic region and hence increasing the effective critical packing parameter. Because EAPB is zwitterionic, the headgroup is self-screening, meaning that the effective area per molecule at the interface is significantly smaller when compared to that of CTAB.^{14,49} Therefore, the intercalation of small molecules into the micelle core increases the critical packing parameter, explaining why the self-assembly of the system is driven to reduce the curvature of the aggregates, resulting in larger, planar bilayer structures.

Also, because phenol is more water-soluble than toluene and marginally surface-active, we believe that these molecules preferentially locate further toward the exterior of the micelles when compared to the completely nonpolar toluene. This is best visualized as a partitioning among the micelle core, headgroup area, and bulk solvent. This could mean that the molecular packing at the interface is denser, which would explain why the addition of phenol results in a continuous bilayer instead of discs. To explore the precise location of phenol and toluene in these samples, a contrast variation SANS experiment could be used, though this would require the deuteration of one or more components.

Mixtures of Wormlike EAPB Solutions with Salt.

Wormlike micellar growth in aqueous solution can be promoted for ionic surfactants when simple salts are incorporated, with common examples being cetyltrimethylammonium bromide (CTAB) with potassium bromide^{5,39} and sodium dodecyl sulfate (SDS) with sodium chloride or sodium bromide.^{50,51} The mechanistic rationale dictating this behavior is that the excess counterions present act to shield the charge repulsions between the surfactant headgroups, facilitating closer packing and hence a higher end-cap energy, causing the surfactant aggregates to extend in one dimension in order to minimize their free energy.³

However, the effects of salts on zwitterionic surfactants that spontaneously form wormlike micelles are not so completely understood. Indeed, the expectation is that any effects should be rather minimal because the amphoteric molecules are conceptually more like nonionic surfactants. Here, we explore the effect of adding a variety of electrolytes with different valency and hydrophobicity to the already wormlike network of EAPB and monitor the structural evolution using combined SANS and USANS (Figure 4). The specific salts investigated are sodium chloride (NaCl), calcium chloride ($CaCl_2$), sodium acetate (CH_3COONa), and tetrabutylammonium bromide ($n-Bu_4NBr$). The salt concentrations chosen span the typical amounts added to induce structural evolution in micellar systems.⁵⁰

At the concentrations measured, little change in the scattering pattern is observed within the SANS q range (0.003 – 0.400 Å^{-1}) for each electrolyte added. Fitting using the flexible cylinder model therefore accurately describes the data within these regions, indicating that salt causes little to no deviation in the local micellar aggregation of EAPB. That is, the worm radius is essentially unchanged. This is perhaps unsurprising because the zwitterionic betaine headgroup is to a large extent self-screening, and the net neutral charge means that it behaves somewhat more like a nonionic surfactant under most circumstances. Hence, further screening of the charge repulsions by the addition of excess salt could be expected to have little effect, accounting for the lack of structural evolution of the micelles on addition of salt, regardless of ion valency or hydrophobicity.

In the majority of samples measured, however, an increase in the slope of the intensity as a function of q in the USANS region (3×10^{-5} – $3 \times 10^{-3} \text{ Å}^{-1}$) from q^{-2} to q^{-3} is observed (Figure 4), as are significant decreases in the calculated values for the persistence length (Supporting Information). Again, this indicates that USANS is in fact crucial in forming a thorough picture of the structural evolution of these systems because the local micellar behavior (on SANS length scales, i.e., up to $\sim 100 \text{ nm}$) is independent of the salt concentration. For sodium chloride, the addition of 0.2 wt % salt induced a slope of q^{-3} at

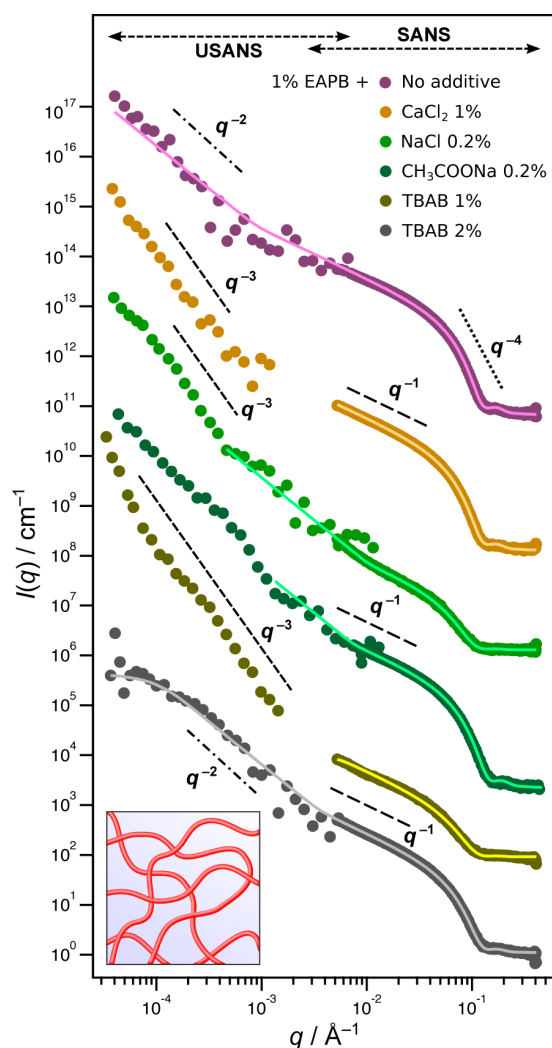


Figure 4. (a) SANS and USANS spectra for solutions with 1% EAPB in D₂O and the specified concentrations of added electrolyte (by mass). Symbols are experimental scattering data, and solid lines are model fits generated as described in the text. Data sets are vertically offset by multiplication for clarity. The dotted, dashed, and dotted-dashed lines have been added to indicate the characteristic slopes of each pattern and are labeled according to their respective gradients: q^{-1} , q^{-2} , q^{-3} , and q^{-4} . The inset has been added to indicate that the samples contain wormlike structures.

low q . Such a slope at low values of q is often interpreted as accompanying phase separation,⁵² but it can also be indicative of the formation of a gel-like network with fractal characteristics.⁴⁰ Notably here, the addition of 0.2 wt % NaCl did not induce obvious phase separation, with the sample remaining clear and optically isotropic, but the addition of 1.0 wt % NaCl did result in phase separation, wherein a dense gel-like EAPB-rich phase separated as a supernatant above an inviscid excess water phase. Interestingly, for calcium chloride at 1 wt %, the sample remained apparently stable, although the scattering at low q in the USANS region again has a slope of q^{-3} , indicating a microstructural change on addition of the salt.⁴⁰ Because only a few concentrations were investigated for these systems, clear trends in salt addition cannot be deduced. However, it is clear from the USANS data and the appearance of the samples that the impact is significant.

Cardiel et al. recently noted that the inclusion of hydrotropic salts in wormlike systems can promote the formation of larger aggregates that are visible only in the q range measurable by USANS and that these structures cannot be accurately fit using a worm model. Instead, the data in this region can be fit using a fractal model, indicating that the resultant structures comprise large, branched domains (i.e., a wormlike micellar network).⁴⁰ These inferences are backed up by very compelling electron microscopy images of the networked micelles. For the samples of EAPB with added salts presented in the current work, the absence of turbidity or cloudiness in these samples eliminates critical scattering due to the precipitation or phase separation of the components as a cause of the increase in q slope, adding credibility to the formation of a fractal network. Chu et al. recently showed that a related sulfobetaine surfactant forms similar branched wormlike networks,⁵³ again suggesting that this mechanism applies here also.

The exception to the trends noted above arises from addition of a hydrophobic electrolyte in the form of tetra-*n*-butylammonium bromide (TBAB). At a loading of 1 wt % of this salt, the same q^{-3} fractal network formation described above is seen. However, at 2 wt % TBAB, the system appears to maintain the characteristic wormlike scattering pattern even at ultralow values of q (Figure 4) and can be consistently fit with the flexible cylindrical micelles model. At this concentration, it is plausible that packing and energy conditions change as a result of the partitioning of the hydrophobic salt into the headgroup region of the micelles or even that the amount of salt added is high enough to more effectively result in capping of the worms, hence branching of the micelles is not necessary. Another potential effect is that the tetrabutylammonium ion is sufficiently hydrophobic such that it can be sequestered inside the micellar core at high concentrations, and such a distribution means that it less effectively participates in the formation of the gelled network as seen for the simpler salts. Such an effect is not without precedent because it was recently shown that alkylammonium counterions can penetrate surfactant self-assemblies and change their curvature.⁵⁴ Indeed, TBAB is used as a phase-transfer catalyst because it exhibits exactly this behavior. However, because of the limited number of concentrations measured here, the specifics of these transitions cannot be claimed and interpretations must be taken with caution. Nonetheless, these data do mark the particular hydrophobic ion as worthy of further investigation as a structure-directing additive in wormlike systems.

Mixtures of Wormlike EAPB Solutions with Other Surfactants. Unlike the addition of salt, surfactant additives appear to cause significant changes in the local nanostructure of EAPB aggregates. The equilibrium self-assembled structures depend largely on the nature of the added surfactant, in terms of its headgroup charge and tailgroup structure (i.e., molecular geometry and critical packing parameter). Interactions between EAPB and the added surfactant are found to disrupt the elongated aggregation occurring in wormlike micelles, giving rise to a broad series of shapes including rods/cylinders, spheres, and ellipsoids (Figure 5), which are discussed in detail below. The emergence of these different microstructures can be explained by synergistic effects from having multiple surfactant species present, which in turn has a significant impact on the critical packing parameter at the interface. The critical packing parameter, P^* , of surfactants is dependent on the volume of the surfactant tailgroup (V_t), the length of the tailgroup (l_t), and

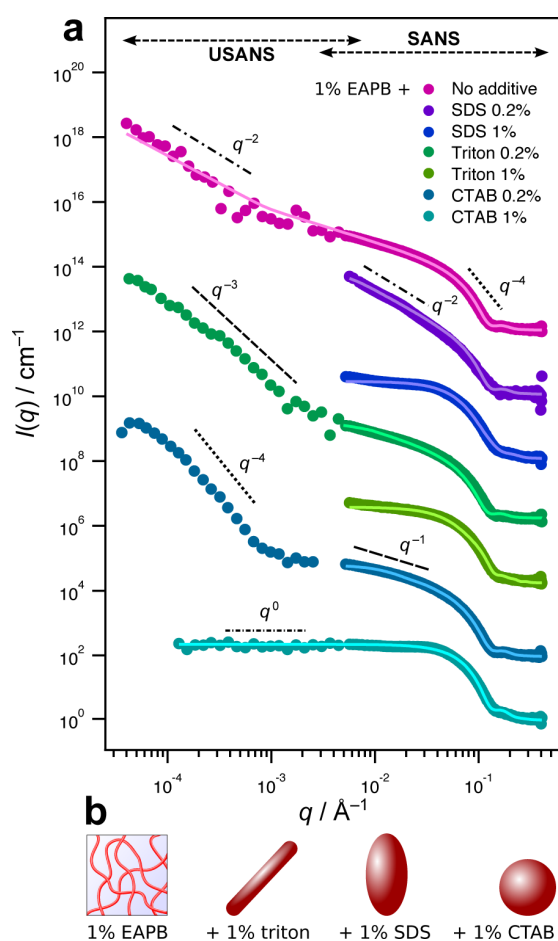


Figure 5. (a) SANS and USANS spectra for solutions with 1% EAPB in D₂O and the specified concentrations of added surfactant (by mass). Symbols are experimental scattering data, and solid lines are model fits generated as described in the text. Data sets are vertically offset by multiplication for clarity. The dotted, dashed, and dotted-dashed lines have been added to indicate the characteristic slopes of each pattern and are labeled according to their respective gradients: q^0 , q^{-1} , q^{-2} , q^{-3} , and q^{-4} . (b) Schematic indicating the specific shape change from worms relating to each additive at 1% by weight.

the effective area per molecule at the interface (A_{hg}), as defined by Israelachvili:⁵⁵

$$P^* = \frac{V_t}{l_c A_{\text{hg}}} \quad (2)$$

For wormlike micelles, the critical packing parameter is typically $1/3 < P^* < 1/2$. Surfactant synergism and its effect on surfactant micellization is a well-known phenomenon, with major contributing factors being intermolecular interactions and thermodynamics.^{56–58} For pure EAPB, the area per headgroup from surface tension data was calculated by Feng et al.¹⁴ as 36 Å². Using the bulk density of erucic acid provides a tailgroup molecular volume of 594 Å³. Using Tanford's equation³⁵ for the molecular length of a hydrocarbon (not accounting for the unsaturation that would likely have little effect) gives a value of 29 Å. Thus, the critical packing parameter for EAPB is calculated to be $P^* = 0.56$, which seems a little high for the formation of wormlike micelles. It could be that the packing in a planar interfacial film is different from that

in a micelle, and thus the area per headgroup calculated from surface tension data is an underestimate. It has also been widely noted that packing parameters are rarely absolute (or indeed absolutely obeyed) and therefore are best taken as a guide.⁵⁹

The addition of a charged cosurfactant in the form of the anionic sodium dodecylsulfate (SDS) caused a change in the structure of EAPB aggregates from worms to ellipsoids when an equal mass percentage of both surfactants was present (Figure 5). The change in structure is likely due to the formation of mixed micelles of the two surfactants. Because SDS has a charged headgroup, the spacing between molecules at the interface will likely experience a net increase due to electrostatic repulsions. The critical packing parameter for SDS is calculated to be $P^* = 0.38$ using surface tension data⁶⁰ and the Tanford formulas for tailgroup length and volume. Thus, at mass fractions of 1 wt % SDS and 1 wt % EAPB (a molar ratio of 1.66:1), the effective critical packing parameter for the mixture can be calculated using a weighted average as $P^* = 0.45$, lower than that for pure EAPB in line with expectation. Interestingly, the intermediate state where a lower molar ratio of 0.33:1 (SDS/EAPB) was used did not form a stable phase, producing instead a cloudy dispersion that was kinetically stable. This sample showed characteristic q^{-2} scattering, potentially indicating bilayer-type structures before eventually resolving into two separate phases. At higher molar ratios of SDS, the system was restabilized and remained clear and isotropic.

When adding a cationic surfactant, cetyltrimethylammonium bromide (CTAB), to EAPB, an equal mass ratio with EAPB (molar ratio 1.32:1 CTAB/EAPB) formed spherical micelles (Figure 5). The calculated packing parameter for CTAB, $P^* = 0.39$, from surface tension data⁴⁹ is essentially equal to that of SDS, but in this instance, the increase in curvature for the mixed system is even more extreme. The effective critical packing parameter of the mixed system is $P^* = 0.46$, again lower than for pure EAPB, suggesting a change to higher-curvature structures. However, this does not explicitly predict the formation of spheres. This may result from a higher effective charge at the micelle interface due to the higher dissociation of CTAB because SDS is notoriously poorly dissociated in micelles (as few as 20% of the surfactant molecules may be dissociated in pure SDS micelles).⁶¹ At a lower molar ratio of 0.26:1 (CTAB/EAPB), a thermodynamically stable dispersion of short, cylindrical rodlike micelles forms—a logical intermediate state between worms and spheres—and for this state, the effective critical packing parameter of the mixture would be $P^* = 0.53$. Interestingly, however, the USANS data also suggests that large spherical structures, most likely vesicles, are also present in this lower molar ratio sample based on the q^{-4} slope in this region as well as the final downturn at the lowest values of q . Hence, the surfactant ratio is clearly of importance in determining the structures and uniformity in these systems. It is noteworthy that in micelles containing a mixture of ionic surfactants the area per headgroup may change in a nonadditive fashion, which has not been accounted for here. Furthermore, in these betaine surfactants the position of the cation is further toward the micelle interior than the anion, which will also likely affect the positioning of the cosurfactant and thus influence micelle structure. Hence, as stated previously, values for the packing parameter should be taken as a guide only.

Mixing the amphoteric EAPB with a nonionic surfactant, Triton X-100 (TX-100, poly(ethylene glycol)-*p*-(1,1,3,3-tetramethylbutyl)-phenyl ether), the difference in structures is

not as profound. Equal mass percentages of TX-100 and EAPB (corresponding to a molar ratio of 0.74:1) resulted in rodlike or cylindrical micelles approximately 10 nm in length (Figure 5). Because TX-100 has a nonionic headgroup, the effective area per molecule at the interface will be lower because of a lack of charge repulsions, and the bulky phenyl ring and two quaternary carbon atoms in the tailgroup give the hydrophobic region a larger volume. The critical packing parameter of TX-100 is $P^* = 0.33$, so the effective critical packing parameter of the mixture is again around $P^* = 0.46$.

Particularly rich and interesting aggregate morphology is seen when mixing EAPB with a surfactant that has an extremely bulky tailgroup. Aerosol-OT (AOT, sodium bis(ethylhexyl) sulfosuccinate) is a branched, dichain surfactant that is widely employed for its ability to form phases with inverse curvature (i.e., inverse micelles and water-in-oil microemulsions).^{62–64} When AOT is added to aqueous EAPB solutions in water, the wormlike network is seen to progressively evolve into vesicles as the concentration of AOT is increased (Figure 6). At lower

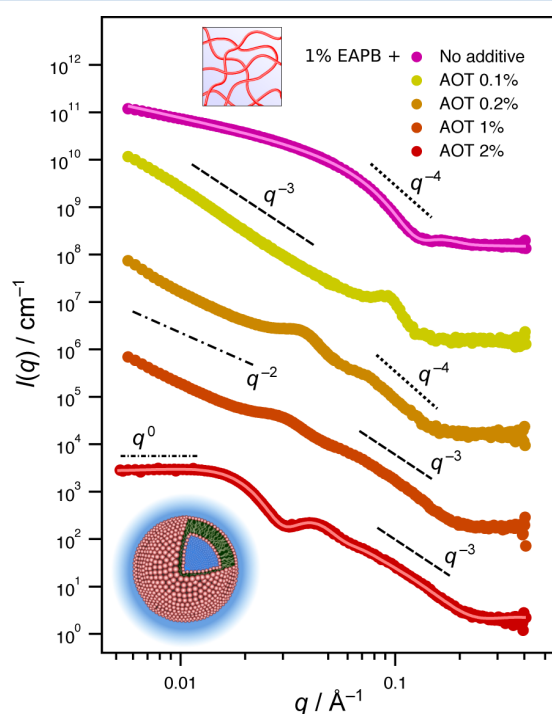


Figure 6. SANS spectra for solutions with 1% EAPB in D₂O and the specified concentrations of added AOT surfactant (by mass). Symbols are experimental scattering data, and solid lines are model fits generated as described in the text. Data sets are vertically offset by multiplication for clarity. The dotted, dashed, and dotted–dashed lines have been added to indicate the characteristic slopes of each pattern and are labeled according to their respective gradients: q^0 , q^{-1} , q^{-2} , and q^{-4} . The schematic insets have been added to show the structural evolution of the system from pure worms to pure vesicles.

loadings of AOT (0.1–1 wt %), SANS analysis suggests that the two surfactants form a mixed system that may include quantities of worms, vesicles, and other weakly interacting bilayer structures. This is further enforced by the slope at low q changing markedly from q^{-1} to q^{-3} , indicating the formation of larger structures above the resolution limit of the technique. This would also explain the cloudy appearance of these samples, which appear to be undergoing a microphase

separation that takes weeks to fully resolve. However, when the mass proportion of AOT is double that of EAPB (i.e., 2 wt %), the sample becomes clear again and the scattering pattern can be very precisely fit using a vesicle model, indicating the presence of a pure vesicle system (Figure 6). The q^0 slope at low q also suggests that the vesicles do not grow larger than the calculated diameter of 16 nm (bilayer thickness of approximately 2.3 nm, see Supporting Information). Spontaneous vesicle formation has been previously observed in mixed surfactant systems,⁶⁵ with theoretical modeling based on curvature energy affirming that the assembly tends to result in a preferred size.⁶⁶ Recently, Fan et al. discovered a similar worm-to-vesicle transition for a straight-chain betaine surfactant when mixed with SDS,⁶⁷ so this behavior is not entirely unexpected. The critical packing parameter of AOT has been reported previously⁶⁸ as $P^* = 1.10$, indicating its strong preference for inverse-curvature phases. The effective critical packing parameter for the vesicle-forming mixture here is therefore calculated to be $P^* = 0.84$, correlating with the small vesicles produced.

Because AOT has two alkyl chains, both of which have ethyl branches, the volume of the hydrophobic region is significantly higher. This would result in the AOT and EAPB molecules finding a mutual packing condition, rendering them unable to achieve the surface curvature required for wormlike micelles. Therefore, the surfactant molecules aggregate into vesicles that have an increased packing parameter ($1/2 < P^* < 1$) and a higher surface curvature. The anionic charge of the AOT headgroups may also have a role to play, and the eventual calculated critical packing parameter for the mixed system of $P^* = 0.84$ may explain why the system forms vesicles instead of bilayers. In two-component vesicle systems, an asymmetric arrangement of the molecules is favored both energetically and entropically to lower the aggregation number.⁶⁹ Furthermore, the distribution of one surfactant occurring more so toward the outside of the vesicle is favored by having a larger headgroup size and area,⁶⁶ which for this system would be AOT. Therefore, the ratio of EAPB to AOT is essential in this process, and a specific ratio is vital for the formation of vesicle-type nanostructures. In this case, 2 wt % AOT to 1 wt % EAPB, which corresponds to a molar ratio of 2.16:1 AOT/EAPB, is the ideal ratio. At these remarkably small vesicle sizes, we expect the AOT molecules to geometrically favor locating at the interior membrane of the vesicles as a result of their bulky tailgroups that favor inverse curvature. This system of curiously small vesicles may be useful as a vector for the capture of water-soluble toxins or drug-delivery vessels, whereby the doping of a particular surfactant can serve as the release mechanism by causing a change in the aggregate structure. Dynamic light scattering of the sample corroborates the SANS investigation, finding a peak at a hydrodynamic diameter of 20 nm, in good agreement with the 16 nm shell diameter obtained from SANS (Supporting Information).

CONCLUSIONS

Aqueous solutions of zwitterionic surfactant erucyl amidopropyl betaine (EAPB) form wormlike micellar aggregates at weight percentages of as low as 0.05% (corresponding to a concentration of 1 mM). Small-angle neutron scattering (SANS) can be effectively employed to elucidate the internal nanostructure within the system. Accessing lower scattering vectors through the application of ultra-small-angle neutron scattering (USANS) proves to be vital to understanding larger-

scale phenomena such as the persistence lengths of the worms and the formation of fractal networks.

Through the combination of EAPB with carefully chosen additives designed to affect the self-assembly behavior in diverse ways, a vast array of structures are observed. Small amounts of oil (toluene) drastically reduce the viscosity of the EAPB solutions, which is accompanied by the formation of dislike structures. The addition of neutral salts appears to have a minimal effect on the local EAPB micelle structure regardless of ion valence or hydrophobicity, although at the larger length scales probed by USANS the salt-dependent formation of fractal wormlike micellar networks⁴⁰ is seen.

Much more significant structural changes can be achieved on mixing surfactant additives into EAPB solutions, resulting in complete structural evolution from worms to an array of other nanostructures depending on the surfactant loadings, due to synergistic effects that alter surfactant packing. Regardless of surfactant headgroup chemistry, from nonionic to anionic and cationic additives, it is seen that molecular geometry is more important in determining the eventual self-assembled structures of these mixed systems. A range of assembly geometries from small spheres to ellipses, rods, and even small, highly curved vesicles are found and can be contextualized by calculating the effective critical packing parameter of the system. These findings present new methods for controlling the internal nanostructure of wormlike micelles and provide fundamental insight into the self-assembly phenomena that result. The ability to finely tune self-assembly, particularly for these viscoelastic fluids, has important implications for their use in oil recovery, drilling lubricants, and machining fluids.

■ ASSOCIATED CONTENT

■ Supporting Information

The Supporting Information is available free of charge on the ACS Publications website at DOI: 10.1021/acs.langmuir.6b01735.

Details of models used to fit SANS data along with fitted parameter values (PDF)

■ AUTHOR INFORMATION

Corresponding Author

[REDACTED]

Present Address

(A.V.) Institute of Petroleum Engineering, Heriot-Watt University, Edinburgh EH14 4AS, UK.

Notes

The authors declare no competing financial interest.

■ ACKNOWLEDGMENTS

This research was supported by an Endeavour Postgraduate Research Fellowship (to A.V.) from the Department of Education of the Australian Government. We acknowledge the support of the Australian Centre for Neutron Scattering, Australian Nuclear Science and Technology Organisation, in providing the neutron research facilities used in this work. This work benefited from SasView software, originally developed by the DANSE project under NSF award DMR-0520547.

■ REFERENCES

- (1) Mason, T. G.; Weitz, D. A. Optical Measurements of Frequency-Dependent Linear Viscoelastic Moduli of Complex Fluids. *Phys. Rev. Lett.* **1995**, *74*, 1250–1253.
- (2) Yethiraj, A.; Striolo, A. Fracking: What Can Physical Chemistry Offer? *J. Phys. Chem. Lett.* **2013**, *4*, 687–690.
- (3) Dreiss, C. A. Wormlike micelles: where do we stand? Recent developments, linear rheology and scattering techniques. *Soft Matter* **2007**, *3*, 956–970.
- (4) Porter, R. S.; Johnson, J. F. The Entanglement Concept in Polymer Systems. *Chem. Rev.* **1966**, *66*, 1–27.
- (5) Candau, S.; Hirsch, E.; Zana, R.; Adam, M. Network properties of semidilute aqueous KBr solutions of cetyltrimethylammonium bromide. *J. Colloid Interface Sci.* **1988**, *122*, 430–440.
- (6) Imai, S.; Shikata, T. Viscoelastic Behavior of Surfactant Threadlike Micellar Solutions: Effect of Additives 3. *J. Colloid Interface Sci.* **2001**, *244*, 399–404.
- (7) Hassan, P. A.; Raghavan, S. R.; Kaler, E. W. Microstructural Changes in SDS Micelles Induced by Hydrotropic Salt. *Langmuir* **2002**, *18*, 2543–2548.
- (8) Walker, L. M. Rheology and structure of worm-like micelles. *Curr. Opin. Colloid Interface Sci.* **2001**, *6*, 451–456.
- (9) Yang, J. Viscoelastic wormlike micelles and their applications. *Curr. Opin. Colloid Interface Sci.* **2002**, *7*, 276–281.
- (10) Rogers, S. A.; Calabrese, M. A.; Wagner, N. J. Rheology of branched wormlike micelles. *Curr. Opin. Colloid Interface Sci.* **2014**, *19*, 530–535.
- (11) Fischer, P.; Rehage, H.; Grüning, B. Linear Flow Properties of Dimer Acid Betaine Solutions with and without Changed Ionic Strength. *J. Phys. Chem. B* **2002**, *106*, 11041–11046.
- (12) Kumar, R.; Kalur, G. C.; Ziserman, L.; Danino, D.; Raghavan, S. R. Wormlike Micelles of a C22-Tailed Zwitterionic Betaine Surfactant: From Viscoelastic Solutions to Elastic Gels. *Langmuir* **2007**, *23*, 12849–12856.
- (13) Kumar, R.; Raghavan, S. R. Photogelling fluids based on light-activated growth of zwitterionic wormlike micelles. *Soft Matter* **2009**, *5*, 797–803.
- (14) Feng, D.; Zhang, Y.; Chen, Q.; Wang, J.; Li, B.; Feng, Y. Synthesis and Surface Activities of Amidobetaine Surfactants with Ultra-long Unsaturated Hydrophobic Chains. *J. Surfactants Deterg.* **2012**, *15*, 657–661.
- (15) Chu, Z.; Dreiss, C. A.; Feng, Y. Smart wormlike micelles. *Chem. Soc. Rev.* **2013**, *42*, 7174–7203.
- (16) Kalur, G. C.; Frounfelder, B. D.; Cipriano, B. H.; Norman, A. I.; Raghavan, S. R. Viscosity Increase with Temperature in Cationic Surfactant Solutions Due to the Growth of Wormlike Micelles. *Langmuir* **2005**, *21*, 10998–11004.
- (17) Davies, T. S.; Ketner, A. M.; Raghavan, S. R. Self-Assembly of Surfactant Vesicles that Transform into Viscoelastic Wormlike Micelles upon Heating. *J. Am. Chem. Soc.* **2006**, *128*, 6669–6675.
- (18) Zhang, Y.; Feng, Y.; Wang, Y.; Li, X. CO₂-Switchable Viscoelastic Fluids Based on a Pseudogemini Surfactant. *Langmuir* **2013**, *29*, 4187–4192.
- (19) Zhang, Y.; Chu, Z.; Dreiss, C. A.; Wang, Y.; Fei, C.; Feng, Y. Smart wormlike micelles switched by CO₂ and air. *Soft Matter* **2013**, *9*, 6217–6221.
- (20) Zhang, Y.; Feng, Y.; Wang, J.; He, S.; Guo, Z.; Chu, Z.; Dreiss, C. A. CO₂-switchable wormlike micelles. *Chem. Commun.* **2013**, *49*, 4902–4904.
- (21) Ketner, A. M.; Kumar, R.; Davies, T. S.; Elder, P. W.; Raghavan, S. R. A Simple Class of Photorheological Fluids: Surfactant Solutions with Viscosity Tunable by Light. *J. Am. Chem. Soc.* **2007**, *129*, 1553–1559.
- (22) Shi, H.; Wang, Y.; Fang, B.; Talmon, Y.; Ge, W.; Raghavan, S. R.; Zakin, J. L. Light-Responsive Threadlike Micelles as Drag Reducing Fluids with Enhanced Heat-Transfer Capabilities. *Langmuir* **2011**, *27*, 5806–5813.

- (23) Lu, Y.; Zhou, T.; Fan, Q.; Dong, J.; Li, X. Light-responsive viscoelastic fluids based on anionic wormlike micelles. *J. Colloid Interface Sci.* **2013**, *412*, 107–111.
- (24) Lin, Y.; Han, X.; Huang, J.; Fu, H.; Yu, C. A facile route to design pH-responsive viscoelastic wormlike micelles: Smart use of hydrotropes. *J. Colloid Interface Sci.* **2009**, *330*, 449–455.
- (25) Chu, Z.; Feng, Y. pH-switchable wormlike micelles. *Chem. Commun.* **2010**, *46*, 9028–9030.
- (26) Helgeson, M. E.; Hodgdon, T. K.; Kaler, E. W.; Wagner, N. J.; Vethamuthu, M.; Ananthapadmanabhan, K. P. Formation and Rheology of Viscoelastic 'Double Networks' in Wormlike Micelle-Nanoparticle Mixtures. *Langmuir* **2010**, *26*, 8049–8060.
- (27) Nettesheim, F.; Liberatore, M. W.; Hodgdon, T. K.; Wagner, N. J.; Kaler, E. W.; Vethamuthu, M. Influence of Nanoparticle Addition on the Properties of Wormlike Micellar Solutions. *Langmuir* **2008**, *24*, 7718–7726.
- (28) Mason, T. G.; Ganesan, K.; van Zanten, J. H.; Wirtz, D.; Kuo, S. C. Particle Tracking Microrheology of Complex Fluids. *Phys. Rev. Lett.* **1997**, *79*, 3282–3285.
- (29) Gisler, T.; Weitz, D. A. Tracer microrheology in complex fluids. *Curr. Opin. Colloid Interface Sci.* **1998**, *3*, 586–592.
- (30) Shibaev, A. V.; Tamm, M. V.; Molchanov, V. S.; Rogachev, A. V.; Kuklin, A. I.; Dormidontova, E. E.; Philippova, O. E. How a Viscoelastic Solution of Wormlike Micelles Transforms into a Microemulsion upon Absorption of Hydrocarbon: New Insight. *Langmuir* **2014**, *30*, 3705–3714.
- (31) Gaynanova, G. A.; Valiakhmetova, A. R.; Kuryashov, D. A.; Kudryashova, Y. R.; Lukashenko, S. S.; Syakaev, V. V.; Latypov, S. K.; Bukharov, S. V.; Bashkirtseva, N. Y.; Zakharova, L. Y. The self-organization and functional activity of binary system based on erucyl amidopropyl betaine - alkylated polyethyleneimine. *Chem. Phys. Lett.* **2013**, *588*, 145–149.
- (32) Gilbert, E. P.; Schulz, J. C.; Noakes, T. J. 'Quokka'-The small-angle neutron scattering instrument at OPAL. *Phys. B* **2006**, *385*, 386–1180–1182.
- (33) Rehm, C.; Brülé, A.; Freund, A. K.; Kennedy, S. J. Kookaburra: the ultra-small-angle neutron scattering instrument at OPAL. *J. Appl. Crystallogr.* **2013**, *46*, 1699–1704.
- (34) Kline, S. R. Reduction and analysis of SANS and USANS data using IGOR Pro. *J. Appl. Crystallogr.* **2006**, *39*, 895–900.
- (35) Tanford, C. Micelle shape and size. *J. Phys. Chem.* **1972**, *76*, 3020–3024.
- (36) Pedersen, J. S.; Schurtenberger, P. Scattering Functions of Semiflexible Polymers with and without Excluded Volume Effects. *Macromolecules* **1996**, *29*, 7602–7612.
- (37) Chen, W.-R.; Butler, P. D.; Magid, L. J. Incorporating Intermicellar Interactions in the Fitting of SANS Data from Cationic Wormlike Micelles. *Langmuir* **2006**, *22*, 6539–6548.
- (38) Schubert, B. A.; Kaler, E. W.; Wagner, N. J. The Microstructure and Rheology of Mixed Cationic/Anionic Wormlike Micelles. *Langmuir* **2003**, *19*, 4079–4089.
- (39) Oelschlaeger, C.; Suwita, P.; Willenbacher, N. Effect of Counterion Binding Efficiency on Structure and Dynamics of Wormlike Micelles. *Langmuir* **2010**, *26*, 7045–7053.
- (40) Cardiel, J. J.; Zhao, Y.; De La Iglesia, P.; Pozzo, L. D.; Shen, A. Q. Turning up the heat on wormlike micelles with a hydrotropic salt in microfluidics. *Soft Matter* **2014**, *10*, 9300–9312.
- (41) Berghausen, J.; Zipfel, J.; Lindner, P.; Richtering, W. Influence of water-soluble polymers on the shear-induced structure formation in lyotropic lamellar phases. *J. Phys. Chem. B* **2001**, *105*, 11081–11088.
- (42) Barnes, H. A. Rheology of emulsions - a review. *Colloids Surf., A* **1994**, *91*, 89–95.
- (43) Zemb, T.; Dubois, M.; Demé, B.; Gulik-Krzywicki, T. Self-Assembly of Flat Nanodiscs in Salt-Free Catanionic Surfactant Solutions. *Science* **1999**, *283*, 816–819.
- (44) Chomczynski, P.; Sacchi, N. The single-step method of RNA isolation by acid guanidinium thiocyanate-phenol-chloroform extraction: twenty-something years on. *Nat. Protoc.* **2006**, *1*, 581–585.
- (45) Nallet, F.; Laversanne, R.; Roux, D. Modelling X-ray or neutron scattering spectra of lyotropic lamellar phases: interplay between form and structure factors. *J. Phys. II* **1993**, *3*, 487–502.
- (46) Singh, M.; Ford, C.; Agarwal, V.; Fritz, G.; Bose, A.; John, V. T.; McPherson, G. L. Structural Evolution in Cationic Micelles upon Incorporation of a Polar Organic Dopant. *Langmuir* **2004**, *20*, 9931–9937.
- (47) Kunitake, T.; Okahata, Y. A totally synthetic bilayer membrane. *J. Am. Chem. Soc.* **1977**, *99*, 3860–3861.
- (48) Kunitake, T. Synthetic Bilayer Membranes: Molecular Design, Self-Organization, and Application. *Angew. Chem., Int. Ed. Engl.* **1992**, *31*, 709–726.
- (49) Szymczyk, K.; Jańczuk, B. The adsorption at solution-air interface and volumetric properties of mixtures of cationic and nonionic surfactants. *Colloids Surf., A* **2007**, *293*, 39–50.
- (50) Magid, L. J.; Li, Z.; Butler, P. D. Flexibility of Elongated Sodium Dodecyl Sulfate Micelles in Aqueous Sodium Chloride: A Small-Angle Neutron Scattering Study. *Langmuir* **2000**, *16*, 10028–10036.
- (51) Arleth, L.; Bergström, M.; Pedersen, J. S. Small-Angle Neutron Scattering Study of the Growth Behavior, Flexibility, and Intermicellar Interactions of Wormlike SDS Micelles in NaBr Aqueous Solutions. *Langmuir* **2002**, *18*, 5343–5353.
- (52) Zemb, T.; Lindner, P. *Neutrons, X-rays, and Light: Scattering Methods Applied to Soft Condensed Matter*; North-Holland, 2002.
- (53) Chu, Z.; Feng, Y.; Su, X.; Han, Y. Wormlike micelles and solution properties of a C22-tailed amidosulfobetaine surfactant. *Langmuir* **2010**, *26*, 7783–7791.
- (54) Pottage, M. J.; Greaves, T. L.; Garvey, C. J.; Tabor, R. F. The effects of alkylammonium counterions on the aggregation of fluorinated surfactants and surfactant ionic liquids. *J. Colloid Interface Sci.* **2016**, *475*, 72.
- (55) Israelachvili, J. N.; Mitchell, D. J.; Ninham, B. W. Theory of self-assembly of hydrocarbon amphiphiles into micelles and bilayers. *J. Chem. Soc., Faraday Trans. 2* **1976**, *72*, 1525–1568.
- (56) Motomura, K.; Yamanaka, M.; Aratono, M. Thermodynamic consideration of the mixed micelle of surfactants. *Colloid Polym. Sci.* **1984**, *262*, 948–955.10.1007/BF01490027
- (57) Bergström, M.; Pedersen, J. S. Formation of Tablet-Shaped and Ribbonlike Micelles in Mixtures of an Anionic and a Cationic Surfactant. *Langmuir* **1999**, *15*, 2250–2253.
- (58) Shiloach, A.; Blankschtein, D. Measurement and Prediction of Ionic/Nonionic Mixed Micelle Formation and Growth. *Langmuir* **1998**, *14*, 7166–7182.
- (59) Nagarajan, R. Molecular packing parameter and surfactant self-assembly: the neglected role of the surfactant tail. *Langmuir* **2002**, *18*, 31–38.
- (60) Muzzalupo, R.; Gente, G.; La Mesa, C.; Caponetti, E.; Chillura-Martino, D.; Pedone, L.; Saladino, M. L. Micelles in Mixtures of Sodium Dodecyl Sulfate and a Bolaform Surfactant. *Langmuir* **2006**, *22*, 6001–6009.
- (61) Tabor, R. F.; Lockie, H.; Chan, D. Y.; Grieser, F.; Grillo, I.; Mutch, K. J.; Dagastine, R. R. Structural forces in soft matter systems: unique flocculation pathways between deformable droplets. *Soft Matter* **2011**, *7*, 11334–11344.
- (62) Eastoe, J.; Sanchez-Dominguez, M.; Cumber, H.; Burnett, G.; Wyatt, P. Photoresponsive Microemulsions. *Langmuir* **2003**, *19*, 6579–6581.
- (63) Nave, S.; Eastoe, J.; Penfold, J. What is so special about Aerosol-OT? 1. Aqueous systems. *Langmuir* **2000**, *16*, 8733–8740.
- (64) Nave, S.; Eastoe, J.; Heenan, R. K.; Steytler, D.; Grillo, I. What is so special about aerosol-OT? 2. Microemulsion systems. *Langmuir* **2000**, *16*, 8741–8748.
- (65) Kaler, E. W.; Murthy, A. K.; Rodriguez, B. E.; Zasadzinski, J. A. N. Spontaneous Vesicle Formation in Aqueous Mixtures of Single-Tailed Surfactants. *Science* **1989**, *245*, 1371–1374.
- (66) Safran, S. A.; Pincus, P.; Andelman, D. Theory of Spontaneous Vesicle Formation in Surfactant Mixtures. *Science* **1990**, *248*, 354–356.

(67) Fan, H.; Zhao, S.; Li, B.; Fan, H.; Kang, W.; Huang, J. Formation and phase transition of hydrogel in a zwitterionic/anionic surfactant system. *RSC Adv.* **2015**, *5*, 27623–27629.

(68) Simmons, B. A.; Irvin, G. C.; Agarwal, V.; Bose, A.; John, V. T.; McPherson, G. L.; Balsara, N. P. Small angle neutron scattering study of microstructural transitions in a surfactant-based gel mesophase. *Langmuir* **2002**, *18*, 624–632.

(69) Israelachvili, J. N.; Mitchell, D. J.; Ninham, B. W. Theory of self-assembly of lipid bilayers and vesicles. *Biochim. Biophys. Acta, Biomembr.* **1977**, *470*, 185–201.

This document contains the specific details regarding the fitting parameters used in modelling the SANS/USANS data presented in the main paper.

Table S1: Fitted parameters and sample compositions for SANS/USANS investigation of EAPB with surfactant and salt additives. The fitted parameters are the persistence (Kuhn) length l_p , the worm radius R_{worm} , sphere radius R_{sphere} , rod radius R_{rod} , rod length l_{rod} , vesicle radius $R_{vesicle}$, the axial and equatorial radii of ellipsoids $R_{A,ellips.}$ and $R_{B,ellips.}$ respectively and the lamellae/vesicle thickness. Samples marked with an asterisk include USANS data in the main paper. Typical fitted uncertainties are $l_p \pm 4$ nm, $R_{worm} \pm 1$ nm, $R_{sphere} \pm 3$ nm, $R_{A,ellips.} \pm 0.5$ nm and $R_{B,ellips.} \pm 5$ nm. Also included are the calculated values for the radius of gyration for wormlike and rodlike micelles, R_g .

Sample additive	EAPB wt%	Additive wt%	Sample appearance	Model ^a	l_p nm	l_{rod} nm	R_{worm} nm	R_g nm	R_{rod} nm	R_{sphere} nm	$R_{A,ellips.}$ nm	$R_{B,ellips.}$ nm	$R_{vesicle}$ nm	Thickness nm
-	0.05		Clear	W			2.9	2.1						
-	0.25		Clear	W			2.9	2.1						
-	0.50		Clear	W			2.9	2.1						
-	1.00		Clear	W			2.9	2.1						
-*	2.00		Clear	W	150		2.7	1.9						
Toluene	1.00	0.1	Clear	W+E	40		2.3	1.6			2.7	107		
Toluene	1.00	0.3	Clear	E							4.0	65		
Toluene	1.00	0.5	Cloudy	W+E	40		2.6	1.8			4.6	96		
Toluene	1.00	1.0	Cloudy	E							4.8	65		
-*	1.00	-	Clear	W	400		2.8	2.0						
CaCl ₂ *	1.00	1.0	Clear	W	150		2.8	2.0						
NaCl*	1.00	0.2	Clear	W	34.6		2.8	2.0						
SDS	1.00	0.2	Cloudy	W	8.2		2.7	1.9						
SDS	1.00	1.0	Clear	E							2.3	4.3		
AOT	1.00	0.1	Cloudy											
AOT	1.00	0.2	Cloudy											
AOT	1.00	1.0	Cloudy											
AOT	1.00	2.0	Clear	V									8.1	2.3
CTAB*	1.00	0.2	Clear	R		33.6		1.9	2.7					
CTAB*	1.00	1.0	Clear	S						2.3				
Triton*	1.00	0.2	Clear	W	85.5		2.9	2.1						
Triton	1.00	1.0	Clear	R		10		1.7	2.4					
Phenol	1.00	0.1	Cloudy											
Phenol*	1.00	1.0	Cloudy	L										3.4
Phenol	1.00	2.0	Cloudy	L										3.2
CH ₃ COONa*	1.00	0.2	Clear	W	55.6		2.8	2.0						
TBAB*	1.00	1.0	Clear	W	60		2.7	1.9						
TBAB*	1.00	2.0	Clear	W	100		2.7	1.9						

^a W = ‘worm’ model, S = sphere, E = ellipsoid, V = vesicle, R = rod, L = lamellar.

Details in relation to the spherical and vesicle models can be found in Guinier and Fournet (1955).¹ The equation for the scattering intensity, $I(q)$, as a function of the scattering vector, q , of spheres is as follows:

$$I(q) = \frac{scale}{V} \left[\frac{3V(\Delta\rho)(\sin(qr) - qr \cos(qr))}{(qr)^3} \right]^2 + bkg$$

Where V is the volume of the scatterer, r is the radius of the sphere in Å, $scale$ is the volume fraction, $\Delta\rho$ is the contrast (difference in scattering length density between the solvent and scatterer) and bkg is the background (cm^{-1}). Similarly, the model providing the form factor, $P(q)$, for a unilamellar vesicle is similarly represented by the following:

$$P(q) = \frac{scale}{V_{shell}} \left[\frac{3V_1(\rho_1 - \rho_2)J_1(qR_1)}{(qR)_1} + \frac{3V_2(\rho_2 - \rho_{solv})J_1(qR_2)}{(qR)_2} \right]^2 + bkg$$

Where V_{shell} is the volume of the shell, V_1 is the volume of the core and V_2 is the total volume. R_1 is the radius of the core and R_1 is the radius from the core to the shell in Å. $J_1 = (\sin x - x \cos x)/x^2$. The ellipsoid model or rods/cylinder model was from Feigin and Svergun (1987):²

$$P(q, \alpha) = \frac{scale}{V} f^2(q) + bkg$$

where

$$f(q) = \frac{3(\Delta\rho)V \sin[qr(R_a, R_b, \alpha)] - qr \cos[qr(R_a, R_b, \alpha)]}{[qr(R_a, R_b, \alpha)]^3}$$

and

$$r(R_a, R_b, \alpha) = [R_b^2 \sin^2 \alpha + R_a^2 \cos^2 \alpha]^{1/2}$$

The two radii, R_a and R_b , represent the radius along the rotational and longitudinal axes of the ellipsoid respectively and are perpendicular to each other. α is the angle between the

ellipsoidal axis and the scattering vector q .

The ‘worm’ model is detailed in Pederson *et al*,³ with the following general equation:

$$I_{WC}(q, L, b, R_{CS}) = c\Delta\rho_m^2 MS_{WC}(q, L, b)P_{CS}(q, R_{CS})$$

Where c is the surfactant concentration, M is the molecular weight of the micelles and $S_{WC}(q, L, b)$ represents the scattering function of a semi-flexible chain without volume effects in which L/b is the number of statistical segments in the chain :

$$S_{WC}(q, L, b) = [(1 - \chi(q, L, b))S_{chain}(q, L, b) + \chi(q, L, b)S_{rod}(q, L)] \Gamma(q, L, b)$$

Chen *et al*⁴ included corrections to the formula by accounting for intermicellar interactions by including the parameter in the following equation, which is currently used in modelling flexible cylinders in SasView:

$$f_{corr}(q) w(qR_G)[1.22(qR_G)^{-1/0.585} + 0.4288(qR_G)^{-2/0.585} - 1.651(qR_G)^{-3/0.585}]$$

A final parameter, the gyration radius R_g , was determined for the wormlike materials based on their cross-sectional radii, r_{xs} , using the following formula:⁵

$$R_g = \frac{r_{xs}}{\sqrt{2}}$$

Lastly, the lamellar model was from Berghausen *et al*⁶ for which the scattering intensity is given by:

$$I(q) = 2\pi \frac{P(q)}{\delta q^2}$$

where the form factor is given by:

$$P(q) = \frac{2\Delta\rho^2}{q^2}(1 - \cos(q\delta))$$

In both equations, δ is the bilayer thickness in Å. For all modelling, the scattering length density (\AA^{-2}) of the scatterer and solvent are taken into account and are represented in the equations as ρ , with the difference or ‘contrast’ being $\Delta\rho$.

As a follow up to the SANS results depicting the presence of vesicles in the 1% EAPB to 2% AOT system, dynamic light scattering (DLS) was performed on a similarly prepared sample in H_2O . The solvent was filtered before mixing to remove traces of dust and the sample analysed using a Brookhaven NanoBrook Omni. Measurements were conducted at 25°C , with scattering intensity from a 640 nm laser measured at the 90° detector position. Particle sizing was then performed on the resultant correlation functions using a ‘thin shells’ model.

The mean effective diameter determined for the vesicles by DLS was approximately 42.45 nm (Fig. S1a), a significantly larger radius than that determined by SANS (16 nm). Analysis of the multi-modal size distribution revealed that in the sample two independent particle sizes exist, one at approximately 20 nm and the other at around 200 nm (Fig. S1b). The presence of the larger size particles explains why the average diameter was much higher than expected based on the SANS results. However, the high intensity peak at 20 nm in the multi-modal data strongly supports the results obtained from SANS. Scattering intensity is known to increase exponentially with particle size, so the fact that the smaller particles have a higher intensity suggests that this is by far the most prevalent species. Analysing the size distribution according to number instead of intensity confirmed this point, as the larger group was seen to disappear entirely in this instance (Fig. S1c). The slightly greater diameter calculated by DLS is most likely due to incorporation of the electrical double-layer thickness. The nature of the larger particles is unknown, as particles of this size are beyond

the regime accessible to SANS (2-100 nm) and USANS was unfortunately not performed on this mixture. However, they are likely to be a small proportion of larger vesicles that may be removed by optimising the system to a more precise EAPB to AOT ratio.

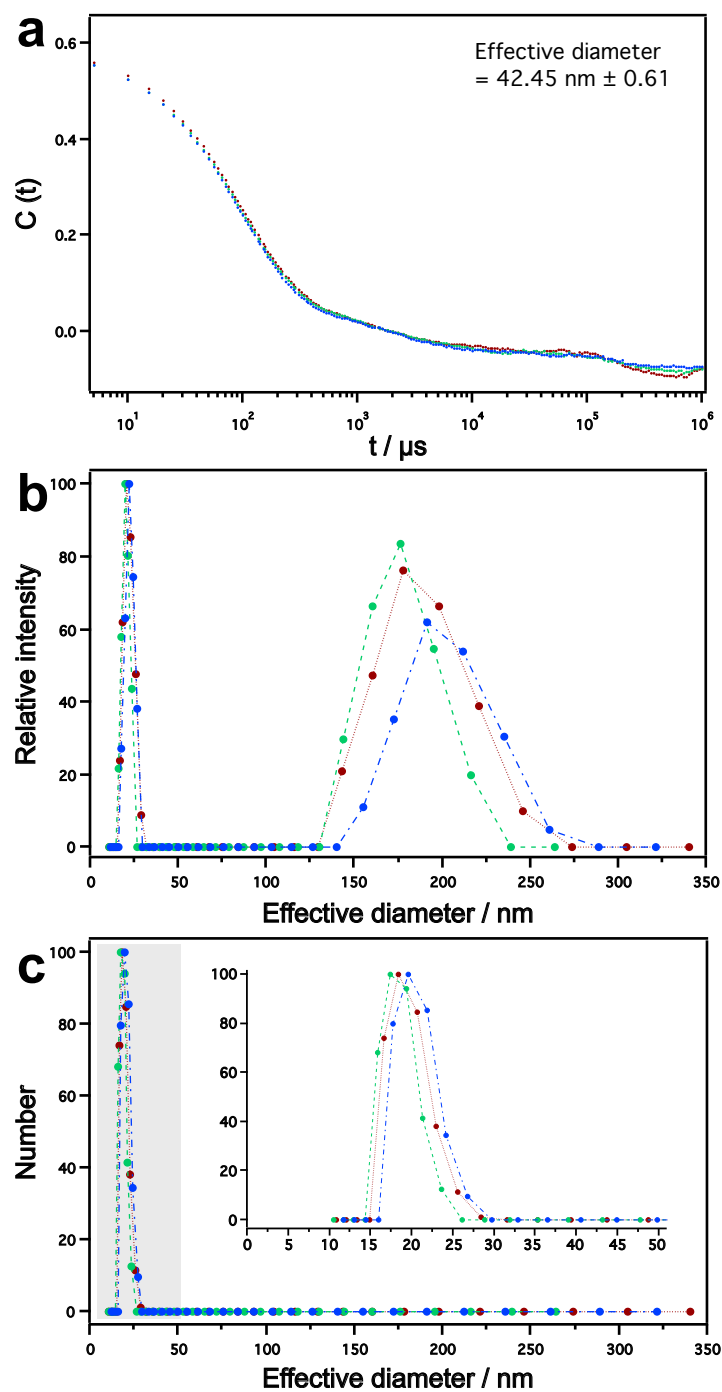


Figure S1: (a) Autocorrelation functions for an aqueous sample of 1 wt% EAPB and 2 wt% AOT. The mean effective diameter for the 3 runs is shown in the corner. (b) Multi-modal size distribution data based on intensity determined from the correlation functions in (a). (c) Multi-modal size distribution data determined by number. The inset is an enlargement of the grey-shaded area.

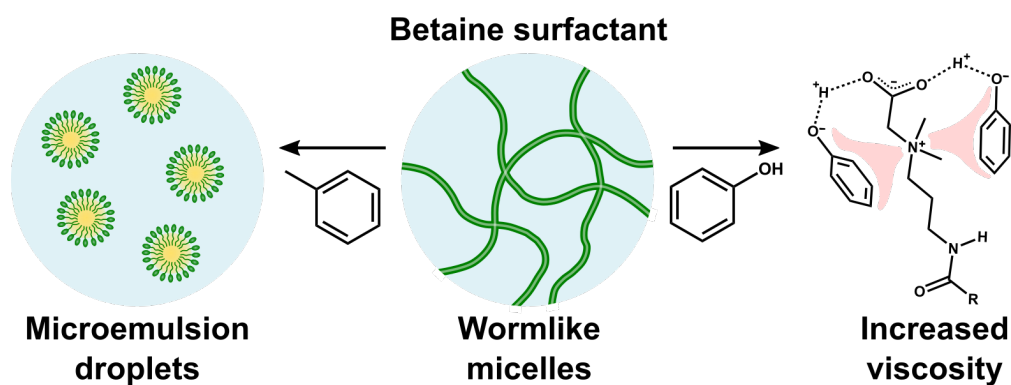
References

- (1) Guinier, A.; Fournet, G. *Small-Angle Scattering of X-Rays*; John Wiley & Sons, 1955.
- (2) Feigin, L. A.; Svergun, D. I. *Structure Analysis by Small-Angle X-Ray and Neutron Scattering*; Plenum, 1987.
- (3) Pedersen, J. S.; Schurtenberger, P. Scattering Functions of Semiflexible Polymers with and without Excluded Volume Effects. *Macromolecules* **1996**, *29*, 7602–7612.
- (4) Chen, W.-R.; Butler, P. D.; Magid, L. J. Incorporating Intermicellar Interactions in the Fitting of SANS Data from Cationic Wormlike Micelles. *Langmuir* **2006**, *22*, 6539–6548.
- (5) Flood, C.; Dreiss, C. A.; Croce, V.; Cosgrove, T.; Karlsson, G. Wormlike Micelles Mediated by Polyelectrolyte. *Langmuir* **2005**, *21*, 7646–7652.
- (6) Berghausen, J.; Zipfel, J.; Lindner, P.; Richtering, W. Influence of water-soluble polymers on the shear-induced structure formation in lyotropic lamellar phases. *J. Phys. Chem. B* **2001**, *105*, 11081–11088.

Appendix B

The effects of small molecule organic additives on the self-assembly and rheology of betaine wormlike micellar fluids

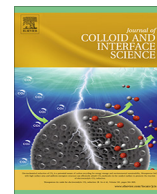
Published: Thomas M. McCoy, Joshua P. King, Jackson E. Moore, Veena T. Kelleppan, Anna V. Sokolova, Liliana de Campo, Madhura Manohar, Tamim A. Darwish and Rico F. Tabor, The effects of small molecule organic additives on the self-assembly and rheology of betaine wormlike micellar fluids. *J. Colloid Interface Sci.*, 2019, **534**, 518-532.





Contents lists available at ScienceDirect

Journal of Colloid and Interface Science

journal homepage: www.elsevier.com/locate/jcis

Regular Article

The effects of small molecule organic additives on the self-assembly and rheology of betaine wormlike micellar fluids



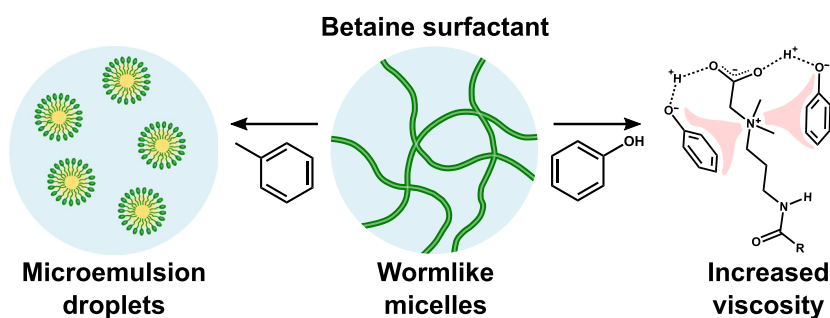
Thomas M. McCoy^a, Joshua P. King^a, Jackson E. Moore^a, Veena T. Kelleppan^{a,1}, Anna V. Sokolova^b, Liliana de Campo^b, Madhura Manohar^c, Tamim A. Darwish^c, Rico F. Tabor^{a,*}

^a School of Chemistry, Monash University, Clayton 3800, Australia

^b Australian Centre for Neutron Scattering, ANSTO, Lucas Heights, New South Wales 2234, Australia

^c National Deuteration Facility, ANSTO, Lucas Heights, New South Wales 2234, Australia

GRAPHICAL ABSTRACT



ARTICLE INFO

Article history:

Received 20 June 2018

Revised 12 September 2018

Accepted 13 September 2018

Available online 14 September 2018

Keywords:

Oleyl amidopropyl betaine

Organic additives

Self-assembly

Wormlike micelles

Microemulsions

Viscosity

Polarity

Aromaticity

ABSTRACT

A model zwitterionic surfactant, oleyl amidopropyl betaine (OAPB), that spontaneously forms viscoelastic wormlike micelles in aqueous solution is mixed with a variety of structurally diverse organic additives. By systematically varying the nature of these additives, insight into the effects of their aromaticity and polarity on the bulk assembly and fluid behaviour of these micelles is gained by the complementary use of small-angle neutron scattering and viscosity measurements. Inclusion of non-polar additives causes the wormlike aggregates to transition into microemulsions above a critical additive concentration; the precise partitioning within the micelle is determined using contrast variation. Alternatively, polar additives do not appear to cause evolution from the wormlike structure, but instead influence the fluid rheology, with some serving to significantly increase viscosity above that of the pure surfactant solution. Addition of these molecules is accompanied by an increase in fluid viscosity when the oxygenated group of the additive is resonance stabilised or acidic. This effect is thought to be a result of surfactant–additive synergism, in which charge screening of the surfactant head-groups causes stronger attractions between molecules, increasing the scission energy of the micelles (*i.e.* reducing their ability to break apart and reform). Further doping of acidic additives past a critical concentration causes phase separation of the wormlike mixtures. According to ultra-small-angle neutron scattering measurements, the incorporation of all additives (polar or non-polar, aromatic or non-aromatic) results in the formation of ‘branched’ wormlike networks. These findings emphasise the significant impact of impurities or additives on the

* Corresponding author.

E-mail address: rico.tabor@monash.edu (R.F. Tabor).

¹ Current address: Axio Pty Ltd, Level 3, 35 Cotham Road, Kew, VIC 3101, Australia.

properties of aqueous wormlike micellar systems formed by zwitterionic surfactants, and could also inform selection of solutes for controlling fluid rheology.

Crown Copyright © 2018 Published by Elsevier Inc. All rights reserved.

1. Introduction

Wormlike micelles (WLMs) are an important form of surfactant self-assembly, as the elongated architecture of these aggregates results in interesting and useful bulk rheological properties [1–3]. Above a critical entanglement or overlap concentration, C^* , solutions of WLMs exhibit huge increases in viscosity, with the resultant fluids having the ability to both store (elastically) and dissipate (viscously) energy in response to shear strain [4–6]. Therefore, WLMs represent an important class of viscoelastic complex fluids, and as such, have been applied as fracturing fluids for oil recovery [7,8], drag-reducing agents [9–11] and thickeners for household products [12,13].

Wormlike aggregation occurs due to the large energy difference between the end-caps and cylindrical body of the micelles [14]. Because the end-caps have a much higher spontaneous curvature than the ‘body’ of the micelles, there is a significantly greater energy penalty associated with their formation [15]. Hence, the surfactants favour unidirectional elongation of the micelle, which ultimately serves to reduce the number of end-caps required. The resultant structure is a long, flexible cylinder or ‘worm’. This effect is controlled by the molecular geometry of the surfactants, and a prediction of the assembly morphology can be made using the surfactant packing parameter, P^* :

$$P^* = \frac{V}{A_0 l_c}$$

where V is the volume of the surfactant tail-group, A_0 is the effective area of the surfactant head-group and l_c is the length of the tail-group [16]. WLMs are expected to form for values within the range of $\frac{1}{3} \leq P^* < \frac{1}{2}$ [17]. The packing parameter, however, is limited in its effectiveness to predict the self-assembly of many surfactant systems due to its inability to account explicitly for intermolecular interactions and thermodynamics, both of which are focal points of this study.

Due to their enormous length and flexibility, and the physical properties that stem from these characteristics, WLMs are considered akin to polymer solutions. However, being noncovalent aggregates, a clear advantage of WLMs over polymers arises from the fact that they can break apart and reform [18,19]. This dynamic behaviour means that in the context of drag reduction or hydraulic fracturing, unlike polymers, WLMs will constantly reassemble following deformation or disaggregation caused by flow or shear strain [20]. Surfactants in these applications therefore have the potential to be recyclable because the microstructure can be spontaneously reformed. In addition, the self-assembling nature of surfactant molecules provides an avenue for altering fluid properties in response to simple additives [21]. For instance, in fracturing fluids for oil recovery, the low interfacial tension of wormlike micellar solutions facilitates flow and penetration of the mixture through the porous media, while the high viscosity enables suspension of large microparticles such as sand proppant [22–24]. However, when the surfactants encounter the oil hydrocarbons they convert into microemulsions, not only encapsulating the oil, but significantly lowering the viscosity, allowing highly efficient fluid withdrawal compared to polymeric fracturing fluids [7,25].

Lastly, an interesting and emerging class of WLMs are zwitterionic betaine surfactant molecules. Because betaines possess a positive (ammonium) and negative (carboxylate) charge in their head-

groups, they are able to form WLMs as single components through self-screening effects [26,27]. Conversely, ionic surfactants often require added electrolytes or high surfactant concentrations to enable sufficient proximity of the like-charged head-groups for packing into WLMs [28–32]. In addition, betaine surfactants have the advantage of low toxicity [33], adding appeal for their use in the aforementioned applications, particularly household products and cosmetics, in which cocamidopropyl betaine is already widely used [34,35].

Previously we have shown that erucyl amidopropyl betaine undergoes structural transitions from WLMs to a broad variety of molecular aggregates upon addition of oil, salts and surfactants [36]. Herein, we characterise and assess samples of oleyl amidopropyl betaine (OAPB) – a significant component of cocamidopropyl betaine [35] – with simple organic additives using complementary SANS and viscosity measurements. By correlating these techniques, insight into the factors that affect self-assembly and structure–function relationships in these systems is gained. The organic additives are adjusted systematically to specifically investigate the effects of aromaticity and polarity on the structure and physical chemistry of OAPB WLMs. Non-polar additives effect transitions of the WLMs into microemulsion droplets, whereas polar additives do not alter the wormlike self-assembly, however do cause marked changes in fluid rheology. The additives and OAPB surfactant are shown in Fig. 1 and their key physicochemical properties are presented in Tables S1 and S2 of the Supplementary material.

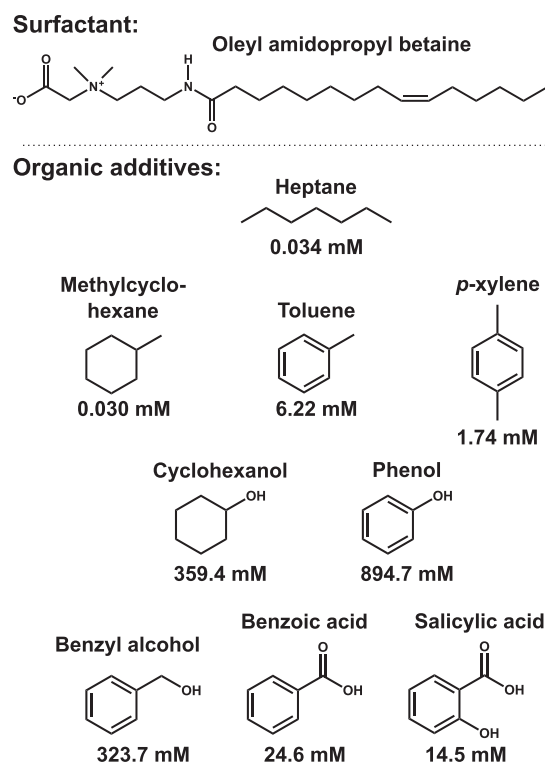


Fig. 1. Summary of the OAPB surfactant and small molecule organic additives used in this study. The respective aqueous solubilities (20–25 °C) of each additive are shown below their structures.

2. Experimental

2.1. Materials

Oleyl amidopropyl betaine (OAPB) was synthesised and purified as described previously [37]. Deuterated OAPB (OAPB-D33) was synthesised at the National Deuteration Facility, Australian Nuclear Science and Technology Organisation (ANSTO), following a modification of the procedure by Feng et al. [38]. D33-oleic acid was first synthesised according to Darwish et al. [39], after which 1 g (3.17 mmol) was added to a 25 mL round bottom flask with molecular sieves. Excess dimethylpropane diamine (10 eq.) was then added, followed by sodium fluoride catalyst (20 mg). The reaction was heated to reflux for 16 h at 160 °C under an inert atmosphere. The mixture was then cooled, and the molecular sieves were removed by suction filtration and washed with methanol (30 mL, $\times 2$). The filtrate was reduced under pressure to remove solvent and unreacted amine. The crude viscous compound (slightly yellow) was then loaded to a silica gel column and eluted with a gradient of *n*-hexane:ethyl acetate (1:1) to ethyl acetate:methanol (1:1). A clear waxy compound was obtained (300 mg, 24%), confirmed to be the oleic amide (see [Supplementary Material](#)).

The oleic amide (300 mg, 0.75 mmol) was dissolved in 25 mL of ethanol, and sodium chloroacetate (1.2 eq.) was added to the solution, followed by 5 mL deionised water. The mixture was heated at reflux for 16 h to yield the final OAPB product. The solvent was then removed and the product was purified and desalted using flash column chromatography (eluent: gradient ethyl acetate:hexane 1:1). The pure product was obtained as a clear waxy compound (200 mg, 58%). Characterisation by NMR and mass spectrometry are available in the [Supplementary Material](#).

All organic additives were ACS reagent grade ($\geq 99\%$) and used as received. Heptane, methylcyclohexane, *p*-xylene, benzyl alcohol and benzoic acid were from Sigma. Toluene and phenol were from Merck. Cyclohexanol was from UNILAB and salicylic acid was from BDH Chemicals. Deuterium oxide (D_2O , 99.8 atom % D) and *p*-xylene- D_{10} (99.0 atom % D) were from Sigma.

2.2. Methods

Small-angle neutron scattering (SANS) measurements were conducted on the Bilby beamline [40] at the Australian Centre for Neutron Scattering, ANSTO. Samples were dissolved in D_2O , with measurements performed at 25 °C in 2 mm path-length, quartz Hellma cells. The raw scattering counts from the detectors were radially isotropic, and normalising against a blocked beam and transmission measurement, were reduced to average absolute intensity profiles as a function of the momentum transfer or scattering vector, q , defined as

$$q = \frac{4\pi}{\lambda} \sin \frac{\theta}{2}$$

where θ is the scattering angle and λ is the wavelength of the incident neutrons (2–18 Å). The main detector was positioned 18 m from the samples while the four curtain detectors were 4 m (left and right detectors) and 5 m (top and bottom detectors), providing a q -range of approximately 0.0015–0.33 Å^{−1}. Absolute intensities were scaled according to the sample thicknesses (2 mm) and using an empty beam measurement. Lastly, the scattering from an empty cell was subtracted from all data sets prior to modelling.

Ultra-small-angle neutron scattering (USANS) measurements were made using the Kookaburra beamline [41,42] at the Australian Centre for Neutron Scattering, ANSTO. The instrument features a Bonse-Hart setup in which two parallel arrays (one rotational) of quintuple-reflection channel-cut silicon crystals monochromate and analyse the beam [43]. A neutron wavelength

of 4.74 Å was used in these measurements, obtaining a maximum q -range of 0.00005–0.005 Å^{−1} (0.1–10 μm length scales). Due to the limited scattering counts for these samples, all USANS measurements are presented as absolute intensity scaled data without desmearing to reduce noise.

Modelling of all scattering data was performed using the software ‘SasView’ (<http://www.sasview.org>). For all data presented throughout, symbols represent the experimental scattering data, and solid lines are the model fits generated as described. All fitting parameters from the models are presented in the [Supplementary Material](#). For modelling all USANS data, a custom slit smear value of 0.0586 Å^{−1} for slit height was incorporated into the fitting algorithm to correct for smearing conditions.

Rheological measurements were performed using an Anton Paar MCR 302 rheometer fitted with double gap geometry. The temperature was controlled at 25 °C and samples were allowed to equilibrate to room temperature for at least one hour prior to the measurement. Viscosity sweeps were run between shear rates of 0.01–100 s^{−1}. For phenol additive samples, amplitude sweeps were run between 0.01–100% shear strain at a constant angular frequency of 10 rad.s^{−1}. Subsequent frequency sweeps were taken in the angular frequency range between 0.1–100 rad.s^{−1} at a constant shear strain of 0.1% selected from the linear viscoelastic region. All samples were subjected to a pre-shear procedure in which samples were sheared for several minutes in order to remove any air bubbles and homogenise the sample prior to analysis. All samples were measured in triplicate and error bars correspond to the standard deviation.

3. Results and discussion

3.1. Pure oleyl amidopropyl betaine

Oleyl amidopropyl betaine (OAPB) is a zwitterionic surfactant in which the hydrophilic head-group consists of a carboxylate anion and quaternary ammonium cation (betaine), which are linked to an amido group via a propyl spacer, and the hydrophobic tail-group is a C18 alkyl chain with a *cis* monounsaturated between carbons 9 and 10 ([Fig. 2a](#)). In aqueous solution, OAPB spontaneously self-assembles into wormlike micelles (WLMs) at concentrations as low as 0.1 mM [37,44]. This behaviour is confirmed by additional small-angle neutron scattering (SANS) measurements ([Fig. 2b](#)), where samples up to 10 mM OAPB can be accurately modelled using an analytical model for the scattering from the flexible cylinders [45]. The model accounts for the cross-sectional radius of the worms, and the Kuhn or persistence length, which describes the length-scale over which the worms are locally rigid. The slight increase in gradient in the Guinier region (low q) from q^{-1} to $q^{-1.2}$ relates to this characteristic, as a conventional cylindrical micelle or ‘rod’ would typically show a continuous low q slope of q^{-1} [46–48], given that the Kuhn length and contour (overall) length of the micelles would be equivalent. The contour lengths of these structures can typically be on the order of microns according to cryo-transmission electron microscopy (cryo-TEM) imaging [49,50], hence this parameter is inaccessible to SANS ($d = 2\pi/q_{min} \approx 400$ nm, for these measurements) and values for length reported in the [Supplementary Material](#) must therefore be taken as theoretical minimum contour lengths.

At the lowest OAPB concentration measured (1 mM), the scattering data lacks the distinct q^{-4} turnover in the Porod (high q , 0.1 Å^{−1}) region, which relates to the cross-section/curvature of the micelles ([Fig. 2b](#)). There are likely a number of factors contributing to this effect: firstly, the Kuhn length is marginally lower at 1 mM OAPB (63.9 nm) compared to 5 and 10 mM (67.9 and 80.4 nm respectively; see [SI, Table S3](#)), indicating less rigid worms.

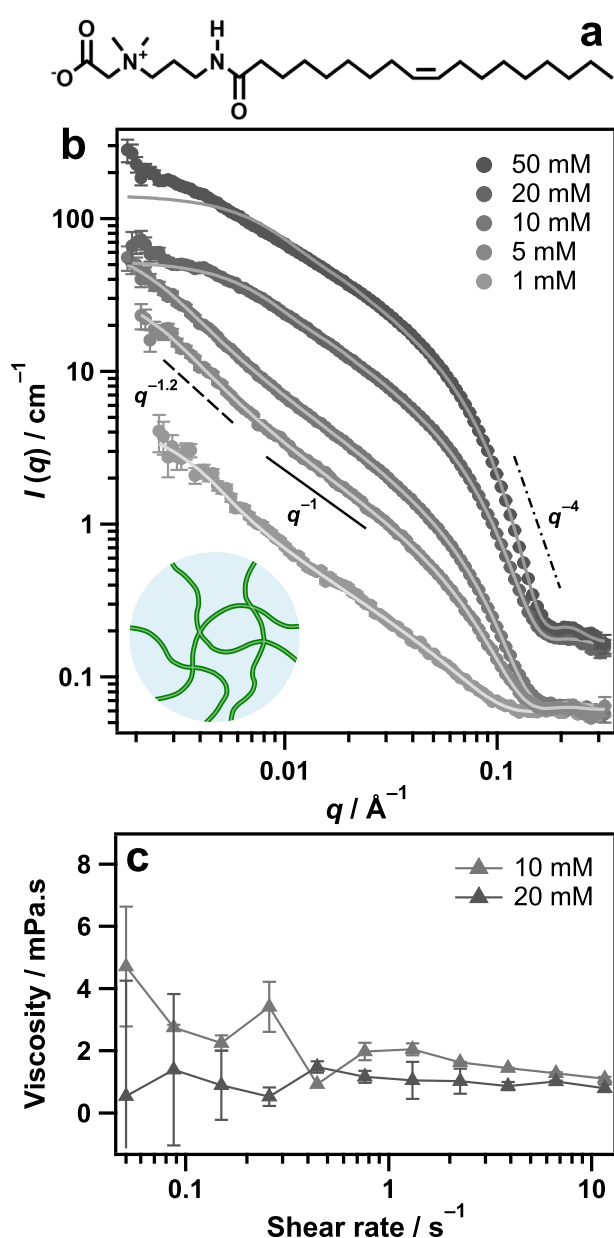


Fig. 2. (a) Chemical structure of oleyl amidopropyl betaine (OAPB). (b) SANS data of pure OAPB solutions in D_2O at different concentrations. Data for 20 and 50 mM have been offset by multiplication ($\times 2.5$) for clarity. The inset is a schematic of the internal wormlike structure as predicted from the fitting. (c) Dynamic viscosity data for similar solutions of OAPB in water.

This result is expected, as higher concentrations often lead to denser packing of the surfactant molecules in the micelles and longer wormlike contour lengths [28,51,52], which would cause the scattering to conform to the steeper slope at lower q values. Similar effects have been observed with ionic surfactants forming wormlike micelles in the presence of added salts, where increases in ionic strength not only served to promote wormlike aggregation, but also led to increases in Kuhn length by charge-screening [30,32,53,54]. The flexibility of wormlike micelles is therefore intrinsically linked to the intermolecular surfactant spacing, and as OAPB is zwitterionic, its self-screening nature results in a closer packing arrangement, which is further reinforced by the decrease in worm radius from 2.6 to 2.1 nm at 1 and 20 mM respectively (see SI, Table S3). The influence of these interactions was incorporated into the flexible cylinder model by Chen and co-workers [51].

The other factors causing the different form factor of the 1 mM OAPB sample are most likely the absence of volume effects, and weak intermicellar interactions (*i.e.* a structure factor contribution), both of which would increase scattering intensity at high q . The length of the surfactant chain with the *cis* double bond according to the Tanford equation is approximately 2.4 nm [55], in good agreement with the SANS results and suggesting moderate interdigitation of the tail-groups in the micelle interior at the higher concentrations.

At 20 and 50 mM, scattering from the OAPB micelles conforms more to a cylindrical (rod-like) form factor (Fig. 2b), and hence was more accurately approximated using a cylinders (rigid) model (see SI, Table S3) [56]. This transition is counter-intuitive based on the previously asserted premise that increasing the surfactant concentration facilitates wormlike aggregation in these systems. The most probable explanation for the change in scattering shape at these concentrations, is that there is now a sufficient volume fraction of surfactant present to introduce an additional structure factor contribution to the scattering, resulting from intermicellar interactions [57,58]. As the original model was designed for dilute polymer solutions, the corrections implemented by Chen and co-workers [51] may therefore not be able to account for all intermicellar interactions of wormlike micelles, and a modelling approach which includes an additional structure factor contribution may be required to accurately describe the scattering of OAPB at high concentrations (≥ 20 mM). As this study is focused on the effects of organic additives on the properties of OAPB wormlike micelles, all subsequent measurements were conducted with an OAPB concentration of 10 mM, so that the scattering data and additive response was not obscured by additional factors. Furthermore at 10 mM OAPB, the dynamic viscosity of the wormlike mixture is only marginally higher than that of pure water (0.89 $\text{mPa}\cdot\text{s}$ at 25 °C), implying that the worms are well below their critical entanglement concentration (Fig. 2c). Therefore at this surfactant concentration, any increases in fluid viscosity can also be attributed to the effects of the additives.

3.2. OAPB with heptane

The first additive explored in this study was the straight-chain hydrocarbon, heptane (C_7H_{16} , Fig. 3). Incorporation of heptane at a 0.5:1 M ratio (heptane:OAPB) did not cause any deviation from the wormlike structure. The Kuhn length was found to increase from 80.4 nm for 10 mM OAPB, to 97.9 nm with 5 mM heptane added (see Supplementary Material, Table S4), suggesting that the oil was intercalating between the surfactant tail-groups, rendering the worms more rigid. As heptane is immiscible with water, this is a reasonable conclusion. At an equimolar concentration of OAPB and heptane, the scattering conforms to a shallower slope at low q , decreasing approximately from q^{-1} to $q^{-0.85}$. Since q^{-1} is representative of scattering from cylindrical objects, and q^0 is representative of scattering from spherical objects [47], a low q slope of $q^{-0.85}$ is most likely indicative of a transitional composition between the two geometries. This was confirmed by the single structure models being ineffective for describing the data, and use of a power-law alone does not provide significant insight for the system. Therefore, the equimolar mixture of OAPB and heptane is presumed to comprise a combination of wormlike and spherical micelles, and as such, these data were accurately modelled using a linear addition of flexible cylinders and spheres models (see Supplementary Material, Table S4). Previous work has suggested that a transitional structure of adjoined spheres in a type of ‘pearl necklace’ aggregate is unfavoured for small amphiphilic molecules, hence, they can exist simultaneously in a mixture, but tend to adopt one shape or the other [3,59]. This phenomenon has also

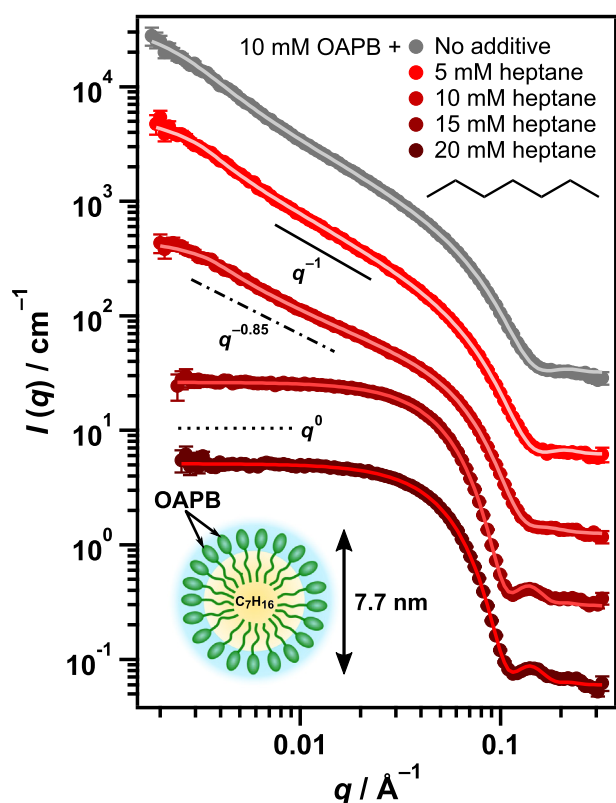


Fig. 3. SANS data from 10 mM OAPB with the specified concentrations of *n*-heptane. Data have been offset by multiplication for clarity ($\times 5$, $\times 20$, $\times 100$ and $\times 500$). Insets show a schematic of the microemulsion droplet structure and its diameter as determined from the fitting (bottom left) and the chemical structure of *n*-heptane.

been observed with cryo-TEM, in which mixtures of surface active polymers and nonionic surfactants self-assembled into discrete flexible cylinders and spheres [50,60–62].

At higher concentrations of heptane (15 and 20 mM) where the oil is in excess (1.5:1 and 2:1, heptane:OAPB), evolution into spherical micelles approximately 7.7 nm in diameter occurs (Fig. 3), to reconfigure the system to a new thermodynamic minimum in the form of a microemulsion where the oil is accommodated in the cores of spherical droplets. These data are modelled using a classical spheres model [63], and the radial polydispersity of these droplets is around 11% (see Supplementary Material, Table S4), indicating a fairly uniform size distribution, characteristic of a microemulsion. Given that heptane is non-polar and comparatively insoluble in water (see Supplementary Material, Table S2) [64], this is an expected transition pathway. Transitions from WLMs to microemulsion droplets have been observed in many surfactant systems [65–71], and Shibaev and co-workers have proposed a mechanism for this process by which the energetically costly, high curvature end-caps of the worms act as seed points for the formation of these droplets [72]. Swollen end-caps on WLMs have again been observed by cryo-TEM [50,60,73].

This theory would support the aforementioned hypothesis of wormlike and spherical micelles co-existing in the equimolar, transitional sample of OAPB and heptane, as uptake of the oil in this manner would result in significant swelling of the end-caps that would eventually have to disconnect from the worms in order for more oil to be encapsulated. This cycle would thus continue until enough oil had been absorbed such that a complete structural evolution to droplets had occurred. Furthermore, due to this change in structure and the resultant disentanglement of the wormlike network, WLM solutions are found to undergo enormous decreases

in fluid viscosity following exposure to oil [36,74,75]. This effect is negligible for OAPB with heptane (see Supplementary Material, Fig. S1), as at this surfactant concentration the dynamic viscosity of the fluid is already minimal. However, with this responsiveness in mind combined with the surfactant's eco-compatibility, OAPB could potentially be a competitive compound for use in oil fields, given that it is shown here to encapsulate essentially double the amount of oil per molecule of surfactant. It should be noted that above 20 mM heptane, excess oil was expelled as macroscopic droplets, indicating that the system is no longer in a stable microemulsion region.

3.3. OAPB with methylcyclohexane, toluene and cyclohexanol

The next additive to be explored with OAPB was methylcyclohexane (C_7H_{14} , Fig. 4a), a cyclic analogue of heptane. Similar to heptane, initial doping of methylcyclohexane into a 10 mM OAPB solution does not alter the wormlike structure of OAPB (Fig. 4a). Interestingly, at the equimolar concentration of 10 mM OAPB and methylcyclohexane, a decrease in low q slope steepness is not apparent as was the case with the equivalent heptane sample. This suggests that the system is not yet in a transitional state of co-existing worms and spheres. Noticeably however, the predicted Kuhn length for the worms in this mixture is 186.3 nm (see Supplementary Material, Table S5), a remarkably high number implying especially stiff worms from the incorporation of the additive. The oil is likely intercalating between surfactant tail-groups resulting in a dense packing arrangement and therefore, highly rigid worms. The sample therefore is likely to be very near the boundary where transition to a microemulsion begins. At 15 mM methylcyclohexane, complete evolution of wormlike OAPB into a microemulsion is evident, with a drop radius of 4.6 nm and polydispersity around 10.5% (see Supplementary Material, Table S5). Again dissimilar to heptane, a sample containing 30 mM methylcyclohexane was amenable to measurement by SANS, since a clear phase separation was not yet present. This demonstrates a higher capacity for solubilisation of methylcyclohexane compared to heptane, suggesting that cyclic compounds may be captured with greater effectiveness due to more efficient packing. This effect may also simply be related to the molecular volume of the additives, which is lower for the cyclic compound. However, given that the microemulsion droplets of OAPB with methylcyclohexane swell to a greater size ($R = 5.1$ nm) compared to those with heptane ($R = 3.9$ nm), the hypothesis of more efficient molecular packing for the cyclic additive is more feasible. The small upturn in the scattering data at lowest q for the 30 mM methylcyclohexane sample is an indication of critical scatter from large objects, presumably clustering of the droplets near a phase boundary.

Of all the non-polar additives examined in this study, the most distinctive self-assembly behaviour occurs with the incorporation of toluene (C_7H_8 , Fig. 4b), the aromatic equivalent of methylcyclohexane, into OAPB WLMs. Similar to the previous hydrocarbon additives, the Kuhn length and radius of the worms increases with the addition of toluene until a critical point where the system collapses into a microemulsion (see Supplementary Material, Table S6). Unlike heptane and methylcyclohexane with 10 mM OAPB, which both shared transitions into microemulsions at additive concentrations of 15 mM, for toluene this occurred at approximately 30 mM. Moreover, where heptane and methylcyclohexane showed excess oil at 30 mM, toluene appeared fully dissolved even at a concentration of 50 mM ($\times 5$ the amount of OAPB). Therefore, the molecular packing and solubilisation of toluene with OAPB is clearly significantly more efficient than the other oils.

The main chemical distinction with toluene versus heptane and methylcyclohexane is its aromaticity, which results in toluene being planar and having a small dipole moment (0.36 D). We

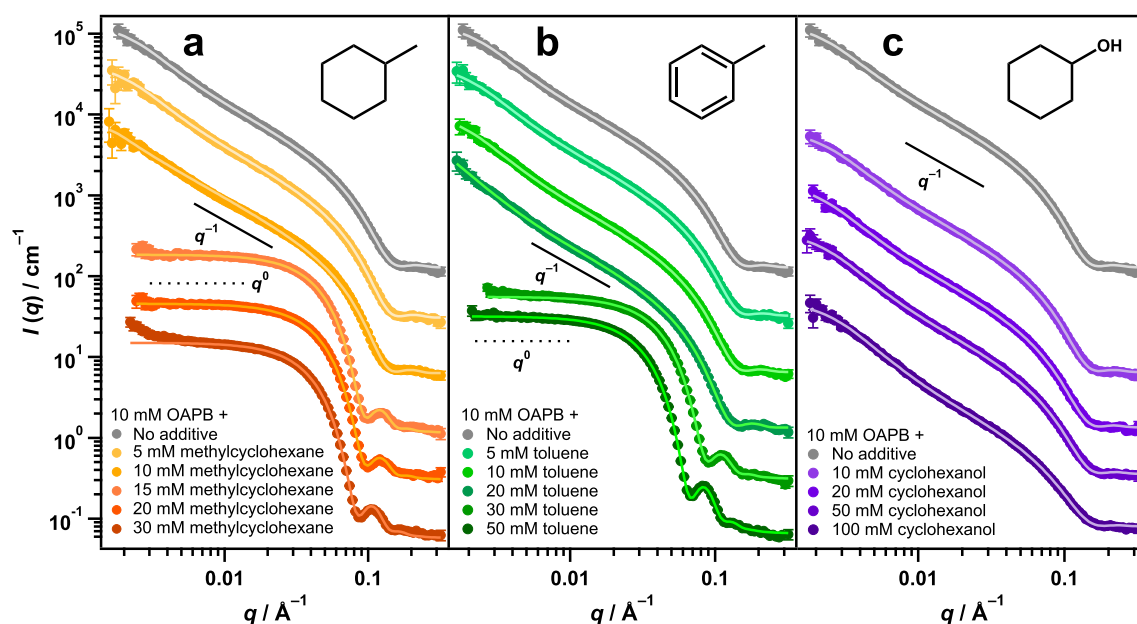


Fig. 4. (a–c) SANS data of 10 mM OAPB with the specified concentrations of methylcyclohexane (a), toluene (b) and cyclohexanol (c). Data have been offset by multiplication for clarity ($\times 5$, $\times 20$, $\times 100$, $\times 500$ and $\times 2000$). Insets show the chemical structures of each additive.

expect that these features impact the co-assembly of toluene with OAPB in two ways: firstly, the aromaticity promotes π - π stacking between toluene molecules, which would allow them to pack more densely in the micelle core. But secondly, the aromaticity and small dipole moment would also allow more favourable partitioning further towards the micelle exterior through similar π - π stacking interactions with the *cis*-unsaturated groups in the center of the OAPB tails. Such behaviour would facilitate the uptake of additional additive, accounting for the higher concentration of toluene required to effect transition of the wormlike network into microemulsion droplets, as well as the larger size of the droplets ($R = 6.5$ nm for 50 mM toluene compared to 5.1 nm for 30 mM methylcyclohexane, see [Supplementary Material Tables S5 and S6](#)). In addition, toluene has a reported aqueous solubility of around 6.22 mM at 25 °C [64], meaning a greater proportion of the additive will partition into the bulk aqueous phase. Similar behaviour has been ascribed to the formation of disc-like micelles in systems of toluene with erucyl amidopropyl betaine [36], a more lipid-like homologue of OAPB with a C22 tail-group. It is worth noting that the procedure for synthesising the erucyl surfactant in the study did not include a desalting step [38], hence an equimolar concentration of NaCl would be present to partially screen repulsions between the surfactant head-groups, which combined with the longer tail-group may explain why the addition of toluene resulted in a transition from worms to disks rather than globular micelles as observed in this work. Again, unsurprisingly the inclusion of methylcyclohexane and toluene did not cause any marked changes in fluid viscosity (see [Supplementary Material, Fig. S2a,b](#)).

The last additive explored in this particular series was cyclohexanol ($C_6H_{11}OH$, [Fig. 4c](#)), a non-aromatic compound similar to methylcyclohexane and toluene but with a hydroxyl group instead of a methyl group attached to the ring, making the compound slightly polar (1.85 *D*). Unlike the other additives described thus far, the addition of cyclohexanol causes little to no deviation from the wormlike scattering form factor of OAPB, even at concentrations of 50 and 100 mM ([Fig. 4c](#)). This indicates that the morphology of the micelles has not changed from flexible cylinders following the solubilisation of the alcohol, a phenomenon that

has also been noted by Hoffman and Ebert [66]. Being a polar molecule and soluble in water up to around 0.35 M at room temperature (see [Supplementary Material, Table S2](#)), cyclohexanol is likely to form an equilibrium between integration into the OAPB micelles and dissolution in the bulk water. Therefore, the obvious explanation for the lack of structural change with cyclohexanol is that the additive is partitioning more towards the micelle exterior, so that it can interact more favourably with the surfactant head-groups through induction polarisation interactions, as well as becoming partially solvated by the bulk water molecules. Since the volume of the hydrophobic micellar cores will not significantly increase by this partitioning, the micelles can remain wormlike rather than having to convert to a spherical morphology in order to entrain the additive.

Of particular interest regarding the addition of cyclohexanol, are the large, incremental decreases in Kuhn length of the OAPB WLMs with each increase in the additive concentration (see [Supplementary Material, Table S7](#)). For pure 10 mM OAPB, the Kuhn length of the worms is 80.4 nm as determined from the fitting, however with a 100 mM concentration of cyclohexanol present, the Kuhn length decreases to approximately 44.8 nm. This effect is subtly evident from the scattering data by the changes in inflection points to higher q values with increasing cyclohexanol concentration ([Fig. 4c](#)), and implies that the worms are much more flexible. Furthermore, the changes provide additional evidence that the additive is locating in the micellar structure, rather than just dissolving in the aqueous solution. The increases in flexibility of the worms with addition of cyclohexanol are rather counter-intuitive, as intercalation of additives usually causes WLMs to stiffen [14,30,53], as with the non-polar additives explored. The solvation of the hydroxyl group of cyclohexanol may serve to increase the spacing between the OAPB head-groups, which is why a small decrease in the worm radii from 2.3 to 2.1 nm, a higher curvature state, is also observed (see [Supplementary Material, Table S7](#)). Curiously, the addition of cyclohexanol did not cause a significant increase in the viscosity of 10 mM OAPB (see [Supplementary Material, Fig. S2c](#)), which could be expected given that intercalation of the additive would translate to greater contour lengths for the

worms. They may still simply be too short to entangle even with the uptake of the additive or the effect is offset by the increased flexibility of the worms.

3.4. OAPB with *p*-xylene: neutron contrast variation

To more thoroughly investigate the internal structure of the microemulsions formed by addition of the non-polar organic additives to OAPB wormlike solutions, a contrast variation experiment

was undertaken with *p*-xylene as the additive (Fig. 5). By selectively deuterating the various components of the mixture (*i.e.* the surfactant and the additive), it is possible to mask their contribution to the overall sample scatter by rendering their scattering length densities similar to that of D₂O (*ca.* $6.35 \times 10^{-6} \text{ \AA}^{-2}$), thus specifically highlighting the scattering from the other component (Fig. 5e). By comparing this to the scattering from the fully hydrogenated compounds, it is possible to determine where each component is enriching within the micelle structure. For

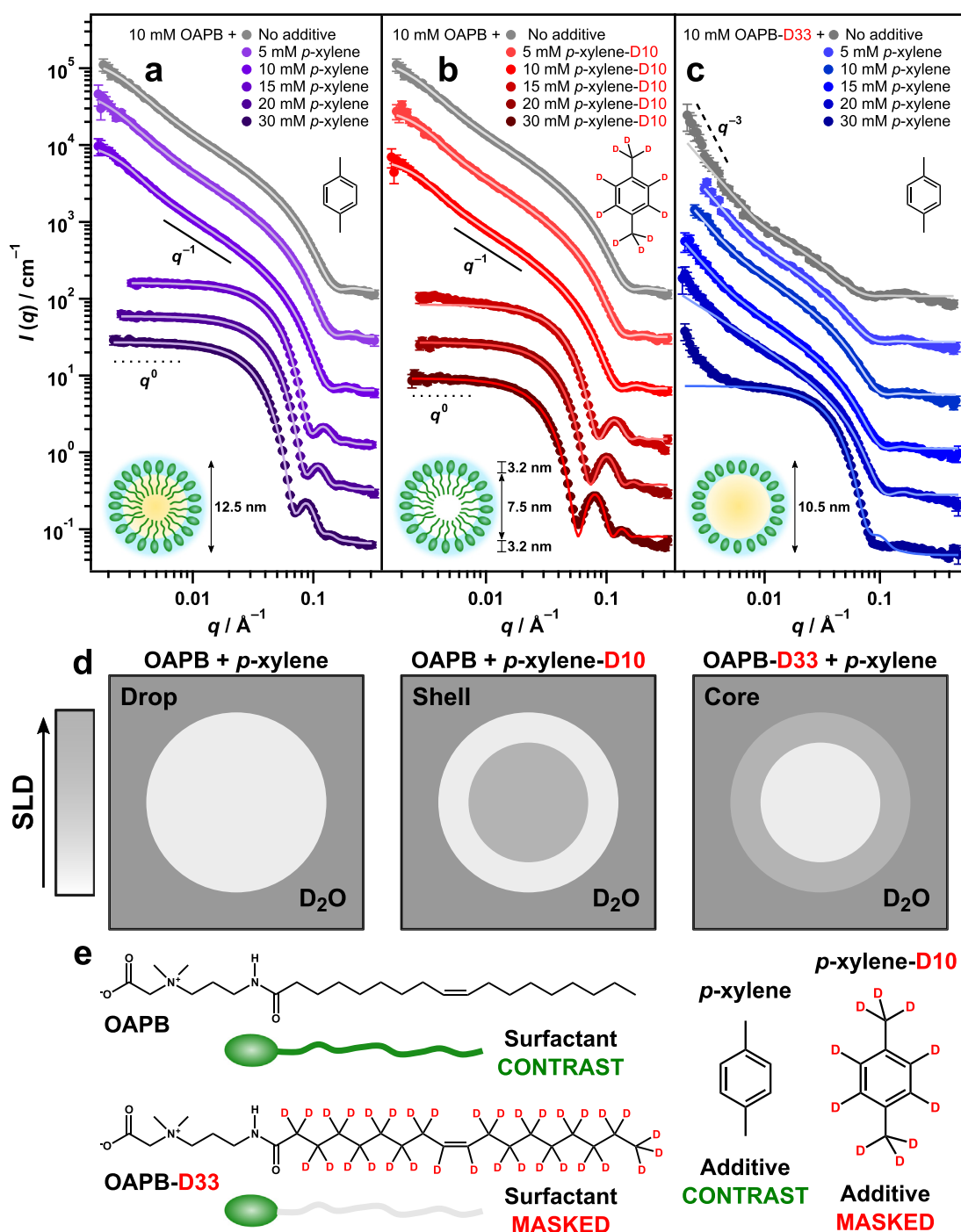


Fig. 5. (a–c) SANS data of 10 mM OAPB with *p*-xylene (a), 10 mM OAPB with *p*-xylene-D10 (b) and 10 mM OAPB-D33 with *p*-xylene (c) at the specified concentrations of added *p*-xylene and *p*-xylene-D10. Data have been offset by multiplication for clarity ($\times 5$, $\times 20$, $\times 100$, $\times 500$ and $\times 2000$). Insets below the figure legends are the chemical structures for *p*-xylene and *p*-xylene-D10, while the insets in the lower left corners are schematics for the microemulsion droplets based on the three contrast conditions and fitting parameters. (d) Schematic showing the contrast variation for neutrons (based on scattering length density) of the microemulsion droplets with deuteration of the different components. (e) Chemical structures of OAPB/OAPB-D33 and *p*-xylene/*p*-xylene-D10, and their neutron scattering contrasts in D₂O.

microemulsions, this usually corresponds to the core (interior) or shell (exterior) of the droplets, and allows a more precise determination of the parameters for each [76,77]. The contrast variation concept by selective deuteration in relation to the core–shell structure of a microemulsion droplet is shown schematically for OAPB and *p*-xylene in D₂O in Fig. 5d.

Similarly to toluene, *p*-xylene is aromatic; however, the full transition to microemulsion droplets when incorporating *p*-xylene with 10 mM OAPB becomes evident at only 15 mM *p*-xylene (Fig. 5a), similar to heptane and methylcyclohexane (Figs. 3 and 4a), but approximately half that of toluene (Fig. 4b). It can be speculated that the presence of the second methyl group in the *para* (opposite) position for *p*-xylene may be serving to negate the effects of the aromatic ring that dominated for toluene, as the difference in transition concentration is much greater than the difference in aqueous solubility for the two compounds (see Supplementary Material, Table 2) [64]. This may be a combination of steric hindrance due to the increased volume of *p*-xylene from the second methyl group, and nullification of the small dipole moment for toluene (see Supplementary Material, Table 2), both of which could inhibit favourable interactions of the additive molecule with the surfactant tail-group unsaturation. Therefore, *p*-xylene may be locating solely in the interior of the droplets, limiting its uptake capacity.

Using deuterated *p*-xylene (*p*-xylene-D10), it is possible to more clearly detect the partitioning of the additive within the micelle structure. The replacement of *p*-xylene with *p*-xylene-D10 in 10 mM OAPB solutions yields resolving of the peak at around 0.1 \AA^{-1} for the higher additive concentrations (Fig. 5b). As the scattering contrast results only from the surfactant molecules in this instance, modelling of these data gives an approximation of the shell thickness using a core–shell model [63]. The core–shell model differentiates scattering from the micelle interior and exterior by assigning different scattering length densities to each region. In the case of OAPB with *p*-xylene-D10, the scattering length density of the micelle core becomes much greater ($\text{ca. } 5.5 \times 10^{-6} \text{ \AA}^{-2}$), confirming enrichment of the additive in the micelle interior (see Supplementary Material, Table S9). This is further supported by modelling, which reveals that the radius of the micelle cores increases from 2.1 to 3.7 nm at 15 and 30 mM *p*-xylene-D10 respectively, whereas the shell thickness only increases slightly from 2.9 to 3.2 nm at these additive concentrations (see Supplementary Material, Table S9). The shell thicknesses determined here would be around the same length as a molecule of OAPB, given that the length of the C18 tail-group with monounsaturations is approximately 2.4 nm from the Tanford equation [55]. Hence, there is most likely only a modest amount of *p*-xylene intercalating between the ends of the surfactant tail-groups.

Using OAPB with deuterated tails (OAPB-D33), the scattering length density of the surfactant tail group becomes approximately $5.9 \times 10^{-6} \text{ \AA}^{-2}$ (see Supplementary Material, Table S1). The scattering contrast now arises from the hydrogenated *p*-xylene, and hence becomes characteristic of the micelle core. Therefore, with negligible contrast for the droplet shell, these data were fit using the homogeneous spheres model [63], rather than the core–shell model. The overall scattering intensities of these samples were much lower because of the reduced contribution from the surfactants (Fig. 5c). But more noticeably, the samples now do not appear to start transitioning to microemulsions until the concentration of *p*-xylene exceeds 20 mM. A possible explanation for this difference may stem from a change in the surfactant properties due to the deuteration of the tail-group. Replacement with deuterium can alter the polarisation and molecular packing of a compound [78], therefore the phase boundary may have moved. Crucially, there is no droplet shell peak at high q , which further asserts the absence of additive molecules partitioning between the surfactant mole-

cules. This is reinforced by modelling the scattering data, which shows that for 30 mM *p*-xylene with 10 mM OAPB-D33, the average radius of the droplets is around 5.2 nm with a polydispersity of 15.9% (see Supplementary Material, Table S10), compared to when the hydrogenated OAPB was used which shows an average diameter of 6.2 nm and a polydispersity of 10.8% (see Supplementary Material, Table S8). This leaves an overall size difference of 2.0 nm; however because the surfactant head-group is hydrogenated, a small contrast step could arise there, which is why the difference in radius may be smaller than expected based on the 3.2 nm thickness determined from the deuterated additive contrast (Fig. 5b). The surfactant head-groups will be solvated by the bulk D₂O, thus this effect would be small.

For the 30 mM *p*-xylene and 10 mM OAPB-D33 mixture, a substantial increase in scattering intensity at low q occurs (Fig. 5c), indicative of critical scatter. This could be due to expelled oil, however the equivalent mixtures for the other contrasts did not exhibit this effect (Fig. 5a,b). The scattering of 10 mM OAPB-D33 without any additive diverges from the flexible cylinders model at lowest q also, increasing to an approximate slope of q^{-3} (Fig. 5c). For this sample, the increase is most likely a result of critical scatter arising from undissolved surfactant, possibly due to the deuteration of the tail-group causing a change in surfactant solubility and molecular packing [78]. Therefore, the *p*-xylene may initially be serving to co-solubilise the surfactant until additive concentrations of 20 mM and above are reached, after which the large excess of *p*-xylene may be causing another type of critical separation as a result of the microemulsion transition, again resulting in a steeper gradient at low q . This agrees with the higher transition concentration of *p*-xylene for the deuterated OAPB.

3.5. OAPB with phenol

The second polar additive explored in this study was phenol ($\text{C}_6\text{H}_5\text{OH}$, Fig. 6a), the aromatic analogue of cyclohexanol. Similarly to cyclohexanol, SANS measurements of 10 mM OAPB with increasing quantities of phenol exhibit only very subtle changes in their scattering (Fig. 6a), which can be readily described by the flexible cylinder model [45,51], indicating that the micelles are remaining wormlike in nature. As with cyclohexanol, modelling reveals significant decreases in the Kuhn length of the worms, from 80.4 nm without phenol to approximately 43.1 nm with 30 mM phenol (see Supplementary Material, Table S11), indicating significantly more flexible worms. As for cyclohexanol, it is likely that the polar phenol molecules partition into the micelle exterior and serve to divide the surfactant head-groups, giving the micelles a more fluid character. For phenol, the Kuhn length of the OAPB worms was found to decrease much more rapidly with each additive increment compared to cyclohexanol, which only showed a drop in Kuhn length to 44.8 nm at 100 mM cyclohexanol (see Supplementary Material, Table S7). It is plausible that phenol interacts more strongly with the surfactant head-groups than cyclohexanol, causing a greater proportion of the additive to partition into the micelle structure, opposed to cyclohexanol where the majority of the additive is partitioning into the bulk aqueous solution [66].

The mechanism we propose to account for this behaviour relates to the aromaticity of phenol (and lack of aromaticity for cyclohexanol), and the resonance structures that stem from this property. Due to the resonance stabilising effect of the aromatic ring, phenol is significantly more acidic than cyclohexanol, with a pK_a of around 10 rather than 16 (see Supplementary Material, Table S2). Therefore, we expect that a proportion of phenol molecules are likely to deprotonate in the solution, resulting in stronger interactions with the zwitterionic betaine head-groups. This is

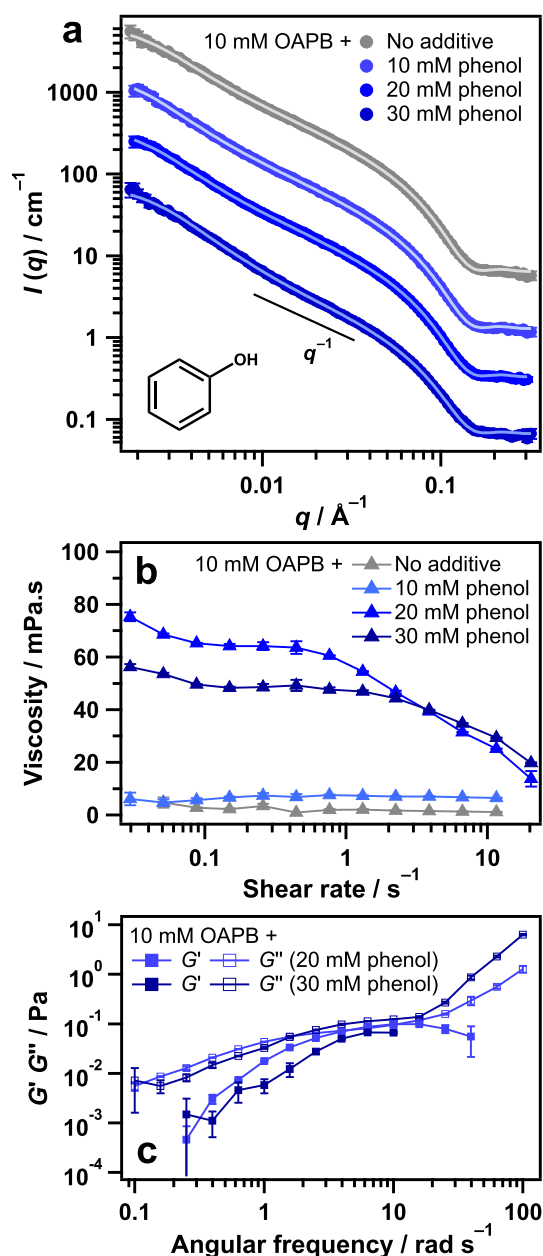


Fig. 6. (a) SANS data of 10 mM OAPB with the specified concentrations of phenol. Data have been offset by multiplication for clarity ($\times 5$, $\times 20$ and $\times 100$). The inset is the chemical structure of phenol. (b) Dynamic viscosity data for similar solutions of OAPB with phenol in water. (c) Corresponding oscillatory shear frequency sweeps showing the storage (G') and loss (G'') moduli versus angular frequency for 10 mM OAPB with 20 and 30 mM phenol.

shown schematically in Fig. 7b, where the phenol molecules are presumed to orient with their aromatic rings towards the interior of the micelles, allowing these electronegative molecules to optimally interact electrostatically with the quaternary ammonium groups in OAPB. In addition, the hydroxyl groups can participate in proton exchange with the carboxylate moieties on OAPB while also being solvated by the bulk water. It must be noted that solution conditions for these experiments would be around pH 7 (i.e. no added acid or base), which is below the pK_a of phenol (ca. 10). However, the carboxylate constituent on the OAPB head-group could act as a weak conjugate base, facilitating deprotonation as well as hydrogen bonding with the phenol hydroxyl groups when co-assembled in the micelle structure. As cyclohexanol will not exhibit these effects due to the lack of resonance stability, its polar-

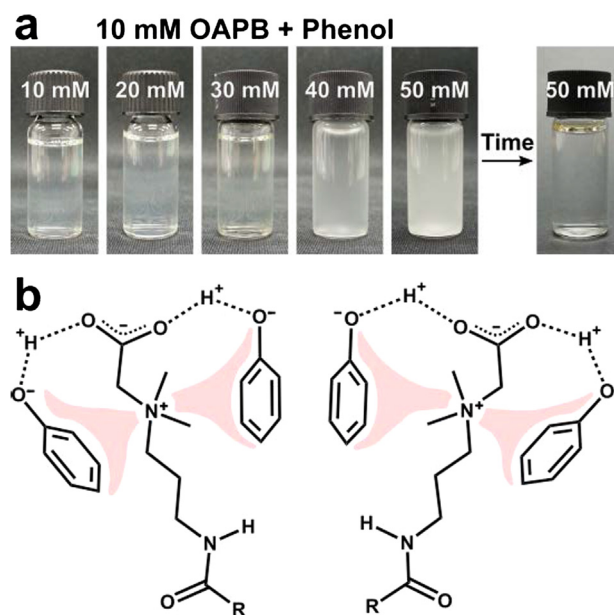


Fig. 7. (a) Samples containing 10 mM OAPB and the specified concentrations of phenol. The cloudy samples (40 and 50 mM phenol) were mixed manually immediately before photographing. The image on the far right is the same sample of 10 mM OAPB with 50 mM phenol, showing the eventual liquid–liquid phase separation that occurs after sufficient time (see yellowish layer around meniscus). (b) Schematic of the proposed mechanism for charge screening by phenol intercalation between OAPB head-groups at the ideal ratio of 2:1 (additive:surfactant). The pale red regions depict the interactions of the deprotonated phenol molecules with the quaternary ammonium in the OAPB head-groups, and 'R' denotes the $C_8=C_9$ tail of OAPB (Fig. 2a). (For interpretation of the references to color in this figure legend, the reader is referred to the web version of this article.)

isation interactions with the OAPB head-groups will be much weaker, hence it does not partition as readily into the micelles as does phenol, despite its aqueous solubility being much lower (see [Supplementary Material, Table S2](#)). This mechanism is similar in concept to salt screening in ionic surfactant systems, which usually leads to greater Kuhn lengths [30,32,53,54]. However, because OAPB is self-screening and phenol possesses a comparatively bulky aromatic ring, the surfactant molecules may be unable to pack more densely despite the charge screening effects from the additive, which may be why the Kuhn length in these systems instead decreases with the doping of phenol.

Interestingly, the addition of phenol also causes substantial increases in the dynamic viscosity of 10 mM OAPB in water (Fig. 6b), an effect that was not induced by cyclohexanol. At 10 mM phenol, where the surfactant: additive ratio is 1:1, viscosity is essentially unchanged. However, at 20 mM phenol, a significant increase in viscosity (ca. $\times 15$ at zero shear) can be observed. At the higher phenol loading, a greater proportion of the additive will partition into the micelle, indicating that synergistic effects between the additive and surfactant molecules are dominant. This likely arises from the proposed partitioning and interaction mechanism of phenol with OAPB (Fig. 7b), where the resonance effect of phenol and the stronger polarisation interactions that occur as a result act to screen the charge between the micelle head-groups. Hence, the intercalation of phenol could be rendering the surfactant more nonionic in nature. Consequentially, attractive interactions between individual molecules within the micelles become more prevalent in the system. Similar mechanistic rationales have been attributed to the formation of viscoelastic WLMs in cationic solutions of cetyltrimethylammonium bromide with phenol and *p*-ethyl phenol [79–81]. We believe that this implication results in two significant changes in the bulk properties of the fluid: firstly,

because the micelles are rendered more flexible they will entangle more readily, but secondly, the stronger interactions between the surfactant and additive molecules means that the micelles will not be as susceptible to disaggregating and reforming as they manoeuvre past each other. This is a higher energy barrier for scission, and corresponds to greater relaxation times for WLMs. Both of these effects would manifest by raising the overall fluid viscosity [19,18].

Increasing the phenol concentration from 20 to 30 mM reduced the dynamic viscosity of 10 mM OAPB in water (Fig. 6b), suggesting that there is an optimal surfactant:additive ratio for enhancing the fluid viscosity. Both mixtures exhibit shear-thinning behaviour, presumably due to shear induced alignment of the worms in solution [4,6,14]. However, by observing the storage and loss moduli (G' and G'' respectively) of these samples as a function of angular frequency (Fig. 6c), it can be seen that the 20 mM phenol sample is more wormlike in nature than the sample with 30 mM phenol. This characteristic is represented by the closeness of the storage and loss moduli in the middle region of the frequency sweep: [82–84] for 20 mM phenol the two moduli overlap, whereas for 30 mM phenol there is a noticeable gap (Fig. 6c). This suggests that beyond a certain additive amount, phenol may start to induce a change in the aggregation from worms to a different self-assembled structure that is less viscoelastic in nature. Again, this change is attributed to the charge screening interaction mechanism between the polar phenol molecules and surfactant head-groups (Fig. 7b), as the effects would act in a cumulative manner with increasing the additive loading.

Further doping of phenol to concentrations of 40 and 50 mM resulted in clouding and eventual phase separation of the mixture (Fig. 7a). This behaviour is similar in nature to the cloud point phenomenon, whereby the solution demixes into a surfactant-rich and surfactant-poor phase above a critical temperature [21]. Cloud points are commonly exhibited by nonionic surfactants as they tend to have stronger attractive interactions due to their lack of charge [85]. Raghavan and co-workers documented similar behaviour for a wormlike micellar system comprising a cationic surfactant and the polar aromatic salt sodium tosylate, attributing phase separation in these mixtures to lower cloud points with additive doping [86]. Initially, the additive increased the solution viscosity, however, further addition of the additive caused the viscosity to decrease until the sample eventually phase separated. They attributed these effects to branching of the worms. It is possible that similar behaviour is occurring in the case of phenol and OAPB at higher additive concentrations, and that the decrease in viscosity for 10 mM OAPB with 30 mM phenol compared to 20 mM phenol marks the onset of this transition. This clouding result does reaffirm the proposed surfactant-additive interaction mechanism (Fig. 7b), in which the intercalation of the resonance stabilised phenol molecules screens the charging across the micelle exterior. The OAPB micelles thus become more nonionic in nature, allowing stronger intermicellar interactions that can cause increased viscosity, but potentially causing phase separation.

3.6. OAPB with benzyl alcohol, benzoic acid and salicylic acid

To further contextualise the different behaviour of phenol and cyclohexanol addition to OAPB WLMs, a complementary series of polar, aromatic additives were incorporated into aqueous OAPB solution: benzyl alcohol, benzoic acid and salicylic acid (Fig. 8a–c). As with the previous polar additives, no deviation from wormlike structure was apparent from the scattering alone, aside from 10 mM OAPB with 10 mM salicylic acid, which appeared to consist of smaller rod-like micelles or cylinders (Fig. 8c). Therefore, it is clear that these additives partition into the micelle structure in a similar fashion to phenol and cyclohexanol, likely locating between

the OAPB head-groups. Benzyl alcohol with OAPB gives very similar effects to cyclohexanol, where the additive can be included at high loadings (up to 100 mM), without causing phase separation or changing the dynamic viscosity of the mixture (Fig. 8a,d). The Kuhn length of the worms also decreases incrementally with benzyl alcohol addition, down to around 51.3 nm at 100 mM benzyl alcohol (see [Supplementary Material, Table S12](#)). Therefore, a similar partitioning equilibrium as with cyclohexanol is expected, whereby a small proportion of the benzyl alcohol molecules co-assemble with the surfactant, forcing the OAPB head-groups further apart and rendering the worms less rigid, where the rest of the additive is dissolved in the bulk solution. Despite benzyl alcohol being aromatic, the hydroxyl group is not acidic due to the resonance effect, and resultant charge interactions with the OAPB head-groups do not occur. Hence, the viscosity of the mixtures does not increase due to stronger intermicellar attractive forces.

Addition of benzoic acid and salicylic acid to 10 mM OAPB yielded physical behaviour more alike that of phenol, causing large increases in the dynamic viscosity of the fluid until further doping of the additives resulted in phase separation (Fig. 8b,c,e,f and [Supplementary Material Fig. S4](#)). At 5 mM benzoic acid, a slight increase in the dynamic viscosity of 10 mM OAPB in water is seen, followed by a significant increase ($\times 10$) at 10 mM (Fig. 8e). For salicylic acid at 5 mM, a much greater increase in viscosity at low shear compared to 5 and 10 mM benzoic acid with 10 mM OAPB was recorded, with the highest viscosity ($\times 10$ that of pure 10 mM OAPB) of all samples obtained in this study (Fig. 8f). Similarly to phenol at higher loadings (≥ 30 mM), increasing the concentration of salicylic acid to 10 mM caused a decrease in viscosity (Fig. 8f). Based on the scattering data, this is presumably because the system had appeared to change to shorter cylindrical micelles that do not entangle as easily (Fig. 8c). These viscosity effects are significantly greater than were observed for the 10 mM phenol sample, suggesting more prevalent surfactant-additive synergism for benzoic and salicylic acid with OAPB compared to phenol. Salicylic acid also phase separated the surfactant at a lower additive concentration of 20 mM (see [Supplementary Material, Fig. S4](#)), where this was only first evident for phenol at 40 mM. Therefore, it is clear that the viscosity and phase separation effects are intrinsically linked to the acidity of the additives (salicylic acid > benzoic acid > phenol).

Salicylic acid is the most acidic additive of the series, with a pK_a of approximately 3.0, due to the additional resonance stability provided by the *ortho* hydroxyl group, followed then by benzoic acid with a pK_a of approximately 4.2 (see [Supplementary Material, Table S2](#)). The mechanism by which these molecules intercalate and interact with the OAPB head-groups is thus expected to be similar to that proposed for phenol, where the deprotonated/resonance additive molecules partition into the micelle exterior to favourably interact with the surfactant head-groups through polarisation interactions (Fig. 7b). The charge of the OAPB head-groups then becomes shielded and as a result, attractive intermolecular interactions become more prevalent due to reduced charge repulsions meaning the micelles are less likely to break apart. Hence, the overall viscosity of the system increases because the relaxation pathway by molecular reorganisation (scission) becomes less energetically favourable. This effect will be amplified for benzoic and salicylic acid due to their greater propensity to proton donate and form resonance structures, which is why larger changes in the rheology of OAPB WLMs are observed with lower concentrations of these compounds compared to phenol. As benzyl alcohol and cyclohexanol lack this key characteristic, their presence in the micelle structure does not modify the electron density across the interface and promote the interactions that result in higher fluid viscosities. Previous work involving doping of surfactant solutions with sodium salts of benzoic and salicylic acid, as well as

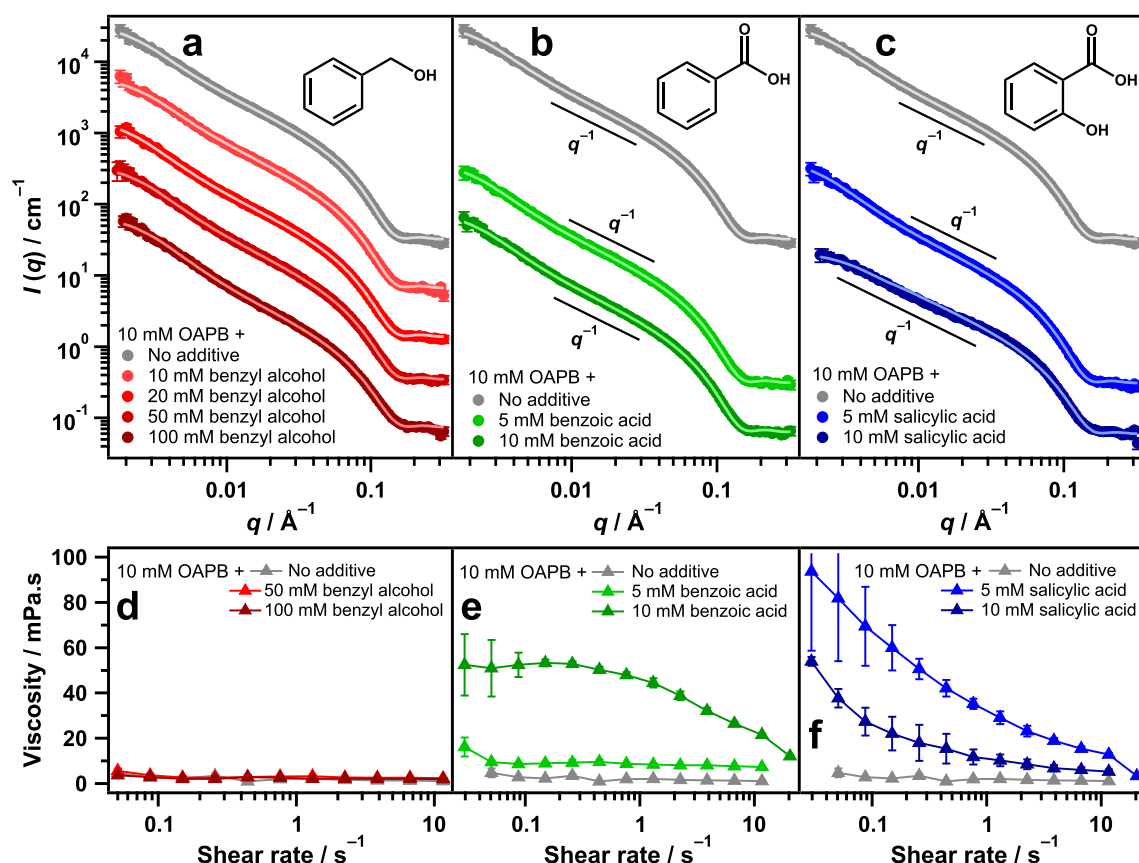


Fig. 8. (a–c) SANS data of 10 mM OAPB with the specified concentrations of benzyl alcohol (a), benzoic acid (b) and salicylic acid (c). Data have been offset by multiplication for clarity ($\times 5$, $\times 20$, $\times 100$ and $\times 500$). Insets are the chemical structures of each additive. (d–f) Dynamic viscosity data for similar solutions of OAPB with benzyl alcohol (d), benzoic acid (e) and salicylic acid (f) in water.

other polar aromatic molecules, arrived at similar mechanistic conclusions as this study, crediting resonance effects in the additives with leading to the enhanced viscoelasticity of WLMs through surfactant-additive synergism; [5,81,86–91] however, these studies were again confined to cationic surfactant systems. The present work appears to be unique not only by its utilisation of a zwitterionic surfactant, but also in that it demonstrates a detailed physical basis for enhancing the viscosity of dilute aqueous solutions of pre-existing WLMs, rather than attempting to promote wormlike transition from simpler micelle morphologies by packing alterations.

Unlike the viscoelastic systems of OAPB with phenol and benzoic acid (Figs. 6b and 8e), mixtures with salicylic acid appear to exhibit shear-thinning behaviour instantaneously (*i.e.* at minimal shear rates), rather than having to overcome a critical shear rate or apparent yielding point (Fig. 8f). This suggests that OAPB with salicylic acid has a lower degree of entanglement than similar mixtures with phenol and benzoic acid, allowing the micelles to align at lower shear rates. This behaviour would also tie in with why the worms appear to evolve into shorter cylindrical micelles at the higher salicylic acid loading (Fig. 8c). Shorter worms would be expected to align much more easily due to a lower degree of entanglement, hence the immediate responsiveness of the OAPB/salicylic acid mixtures to the shear stimulus. This likely arises from the much higher acidity of salicylic acid compared to phenol and benzoic acid, which causes it to more strongly induce the charge screening effect between the surfactant head-groups and move the phase boundary. The transition towards phase separation therefore most likely involves the additive molecules locating preferentially at the high curvature end-caps of the micelles. Partitioning of this nature would correspond to a lower energy for end-cap formation, translating to shorter worms and reduced vis-

cosity. Attractive intermolecular interactions may contribute to why the system of 10 mM salicylic acid with 10 mM OAPB is more viscous than the pure 10 mM surfactant solution (Fig. 8f), despite clearly containing shorter micelles.

3.7. USANS: OAPB branched networks

Ultra-small-angle neutron scattering operates down to extremely low q values, shedding light on the microstructure of materials ($d = 2\pi/q_{\min} \approx 15 \mu\text{m}$, for these measurements). Because these samples were more weakly scattering than is ideal for USANS, the data are presented as absolute intensity plots without desmearing (accounting for instrument geometry) to reduce noise. To correct for smearing, a custom slit smear height of 0.0586\AA^{-1} was incorporated into the modelling. These data were modelled with two-power law functions; the crossover point marks the point of inflection of the scattering fit to the second slope exponent. For pure OAPB at 10 mM, the low q values (higher q values for USANS) follow a slope of approximately $q^{-1.5}$ (Fig. 9a). A slope of $q^{-5/3}$ is associated with a random self-avoiding walk [92], a characteristic of ideal, non-interacting polymers and WLMs, which is likely the behaviour being exhibited by OAPB at this concentration. The scattering intensity then appears to flatten at a crossover point of $9.82 \times 10^{-4} \text{\AA}^{-1}$ (640 nm), indicating that the worms do not extend to length scales beyond this value. At 50 mM, the scattering exhibits a shallower slope, meaning smaller or higher curvature objects such as spheres or ellipsoids [47]. But as with the equivalent SANS measurement at this concentration (Fig. 2b), the data may be obscured by interactions that are unaccounted for in these models. The small upturn in the slope at ultra-low q could be implicit of a higher order structure at very large length scales.

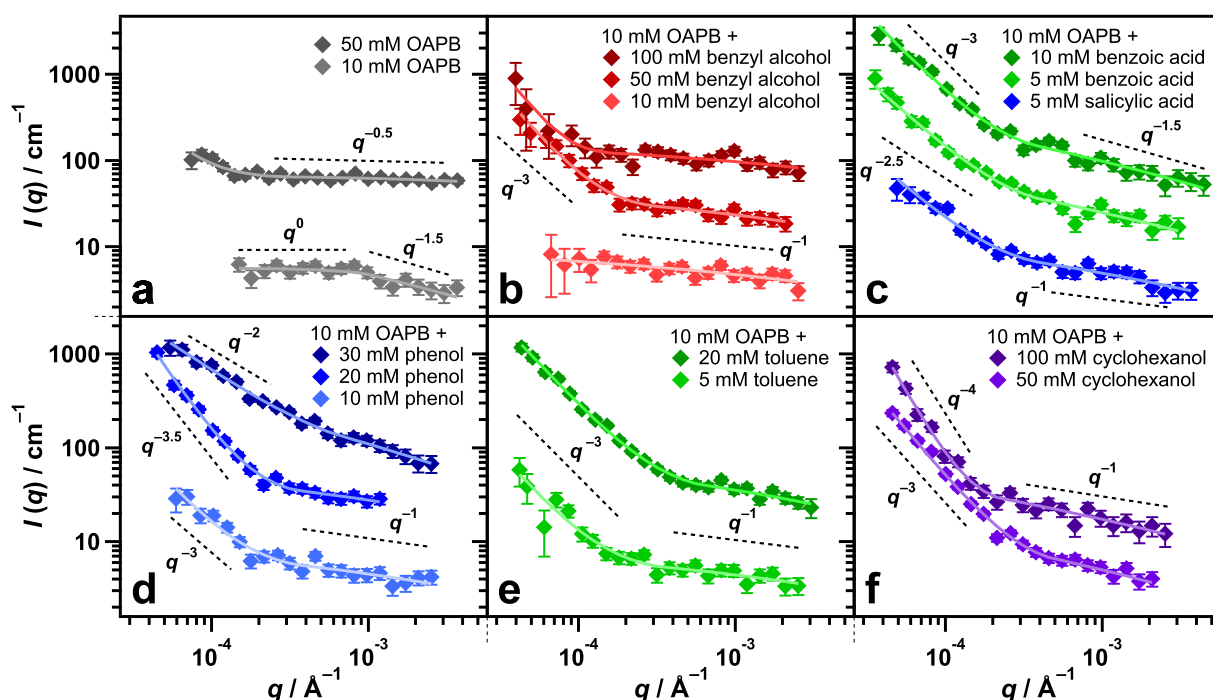


Fig. 9. (a–f) USANS data of pure OAPB at 10 mM and 50 mM (a), and 10 mM OAPB with the specified concentrations of benzyl alcohol (b), benzoic acid and salicylic acid (c), phenol (d), toluene (e) and cyclohexanol (f). Data have been offset by multiplication for clarity ($\times 5$ and $\times 20$). Slopes are presented as approximate integers and half integers based on the custom slit smear height of 0.0586 \AA^{-1} . The precise slopes determined from the fitting are in Table S14 of the Supporting Information.

For 10 mM OAPB with additives present, rather than tapering off as was the case with the pure surfactant solution, the scattering at ultra-low q tends to conform to much higher slope values (Fig. 9b–f). High scattering exponents such as q^{-3} or q^{-4} are characteristic of fractal aggregates, which are self-consistent structures that are chaotic (essentially random) in their aggregation [93,94]. A well known phenomenon in wormlike micellar systems is the entropy driven formation of ‘branched’ networks, whereby the micelles form junctions with other micelle bodies in order to overcome the energy penalty of creating end-caps [3,14,15,61]. This phenomenon has also been proven by cryo-TEM [50]. However, scattering measurements allow for a statistical comparison of the network characteristics, and the size regime for these types of systems is accessible only to USANS (or USAXS).

Mechanistically, the amount of additive appears to be intrinsically linked to the formation of junctions in these systems, as increases in additive concentration tended to result in shifts to higher power laws at ultra-low q . The exponent relates to the complexity of the fractal [93,94], thus, higher slopes likely indicate increased branching in the wormlike network. The exception to this behaviour was toluene (Fig. 9e), which shows a minimal change in gradient from $q^{-2.9}$ at 5 mM toluene to $q^{-2.8}$ at 20 mM toluene, suggesting little change in the system microstructure. Furthermore the crossover points appear to be shifting to lower q values, suggesting that the additives are also causing elongation of the worms. Another exception to these trends is the sample of 10 mM OAPB with 30 mM phenol (Fig. 9d). This mixture instead conforms to a slope of around q^{-2} , which could be indicative of large lamellae or bilayer structures [46,95]. However, it is more feasible that the system is evolving to a lower order fractal that eventually transitions into shorter cylindrical micelles or rods as observed for salicylic acid (Fig. 8c), hence why a decrease in viscosity and eventual phase separation was observed at higher phenol concentrations (Figs. 6b and 7a). This hypothesis would also align with the formation of the branched network Raghavan and co-workers proposed for their system of cationic surfactant and sodium tosylate [86].

At low q , before the crossover points to branched networks, scattering slopes of all samples with additive included are approximately between q^{-1} and $q^{-1.5}$, indicating cylindrical or wormlike networks. The mixture of 10 mM benzyl alcohol with 10 mM OAPB was the only sample that could be modelled with a single power law (ca. q^{-1}), indicating an absence of branching (Fig. 9b). It is clear that this particular additive is indeed incorporating into the micelle structure, as the q^{-1} slope continues down to ultra-low q , whereas for the equivalent sample without the additive, a tendency to a gradient of q^0 at low q was seen (Fig. 9a). However, as mentioned previously, it is likely that a proportion of this additive is also dissolved in the bulk aqueous solvent due to weaker interactions with the surfactant head-groups. Therefore, a larger amount of benzyl alcohol must be added to cause branching of the OAPB micelles. The same could be said for 10 mM cyclohexanol, as the scattering from this sample was considerably weaker and noisier even than pure 10 mM OAPB, potentially due to greater solvation from the bulk D_2O . Hence, this data set has been omitted since a model could not be reliably employed.

Curiously, the evidence of branching in these systems implies that the formation of a branched, wormlike network is not strongly related to the overall viscosity of the system, as all additives caused this property. Contrary to entanglement, branching has in fact been thought to cause decreases in viscosity, as the junctions can slide along the shaft, providing an additional pathway to relaxation [1,14,96–99]. These findings support that branching (and even elongation) of the worms does not necessarily tie in with increased viscosity, and that the changes in reptation and scission capabilities, as well as intermicellar interactions brought about by synergistic effects between the additive and surfactant head-groups are the key factors influencing viscosity in these systems. The full list of USANS samples and their precise two-power law fitting parameters are presented in Table S14 of the Supplementary Material. Note, the values for the crossover points and power laws may not appear exactly as one would deduce by observing the data; this is again due to the lack of

desmearing, but is accounted for in the fitting by inclusion of the custom slit smear height.

4. Conclusions

The effects of a variety of organic additives on the formation of zwitterionic wormlike micelles has been systematically explored using a combination of small-angle neutron scattering and viscosity measurements. Without additives present, the zwitterionic surfactant oleyl amidopropyl betaine (OAPB) spontaneously forms wormlike micelles in aqueous solution, however at concentrations as high as 20 mM, the system shows no evidence of viscoelasticity, with a zero shear viscosity only slightly higher than water.

When incorporating non-polar hydrocarbon additives into the wormlike network, a structural ‘collapse’ into microemulsion droplets was observed at a critical concentration or phase boundary due to enrichment into the micellar cores, an effect that was confirmed by contrast variation scattering measurements. For most of these additives, this effect occurred at approximately a surfactant: additive ratio of 1:1.5, with the exception of toluene, which required triple the amount in order to induce the microemulsion transition. This result is attributed to a different partitioning within the micelle structure, driven by favourable π - π stacking interactions with the unsaturated group in the OAPB tail.

Where polar additives were included, little deviation from the wormlike geometry was apparent, however significant differences in worm properties could be observed. We infer that polar additives intercalate between the surfactant head-groups and render the worms more flexible, presumably by reducing surfactant packing density. For cyclohexanol and benzyl alcohol, two polar additives in which the hydroxyl groups are not resonance stabilised, no changes in the fluid viscosity were recorded. However, in the cases of phenol, benzoic acid and salicylic acid, where the oxygen-containing functional groups are part of the aromatic delocalisation, significant increases in fluid viscosity are apparent. We interpret this change in fluid behaviour as arising from the higher propensity of these compounds to proton donate, which results in additional screening of the charge associated with each surfactant head-group.

Ultra-small-angle neutron scattering of these systems revealed a significant increase to higher magnitude gradients at low q ($\geq q^{-2.5}$). This typically indicates formation of fractal aggregates or ‘branched’ networks in the context of wormlike systems, an effect not seen for the pure surfactant solutions. This change however, was often not accompanied by an increase in fluid viscosity, implying that the improved viscoelastic behaviour of the system with the acidic additives did not necessarily stem from the development of a branched network. Rather, the enhanced viscosity is believed to be caused by charge screening between the surfactant head-groups imparted by the additive molecules which results in a higher micelle scission energy, limiting the micelle ability to break and reform, further promoting entanglement [18,19].

The results presented in this work provide insight into the response of zwitterionic wormlike micellar systems to organic additives, and how certain additives may counteract or complement desired effects on solution texture. Potential applications of this insight could include efficient and environmentally friendly materials for oil recovery and designed thickening or thinning mechanisms for complex fluids based on wormlike micelles.

Acknowledgements

We would like to acknowledge the Australian Centre for Neutron Scattering and the National Deuteration Facility, Australian Nuclear Science and Technology Organisation, for beam-time and

provision of materials. The National Deuteration Facility is partly supported by the National Collaborative Research Infrastructure Strategy – an initiative of the Australian Government. We also thank the Australian Institute of Nuclear Science and Engineering for travel support (T.M.M.), as well as the Monash Centre for Atomically Thin Materials for additional funding. This work was supported in part by the grant of an ARC Future Fellowship (FT160100191) to R.F.T.

Appendix A. Supplementary material

Supplementary data associated with this article can be found, in the online version, at <https://doi.org/10.1016/j.jcis.2018.09.046>.

References

- [1] Dreiss C.A., Y. Feng, Wormlike Micelles: Advances in Systems, Characterisation and Applications, vol. 6, Royal Society of Chemistry, 2017.
- [2] J. Yang, Viscoelastic wormlike micelles and their applications, *Curr. Opin. Colloid Interface Sci.* 7 (2002) 276–281.
- [3] S. Ezrahi, E. Tuval, A. Aserin, Properties, main applications and perspectives of worm micelles, *Adv. Colloid Interface Sci.* 128 (2006) 77–102.
- [4] N.A. Spenley, M.E. Cates, T.C.B. McLeish, Nonlinear rheology of wormlike micelles, *Phys. Rev. Lett.* 71 (1993) 939–942.
- [5] S.R. Raghavan, E.W. Kaler, Highly viscoelastic wormlike micellar solutions formed by cationic surfactants with long unsaturated tails, *Langmuir* 17 (2001) 300–306.
- [6] F. Lequeux, Structure and rheology of wormlike micelles, *Curr. Opin. Colloid Interface Sci.* 3 (1996) 341–344.
- [7] M. Samuel, R. Card, E. Nelson, J. Brown, P. Vinod, H. Temple, Q. Qu, D. Fu, et al., Polymer-free fluid for fracturing applications, *SPE Drill. Completion* 14 (1999) 240–246.
- [8] X. Liu, M. Yi, J. Zhao, et al., Visco-elastic surfactant based fracturing fluids, *Oilfield Chem.* 18 (2001) 273–277.
- [9] D. Ohlendorf, W. Interthal, H. Hoffmann, Surfactant systems for drag reduction: physico-chemical properties and rheological behaviour, *Rheol. Acta* 25 (1986) 468–486.
- [10] J.L. Zakin, B. Lu, H.-W. Bewersdorff, Surfactant drag reduction, *Rev. Chem. Eng.* 14 (1998) 253–320.
- [11] N.A. Tuan, H. Mizunuma, High-shear drag reduction of surfactant solutions, *J. Non-Newton. Fluid Mech.* 198 (2013) 71–77.
- [12] W.L. Smith, Viscoelastic cleaning compositions with long relaxation times, US Patent 4,900,467, 1990.
- [13] D. Balzer, Aqueous viscoelastic surfactant solutions for hair and skin cleaning, US Patent 5,965,502, 1999.
- [14] C.A. Dreiss, Wormlike micelles: where do we stand? Recent developments, linear rheology and scattering techniques, *Soft Matter* 3 (2007) 956–970.
- [15] N. Dan, S. Safran, Junctions and end-caps in self-assembled non-ionic cylindrical micelles, *Adv. Colloid Interface Sci.* 123 (2006) 323–331.
- [16] J.N. Israelachvili, D.J. Mitchell, B.W. Ninham, Theory of self-assembly of hydrocarbon amphiphiles into micelles and bilayers, *J. Chem. Soc. Faraday Trans. 2* (1976) 1525–1568.
- [17] J.N. Israelachvili, *Intermolecular and Surface Forces*, Academic Press, San Diego, 1991.
- [18] M. Cates, Reptation of living polymers: dynamics of entangled polymers in the presence of reversible chain-scission reactions, *Macromolecules* 20 (1987) 2289–2296.
- [19] M. Cates, S. Candau, Statics and dynamics of worm-like surfactant micelles, *J. Phys.: Condens. Matter* 2 (1990) 6869–6892.
- [20] M.R. Stukan, E.S. Boek, J.T. Padding, W.J. Briels, J.P. Crawshaw, Flow of wormlike micelles in an expansion-contraction geometry, *Soft Matter* 4 (2008) 870–879.
- [21] M.J. Rosen, J.T. Kunjappu, *Surfactants and Interfacial Phenomena*, John Wiley & Sons, 2012.
- [22] C. Williams, P. McElfresh, M. Khodaverdian, A. Mahadev, M. Ruzic, A. Gabrysch, Non-ionic fracture fluids can recover 90% permeability after proppant run, *Offshore* 61 (2001) 76–78.
- [23] P.F. Sullivan, M.K. Panga, V. Lafitte, Applications of Wormlike Micelles in the Oilfield Industry, in: *Wormlike Micelles*, Royal Society of Chemistry, 2017, pp. 330–352.
- [24] P. Bajpai, J. Singh, A. Mandal, K. Ojha, The synthesis and characterization of a clean hydrofracturing fluid, *Petrol. Sci. Technol.* 28 (2010) 1750–1760.
- [25] A. Kianinejad, M. Saidian, M. Mavaddat, M.H. Ghazanfari, R. Kharrat, D. Rashtchian, Worm-like micelles: A new approach for heavy oil recovery from fractured systems, *Can. J. Chem. Eng.* 93 (2015) 951–958.
- [26] Y. Chevalier, F. Melis, J.P. Dalbiez, Structure of zwitterionic surfactant micelles: micellar size and intermicellar interactions, *J. Phys. Chem.* 96 (1992) 8614–8619.
- [27] R. Kumar, G.C. Kalur, L. Ziserman, D. Danino, S.R. Raghavan, Wormlike micelles of a C22-tailed zwitterionic betaine surfactant: from viscoelastic solutions to elastic gels, *Langmuir* 23 (2007) 12849–12856.

- [28] L.J. Magid, The surfactant–polyelectrolyte analogy, *J. Phys. Chem. B* 102 (1998) 4064–4074.
- [29] S. Candau, E. Hirsch, R. Zana, Light scattering investigations of the behavior of semidilute aqueous micellar solutions of cetyltrimethylammonium bromide: analogy with semidilute polymer solutions, *J. Colloid Interface Sci.* 105 (1985) 521–528.
- [30] S. Candau, E. Hirsch, R. Zana, M. Adam, Network properties of semidilute aqueous KBr solutions of cetyltrimethylammonium bromide, *J. Colloid Interface Sci.* 122 (1988) 430–440.
- [31] L. Arleth, M. Bergström, J.S. Pedersen, Small-angle neutron scattering study of the growth behavior, flexibility, and intermicellar interactions of wormlike SDS micelles in NaBr aqueous solutions, *Langmuir* 18 (2002) 5343–5353.
- [32] L.J. Magid, Z. Li, P.D. Butler, Flexibility of elongated sodium dodecyl sulfate micelles in aqueous sodium chloride: a small-angle neutron scattering study, *Langmuir* 16 (2000) 10028–10036.
- [33] J.E. Hunter, J.F. Fowler, Safety to human skin of cocamidopropyl betaine: a mild surfactant for personal-care products, *J. Surfactants Deterg.* 1 (1998) 235–239.
- [34] R.E. Bolich Jr, Shampoo compositions, US Patent 4,452,732, 1984.
- [35] H. Leidreiter, B. Gruning, D. Kaseborn, Amphoteric surfactants: processing, product composition and properties, *Int. J. Cosmet. Sci.* 19 (1997) 239–253.
- [36] T.M. McCoy, A. Valiakhmetova, M.J. Pottage, C.J. Garvey, L. de Campo, C. Rehm, D.A. Kuryashov, R.F. Tabor, Structural evolution of wormlike micellar fluids formed by Erucyl Amidopropyl betaine with oil, salts, and surfactants, *Langmuir* 32 (2016) 12423–12433.
- [37] V.T. Kelleppan, J.E. Moore, T.M. McCoy, A.V. Sokolova, L. de Campo, B.L. Wilkinson, R.F. Tabor, Self-assembly of long-chain betaine surfactants: effect of tailgroup structure on wormlike micelle formation, *Langmuir* 34 (2017) 970–977.
- [38] D. Feng, Y. Zhang, Q. Chen, J. Wang, B. Li, Y. Feng, Synthesis and surface activities of amidobetaine surfactants with ultra-long unsaturated hydrophobic chains, *J. Surfactants Deterg.* 15 (2012) 657–661.
- [39] T.A. Darwish, E. Luks, G. Moraes, N.R. Yepuri, P.J. Holden, M. James, Synthesis of deuterated [D32] oleic acid and its phospholipid derivative [D64] dioleoyl-sn-glycero-3-phosphocholine, *J. Labelled Compd. Radiopharm.* 56 (2013) 520–529.
- [40] A. Sokolova, J. Christoforidis, A. Eltoaji, J. Barnes, F. Darmann, A.E. Whitten, L. de Campo, BILBY: Time-of-flight small angle scattering instrument, *Neutron News* 27 (2016) 9–13.
- [41] C. Rehm, A. Brülé, A.K. Freund, S.J. Kennedy, Kookaburra: the ultra-small-angle neutron scattering instrument at OPAL, *J. Appl. Crystallogr.* 46 (2013) 1699–1704.
- [42] C. Rehm, L. de Campo, KOOKABURRA: the ultra-small-angle neutron scattering instrument at ANSTO, *Neutron News* 27 (2016) 30–32.
- [43] C. Rehm, L.d. Campo, A. Brülé, F. Darmann, F. Bartsch, A. Berry, Design and performance of the variable-wavelength Bonse–Hart ultra-small-angle neutron scattering diffractometer KOOKABURRA at ANSTO, *J. Appl. Crystallogr.* 51 (2018) 1–8.
- [44] D. Kuryashov, O. Philippova, V. Molchanov, N.Y. Bashkirtseva, I. Diyarov, Temperature effect on the viscoelastic properties of solutions of cylindrical mixed micelles of zwitterionic and anionic surfactants, *Colloid J.* 72 (2010) 230–235.
- [45] J.S. Pedersen, P. Schurtenberger, Scattering functions of semiflexible polymers with and without excluded volume effects, *Macromolecules* 29 (1996) 7602–7612.
- [46] O. Glatter, The interpretation of real-space information from small-angle scattering experiments, *J. Appl. Crystallogr.* 12 (1979) 166–175.
- [47] R. Mittelbach, O. Glatter, Direct structure analysis of small-angle scattering data from polydisperse colloidal particles, *J. Appl. Crystallogr.* 31 (1998) 600–608.
- [48] G. Fritz, A. Bergmann, Interpretation of small-angle scattering data of inhomogeneous ellipsoids, *J. Appl. Crystallogr.* 37 (2004) 815–822.
- [49] L. Ziserman, L. Abezgauz, O. Ramon, S.R. Raghavan, D. Danino, Origins of the viscosity peak in wormlike micellar solutions. 1. Mixed cationic surfactants. A cryo-transmission electron microscopy study, *Langmuir* 25 (2009) 10483–10489.
- [50] D. Danino, Cryo-TEM of soft molecular assemblies, *Curr. Opin. Colloid Interface Sci.* 17 (2012) 316–329.
- [51] W.-R. Chen, P.D. Butler, L.J. Magid, Incorporating intermicellar interactions in the fitting of SANS data from cationic wormlike micelles, *Langmuir* 22 (2006) 6539–6548.
- [52] B.A. Schubert, E.W. Kaler, N.J. Wagner, The microstructure and rheology of mixed cationic/anionic wormlike micelles, *Langmuir* 19 (2003) 4079–4089.
- [53] L. Magid, Z. Han, Z. Li, P. Butler, Tuning microstructure of cationic micelles on multiple length scales: The role of electrostatics and specific ion binding, *Langmuir* 16 (2000) 149–156.
- [54] C. Oelschlaeger, P. Suwita, N. Willenbacher, Effect of counterion binding efficiency on structure and dynamics of wormlike micelles, *Langmuir* 26 (2010) 7045–7053.
- [55] C. Tanford, Micelle shape and size, *J. Phys. Chem.* 76 (1972) 3020–3024.
- [56] L. Feigin, D.I. Svergun, G.W. Taylor, General principles of small-angle diffraction, in: *Structure Analysis by Small-angle X-ray and Neutron Scattering*, Springer, 1987, pp. 25–55.
- [57] J.B. Hayter, J. Penfold, Determination of micelle structure and charge by small-angle neutron scattering, *Colloid Polym. Sci.* 261 (1983) 1022–1030.
- [58] J.B. Hayter, J. Penfold, Self-consistent structural and dynamic study of concentrated micelle solutions, *J. Chem. Soc., Faraday Trans. I* 77 (1981) 1851–1863.
- [59] G. Porte, Micellar growth, flexibility and polymorphism in dilute solutions, in: *Micelles, Membranes, Microemulsions, and Monolayers*, Springer, 1994, pp. 105–151.
- [60] K. Shimoni, D. Danino, Imperfect dissolution in nonionic block copolymer and surfactant mixtures, *Langmuir* 25 (2009) 2736–2742.
- [61] A. Bernheim-Groswasser, E. Wachtel, Y. Talmon, Micellar growth, network formation, and criticality in aqueous solutions of the nonionic surfactant C12E5, *Langmuir* 16 (2000) 4131–4140.
- [62] P.A. FitzGerald, K. Chatjaroenporn, X. Zhang, G.G. Warr, Micellization of monomeric and poly- ω -methacryloyloxyundecyltrimethylammonium surfactants, *Langmuir* 27 (2011) 11852–11859.
- [63] A. Guinier, G. Fournet, C. Walker, *Small Angle Scattering of X-rays*, J. Wiley & Sons, New York, 1955.
- [64] J. Polak, B.C.-Y. Lu, Mutual solubilities of hydrocarbons and water at 0 and 25°, *Can. J. Chem.* 51 (1973) 4018–4023.
- [65] H. Hoffmann, W. Ulbricht, Transition of rodlike to globular micelles by the solubilization of additives, in: *Physics of Amphiphilic Layers*, Springer, 1987, pp. 334–345.
- [66] H. Hoffmann, G. Ebert, Surfactants, micelles and fascinating phenomena, *Angew. Chem. Int. Ed.* 27 (1988) 902–912.
- [67] U. Menge, P. Lang, G. Findenegg, From oil-swollen wormlike micelles to microemulsion droplets: a static light scattering study of the L1 phase of the system water+ C12E5+ decane, *J. Phys. Chem. B* 103 (1999) 5768–5774.
- [68] U. Menge, P. Lang, G. Findenegg, P. Strunz, Structural transition of oil-swollen cylindrical micelles of C12E5 in water studied by SANS, *J. Phys. Chem. B* 107 (2003) 1316–1320.
- [69] C. Rodriguez-Abreu, K. Aramaki, Y. Tanaka, M.A. Lopez-Quintela, M. Ishitobi, H. Kunieda, Wormlike micelles and microemulsions in aqueous mixtures of sucrose esters and nonionic cosurfactants, *J. Colloid Interface Sci.* 291 (2005) 560–569.
- [70] T. Sato, D.P. Acharya, M. Kaneko, K. Aramaki, Y. Singh, M. Ishitobi, H. Kunieda, Oil-induced structural change of wormlike micelles in sugar surfactant systems, *J. Dispers. Sci. Technol.* 27 (2006) 611–616.
- [71] M. Miyake, A. Asano, Y. Einaga, Size change of the wormlike micelles of pentaerythritol, hexaoxyethylene, and heptaerythritol dodecyl ethers with uptake of n-dodecane, *J. Phys. Chem. B* 112 (2008) 4648–4655.
- [72] A.V. Shibaev, M.V. Tamm, V.S. Molchanov, A.V. Rogachev, A.I. Kuklin, E.E. Dormidontova, O.E. Philippova, How a viscoelastic solution of wormlike micelles transforms into a microemulsion upon absorption of hydrocarbon: new insight, *Langmuir* 30 (2014) 3705–3714.
- [73] D. Danino, L. Abezgauz, I. Portnaya, N. Dan, From discs to ribbons networks: the second critical micelle concentration in nonionic sterol solutions, *J. Phys. Chem. Lett.* 7 (2016) 1434–1439.
- [74] V.S. Molchanov, O.E. Philippova, A.R. Khokhlov, Y.A. Kovalev, A.I. Kuklin, Self-assembled networks highly responsive to hydrocarbons, *Langmuir* 23 (2007) 105–111.
- [75] A.V. Shibaev, V.S. Molchanov, O.E. Philippova, Rheological behavior of oil-swollen wormlike surfactant micelles, *J. Phys. Chem. B* 119 (2015) 15938–15946.
- [76] J. Eastoe, K.J. Hetherington, J.S. Dalton, D. Sharpe, J.R. Lu, R.K. Heenan, Microemulsions with didodecyltrimethylammonium bromide studied by neutron contrast variation, *J. Colloid Interface Sci.* 190 (1997) 449–455.
- [77] L. Arleth, J.S. Pedersen, Droplet polydispersity and shape fluctuations in AOT [bis (2-ethylhexyl) sulfosuccinate sodium salt] microemulsions studied by contrast variation small-angle neutron scattering, *Phys. Rev. E* 63 (2001) 061406.
- [78] D. Wade, Deuterium isotope effects on noncovalent interactions between molecules, *Chem.-Biol. Interact.* 117 (1999) 191–217.
- [79] D. Varade, C. Rodríguez-Abreu, J.G. Delgado, K. Aramaki, Viscoelasticity and mass transfer in phenol–CTAB aqueous systems, *Colloid Polym. Sci.* 285 (2007) 1741–1747.
- [80] M. Singh, C. Ford, V. Agarwal, G. Fritz, A. Bose, V.T. John, G.L. McPherson, Structural evolution in cationic micelles upon incorporation of a polar organic dopant, *Langmuir* 20 (2004) 931–9937.
- [81] T.H. Ito, P.C. Miranda, N.H. Morgon, G. Heerdt, C.A. Dreiss, E. Sabadini, Molecular variations in aromatic cosolutes: critical role in the rheology of cationic wormlike micelles, *Langmuir* (2014).
- [82] Z. Yan, C. Dai, M. Zhao, G. Zhao, Y. Li, X. Wu, Y. Liu, M. Du, Multi-responsive wormlike micelles based on N-alkyl-N-methylpiperidinium bromide cationic surfactant, *J. Surfactants Deterg.* 18 (2015) 739–746.
- [83] A. Ping, P. Geng, X. Wei, J. Liu, J. Zhang, D. Sun, X. Guo, M. Yang, Rheological properties of wormlike micelles formed in aqueous systems of 3-Alkoxy-2-hydroxypropyl trimethyl ammonium bromides in the presence of sodium octanoate, *J. Surfactants Deterg.* 18 (2015) 1117–1126.
- [84] J.E. Moore, T.M. McCoy, L. de Campo, A.V. Sokolova, C.J. Garvey, G. Pearson, B.L. Wilkinson, R.F. Tabor, Wormlike micelle formation of novel alkyl-tri (ethylene glycol)-glucoside carbohydrate surfactants: Structure–function relationships and rheology, *J. Colloid Interface Sci.* (2018).
- [85] O. Glatter, G. Fritz, H. Lindner, J. Brunner-Popela, R. Mittelbach, R. Strey, S.U. Egelhaaf, Nonionic micelles near the critical point: micellar growth and attractive interaction, *Lang.* (2000).

- [86] S.R. Raghavan, H. Edlund, E.W. Kaler, Cloud-point phenomena in wormlike micellar systems containing cationic surfactant and salt, *Langmuir* 18 (2002) 1056–1064.
- [87] Z. Lin, J. Cai, L. Scriven, H. Davis, Spherical-to-wormlike micelle transition in CTAB solutions, *J. Phys. Chem.* 98 (1994) 5984–5993.
- [88] V. Aswal, P. Goyal, P. Thiagarajan, Small-angle neutron-scattering and viscosity studies of CTAB/NaSal viscoelastic micellar solutions, *J. Phys. Chem. B* 102 (1998) 2469–2473.
- [89] A.R. Rakitin, G.R. Pack, Necessity of aromatic carboxylate anions to be planar to induce growth of cationic micelles, *Langmuir* 21 (2005) 837–840.
- [90] R.K. Rodrigues, M.A. da Silva, E. Sabadini, Worm-like micelles of CTAB and sodium salicylate under turbulent flow, *Langmuir* 24 (2008) 3875–3879.
- [91] V. Lutz-Bueno, S. Isabetini, F. Walker, S. Kuster, M. Liebi, P. Fischer, Ionic micelles and aromatic additives: a closer look at the molecular packing parameter, *Phys. Chem. Chem. Phys.* 19 (2017) 21869–21877.
- [92] P.-G. de Gennes, *Scaling Concepts in Polymer Physics*, Cornell University Press, 1979.
- [93] D.F.R. Mildner, P.L. Hall, Small-angle scattering from porous solids with fractal geometry, *J. Phys. D: Appl. Phys.* 19 (1986) 1535–1545.
- [94] G. Bushell, Y. Yan, D. Woodfield, J. Raper, R. Amal, On techniques for the measurement of the mass fractal dimension of aggregates, *Adv. Colloid Interface Sci.* 95 (2002) 1–50.
- [95] J. Berghausen, J. Zipfel, P. Lindner, W. Richtering, Influence of water-soluble polymers on the shear-induced structure formation in lyotropic lamellar phases, *J. Phys. Chem. B* 105 (2001) 11081–11088.
- [96] F. Lequeux, Reptation of connected wormlike micelles, *EPL* 19 (1992) 675.
- [97] T. Drye, M. Cates, Living networks: The role of cross-links in entangled surfactant solutions, *J. Chem. Phys.* 96 (1992) 1367–1375.
- [98] R. Granek, M. Cates, Stress relaxation in living polymers: results from a Poisson renewal model, *J. Chem. Phys.* 96 (1992) 4758–4767.
- [99] S.A. Rogers, M.A. Calabrese, N.J. Wagner, Rheology of branched wormlike micelles, *Curr. Opin. Colloid Interface Sci.* 19 (2014) 530–535.

Supplementary Material - The effects of small molecule organic additives on the self-assembly and rheology of betaine wormlike micellar fluids

Thomas M. McCoy,¹ Joshua P. King,¹ Jackson E. Moore,¹ Veena T. Kelleppan,¹
Anna V. Sokolova,² Liliana de Campo,² Madhura Manohar,³ Tamim A. Darwish,³
Rico F. Tabor^{1,*}

¹School of Chemistry, Monash University, Clayton 3800, Australia

²Australian Centre for Neutron Scattering, ANSTO, Lucas Heights, New South Wales 2234, Australia

³National Deuteration Facility, ANSTO, Lucas Heights, New South Wales 2234, Australia

*To whom correspondence should be addressed; E-mail: rico.tabor@monash.edu

This document includes all details and fitting parameters used in the modelling of the SANS and USANS data presented in the main paper, as well as characterisation details for the deuterated surfactant. The SasView models used for fitting SANS data include: flexible cylinders (worms),^{1,2} cylinders (rods),³ spheres and core-shell spheres.⁴ For USANS data modelling was achieved using power laws. A summary of the physicochemical properties for each organic additive are present in Table S2.

Table S1: Chemical properties of oleyl amidopropyl betaine (OAPB) and deuterated oleyl amidopropyl betaine (D33-OAPB). Note the significant difference in scattering length density (SLD) for the hydrogenated and deuterated tail-groups.

Surfactant	Appearance	Chemical formula	Molecular weight g/mol	SLD (tail) $\text{\AA}^{-2} \times 10^{-6}$
OAPB	Waxy yellow solid	$\text{C}_{25}\text{H}_{48}\text{O}_3\text{N}_2$	424.66	0.078
D33-OAPB	Waxy colourless solid	$\text{C}_{25}\text{H}_{15}\text{D}_{33}\text{O}_3\text{N}_2$	457.57	5.936

H NMR and mass spectrometry characterisation of D33-OAPB

Intermediate product: D33-N-(3-(dimethylamino)propyl)oleamide

^1H NMR (400 MHz, CDCl_3): ^2H NMR (60 MHz, CDCl_3): δ 5.29, 2.03, 1.87, 1.45, 1.13, 0.73 ppm;
 ^{13}C NMR (100.6 MHz, CDCl_3): δ 174.3 (CO), 129.7 (C=CH), 57.8 (CH_2), 45.3 ($\text{CH}_3 \times 2$), 38.5 (CH_2), 26.5 (CH_2) ppm

Electrospray mass spectrum (+ve) m/z: D₃₃ chain predicted: 400.57 $[\text{M}+\text{H}]^+$, found: 400.62 $[\text{M}+\text{H}]^+$ with isotopic distribution D₃₃: 2.7%, D₃₂: 30%, D₃₁: 27%, D₃₀: 23%, D₂₉: 11%

Final product: D33-2-(dimethyl(3-oleamidopropyl)ammonio)acetate

^1H NMR (400 MHz, CDCl_3): 8.06 (d, 1H), 5.27 (s, 1H), 3.59 (s, 2H), 3.20 (s, 6H), 1.93 (s, 2H); ^2H NMR (60 MHz, CDCl_3): δ 5.30, 1.89, 1.16, 0.76 ppm; ^{13}C NMR (100.6 MHz, CDCl_3): δ 174.3 (CO), 166.25 (CO), 129.6 (C=CH), 64.89 (CH_2), 62.97 (CH_2), 50.18 ($\text{CH}_3 \times 2$), 36.19 (CH_2), 23.10 (CH_2) ppm

Electrospray mass spectrum (+ve) m/z: Predicted 480.85 $[\text{M}+\text{Na}]^+$, found: D33: 480.6 $[\text{M}+\text{Na}]^+$ with isotopic distribution D₃₃: 2.9%, D₃₂: 28%, D₃₁: 30%, D₃₀: 23%, D₂₉: 11%

Table S2: Physicochemical properties for all organic additives used in this study. The reported solubilities are at approximately 25°C, and for the hydrocarbon additives were determined by gas chromatography.^{5,6}

Additive	Appearance	Molecular weight g/mol	Density g/mL	Aqueous solubility mM	pK_a	Dipole moment D	Aromaticity	SLD $\text{\AA}^{-2} \times 10^{-6}$
Heptane	liquid	100.21	0.68	0.034	50	0.0	Non-aromatic	-0.80
Methylcyclohexane	liquid	98.19	0.77	0.030	50	0.0	Non-aromatic	-0.36
Toluene	liquid	92.14	0.87	6.22	41	0.36	Aromatic	1.09
<i>p</i> -xylene	liquid	106.16	0.86	1.74	41	0.0	Aromatic	0.90
<i>p</i> -xylene-D10	liquid	116.23	0.95	-	41	0.0	Aromatic	6.21
Cyclohexanol	solid	100.16	0.96	359.4	16	1.85	Non-aromatic	0.05
Phenol	solid	94.11	1.07	894.7	10	1.22	Aromatic	1.45
Benzyl alcohol	liquid	108.14	1.04	323.7	15.4	1.67	Aromatic	1.25
Benzoic acid	solid	122.12	1.27	24.6	4.2	1.72	Aromatic	1.76
Salicylic acid	solid	138.12	1.44	14.5	3.0, 13.8	2.65	Aromatic	1.81

Table S3: SANS fitting parameters for pure OAPB solutions at different concentrations, using either a flexible cylinder (worms) model or cylinder (rods) model. Scattering length densities of the solvent (D_2O) and micelles were kept constant at 6.3 and $1 \times 10^{-6} \text{ \AA}^{-2}$ respectively. A polydispersity value of 10% was applied to the radius of the worms and cylinders.

[OAPB] mM	Model	Length nm	Kuhn length nm	Radius nm
1	Worms	239.4	63.9	2.6
5	Worms	357.2	67.9	2.3
10	Worms	321.5	80.4	2.3
20	Cylinders	61.0	-	2.1
50	Cylinders	54.4	-	2.1

Table S4: SANS fitting parameters for OAPB with different concentrations of *n*-heptane. Scattering length densities of the solvent (D_2O) and micelles were kept constant at 6.3 and $1 \times 10^{-6} \text{ \AA}^{-2}$ respectively. A polydispersity value of 10% was applied to the radius of the worms (R_{worms}). The polydispersity for the radius of spheres ($R_{spheres}$) was determined from the fitting algorithm. For modelling the sample with 10 mM heptane, an additive model of spheres and worms was used in which the polydispersity of all radii was set to 15%.

[OAPB] mM	Additive	[Additive] mM	Model	$R_{spheres}$ nm	Polydispersity spheres %	Length nm	Kuhn length nm	R_{worms} nm
10	-	-	Worms	-	-	321.5	80.4	2.3
10	Heptane	5	Worms	-	-	227.8	97.9	2.4
10	Heptane	10	Spheres + Worms	3.1	-	157.3	91.1	2.5
10	Heptane	15	Spheres	3.9	10.9	-	-	-
10	Heptane	20	Spheres	3.9	11.1	-	-	-

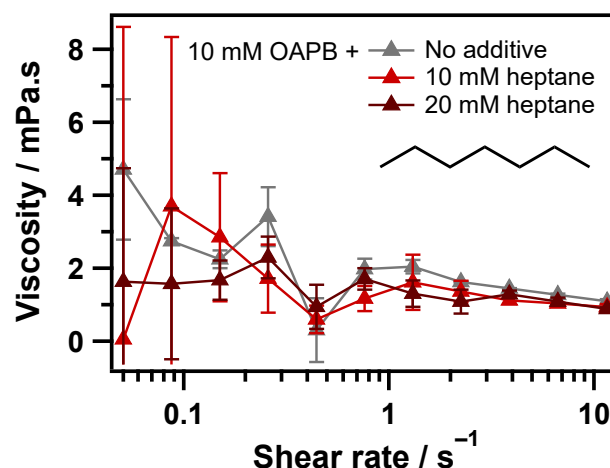


Figure S1: Dynamic viscosity data for solutions of OAPB with *n*-heptane in water. The inset is the chemical structure of *n*-heptane.

Table S5: SANS fitting parameters for OAPB with different concentrations of methylcyclohexane. Scattering length densities of the solvent (D_2O) and micelles were kept constant at 6.3 and $1 \times 10^{-6} \text{ \AA}^{-2}$ respectively. A polydispersity value of 10% was applied to the radius of the worms (R_{worms}). The polydispersity for the radius of spheres ($R_{spheres}$) was determined from the fitting algorithm.

[OAPB] mM	Additive	[Additive] mM	Model	$R_{spheres}$ nm	Polydispersity spheres %	Length nm	Kuhn length nm	R_{worms} nm
10	-	-	Worms	-	-	321.5	80.4	2.3
10	Methylcyclohexane	5	Worms	-	-	345.4	85.7	2.4
10	Methylcyclohexane	10	Worms	-	-	305.2	186.3	2.5
10	Methylcyclohexane	15	Spheres	4.6	10.4	-	-	-
10	Methylcyclohexane	20	Spheres	4.5	10.3	-	-	-
10	Methylcyclohexane	30	Spheres	5.1	10.6	-	-	-

Table S6: SANS fitting parameters for OAPB with different concentrations of toluene. Scattering length densities of the solvent (D_2O) and micelles were kept constant at 6.3 and $1 \times 10^{-6} \text{ \AA}^{-2}$ respectively. A polydispersity value of 10% was applied to the radius of the worms (R_{worms}). The polydispersity for the radius of spheres ($R_{spheres}$) was determined from the fitting algorithm.

[OAPB] mM	Additive	[Additive] mM	Model	$R_{spheres}$ nm	Polydispersity spheres %	Length nm	Kuhn length nm	R_{worms} nm
10	-	-	Worms	-	-	321.5	80.4	2.3
10	Toluene	5	Worms	-	-	378.4	80.4	2.3
10	Toluene	10	Worms	-	-	441.1	82.6	2.4
10	Toluene	20	Worms	-	-	997.4	99.7	2.7
10	Toluene	30	Spheres	5.0	11.0	-	-	-
10	Toluene	50	Spheres	6.5	10.9	-	-	-

Table S7: SANS fitting parameters for OAPB with different concentrations of cyclohexanol. Scattering length densities of the solvent (D_2O) and micelles were kept constant at 6.3 and $1 \times 10^{-6} \text{ \AA}^{-2}$ respectively. A polydispersity value of 10% was applied to the radius of the worms.

[OAPB] mM	Additive	[Additive] mM	Model	Length nm	Kuhn length nm	Radius nm
10	-	-	Worms	321.5	80.4	2.3
10	Cyclohexanol	10	Worms	311.2	74.4	2.3
10	Cyclohexanol	20	Worms	365.5	73.3	2.3
10	Cyclohexanol	50	Worms	373.6	62.7	2.2
10	Cyclohexanol	100	Worms	367.7	44.8	2.1

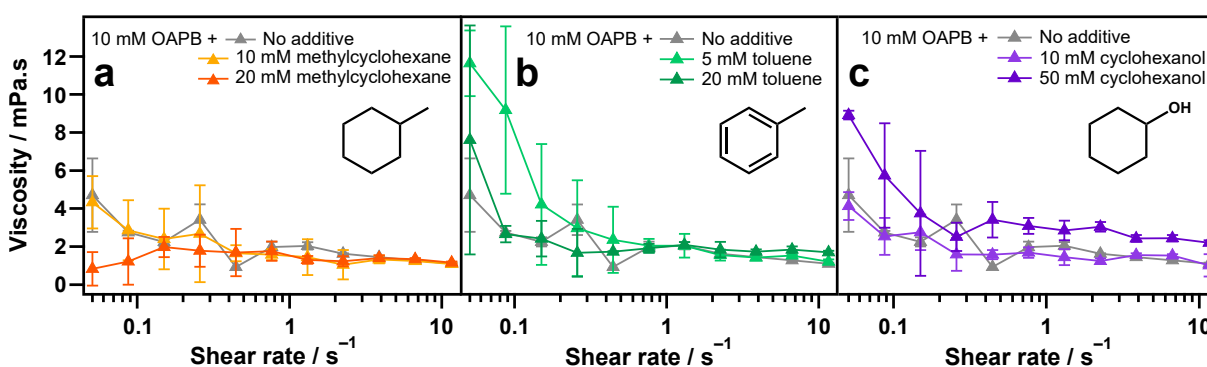


Figure S2: (a-c) Dynamic viscosity data for solutions of OAPB with methylcyclohexane (a), toluene (b) and cyclohexanol (c) in water. Insets are the chemical structures of each additive.

Table S8: SANS fitting parameters for OAPB with different concentrations of *p*-xylene. Scattering length densities of the solvent (D_2O) and micelles were kept constant at 6.3 and $1 \times 10^{-6} \text{ \AA}^{-2}$ respectively. A polydispersity value of 10% was applied to the radius of the worms (R_{worms}). The polydispersity for the radius of spheres ($R_{spheres}$) was determined from the fitting algorithm.

[OAPB] mM	Additive	[Additive] mM	Model	$R_{spheres}$ nm	Polydispersity spheres %	Length nm	Kuhn length nm	R_{worms} nm
10	-	-	Worms	-	-	321.5	80.4	2.3
10	<i>p</i> -Xylene	5	Worms	-	-	402.0	84.2	2.4
10	<i>p</i> -Xylene	10	Worms	-	-	332.3	96.3	2.7
10	<i>p</i> -Xylene	15	Spheres	4.5	10.1	-	-	-
10	<i>p</i> -Xylene	20	Spheres	5.0	9.8	-	-	-
10	<i>p</i> -Xylene	30	Spheres	6.2	10.8	-	-	-

Table S9: SANS fitting parameters for OAPB with different concentrations of *p*-xylene-D10. Scattering length densities of the solvent (D_2O) and micelle shells were kept constant at 6.3 and $1 \times 10^{-6} \text{ \AA}^{-2}$ respectively. Due to the difference in SLD of the deuterated *p*-xylene (Table 2), samples with a spherical form factor were modelled with a core-shell sphere model instead of a standard sphere model, as with the other systems. Therefore, calculation of the scattering length density for the micelle core (SLD core) was included in the fitting algorithm. A polydispersity value of 10% was applied to the radius of the worms (R_{worms}). No polydispersity was included in data modelled with core-shell spheres.

[OAPB] mM	Additive	[Additive] mM	Model	R_{core} nm	Shell thickness nm	SLD core $\times 10^{-6} \text{ \AA}^{-2}$	Length nm	Kuhn length nm	R_{worms} nm
10	-	-	Worms	-	-	-	321.5	80.4	2.3
10	<i>p</i> -Xylene-D10	5	Worms	-	-	-	279.7	82.7	2.5
10	<i>p</i> -Xylene-D10	10	Worms	-	-	-	285.3	92.2	2.9
10	<i>p</i> -Xylene-D10	15	Core-shell spheres	2.1	2.9	4.65	-	-	-
10	<i>p</i> -Xylene-D10	20	Core-shell spheres	2.7	3.0	5.48	-	-	-
10	<i>p</i> -Xylene-D10	30	Core-shell spheres	3.7	3.2	5.47	-	-	-

Table S10: SANS fitting parameters for d-OAPB with different concentrations of *p*-xylene. Scattering length densities of the solvent (D₂O) and micelles were kept constant at 6.3 and $1 \times 10^{-6} \text{ \AA}^{-2}$ respectively. No polydispersity was applied to the radius of the worms or cylinders. The polydispersity for the radius of spheres ($R_{spheres}$) in the 30 mM *p*-xylene data set was determined from the fitting algorithm.

[D33-OAPB] mM	Additive	[Additive] mM	Model	$R_{spheres}$ nm	Polydispersity spheres %	Length nm	Kuhn length nm	Radius nm
10	-	-	Worms	-	-	609510.0	40.0	4.1
10	<i>p</i> -Xylene	5	Worms	-	-	84020.0	48.2	3.5
10	<i>p</i> -Xylene	10	Worms	-	-	5463.7	65.1	3.3
10	<i>p</i> -Xylene	15	Worms	-	-	4841.8	71.7	3.3
10	<i>p</i> -Xylene	20	Cylinders	-	-	321.7	-	3.2
10	<i>p</i> -Xylene	30	Spheres	5.2	15.9	-	-	-

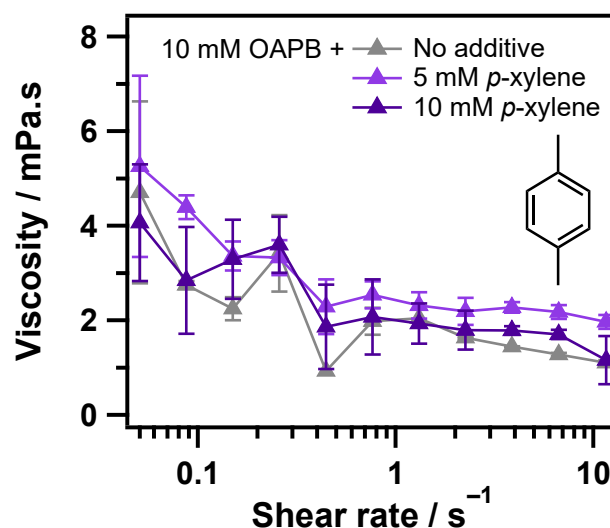


Figure S3: Dynamic viscosity data for solutions of OAPB with *p*-xylene in water. The inset is the chemical structure of *p*-xylene.

Table S11: SANS fitting parameters for OAPB with different concentrations of phenol. Scattering length densities of the solvent (D_2O) and micelles were kept constant at 6.3 and $1 \times 10^{-6} \text{ \AA}^{-2}$ respectively. A polydispersity value of 10% was applied to the radius of the worms.

[OAPB] mM	Additive	[Additive] mM	Model	Length nm	Kuhn length nm	Radius nm
10	-	-	Worms	321.5	80.4	2.3
10	Phenol	10	Worms	445.9	73.4	2.3
10	Phenol	20	Worms	382.4	71.6	2.3
10	Phenol	30	Worms	422.5	43.1	2.2

Table S12: SANS fitting parameters for OAPB with different concentrations of benzyl alcohol. Scattering length densities of the solvent (D_2O) and micelles were kept constant at 6.3 and $1 \times 10^{-6} \text{ \AA}^{-2}$ respectively. A polydispersity value of 10% was applied to the radius of the worms.

[OAPB] mM	Additive	[Additive] mM	Model	Length nm	Kuhn length nm	Radius nm
10	-	-	Worms	321.5	80.4	2.3
10	Benzyl alcohol	10	Worms	289.5	72.1	2.3
10	Benzyl alcohol	20	Worms	387.3	72.5	2.2
10	Benzyl alcohol	50	Worms	350.1	64.2	2.2
10	Benzyl alcohol	100	Worms	348.7	51.3	2.1

Table S13: SANS fitting parameters for OAPB with different concentrations of benzoic acid and salicylic acid. Scattering length densities of the solvent (D_2O) and micelles were kept constant at 6.3 and $1 \times 10^{-6} \text{ \AA}^{-2}$ respectively. A polydispersity value of 10% was applied to the radius of the worms.

[OAPB] mM	Additive	[Additive] mM	Model	Length nm	Kuhn length nm	Radius nm
10	-	-	Worms	321.5	80.4	2.3
10	Benzoic acid	5	Worms	375.0	76.9	2.3
10	Benzoic acid	10	Worms	370.0	74.9	2.3
10	Salicylic acid	5	Worms	412.6	71.2	2.3
10	Salicylic acid	10	Cylinders	127.1	-	2.1

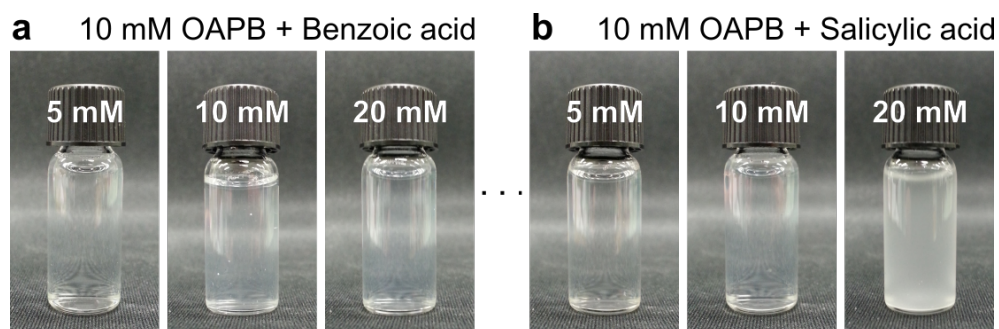


Figure S4: Samples containing 10 mM OAPB and the specified concentrations of benzoic acid (a) and salicylic acid (b).

Table S14: USANS two-power law fitting parameters for OAPB with different concentrations of the specified organic additives. In all instances, background was omitted from the fitting (i.e. set to 0). Note: a single power law was used to model the sample with 10 mM benzyl alcohol.

[OAPB] mM	Additive	[Additive] mM	Lower q power	Higher q power	Crossover point $\text{\AA}^{-1} \times 10^{-4}$
10	-	-	0.16	1.35	9.82
50	-	-	3.34	0.50	3.05
10	Phenol	10	2.90	1.05	3.43
10	Phenol	20	3.44	1.07	3.44
10	Phenol	30	2.16	1.43	6.08
10	Cyclohexanol	50	3.03	1.31	4.53
10	Cyclohexanol	100	3.99	1.26	2.15
10	Toluene	5	2.92	0.99	3.23
10	Toluene	20	2.82	1.11	5.96
10	Benzyl alcohol	10	-	0.96	-
10	Benzyl alcohol	50	3.17	1.02	2.86
10	Benzyl alcohol	100	3.83	0.89	1.57
10	Benzoic acid	5	2.67	1.32	3.79
10	Benzoic acid	10	2.86	1.36	3.49
10	Salicylic	5	2.64	1.20	3.74

References

- [1] Pedersen, J. S., Schurtenberger, P. Scattering Functions of Semiflexible Polymers with and without Excluded Volume Effects. *Macromolecules* **1996** *29*, 7602–7612.
- [2] Chen, W.-R., Butler, P. D., Magid, L. J. Incorporating intermicellar interactions in the fitting of SANS data from cationic wormlike micelles. *Langmuir* **2006** *22*, 6539–6548.
- [3] Feigin, L., Svergun, D. I., Taylor, G. W. General principles of small-angle diffraction. In *Structure analysis by small-angle X-ray and neutron scattering*. Springer, **1987**, pages 25–55.
- [4] Guinier, A., Fournet, G., Walker, C. *Small angle scattering of X-rays*. J. Wiley & Sons, New York, **1955**.
- [5] Polak, J., Lu, B. C.-Y. Mutual solubilities of hydrocarbons and water at 0 and 25°C. *Can. J. Chem.* **1973** *51*, 4018–4023.
- [6] Marche, C., Ferronato, C., Jose, J. Solubilities of Alkylcyclohexanes in Water from 30°C to 180°C. *J. Chem. Eng. Data* **2004** *49*, 937–940.